DETERMINATION OF LOAD PATH THROUGH CONCRETE CROSSTIE AND FASTENING SYSTEM: A LABORATORY AND FIELD INVESTIGATION

BY

SIHANG WEI

DISSERTATION

Submitted in partial fulfillment of the requirements
for the degree of Doctor of Philosophy in Civil Engineering
in the Graduate College of the
University of Illinois at Urbana-Champaign, 2017

Urbana, Illinois

Doctoral Committee:

Professor David A. Lange, Chair
Professor Daniel A. Kuchma, Director of Research
Professor Billie F. Spencer Jr.
Associate Professor Bassem O. Andrawes
Senior Lecturer and Research Scientist J. Riley Edwards

ABSTRACT

US railways move more freight (measured in tonne-kms) by rail than by any other means. This is done over an extensive network of primarily private freight railway lines that also transport passenger trains. To enable the expansion of high-speed passenger rail service using shared passenger/freight infrastructure, the US Department of Transportation Federal Railroad Administration (FRA) sponsored a research project to investigate infrastructure design and performance challenges. This is a multi-faceted research project for which one element is laboratory and field investigation of the load path from rail-wheel to precast concrete crossties.

In this research, the behavior of crosstie and fastening system is investigated through material-level, component-level and system-level laboratory and field experiments. The system-level experiments use three primary test setups. One of these setups, referred to as a static single-crosstie and fastening system experiment, enables the application of a downward and outward lateral force from the contact point of an idealize wheel through to the crosstie. Displacements and strains from each component were collected to understand the load path under simplified loading conditions. In addition to examining the factors that influence the flow of forces, a key objective of this work was to calibrate a means of displacement and strain measurements for use in rail corridors to determine the flow of forces from wheels through to crossties.

The second test setup uses the full-scale Track Loading System (TLS) to conduct similar tests and measurements over a multi-crosstie system in laboratory. A 22-feet long section of track including eleven concrete crossties that was loaded by vertical and lateral actuators over a 32-inch wheel set with varying ratios of lateral to vertical force from the wheel to rail.

The third test setup is the full-scale field experiment performed at the Transportation Technology Center (TTC) in Pueblo, CO. Five adjacent crossties in tangent and curved track were instrumented and loaded by Track Loading Vehicle (TLV) with static wheel loads. Dynamic tests were conducted with passenger and freight train consists at various speeds. Measurements including the wheel-rail interaction forces, rail seat vertical reactions, shoulder lateral reactions, and component strain and displacements.

The data collected from the three system-level experiments was used to clarify the load path, target areas of uncertainty, investigate the behavior of each component under extreme static loading and cyclical dynamic loading, as well as calibrate and validate a 3-D finite element model being developed at UIUC. In addition, this research offers suggestions for the instrumentation, testing, data-analysis and current design recommendations of concrete crosstie and fastening systems.

ACKNOWLEDGEMENT

I'm really honored and grateful to be involved in the UIUC RAILTEC research group since 2011. Without the tremendous help from the team, I couldn't have been even close to the goal of my research. This study is a part of a bigger project sponsored by Federal Railroad Administration (FRA), which is consisted by three major parts: laboratory experimentation, field experimentation and finite-element analysis. I feel that I focus on unveiling a big puzzle piece by piece, in which the great teamwork always motivate me and support me.

I am using this opportunity to express my gratitude to my advisor Professor Daniel A. Kuchma. Under his guidance and encouragement, I not only gained the ability to design and run experiments, but also learned to be kind, to be patient and never to give up. I would say Professor Daniel A. Kuchma opened the door to the railroad for me, J. Riley Edwards, Professor David A. Lange and Professor Bassem Andrawes lightened up the track for me running to the destination. Without J. Riley Edwards's remarkable leadership, we can never form such a strong team to combine various types of large-scale experiments with analytical work and complete in only three years. Only with Professor David A. Lange's extensive knowledge and great experience, the field trips to the Transportation Technology Center (TTC) can be possible and successful. I couldn't thank more to Professor Bassem Andrawes to the lessons on the finite-element analysis and suggestions on building a bridge between modeling and testing. This research project would not have been possible without the support from Marcus Dersch as the research engineer, his solid knowledge and professional coordination made everything flowing smoothly. I would also thank Profess Billie F. Spencer on the valuable advices on rail-vehicle dynamics.

Working with a great team has always been a fascinating process, and I would like to express my deepest appreciation to all my research partners: Justin Grasse, Christopher Rapp, Ryan Kernes, Thiago Bizarria, Kartik Manda, Brent Williams and Matthew Greve in field and laboratory testing, Zhe Chen, Moochul Shin and Zijian Zhang in finite-element modeling, and Brandon Van Dyk in international survey and load quantification.

I would also say I'm very lucky to work in the Newmark Lab, I acknowledge Timothy Prunkard, Mark Killion, Donald Marrow and Darold Marrow for their consistent support and friendship.

Contents

List of Figures

List of Tables

1. Introduction

To meet the demands of increasing freight axle loads and cumulative gross tonnages, as well as high-speed passenger rail development in North America, the performance and service life of concrete railway crossties must be improved. As a part of a study funded by the Federal Railroad Administration (FRA) aimed at improving the behavior of concrete crossties and fastening systems, laboratory and field experimentation was performed by a research team from the University of Illinois at Urbana-Champaign. The full load path from wheel-rail contact through concrete crosstie and fastening system to ballast was investigated using various instrumentations. The clarification of the load path will help to gain a deep understanding of the behavior of crossties and fasteners, and therefore will lead to build improved practices for design.

1.1 Research Background

Railroad crosstie provides support for the rails in the track system (**Figure 1.1**). Laid beneath the rails in the perpendicular direction, the crossties maintain the track gauge while supporting the rails. As support, crossties transfer and distribute loads from wheel-rail contact to ballast, withstand vertical, lateral and longitudinal movement of rail, perform as base plate for fastening systems to hold the rail, and also provide insulation between the two parallel rails (Taherinezhad et al. 2013). A constant distance between ties is used to prevent plastic deformation and track irregularities. The ties are placed on a layer of ballast over subgrade to distribute the loads more evenly, and to stabilize the track while providing some elasticity. The rail fastening system provides a means of mounting rails to crossties, which avoids the relative movement of rail and keeps the track gauge constant. The fastening system is consisted by a series of components including rail clamps, shoulders, rail pads, abrasion frames and insulators (for concrete crossties)

(**Figure 1.2**). When static and dynamic wheel loads are applied through the wheel-rail interaction, this rail-track system can be seen as a load distributing structure. In this system, the wheel loads transmit from rail to fastening components, then go through concrete crossties and reach ballast layer and subgrade.

Figure 1.1 Use of Crossties in Track System

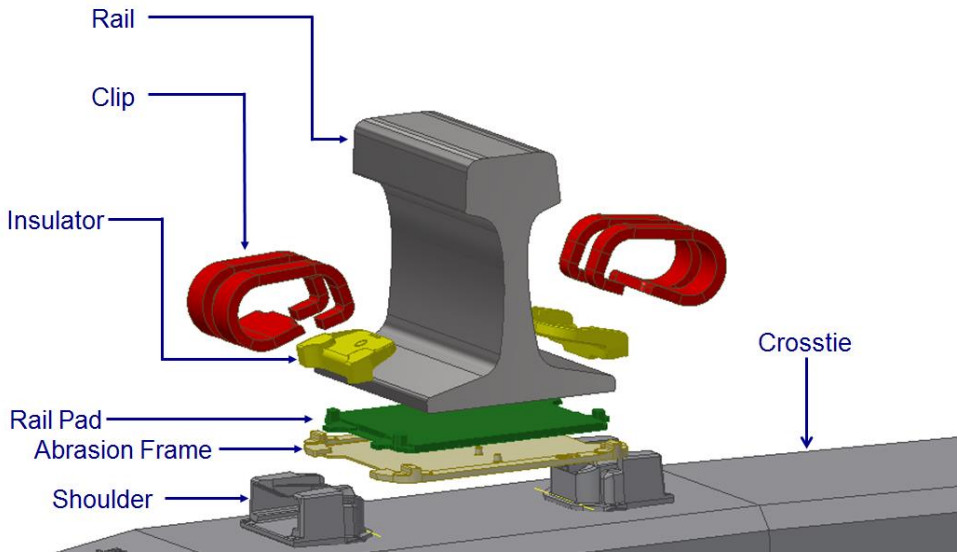

Figure 1.2 Assembly of Concrete Crosstie and Fastening System

As early as 1893, concrete crossties were used experimentally on railroad lines in United States (Hay, 1982). However, they were not used in major railway lines in North America until the first test installations were made on the Seaboard Airline and the Atlantic Coast Line in 1960s, which was pushed by the increasing costs of timber and the success of prestressed ties in Europe. In 1958, a completely new tie was designed for AMTRAK's requirements and installed in Wyoming and California in 1960. This tie was developed from the Gerwick monoblock tie but with a higher prestressing force (McQueen, 1983). About the same time, Santa Fe-Pomeroy installed a series of ties in 34 locations with a wide variety of climatic conditions and one location in heavy-haul mainline track. Since then, during the concrete tie design and installation practice, the knowledge of track forces has been accumulated and resulted in up-grading concrete tie specifications and recommendations. Through1970s, laboratory testing and field testing were carried to investigate the rail and fastener stress, as well as tie bending moments corresponding to different tie spacing which caused by static and dynamic wheel loads. Tests results were used

to optimize the design to meet the requirements, while computers were employed to achieve this goal for the first time.

Nowadays, prestressed concrete crossties are widely used globally, especially in Europe and Asia. As a comparison, as of January 2008 in North America, the market share for traditional wood ties was approximately 91.5%. The remaining is consisted by concrete, steel and composite ties (RT&S 2008). However, because of the excellent durability and capacity (IHHA 2009), the use of prestressed concrete crossties in the North American market is rapidly booming.

Comparing to the rest of the world, the operating environment of the railroad system in North America is unique: it allows the heavy axle freight traffic and high-speed passenger traffic sharing infrastructures. Because most of the current track systems were designed under the practices for slower-moving, heavy-axle freight trains, one challenge is to estimate the behavior of current system and upgrade this system to meet the new requirements.

1.2 Challenges of Running Heavy Haul and High Speed Passenger Train on Current Track Systems

The conventional track system is consisted by superstructure, including rails, crossties, fasteners, and substructure, including ballast, sub-ballast and subgrade. Different types of ballast-less track have been applied in the last decades; however, the ballasted tracks are still being used as the most popular around the world, even for high speed passenger trains (Taherinezhad et al. 2013).

To meet the requirement of running heavy haul and high speed passenger trains on the shared track system in North America, design of each components in this system needs to be studied and may be lead to upgrade. As stated in IHHA guidelines (2001), it is not adequate to

change one part of the railway system without examining its influence over the other parts of the system. For example, increasing car weight will affect the track and bridges in terms of capacity and deflections, changing rail properties may lead to unexpected wheel behavior, replacing wood ties by concrete ties will bring different rail seat load distribution, etc. (IHHA 2001). Therefore, a balance needs to be found to tie all the components to form a robust system. The key to build a successful track system is to ensure the stress level in the structural elements including the rails, crossties, fastenings and ballast and the materials comprising these elements never surpass their elastic limits (IHHA 2009). To judge whether or not a system can be considered as "successful", IHHA (2009) introduced some key performance indicators that have to be measured and treated as maintenance responses, including: axle load limit, kms of track under speed restriction, average track maintenance cost, track quality index, etc. Guided by these key performance indicators, measurements need to be taken to comprehensively evaluate the current crosstie and fastening system as a part of railroad infrastructure.

In the current design approach used in North America, the stress of each component in the rail and fastening system is kept below the elastic limit while a static or quasi-static wheel load multiplied by an impact factor is applied. And thus, it is crucial to know the relationship of train operating speed, axle load, track structure stiffness with the impact load multiplier in both vertical and lateral directions.

1.3 Need of Clarifying the Load Path from Wheel to Ballast Going Through Crosstie and Fastening Systems

Concrete crossties and fastening systems play an important role in the track system, as they connect the super-structure and sub-structure. Their performance is dependent on the structural properties of other components in this system, and their performance will influence the global

behavior of the system. When trains travel through the track super-structure, different types of loads which varying in a large range are applied to the rails. behavior of crosstie and fastening systems highly dependent on the magnitude and characteristics of these applied loads as well as their path. Therefore, a qualitative and quantitative understanding of how the loads transfer from super-structure to sub-structure is necessary to determine the demands each component in this system needs to withstand. Although many research and efforts have been established to quantify the applied wheel load and explore the load path in the track structure, no clear consensus has been reached.

The ultimate goal of the experimental investigation is to clarify the load path as well as structural behavior of each component under static and dynamic loading, which will lead to establish the knowledge requirements of upgrading the crosstie and fastening system to meet the structural and durability requirements of running heavy haul and high speed passenger trains. The purpose of laboratory experimentation is to enhance the understanding of the system behavior under simulated representative loading conditions. In addition, the controlled experiments in the laboratory environment result in fewer variables and clear boundary conditions, which could be used to validate the assumptions made in analytical and finite-element solutions. The increased control of variables also helps to clarify how much changing a parameter affected the system. The repeatable laboratory experiments also bring a large set of data that will lead to decrease the experimental error. The objective of field experimentation is to quantify and quantify the loading demands placed on the individual crosstie and fastening system components as well as the system as a whole under a variety of operational conditions. From the comparison with laboratory testing results, the source of this variety can be clarified. The influence of dynamic and impact loading to the system can also be examined via the field

experiments. Therefore, combining the laboratory and field experiments, a comprehensive understanding of the load path mechanics from the wheel-rail interface, through fastening system, into the concrete crosstie and reach the ballast can be established.

1.4 Objectives of Ph.D. Research

The overall objective of this research is to advance the understanding of the behavior of railroad crosstie and fastening systems under various loading cases so to develop mechanistic design approaches that supplant ineffective empirical practices. Specifically, the loading demands are to be quantified from literature review and field testing first. The magnitude of vertical and lateral wheel loads corresponding to different types of vehicles and speeds of trains is to be determined. Following this study of loading demands, the load transfer from wheel-rail interface through concrete crosstie and fastening systems to ballast is to be clarified through various measurements – including force, deflection, and strain measurements – in both laboratory and field testing. The load path under static loading is to be determined first, following with that under dynamic loading. The behavior of each component in the system, including concrete crosstie, fastening clip and rail pad under extreme static loading and cyclical dynamic loading will be examined and models developed when possible. Dynamic characters of the system will be examined and modeled when possible through field testing. The effect of impact loading will also be examined.

1.5 Organization of Thesis

Chapter 1 introduces the history and the present design situation for railroad track system with concrete crosstie and fastening systems, the challenge faced to running heavy axle freight car and

high-speed passenger car on shared track, the need of load path clarification, as well as the objective of the research.

Chapter 2 presents the relevant literature review, including: the benefit of using concrete crosstie instead of using wood ties, failure mode investigations, current wheel load databases, a review of the current design practices, and previous experimental studies and numerical modeling approaches.

Chapter 3 presents the laboratory and field study plan. Testing methods and facilities will be briefly introduced. Three levels of experimental plan including material – level, component – level and system – level will be described, and instrumentation and testing methodologies will also be reviewed.

Chapter 4 presents the major finding from load path analysis. Laboratory and field testing results will be expressed and discussed. How the load transfers from wheel to rail, and then distributes to supporting concrete crossties will be discussed. The system behavior under static and dynamic wheel loads will also be compared and presented.

Chapter 5 focuses on the analysis of concrete crosstie behavior. The crosstie loading and support conditions, as well as the bending moment distribution under typical wheel loads will be described. The crosstie design under the current design recommendations will be evaluated, and presented.

Chapter 6 presents the analysis of the structural behavior of fastening clips. Initial and change of clamping force, as calculated via strain measurements, will be given. Strain distribution along the clip will also be presented.

Chapter 7 will be the discussion of the effect of impact loading. The sources of impact loads will be studied from field investigation. With the help of finite-element modeling, the structural response mechanism will be clarified.

Chapter 8 will be conclusions of the findings obtained from the research. Suggestions for the current design procedure and recommendations for future research will be given.

2. Literature Review

2.1 Benefit of Using Concrete Crosstie to Replace the Traditional Wooden Crosstie

Traditional wooden crossties have been used for more than two hundred years. While making decision whether or not using concrete crossties to replace them, two basic criteria must be followed: performance and economics (Zarembski 1993). The performance criterion addresses the capability of components to sufficiently function and survive in the field environment. The economic criterion addresses whether the cost of the component is economic with respect to other similar products, however, it comes into play only if the first criterion (performance) is satisfied. Although the design of concrete crossties appeared a long time ago, they haven't been qualified to use in the field and adequate to withstand the severe loading environment of North American freight operations until as late as 1970s. Once the concrete crossties can function and survive in the heavy haul environment, i.e. they meet the performance criterion, commercial railways evaluated economic issues of using this alternative components to replace the traditional wooden crossties. However, making an economic comparison is complex due to the different lives, different maintenance activities exhibited in different crosstie and fastener systems. In addition, the lives and behavior of track component may vary significantly as function of track and traffic characteristics, as well as individual practices operated by each railroad company.

To effectively address the significant differences mentioned above, ZETA-TECH Associates, Inc. (Zarembski 1993) developed life cycle computer models. An analytical approach which comparing the "present worth" of each alternative system was utilized in the methodology incorporated in such models. For each system, initial costs and life cycle costs were compared. In life cycle costs, track characteristics, traffic characteristics, economic

characteristics and maintenance activities that influence the component lives and corresponding costs were considered. From such analysis, no single conclusion was made, i.e. which system was better. However, the benefits of wood vs. concrete crossties were found dependent on specific loading and environment conditions. For example, as shown in **Figure 2.1**, the Return on Investment (ROI) for concrete crosstie track is positive (indicating a benefit in replacing the wood ties by concrete ones) when the annual tonnage level is greater than approximately 32 MGT. This finding suggests that concrete crossties could be used for a heavy haul line in long term consideration.

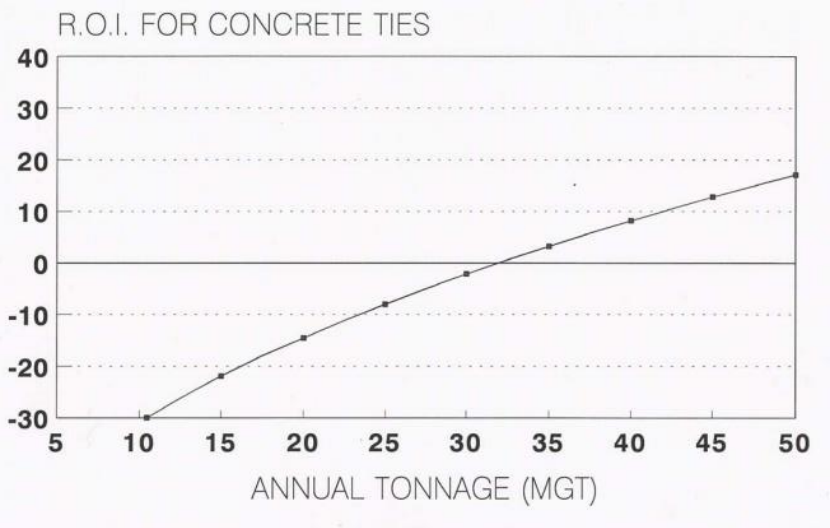

Figure 2.1 Economic Benefit Analysis of Wood vs. Concrete Ties (Zarembski 1993)

Rather than initial cost, strength, durability and stability offered by concrete crossties is important to successful operation of newer high speed trains (Kash 1983). Even though hardwood ties in North America are more plentiful and initially cheaper than concrete ties, the long-term economy of using concrete ties is considerable. There long-term benefits include the longer life which is 40 to 50 years for concrete vs. 25 years for wood, lower track maintenance costs, potential for higher safe speeds, fuel economy and longer rail life. The longer span

between two prestressed concrete crossties (24 inch comparing with 19.5 inch for wood ties) also results in a saving of 609 ties per mile.

2.2 Investigation of the Failure Mode of the Current Track System

From early research, the strength criteria were applied to reduce the tolerance level of track responses that might cause track damage (Doyle, 1974). The main track responses and the corresponding track failure modes are presented in **Table 2.1**.

Table 2.1 Relationship Between Track Response and Track Damage

Track Response	Track Damage
Rail head contact stresses	Rail batter and shelling
Rail shear forces and web shear stresses	Web and bolt hole failures
Rail bending moments	Rail fracture and fatigue
Sleeper loads	Ballast and Sleepers
Track displacement	Ballast

In their early use, concrete crossties had frequent failures both in the United States and abroad due to corrosion and loosening of fastenings, shattering under impact and crushing under the rail (Hay 1982). Prestressing is applied for concrete crossties are designed to resist bending moment failure with less weight. When extreme bending moments are applied, hairline cracks form at the lower fibers of a tie which will lead to failure. In a prestressed concrete crosstie, the existence of the prestressing strands restrains the cracking tendencies by holding them tightly

together (**Figure 2.2**). However, the success of prestressing is dominated by the bonding between contact surface of concrete and steel strands.

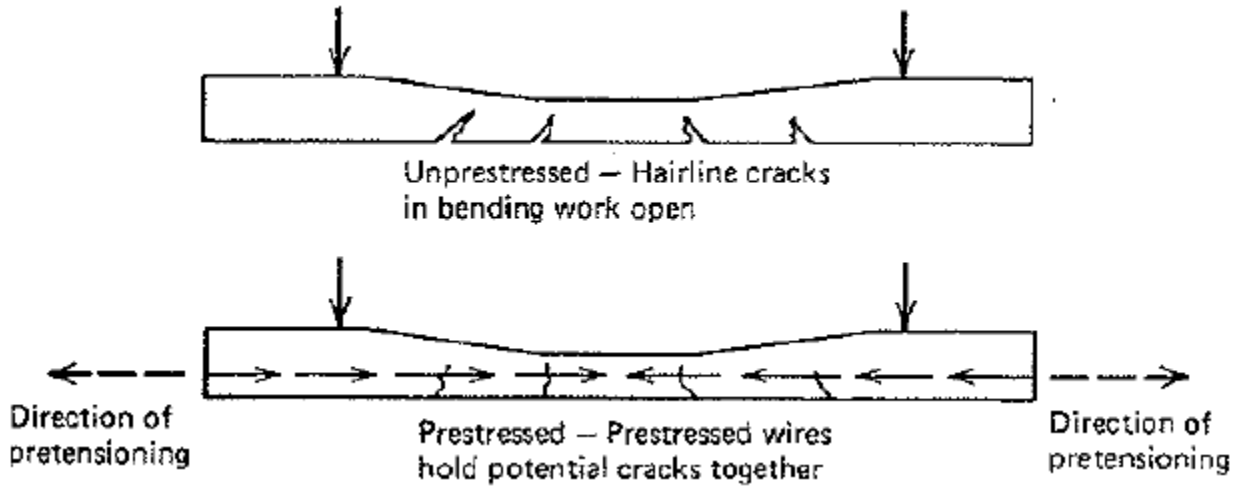

Figure 2.2 Concept of Prestressing in Concrete (Hay 1982)

Three basic modes are used to classify the failure of concrete crossties in ballasted track: support failure, stability failure and electrical isolation failure (Zeman 2009). Support failure leads to failing to adequately distribute loads from wheel-rail contact through concrete crosstie and fasteners to ballast. Support failure is usually found through the deterioration of other components in a track system, which including ballast crushing, subgrade failure, rail flaws and rail breaks. Stability failure is due to improper change of track geometry including gauge, surface, line and super-elevation. Electrical isolation failure occurs due to shunted track circuit when a concrete crosstie is exposed to a high moisture environment associated with broken, worn or missing insulators or tie pads on each rail seat. Zeman (2009) also pointed out several potential failure modes that need to be considered in design (**Table 2.2**).

Table 2.2 Potential Failure Causes for Processes Within the Failure Modes (Adapted from Zeman 2009)

Failure Mode Processes	Potential Failure Causes
Concrete Deterioration	Low concrete strength; low prestress force; high curing temperature; reactive aggregates; fines intrusion; moisture intrusion; low abrasion resistance (concrete); poor pore system in cement; prestress diameter too large; too much steel in the cross-section; pad too soft; pad too hard; pad geometry creates high hydraulic pressures; pad stiffness changes too much over time
Fastener Damage	Fines intrusion; moisture intrusion; pad too soft; pad too hard; pad geometry creates high hydraulic pressures; pad stiffness changes too much over time; insulator not durable enough; fastener design creates concentrated stresses; spring clip too stiff; spring clip too flexible; low fatigue strength for spring clip
Loss of Prestress	Low concrete strength; high prestress force; poor bonding surface on prestress; prestress diameter too large
Poor Bearing	Undersized bearing areas
Longitudinal Shoving	Low bottom and side friction with ballast
Lateral Shoving	Low bottom and side friction with ballast
Excessive Stiffness	High concrete strength; high prestress force

Zeman (2009) cooperated with the Association of American Railroads (AAR) and developed a survey for North American railroads and transit authorities requesting ranking values for prioritizing failure modes (**Table 2.3**). It was found from the survey, especially for the major railroads, the problems were more associated with wheel load due to higher traffic volumes and heavier axle loads. Rail seat deterioration (RSD), fastener wear, derailment damage and cracking from center binding were the most critical failure mode found from the survey.

Table 2.3 The Most Critical Concrete Tie Problems for Major North American Railroads; Ranked from 1 to 8 with 8 Being the Most Critical (Adapted from Zeman 2009)

Most Critical Concrete Crosstie Related Problems	Average Rank
Rail seat deterioration (RSD)	6.83
Shoulder/fastener wear or fatigue	6.67
Derailment damage	4.83
Cracking from center binding	4.58
Cracking from dynamic loads	1.83
Tamping damage	1.83
Other (ex: manufactured defect)	1.33
Cracking from environmental or chemical degradation	1.25

Van Dyk (2012) expended the source of the survey into 46 organizations, in which 28 responses were received from Asia (5), Australia (5), Europe (8) and North America (10). The updated failure mechanism is shown in **Table 2.4** (only for North American responses). The order of the causes of crosstie failure modes remained similar with Zeman's results (2009).

Table 2.4 The Most Critical Concrete Tie and Fastening System Problems According to North American Responses; Ranked from 1 to 8 with 8 Being the Most Critical (Adapted from Van Dyk 2012)

Most Critical Concrete Crosstie Related Problems	Average Rank
Deterioration of concrete material beneath the rail	6.43
Shoulder/fastening system wear or fatigue	6.38
Cracking from dynamic loads	4.83
Derailment damage	4.57
Cracking from center binding	4.50
Tamping damage	4.14
Other (e.g. manufactured defect)	3.57
Cracking from environmental or chemical degradation	3.50

The same information collected from the international respondents is shown in **Table 2.5**. The most critical problem expressed by the international respondents turned to be tamping damage. An interesting found from the survey was the deterioration of concrete material beneath the rail dropped from the top of the list according to North American responses to the bottom according to international responses.

Table 2.5 The Most Critical Concrete Tie and Fastening System Problems According to International Responses; Ranked from 1 to 8 with 8 Being the Most Critical (Adapted from Van Dyk 2012)

Most Critical Concrete Crosstie Related Problems	Average Rank
Tamping damage	6.14
Shoulder/fastening system wear or fatigue	5.50
Cracking from center binding	5.36
Cracking from dynamic loads	5.21
Cracking from environmental or chemical degradation	4.67
Derailment damage	4.57
Other (e.g. manufactured defect)	4.09
Deterioration of concrete material beneath the rail	3.15

The most prevalent failures result in the deficiencies of concrete crosstie and fastening system (Van Dyk 2012), there was also a contrast between the results from North American respondents (**Table 2.6**) and international respondents (**Table 2.7**). The concrete deterioration beneath the rail was expressed as the most common as well as the most severe failure causes in North America; while from the international respondents, the most prevalent failure cause was the fastening system damage. The possible reason for the large bias was believed to differences inthe manufacturing technique.

Table 2.6 The Most Prevalent Failure Causes Resulting in Concrete Crosstie and Fastening System Deficiencies According to North American Responses (Adapted from Van Dyk 2012)

Failure Causes Resulting in Deficiencies	Percentage of Responses (%)
Concrete deterioration beneath the rail	71
Fastening system damage	43
Poor bonding of concrete to prestress	43
Poor material quality or behavior (of clamp, insulator, rail pad, or crosstie)	29
Poor environmental conditions (e.g. moisture or fines intrusion)	29
Manufacturing flaws	29
Improper component design (of clamp, insulator, rail pad, or crosstie)	29
Deficient concrete strength	14
Improper prestress force	14
Other	14

Table 2.7 The Most Prevalent Failure Causes Resulting in Concrete Crosstie and Fastening System Deficiencies According to International Responses (Adapted from Van Dyk 2012)

Failure Causes Resulting in Deficiencies	Percentage of Responses (%)
Fastening system damage	50
Poor material quality or behavior (of clamp, insulator, rail pad, or crosstie)	44
Manufacturing flaws	44
Improper component design (of clamp, insulator, rail pad, or crosstie)	38
Concrete deterioration beneath the rail	38
Poor environmental conditions (e.g. moisture or fines intrusion)	31
Other	31
Poor bonding of concrete to prestress	25
Deficient concrete strength	19
Improper prestress force	6

In Sweden, Thun (2007) found some concrete crossties started to crack after only 10 – 15 years, some of which experienced a severe deterioration that even lost their bearing capacity. Out of 3 million concrete crossties that have been inspected, approximately 500,000 crossties suffered from more or less severe cracking. The main cause of the cracking was believed to be due to Delayed Ettringite Formation (DEF). DEF has been discussed in the concrete community during the last a few years and is believed leading to an internal expansion then cracking gradually. DEF may also be accelerated if the crosstie is exposed in extreme weather condition that associated with moisture or cyclic frost erosion (Thun et al. 2008). As DEF damage has been broadly reported as a main cause of the concrete crosstie damage, many countries have

developed recommendations, in which the use of heat curing is being paid particular attention. Thun et al. also classified the types of concrete cracking on a crosstie based on its severity. Three classes were used, the typical damage for each class was no visible cracks, initial degradation, and severe cracking. **Figure 2.3** shows several types of typical cracking found from multiple concrete crossties. Vertical cracks developed from the fasteners downward and crack pattern propagating at the end of the crossties were believed to be less severe, and no significant degradation of load carrying capacity was found. Densely covered cracking at the end of crossties, horizontal cracks generated at the crosstie center, and severe vertical cracks from fasteners pointing downward may cause a certain degree of degradation in load capacity.

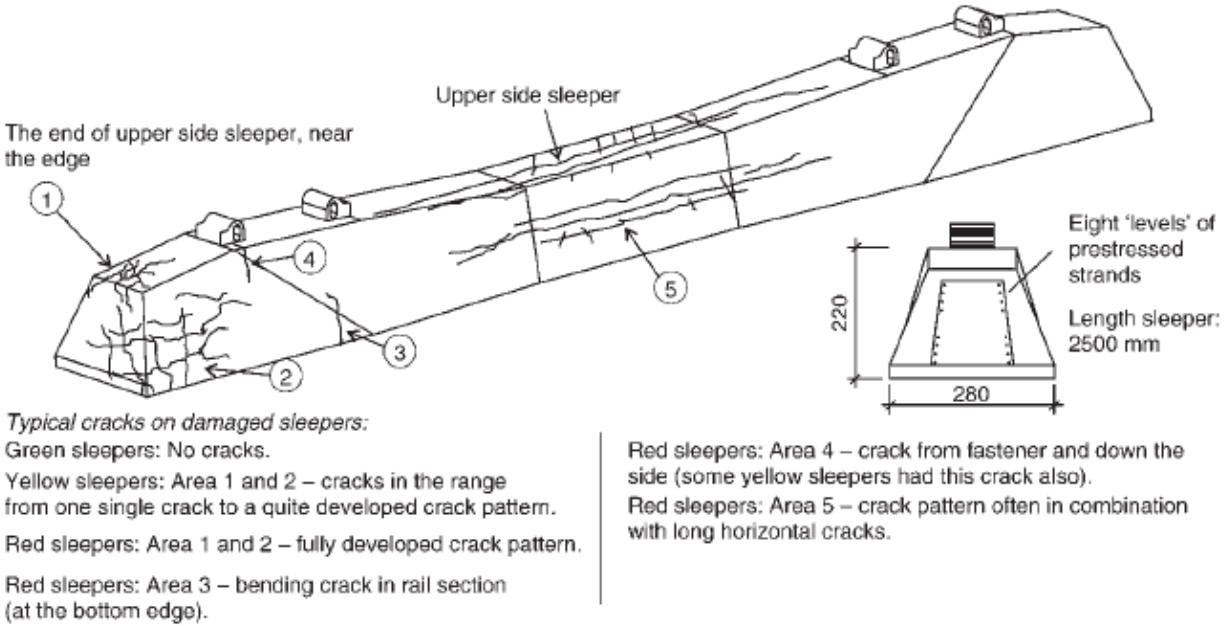

Figure 2.3 Drawing of a Typical Damaged Concrete Crosstie with Characteristic Cracking Pattern Classified (Thun et al. 2008)

Taherinezhad et al. (2013) reviewed the design of concrete crosstie in various countries (areas), including Australia, USA, India, Iran, and found high strength concrete (HSC) with a strength over 7,000 psi (50 MPa) was mostly used. Due to the use of HSC, higher prestressing

load can be applied and this benefits the capacity of a crosstie. At the same time, however, it should be noticed that special behavior of HSC results in the reduction in ductility (Mendis 2003). As a brittle material, the using of HSC under extreme loading case may cause cracking, which was ranked as a common failure mode from the international survey (Van Dyk et al. 2014).

2.3 Current Database of Wheel Load Demand

The starting point of the design of a particular track system is to calculate the design wheel load (Doyle 1982). In design of the track structure, several types of loads can be used including static, quasi-static, dynamic and impact loads (Van Dyk 2014). The static load is defined as due to the weight of the rail vehicle at rest; the quasi-static load is used when train passes curved track, the actual wheel load combined static load with centripetal force associated with speed and curvature; the dynamic load considers the increment of load due to high-frequency wheel-rail interaction; the impact load is caused by the track and vehicle irregularities, which usually creates the highest loads with short duration in the track structure.

The nominal vehicle axle load is usually measured for the static condition, but the dynamic vertical and lateral forces due to the rolling stock at a certain speed should be used in design analysis (Doyle 1980). In general, the nominal axle load being scaled up with an impact factor is used as the design vertical wheel load. Several types of impact factor formulae are currently used to calculate the design vertical wheel load. The American Railroad Engineering Association (AREA) suggested use vehicle speed and wheel diameter to determine the impact factor (Prause 1974). From statistical approach, Eisenmann (1972) derived an equation calculating the impact factor associated with the track condition, vehicle speed and confidence limit. The Office of Research and Experiments (ORE) of the International Union of Railways

developed a comprehensive method to determine the impact factor based upon the measured track results (ORE 1965). Using ORE's formulae, the relationship between the maximum value of the impact factor and the train speed can be calculated for various standards of track. British Railways (BR) developed a model for a discrete irregularity – for example dipped rail joint – that combined the effect of vehicle speed, unsprung mass and track irregularities (Jenkins et al 1974, Railway Gazette 1970, Koffmann 1972). Doyle (1980) compared the four major types of impact factor formulae (**Figure 2.4**). A few general conclusions were reached although these formulae that are not specifically interrelated. Doyle (1980) also introduced several other expressions to determine the magnitude of the impact factor, such as the Indian Formula (Agarwal 1974), the German Formula (Schramm 1961), the South African Formula (Lombard 1974), the Clarke Formula (Clarke 1957) and the WMATA (Washington Metropolitan Area Transit Authority) Formula (Prause et al 1974).

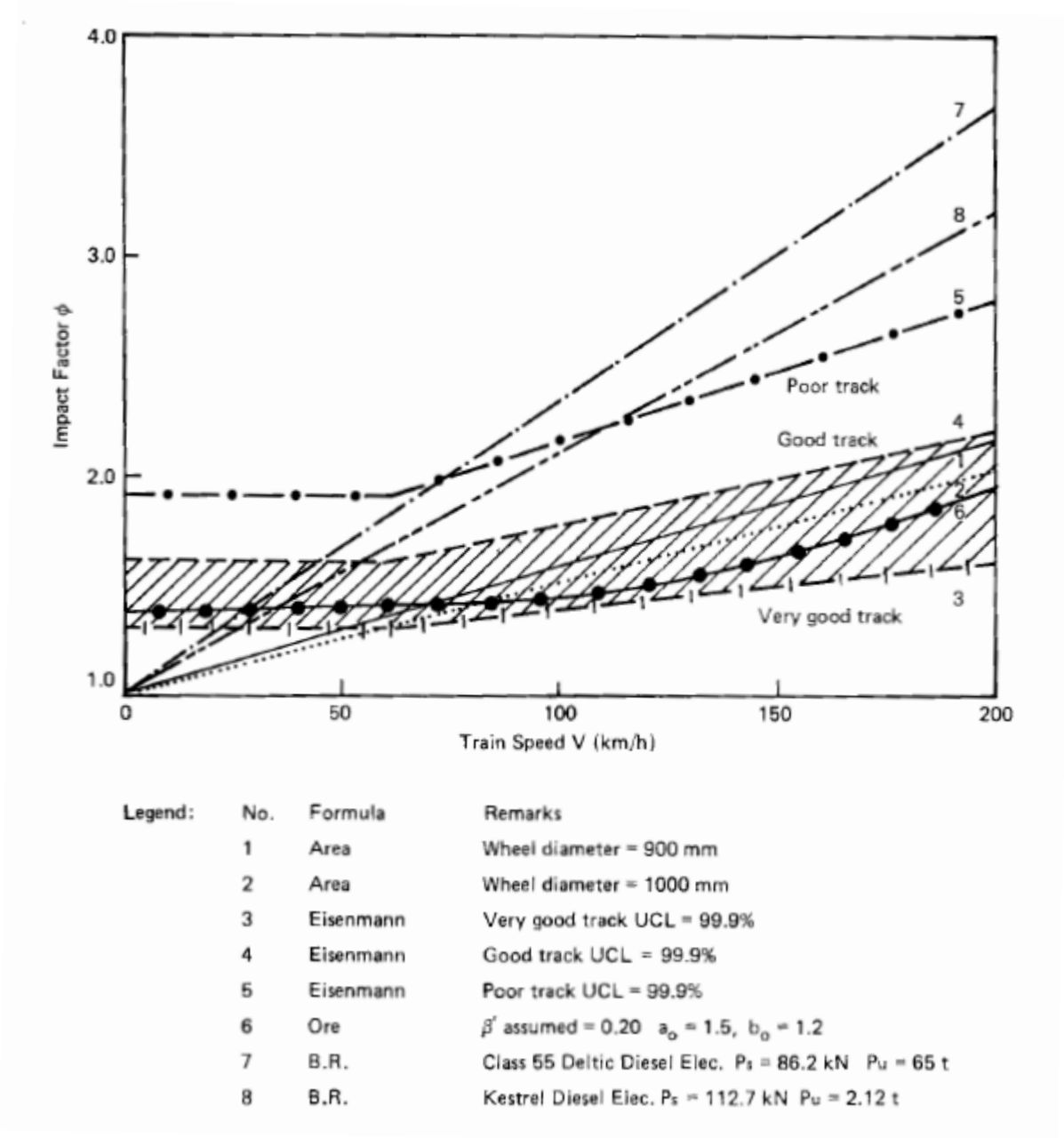

Figure 2.4 Comparison of Impact Factor Formulae (Doyle 1980)

Doyle (1982) also made a detailed comparison of the train vehicle and track parameters that are in the formulae to calculate the impact factor (**Table 2.8**). It is found in all of these formulae that train speed is a key factor that couldn't be ignored even for a simplified estimation. As the basic geometric parameter, wheel diameter was included in three methods. Both track

modulus and track maintenance conditions were used twice. For the rest of the parameters, each formula has its own concern and focus.

Table 2.8 Vehicle and Track Parameters Included in Impact Factor Formulae (Doyle 1982, Adapted by Van Dyk et al. 2014)

		Vehicle Parameters Included						Track Parameters Included					
Dynamic Factor	Expression for ϕ	Train Speed	Wheel Diameter	Static Wheel Load	Unsprung Mass	Vehicle Center of Gravity	Locomotive Maintenance Condition	Track Modulus	Track Stiffness at Rail Joint	Track Joint Dip Angle	Cant Deficiency in Curves	Curve Radius	Track Maintenance Condition
Talbot (*10*)	$1+\frac{33V}{100D}$	•	•										
Indian Railways (*11*)	$1+\frac{V}{3\sqrt{U}}$	•						•					
Eisenmann (*12*)	$1+\delta\eta t$	•											•
ORE/ Birmann (*13*)	$1+\alpha+\beta+\gamma$	•				•	•				•	•	•
German Railways (*5*)	$1+\frac{11.655V^2}{10^5}-\frac{6.252V^3}{10^7}$	•											
British Railways (*4*)	$1+14.136(\alpha_1+\alpha_2)V\sqrt{\frac{D_j P_u}{g}}$	•		•	•				•	•			
South African Railways (*4*)	$1+0.312\frac{V}{D}$	•	•										
Clarke (*4*)	$1+\frac{15V}{D\sqrt{U}}$	•	•					•					
WMATA (*6*)	$(1+0.0001V^2)^{\frac{2}{8}}$	•											
Sadeghi (*7*)	$1.098+0.00129V+2.59(10^{-6})V^2$	•											
AREMA C30	For $20<V<120$: $0.6+0.005V$	•											

Because most of these old methods being developed before 1980s were only empirical formula with a lack of mechanistic basis, they may not predict the amplification factor for dynamic wheel load representatively. To determine the actual dynamic wheel load applied to the rail, Van Dyk et al. (2014) analyzed large amount of field data recorded by the Wheel Impact Load Detector (WILD). The recorded dynamic factors corresponding to locomotive, freight car and passenger car passage are compared with the predicted values calculated from the formulae mentioned above (**Figure 2.5**). One finding from the output figure is the dynamic loads created by many wheels were much higher than the expected values based on existing design formulae. Van Dyk et al. (2014) used an additional impact factor to adequately represent the actual loading conditions. It should be noticed that, the impact factor used by Van Dyk et al. (2014) indicated the magnitude of the wheel load, which was different from the impact factor used in the AREMA Manual that especially related to the flexural design of the crosstie. In the same paper, a greater impact factor was found for lighter rolling stock. And thus, it was suggested that either a higher impact factor or a different way of design should be applied to match the entire loading spectrum.

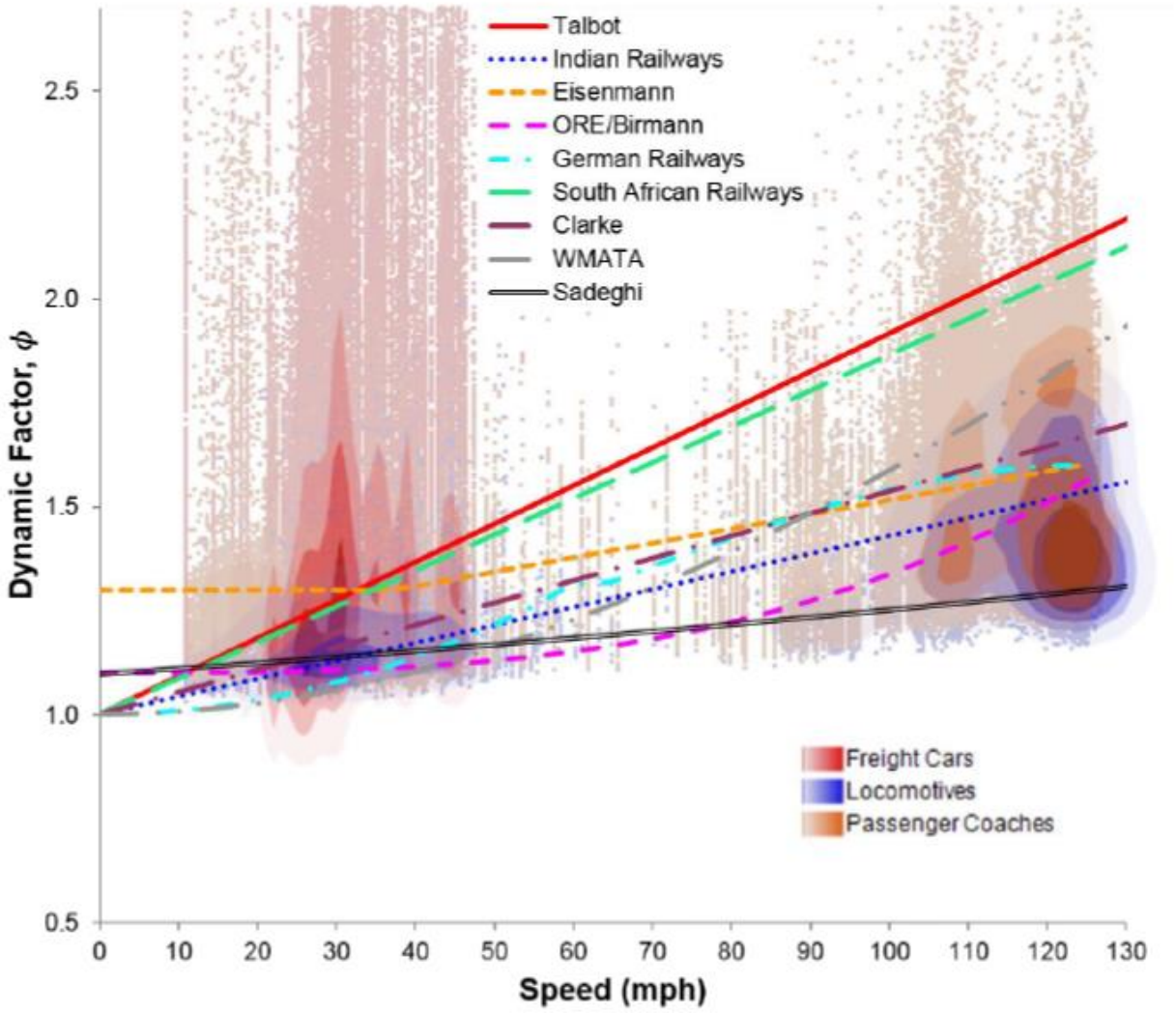

Figure 2.5 Peak/nominal Wheel Load Ratios on Amtrak at Edgewood, Maryland (WILD Data from November 2010) and Design Dynamic Factors (Van Dyk et al. 2014)

As for the design of lateral wheel load, its magnitude was believed to be dependent upon the curve radius of the track, the vehicle speed, the length of the vehicle wheel base and its bogie configuration, as well as the tracking motion of vehicles in the train consist (Doyle 1982). Like the vertical forces, the lateral load (track shift force) can be divided into different parts such as quasistatic force due to track plane of acceleration and uneven distribution of forces between different wheel sets in a bogie, dynamic force due to track irregularities and self-generated

vehicle motions, as well as forces due to adjustment errors (Andersson et al. 2013). In general, both of quasistatic and dynamic behavior of vehicle-track interaction influence lateral loads, in which, the dynamic part is mainly dependent on the stiffness of vehicle suspension system.

To determine the lateral wheel load (guide force) due to flange contact when wheel is negotiating curves, Birmann (1966) designed and used a series of field experiments for various locomotive and wagon bogie. This work concluded that track curvature played a more important role than vehicle speed.

Based on experimental results, the ORE (1965) developed an equation to estimate the magnitude of the lateral load. As the equation was carried out from the observed maximum envelope of experimental results, it was only dependent on the track curvature (radius). Olson et al (1960) derived another equation to determine the design lateral load – which was only dominated by the vehicle speed – also from the field testing results. Efforts through the lateral loads when wheel negotiating curves were also carried on by British Rail (Koffmann 1972).

2.4 Study and Comparison on the Current Design Recommendations

As a loading distributing system, the conventional rail track structure transmits the cyclic loads associated with the passage of vehicle wheels from the rails to the concrete crossties and then to the formation through a protective ballast layer (Doyle, 1980). The current practice for designing the railway track structure aims at satisfying several criteria for the strength of individual components (Prause and Meacham, 1974), which including allowable rail bending stress, allowing crosstie bending stress, allowable ballast pressure and allowable subgrade pressure. Utilizing these criteria, the structural design procedure for conventional ballasted track is presented in **Figure 2.6**.

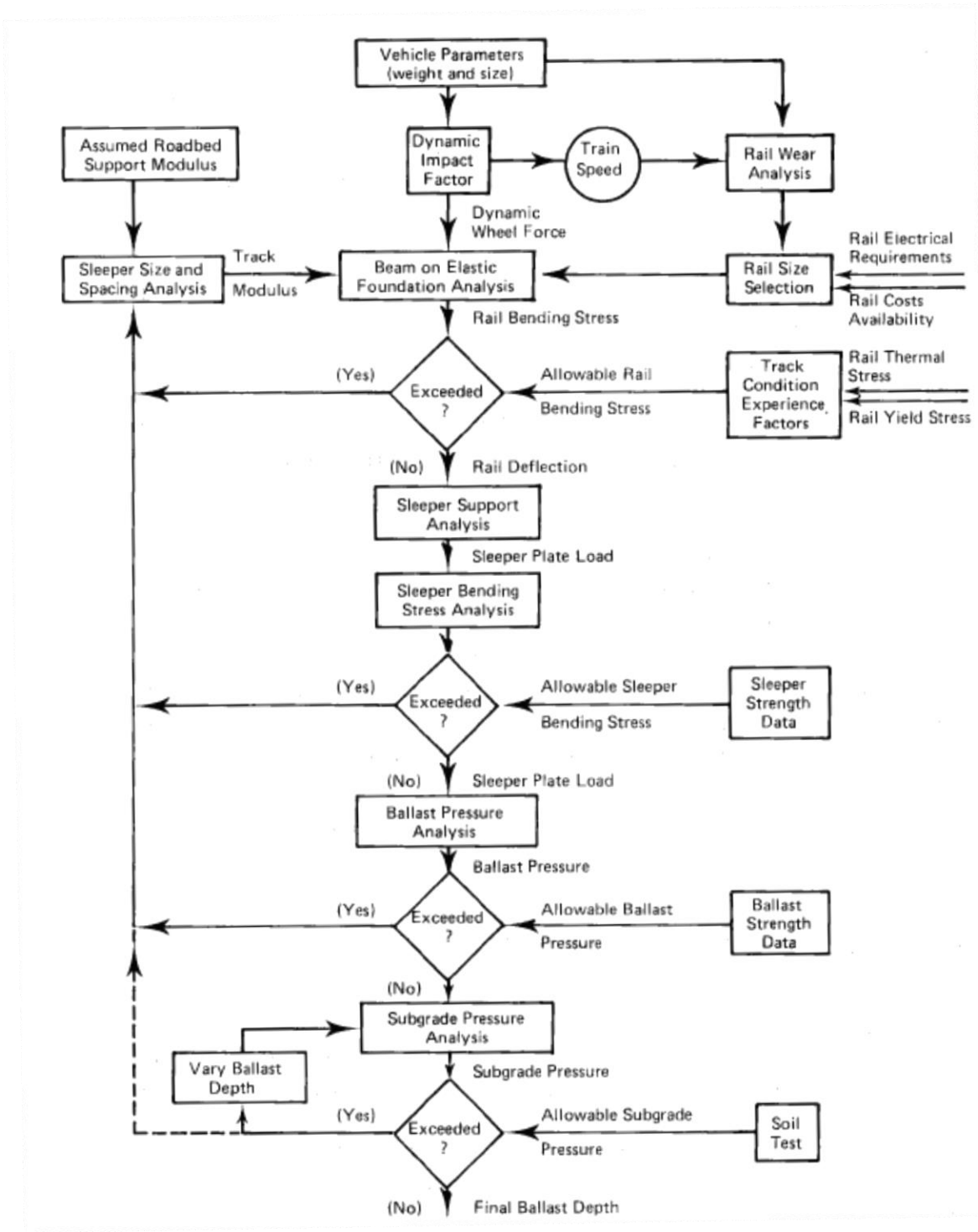

Figure 2.6 Flow Chart for Conventional Ballasted Track Structure Design (Prause and Meacham, 1974)

As a component of track system, concrete crossties are designed to transfer the vertical, lateral and longitudinal rail seat loads to the ballast and formation, and to maintain the track gauge and alignment by providing a reliable support for the rail fasteners (Prause and Meacham, 1974). The vertical rail seat loads bring a bending moment to the crosstie which is subjected to the condition of the ballast lying underneath. Under the lateral and longitudinal applied load, the performance of a crosstie is dependent upon its size, shape, surface geometry, weight and spacing.

In AREMA Chapter 30 (2012), the current recommendations have covered materials, physical dimensions, vertical design loads, structural strength, and other considerations for prestressed monoblock reinforced concrete crossties.

AREMA (2012) defined the load environmental applied to North American Freight, which includes vertical, horizontal, and longitudinal loads at the wheel-rail interface (**Table 2.9**). The vertical load was affected by crosstie spacing, crosstie dimensions, load distribution, impact factors, ballast and subgrade, as well as ballast and ballast pressure. Each of the factors mentioned above is included in the vertical design load calculations. The same loading distribution is used for both vertical and lateral wheel loads.

Table 2.9 Wheel to Rail Loads (kips) (AREMA 2012)

CURVE	<2 DEG			2-5 DEG			>5 DEG		
SPEED	VERT	LAT	LONG	VERT	LAT	LONG	VERT	LAT	LONG
MAINLINE FREIGHT									
<40	80	20*	50	80	30*	50	80	30	50
40 to 60	120	30*	50	120	30*	50	120	30	50
>60	120	30	50	120	30	50	**	**	**
LIGHT DENSITY FREIGHT (no A/C Traction)									
<40	80	20	30	80	30*	30	80	30	30
40 to 60	120	30	30	120	30	30	120	30	30
>60	120	30	30	120	30	30	**	**	**
HIGH SPEED PASSENGER									
<90	100	10	25	100	18	25	100	20*	25
>90	100	18	25	100	18	25	**	**	**
TRANSIT									
No data available									

* This data estimated or interpolated

** Generally accepted superelevation practice excludes these values

Based on the current AREMA recommendations (2012), to launch a new design of a concrete crosstie, it should be started from material selection. Following the clarification of material properties, the track machinery limitations and self-weight limitations should be checked. Specific dimensional requirements should be considered next, which including crosstie length, width, depth, track gauge, rail cant, rail seat plane, differential tilt of rail seats, protrusion of pretensioning tendons, concrete coverage for corrosion protection of reinforcement, tolerances for placing reinforcement, and surface finish.

To assign all the properties mentioned above, necessary communication with purchasers and crosstie manufacturers is needed. The major task for a designer is to perform necessary calculation to obtain the demand of crosstie flexural strength, then design the crosstie as a bending component to reach the strength capacity and other requirements.

To make sure the design will meet all the requirements, there are several standard tests recommended by AREMA (2012) that need to be performed, which including:

a. minimum negative/positive flexural cracking capacity test at the rail seats;

b. minimum negative/positive flexural cracking capacity test at the center of the crosstie;

c. rail seat repeated-load test;

d. bond development or tendon anchorage test.

A sample calculation following AREMA Chapter 30 Section 4.4.1 is given here to illustrate the current design approach.

Crosstie length is pre-determined to be 102" (8'6"), then the unfactored positive bending moment at rail seat is taken as 300 kips-in (**Figure 2.6**).

The factored design flexural strength at rail seat and tie center is calculated as follow:

a) Using the given equation $M = B \cdot V \cdot T$ to find the factored design positive bending moment at the center of the rail seat.

Where B is the unfactored bending moment which has been selected as 300 kips-in, V and T are the speed factor and the tonnage factor which are obtained from **Figure 2.7**. To obtain these two factors, the speed and the annual tonnage need to be assumed. In this sample calculation, the speed of the freight train is set as 40 mph which will lead to V=0.8; and the annual tonnage is set to be 55 MGT which will lead to T=1.0.

Now the factored positive rail seat bending moment can be calculated as

$$M = B \cdot V \cdot T = 300 \cdot 0.8 \cdot 1.0 = 240\ kips - in$$

b) Assuming tie pads are used, and thus the reduction of positive bending moments is neglected.

c) **Table 2.10** is used to find the design bending moment at rail seat and tie center. The calculated design positive/negative bending moments at rail seat/tie center are listed in **Table 2.11**.

Table 2.10 Bending Moment Calculations (AREMA 2012)

Tie Length	Rail Seat Negative	Center Negative	Center Positive
7′-9″ (2.360 m)	0.72M	1.13M	0.61M
8′-0″ (2.440 m)	0.64M	0.92M	0.56M
8′-3″ (2.520 m)	0.58M	0.77M	0.51M
8′-6″ (2.590 m)	0.53M	0.67M	0.47M
9′-0″ (2.740 m)	0.46M	0.57M	0.40M

Table 2.11 Factored Design Bending Moments (kips-in)

Rail seat	Positive	240
	Negative	127
Tie center	Positive	113
	Negative	161

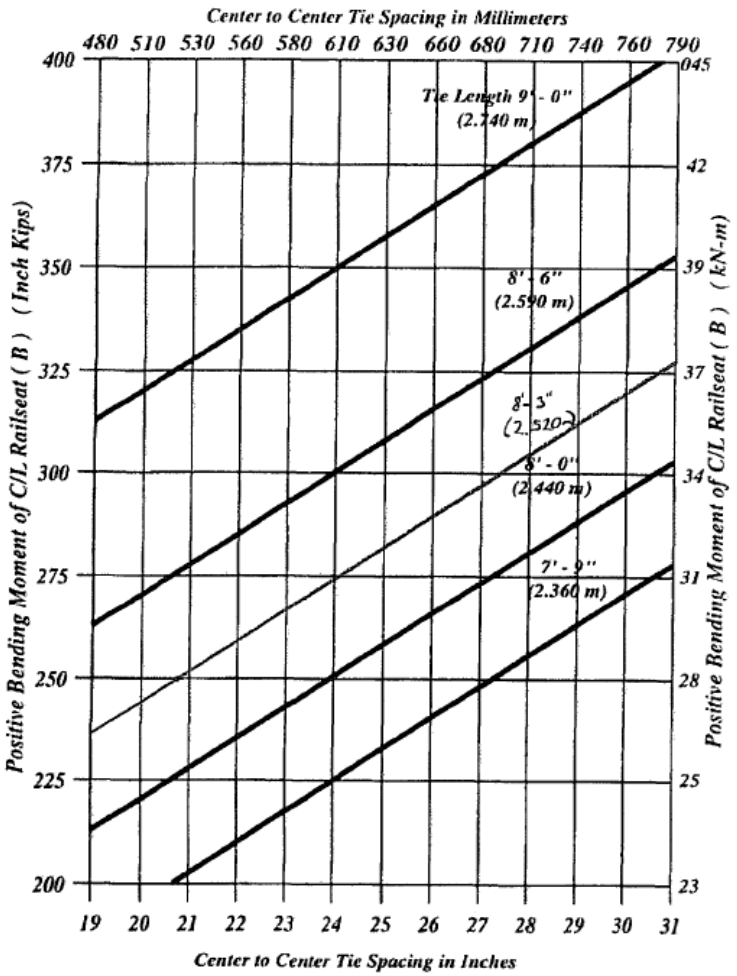

Figure 2.7 Unfactored Bending Moment at Centerline of Rail Seat (AREMA 2012)

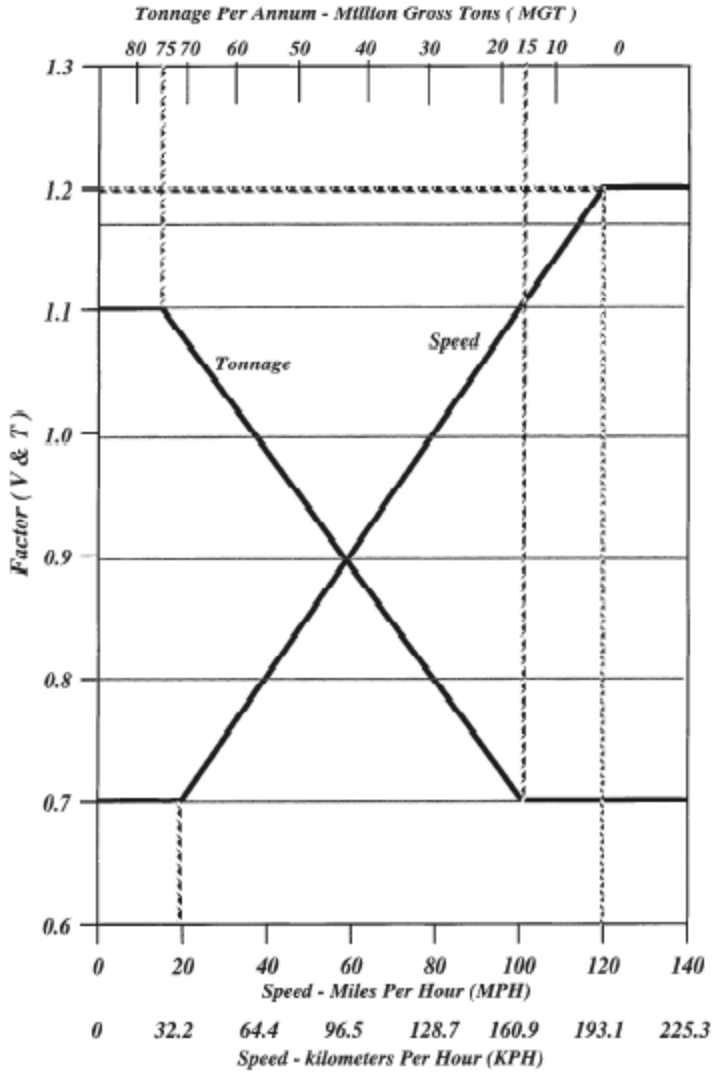

Figure 2.8 Tonnage and Speed Factors (ARMA 2012)

Using the factored design moments listed in **Table 2.11**, the pre-tensioning prestressed concrete crosstie can be thus designed. The next task for the designer is to arrange the prestressed reinforcement. The number of prestressed wires, their locations, and pre-tensioning load need to be designed in details. In this sample calculation, the LBFoster 505S crosstie is selected as an example to validate the design has met the bending capacity requirement. The wire pattern is shown in **Figure 2.8**. The comparison between the crosstie design demand (the factored bending moments calculated before) and capacity is shown in **Table 2.12**. It could be

found, the bending moment capacities have exceeded the design demand. At rail seat, both of demand and capacity are higher for positive bending; at the tie center, both of demand and capacity are higher for negative bending.

Table 2.12 Comparison of Design Demand and Capacity in Bending Moments (kips-in)

Location	Positive/Negative	Demand	Capacity
Rail seat	Positive	240	406
	Negative	127	220
Tie center	Positive	113	197
	Negative	161	257

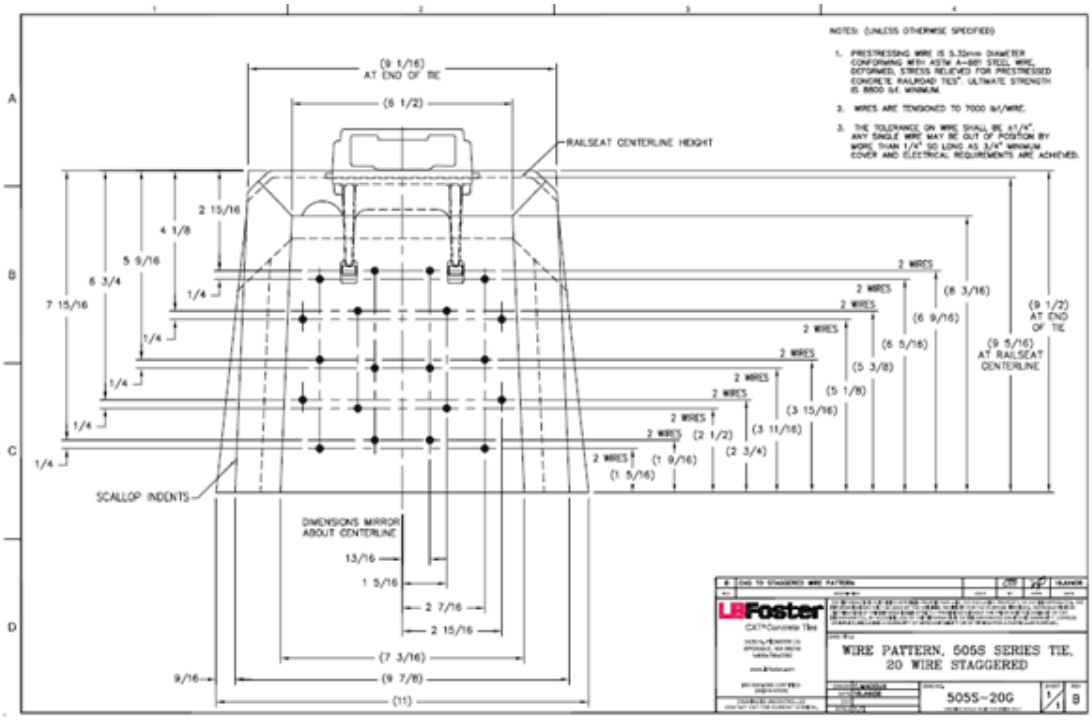

Figure 2.9 LBFoster 505S Pre-tensioning Prestressed Concrete Crosstie

After the design of the prestressed concrete tie has been made, some additional design considerations need to be satisfied:

a. “The design needs to follow ACI 318.”

b. “The maximum precompression after all losses at any point in the crosstie should not exceed 2,500 psi.” After running a simple calculation, the maximum stress due to the precompression takes place at the tie center is found as 2,396 psi, which is lower than 2,500 psi.

c. “The minimum pre-compressive stress at any vertical cross-section through the rail seat area should be 500 psi.” After running relative analysis, the minimum stress picked up from real seat area due to the precompression is 810 psi, which is greater than 500 psi.

Looking at the current design approach, it could be found that once the crosstie dimensions and spacing have been set, a design chart (**Figure 2.6**) is used to find the unfactored bending moment no matter what the actual wheel load is. The maximum wheel load and the crosstie-ballast contact condition, which are necessary to calculate the crosstie bending moment capacity, have been pre-assumed but not yet specified in AREMA design recommendations. To involve the wheel load and wheel-rail dynamic interaction into design, AREMA uses another design chart that considers train speed and annual tonnage (**Figure 2.7**) to scale up the calculated unfactored bending moment. The current design methodology may meet the requirement of the common case, but based on the average of statistical data, it neglects the destructive force in the extreme case which might cause failure of the track system. A safe way of design should specify all the input factors, which including cross dimensions, spacing, axle load, load distribution, train speed, wheel profile, car suspensions, crosstie-ballast contact conditions, etc. A successful design also needs to ensure a specific safety margin.

As comparison, UIC 713 has specified some of the input factors to calculate the design bending moment. The design loading is assigned first, in which the derivation of design loading takes account of the design static axle load, dynamic factors, and the influence of the track

structure in sharing applied axle loads between crossties and the variability of the track support. The exceptional and accidental impact loads are also considered in UIC 713 by using a scaling factor.

2.5 Experimental Approaches to Clarify the Load Path

Field testing and measurement, as well as large-scale material and model testing, were completed by Norwegian Geotechnical Institute (NGI) in 2005. For the field testing, sixteen sites of the Swedish, Spanish and French networks were selected to collect data. For each site, data concerning track (plan design, slope and profile), traffic (maximum speed, cumulated tonnage on a given time span), geotechnical context were collected and used as input; dynamic and static measurements including stresses at the bed layers, contact stress sleeper-ballast layer, rail stresses, permanent settlements and deflections caused by circulating trains, vibrations, temperature and water content as well as meteorological parameters were recorded as data output. Some of the instrumentations are shown in **Figure 2.10 (a – e)**.

Figure 2.10 a) Diesel-electric Locomotive Used During Tests in April b) PSD Laser Displacement Transducer at Section 2A c) Pressure Cells for Vertical Stress Measurement at Sleeper Base d) Relative Displacement Sleeper-sub-ballast Sensors (Under Sleeper) e) Accelerometer in the Sub-ballast Layer f) Borings Protected by Pipes for Geophone Installation

Some of the presented displacement measurements (NGI) show a clear trend and can be used in future comparisons. The crosstie global vertical deflection and the rail pad compression deflection are shown in **Table 2.13**, and the average lateral deflection of rail measured from the neutral axis is presented in **Table 2.14**. It was found the magnitude of vertical crosstie global deflection could be five times higher than the rail pad compression. There was no clear evidence showing a strong correlation between the train speeds with these measured deflections.

Table 2.13 Whole Track (Zimmer) Deflection and Rail Pad Deformation (NGI 2005)

Vehicle	BB16500 (100 km/h)		1300, 3000 (75 km/h)		BB 15000 (120 km/h)	
Wheel	front	back	front	back	front	back
Zimmer (mm)	1.8	1.7	1.6	13.0	2.0	2.1
Rail pad (mm)	0.3	0.4	0.3	0.6	0.4	0.5

Table 2.14 Average Deflection of Rail (NGI 2005)

Engine	BB 16 500 (100 km/h)		1 300 and 3 000 (75 km/h)		BB 15 000 (120 km/h)	
Wheel	front	back	front	back	front	back
Deflection rail 1 (mm)	1.4	1.4	1.7	1.4	2.0	1.8
Deflection rail 2 (mm)	1.5	1.7	2.0	1.9	2.1	1.9

Laboratory testing was also accomplished by NGI (2005) using a full-scale track box to reproduce the soil/track conditions at field (**Figure 2.10**). The track box was built with a steel box with dimensions of 4×5×21m which was filled with layers of soil. Hydraulic actuators were used to applied out of phase loads at 6 points on each rail to simulate the wheel load. A series of measurements, including soil pressure, displacement and acceleration taken at various locations were recorded.

Figure 2.11 Track Box During Testing (NGI 2005)

Thun et al. (2008) examined the remaining load carrying capacity of cracked concrete crossties in laboratory testing. Concrete cores were obtained from drilling, uniaxial tensile and compressive strength tests were performed. The mean concrete compressive and tensile strength was found as 100.4 MPa and 3.8 MPa respectively. Two bending capacity tests were performed including center-negative bending test (i.e. the crosstie was placed upside down on bearing at each rail seat) and rail seat positive bending test. From the center-negative bending test, for a worst damaged crosstie with big pieces of concrete missing, degradation was found in bending capacity at the mid-point of the crosstie (19 kN.m versus 32 kN.m for a healthy crosstie). However, the bending capacity of these crossties with worst damage was found to still provide the required moment capacity. In addition, no significant decreasing of bending capacity was observed until the typical longitudinal cracks in the middle of the crosstie appeared. A large decrease in moment capacity was found at the rail seat for a severe cracked crosstie. The bending moment capacity can drop dramatically from 45 kN·m to merely 9 kN·m. Under this significant degradation, most of the heavily damaged crossties couldn't meet requirements. One

observation was that if the wire started to slip when loading, then the failure phase would start almost immediately. For crossties with less severe crack pattern, shear failure was found in most cases.

In the same research (Thun et al. 2008), horizontal load capacity of the fastener was tested. Structural failure of the crosstie was found to be caused by the development of vertical cracks from the fastener pointing downward and a horizontal crack developing along the wires. For healthy crossties, the horizontal load capacities were recorded as 100 – 130 kN, which was several times higher than the lateral wheel load. For the most damaged crosstie with worst crack pattern, the horizontal load capacity was found as 18 kN which may still function. Small cracks were believed to not decrease the horizontal load capacity; however, if both longitudinal and vertical cracks appeared, the load capacity was considered to reduce significantly.

As for the fatigue capacity of crossties investigated by the same group (Thun et al. 2008), approximately 50% of crossties with cracking survived after the required 2 million load cycles, which is equivalent to train passage within about 7 years. Full crossties were used in the fatigue tests. It was believed improper to run fatigue test using only one-half of a crosstie (i.e. to divide a crosstie into two halves from the middle), because they can have very different bearing capacity at the rail seat even with a similar crack pattern. The fatigue capacity of the studied cracked crossties varied a lot, and no relation was found between the visible crack pattern and the fatigue capacity. In the worst case, only after a few hundred load cycles, the cracked crosstie lost its bearing capacity and failed.

Kerokoski et al. (2012) compared the behavior of unused and used (served over 30 years in Finnish railway lines) crossties under static and dynamic loading via laboratory tests (**Figure 2.12 a**). Static tests were performed at rail seat section and crosstie center, in which 4 new

crossties and 10 used crossties were tested for each location. For dynamic testing, 2 new crossties and 2 used crossties were loaded for the same locations (rail seat and crosstie center). During the loading tests, concrete deformation in terms of strain was measured using a loop-shaped strain gauge model with four conventional strain gauges glued on its inner surface (**Figure 2.12 b**).

a **b**

Figure 2.12 a) Crosstie Loading Frame; b) Loop-shaped Concrete Strain Gauge (Kerokoski et al. 2012)

All of new crossties and most of used crossties passed the rail seat loading tests corresponding to the criteria of Standard EN 13230-2 (2009), only one degraded crosstie manufactured in 1974 failed. Except the degraded crosstie from 1974, of which the compression-bending failure was found to be the major failure mechanism: the failure mode of the rest rail seats can be mostly classified as bending failure or shear-bending failure. In most cases, no slipping of the prestressed strands was observed in the static loading tests at rail seat. In addition, a crack on the bottom surface of concrete beneath the rail seat was found for each

used crosstie. The researchers believed that the occasional cracks were mostly insignificant when the crosstie is subjected to static loading. Similar results were found for static bending tests operated at crosstie center. Only three used crossties with pre-existing vertical cracks didn't meet the required bending moment capacity. The cracking and failure loads recorded from dynamic tests were slightly lower than those of static tests. In overall, the used crossties were believed much more resistant to loading than predicted by calculations.

2.6 Numerical Approaches to Clarify the Load Path

Many innovative studies in the modeling of concrete sleepers and fastening systems have been done by researchers. As the fundamental study of the concrete crosstie and fastening system, mathematical models were built to find the structural response under dynamic loading cases. Fröhling (1998) developed a new method to predict track deterioration under dynamic wheel loading with varying track stiffness. In this method, a vehicle model is linked to settlement equation based on measureable track parameters. In this research, an eleven degree-of-freedom vehicle/track model was built (**Figure 2.13**) and equations were derived to calculate the dynamic wheel-rail contact force. The results obtained from the mathematical model simulation were validated by the output from the multi-body model built in the multi-body simulation program MEDYNA. The comparison showed the approximation of the eleven-degree-of-freedom model could effectively provide trustable results, including the wheel load, the vertical displacement across the secondary suspension and the dominant frequencies of the system.

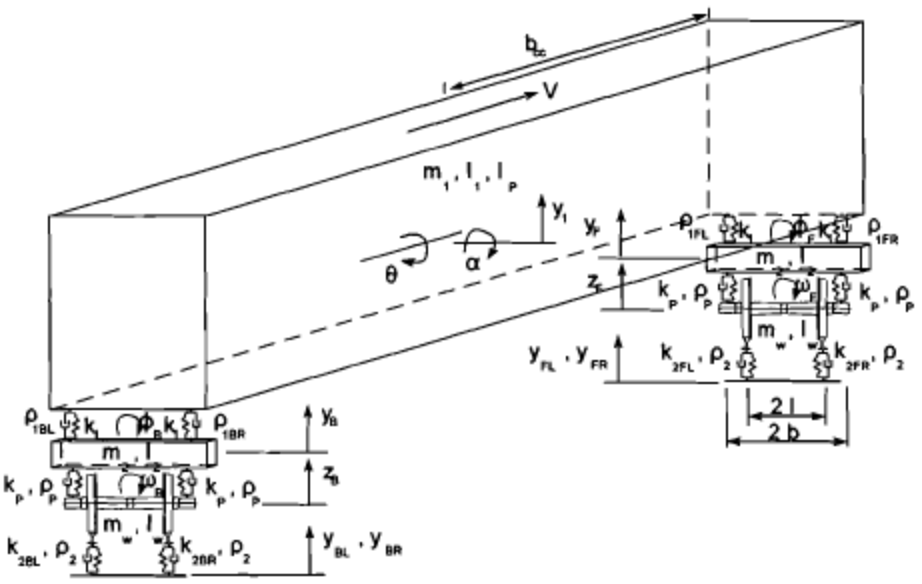

Figure 2.13 Eleven Degree-of-Freedom Vehicle/Track Model (Fröhling 1998)

Various finite-element models were built to gain a detailed understanding of the behavior of the crosstie and fastening system. Yu et al. (2011) developed an individual concrete crosstie model that considered the macroscopic heterogeneity and material nonlinearity. In their model, the steel-concrete interfaces were modeled with assigned bond-slip relationships. The ballast and subgrade beneath the track were also modeled as supports. The modeling results from two separate concrete crossties were compared; one was a crosstie with eight prestressing strands and another contained twenty four prestressing wires.

For the conventional finite-element modeling, full contact between crossties and ballast is typically assumed as one of the boundary conditions. However, in reality, voids and pockets between the contact of concrete surface and ballast were often found that could cause problems to the crossties and track system. Kaewunruen and Remennikov (2007) investigated the free vibration response characteristics of in-situ railway concrete crossties. A dynamic model of the railway track system incorporating concrete crossties was developed using finite-element

method. Several types of support conditions were studied, and the free vibration analysis of crossties corresponding to each condition was completed. Five basic dynamic mode shapes with respect to the five lowest frequencies of a crosstie were studied (**Figure 2.14**) under five different crosstie-ballast contact conditions (**Figure 2.15**). For the results, in summary, the dynamic behavior of the in-situ crosstie in the track system was found to be softened by the imperfect support conditions. The frequencies with respect to each mode shape were found decreasing with the increasing size of voids, which would lead to a reduction of track stiffness.

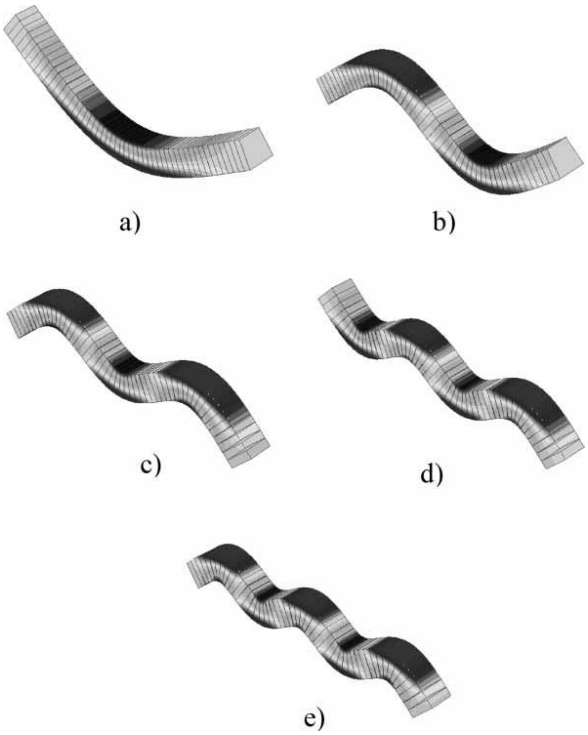

Figure 2.14 Mode Shapes of a Free-free Crosstie: a) – f) Corresponding to First to Fifth Mode (Kaewunruen and Remmenikov 2007)

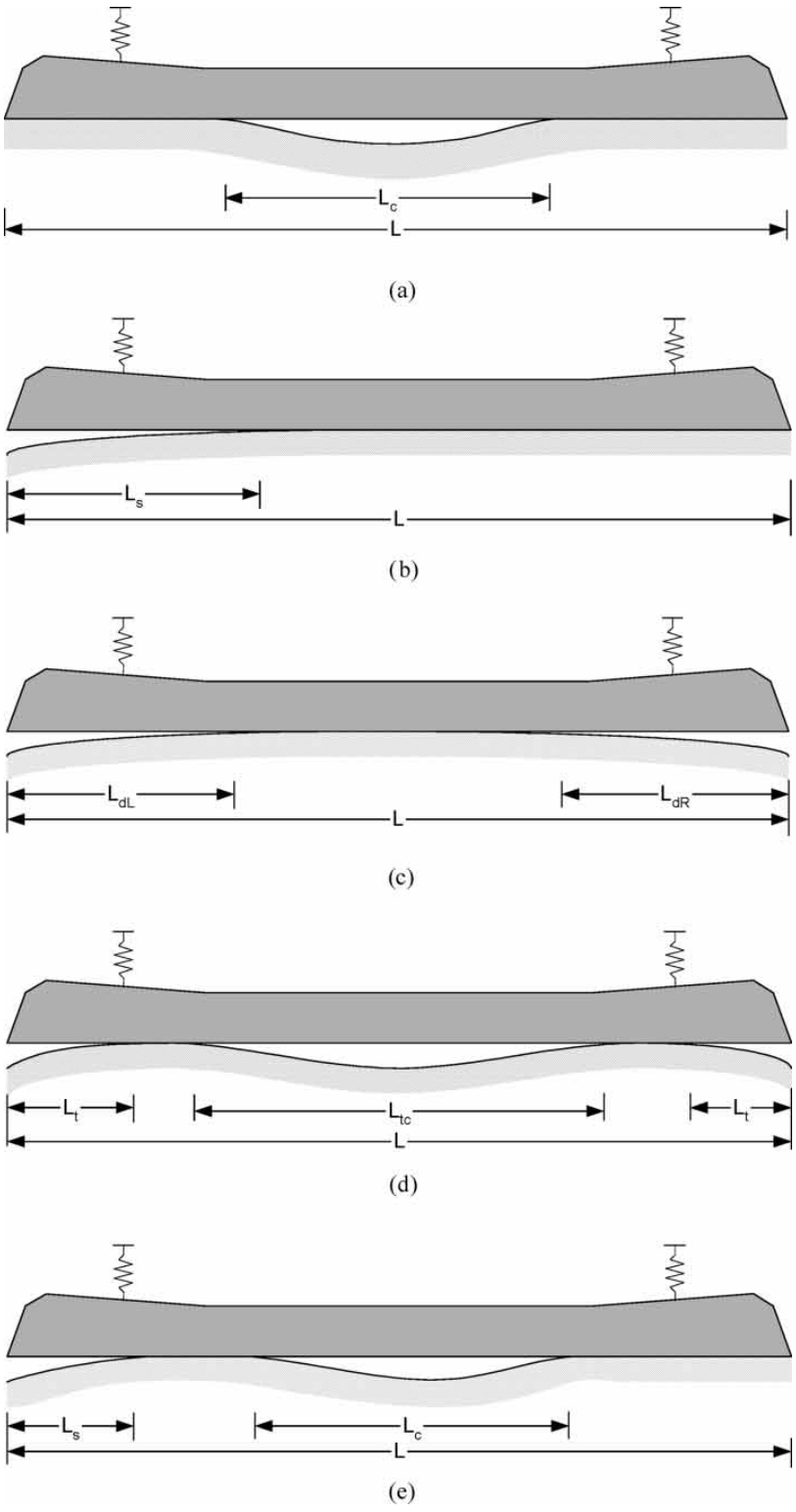

Figure 2.15 Crosstie-ballast Contact Patterns: a) Central Void; b) Single Hanging; c) Double Hanging; d) Triple Hanging; e) Side-central voids

Lundqvist and Dahlberg (2005) developed a track model including 30 concrete crossties in which three were modeled to have flexible characters. This track length was believed long enough to exclude the influence of boundary conditions and initial effects. The ballast and subgrade track bed was modeled as a continuum with elastic properties. This model utilized non-reflecting boundary conditions to prevent the artificial stress wave reflections that generated at the boundaries from re-entering the model and contaminating the results. Under this condition, shear and pressure waves were absorbed, and thus no reflections would occur. In this research, the authors believed in the field environment, a large number of crossties were improperly supported, which would increase the variations of the dynamic wheel-rail interaction forces, and thus speeded up the track structure deterioration rate. In addition, due to bad support, the uneven loading of the ballast may cause irregular settlement of the track, which would make the support condition worse. Another influence brought by the bad support is rail head corrugation growth and damage to track components. Based on the analysis of the finite-element modeling results, it was found that a 1 mm gap between crosstie and ballast can increase the vertical wheel load by 70 percent. For unsupported crossties, an increase of train speed would result in a higher wheel load, as well as greater deflections and component stresses.

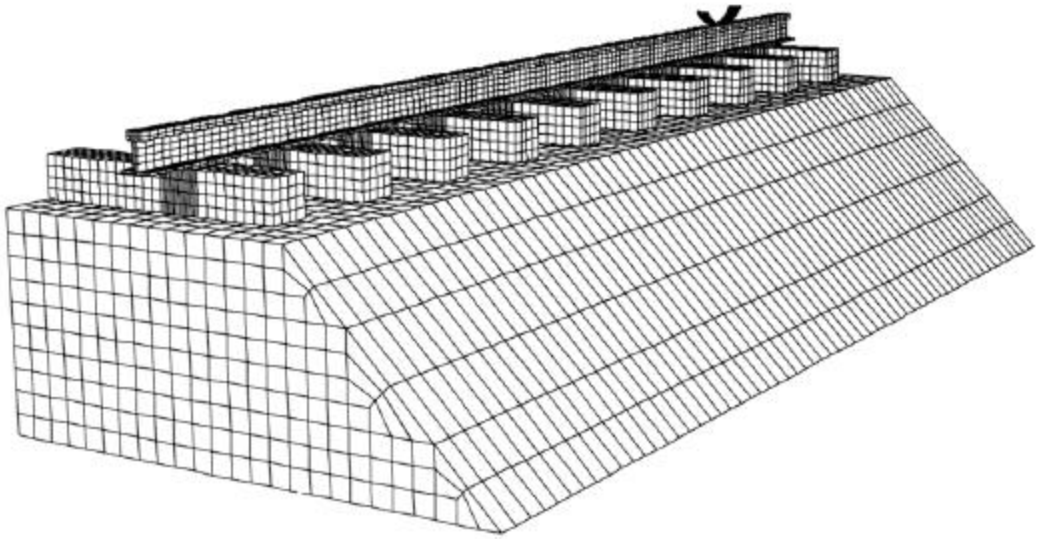

Figure 2.16 Part of the Train/track Model Consisting of Rigid Wheel, Rail, Rail Pads, Rigid and Flexible Sleepers, and Ballast/Subground (Lundqvist and Dahlberg 2005)

3. Laboratory and Field Research Study Plan

3.1 Overview and Overall Objectives of Experimental Study

3.1.1 Purpose

The purpose of laboratory and field experimentation was to enhance the understanding of concrete crosstie and fastening system behavior under simulated and true loading conditions. The experiments aimed at quantifying the loading demands placed on the individual crosstie and fastening system components as well as the system as a whole under a variety of operational conditions. Controlled experiments in the laboratory resulted in fewer variables compared to experiments in the field. Relative to the field, experimentation conducted in the laboratory was easier to replicate with greater frequency. Increased control of variables helped clarify how changing a parameter affected the system. Repeatable laboratory experiments resulted in larger sets of data which decreased experimental error. The field experiments were associated with realistic variables such as support and loading conditions, or dynamic wheel loading. Combining the data collected from laboratory and field, the conclusions providing answers to critical questions about the design and performance of concrete crossties and fastening systems, providing a baseline for mechanistic design.

3.1.2 Objectives

To achieve the overall purpose of gaining a deeper understanding of crosstie and fastening system behavior, the objectives of the laboratory and field experimentation study were:

1) **Determination of System Load Path** – Understand load transfer mechanics of the crosstie and fastening system from the wheel-rail interface, through the fastening

system, and into the crosstie.

2) **Quantification of Crosstie-Fastener Response** – Analyze the characteristic deformation and deflection of all components.

3) **Development of Analytical Model** – Provide reliable data to develop and validate the three-dimensional finite element model (FEM) of the crosstie and fastening system.

3.2 Experimental Setups

Many measurements were acquired to accomplish the objectives described above. These measurements were captured during material – level, component – level and system – level experimental programs conducted in laboratories and at a field site. The experimental work was cooperated with the UIUC RAILTEC group, including Dr. Daniel A. Kuchma, Dr. David. A. Lange, J. Riley Edwards, Marcus Dersch, Justin Grasse, Christopher Rapp, Ryan Kernes, Thiago Bizarria, Kartik Manda, Brent Williams, Zhe Chen and Moochul Shin. The following equipment are used to conduct the laboratory and field experiments.

3.2.1 Uniaxial Loading Machine

The uniaxial loading machine was used to test the compression and flexural behavior of concrete crosstie and fastening system components (**Figure 3.1**). The uniaxial loading machine used a hydraulically-powered actuator to apply a load up to 100,000 lbf in the vertical direction, perpendicular to the loaded face of the component being tested. A ball-joint cast in the upper loading head minimized the effect of eccentric loading and the machine was adjusted to fit components with varying dimensions. A calibrated load cell was used to monitor applied load.

Figure 3.1 Uniaxial Loading Machine

3.2.2 Static Load Testing Machine

The Static Load Testing Machine (SLTM) was used to apply loads to a concrete crosstie and fastening system, to test the behavior of rail, and calibrate strain gauge configurations installed in various locations on the rail (**Figure 3.2**). The SLTM used a hydraulic jack to apply vertical load supported by an overhead loading frame. The SLTM loading head used a simplified wheel profile to apply a fixed combination of vertical and lateral load on both rails simultaneously. The angle between the normal direction of the contact surface of the loading head and the vertical plane is designed to be 26.5°, equating to a lateral to vertical force (L/V) ratio of 0.5 applied to both rails. The loading head could also be modified to apply pure vertical loads. A calibrated load cell was used to monitor applied loads.

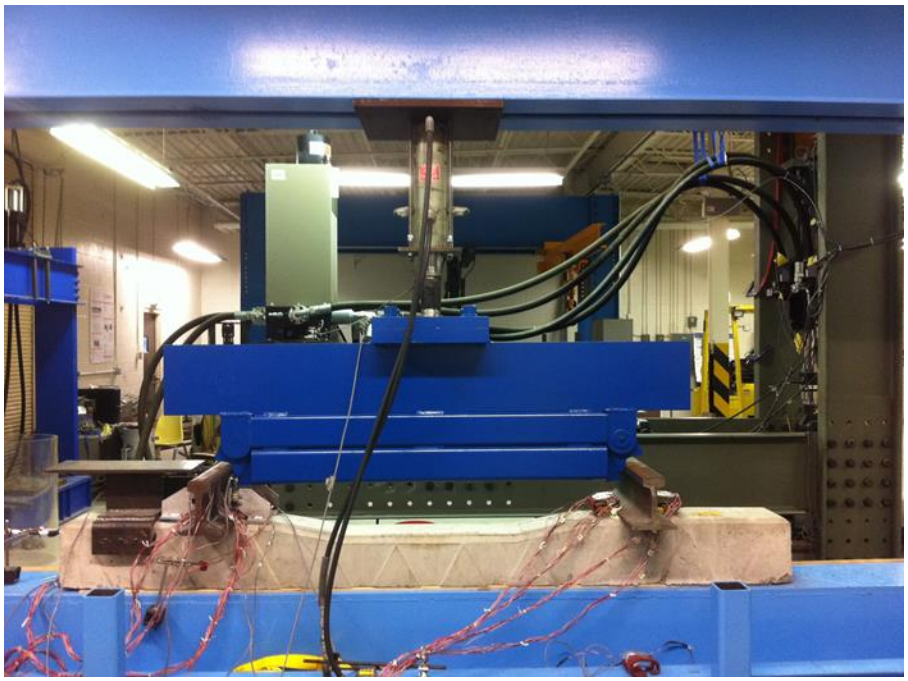

Figure 3.2 Static Load Testing Machine (SLTM)

3.2.3 Pulsating Load Testing Machine

The Pulsating Load Testing Machine (PLTM) was used to apply loads to a single concrete crosstie and fastening system and to determine the magnitudes and distribution of applied forces (**Figure 3.3**). Static or dynamic vertical and lateral loads were applied to the rail on one rail seat of a full-scale concrete crosstie with a complete fastening system assembly installed. Vertical and lateral loads were adjusted separately using a control system. The PLTM used three hydraulic actuators (two vertical and one lateral) mounted on a self-balanced steel frame and a loading head. The loading head was bolted to the head of a two-foot segment of 136RE rail. The actuators were calibrated for load and displacement prior to installation.

Figure 3.3 Pulsating Load Testing Machine (PLTM)

3.2.4 Static Tie Tester

The Static Tie Tester (STT) (**Figure 3.4**) was used to apply loads to test the bending and compression behavior of concrete crossties. Rail seat compression tests, rail seat positive and negative bending tests, and tie center positive and negative bending tests were conducted. The STT used a hydraulic cylinder to apply loads to the rail seat or center of a crosstie up to a maximum capacity of 100,000 lbf. A calibrated pressure gauge was used to monitor the applied loads.

Figure 3.4 Static Tie Tester (STT)

3.2.5 Portable Track Loading Tools

Three portable track loading tools were used in the laboratory: the Delta Frame (**Figure 3.5**), the Portable Track Loading Fixture (PTLF), and the Gauge Restraint Measurement System (GRMS). The Delta Frame was used to apply loads to the rail and to calibrate instrumentation installed on the rail. Vertical loads up to 50,000 lbf and lateral loads up to 10,000 lbf were applied to the rail, separately. The Delta Frame used a hydraulic cylinder to apply loads. Vertical loads were applied using an upward facing steel triangular frame with loads applied in the center of the bottom side of the frame and reacting off the rail at the two bottom corners. Lateral loads were applied by disassembling the triangular frame into a straight section laid perpendicular between the two rails.

The PTLF was used to apply lateral loads in a similar fashion to the delta frame up to 10,000 lbf. The PTLF used a hydraulic cylinder to apply lateral loads.

The GRMS was used to apply lateral loads in a similar fashion to the delta frame and PTLF up to 10,000 lbf. The GRMS used a hydraulic cylinder to apply lateral loads. Calibrated load cells were used to monitor applied loads.

Figure 3.5 Delta Frame – Vertical Load Orientation

3.2.6 Full-Scale Track Loading System

The Full-Scale Track Loading System (TLS) was used to apply loads to a 22-feet long section of a concrete crosstie track (**Figure 3.6**). Track components were assembled on a full cross-section of track that included eleven crossties spaced at 24 inches on center. Static or dynamic combinations of vertical and lateral loads were applied to the journals of a 36-inch wheel set. Vertical and lateral loads were adjusted separately using a control system. The TLS used two hydraulic actuators mounted vertically and a hydraulic cylinder mounted laterally on a self-balanced steel frame. A special assembly for each journal was designed to attach one vertically-mounted actuator and the horizontally-mounted hydraulic cylinder to one journal and the second

vertically-mounted actuator to the opposite journal. The actuators were calibrated for load and displacement.

Figure 3.6 Full-Scale Track Loading System (TLS)

3.2.7 Railroad Test Track (RTT) at the Transportation Technology Center (TTC) in Pueblo, CO

The field experiments were conducted on two sections of track both at the TTC in Pueblo, CO. For both sections, 15 new concrete crossties were installed and tamped prior to experimentation. One section was on a tangent segment of the RTT. The area shaded by red in **Figure 3.7 (a)** noted the location of the testing segment at RTT (Loop 4 in **Figure 3.7 (a)**).

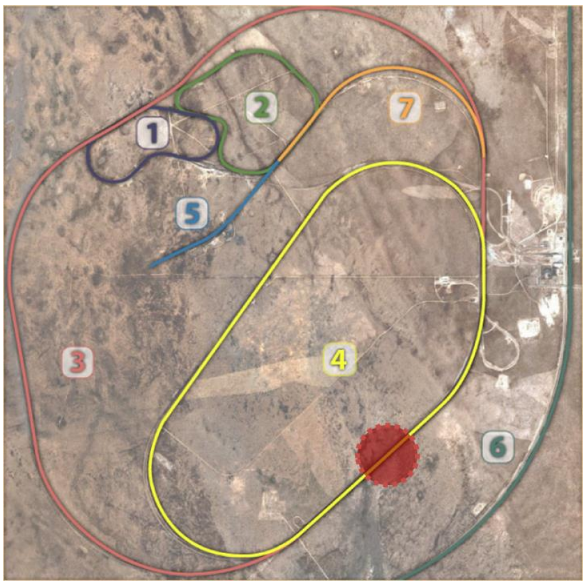

a)

b)

Figure 3.7 a) The Tangent Testing Segment at RTT b) Instrumented Crossties and Fastening Systems at RTT

3.2.8 High Tonnage Loop (HTL) at TTC, CO

The second testing section was on a curved segment of the HTL as shown under the blue shade in **Figure 3.8 (a)**. The curvature for the testing section at HTL was approximately five degrees (5°).

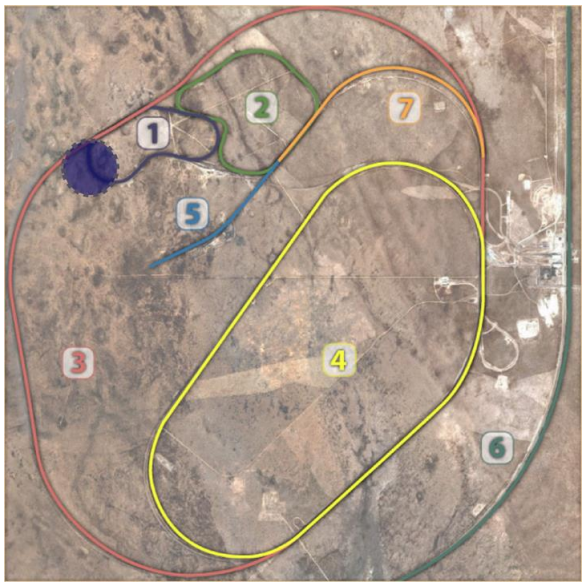

a)

b)

Figure 3.8 a) The Curved Testing Segment at HTL b) Instrumented Crossties and Fastening Systems at HTL

3.3 Instrumentation Equipment

3.3.1 Strain Gauges

Strain gauges were used to measure the forces in track components induced from applied loads. Several types of strain gauges were used in this project based on the application. Standard 120-ohm foil type shear strain gauges were used for quarter bridge circuits (**Figure 3.9**). Shear strain gauges in a chevron pattern with two 120-ohm gauges oriented 90° to each other were used for full bridge circuits. 120-ohm concrete internal (embedment) and concrete surface strain gauges were also used. Strains were measured to an accuracy of about microstrain. Strain bridges were calibrated with a load cell of known calibration in order to resolve strain measurements into forces.

Figure 3.9 Standard 120-ohm Foil Type Shear Strain Gauge

3.3.2 Potentiometers

Displacement transducers called linear potentiometers were used to measure relative displacement between components and global displacements of components relative to a known baseline (**Figure 3.10**). Potentiometers had a maximum stroke length of 1.1 inch and were

accurate to one thousandth of an inch. Potentiometers used a known calibration factor from the manufacturer.

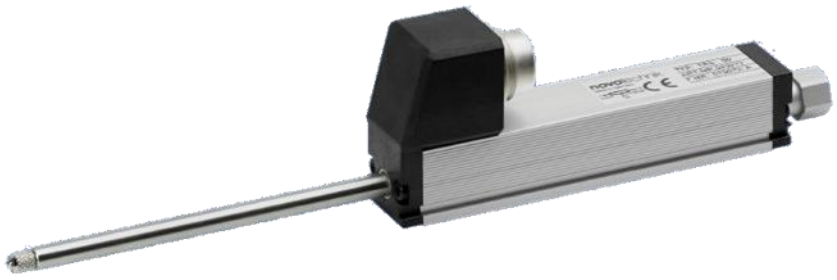

Figure 3.10 Linear Potentiometer

3.3.3 Matrix Based Tactile Surface Sensors

Matrix Based Tactile Surface Sensors (MBTSS) were used to quantify the load magnitude and pressure distribution on the rail seat of concrete crossties (**Figure 3.11**). MBTSS use pressure-sensitive ink printed in rows and columns to form a grid. The resistivity of the ink changes as load is applied resulting in a higher voltage output to the software. Protective layers were placed between the rail pad assembly and the MBTSS as well as between the MBTSS and the rail seat to prevent shear and puncture damage. MBTSS data were recorded with software designed specifically for MBTSS instrumentation and did not require calibration.

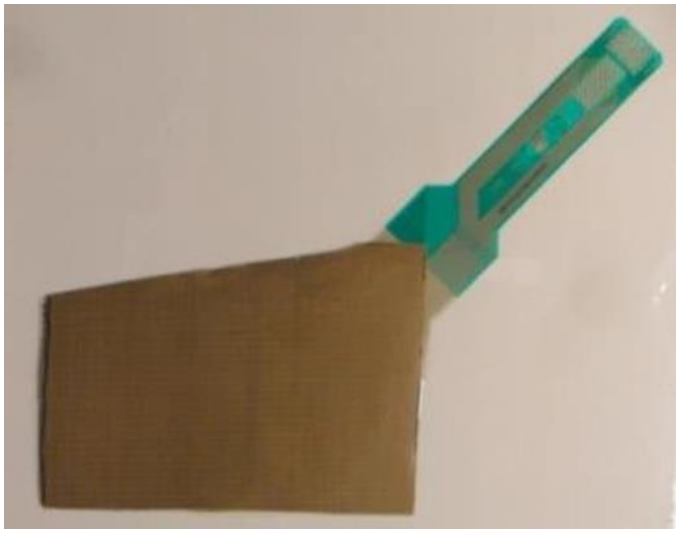

Figure 3.11 Matrix Based Tactile Surface Sensors (MBTSS)

3.3.4 Compact Data Acquisition

A National Instruments (NI) compact data acquisition (cDAQ) system was used to record data from strain bridges and potentiometers (**Figure 3.12**). Strain bridges and potentiometers were connected to the cDAQ. cDAQ output signals from strain bridges and potentiometers were recorded through a NI LabView program developed specifically for the instrumentation.

Figure 3.12 Compact Data Acquisition (cDAQ) System

3.4 Instrumentation Measurement

3.4.1 Strain Measurement

Generally the applied load and reaction force measurement were realized by measuring strain, while conducting with necessary calibration process. Additional strain measurement was used to determine the structural deformation of each component, and thus to understand the load path. Rail strain, internal concrete crosstie strain, external concrete crosstie strain, fastening clip strain and fastening shoulder strain were measured in the laboratory and field studies.

3.4.1.1 Rail Strain Measurement

Rail deformation was measured with strain gauges under vertical and lateral wheel loads (**Figure 3.13**). A bending moment diagram of a rail cross-section was output from these strain data. Based on the strain measurements, the deformed shape of rail was also output.

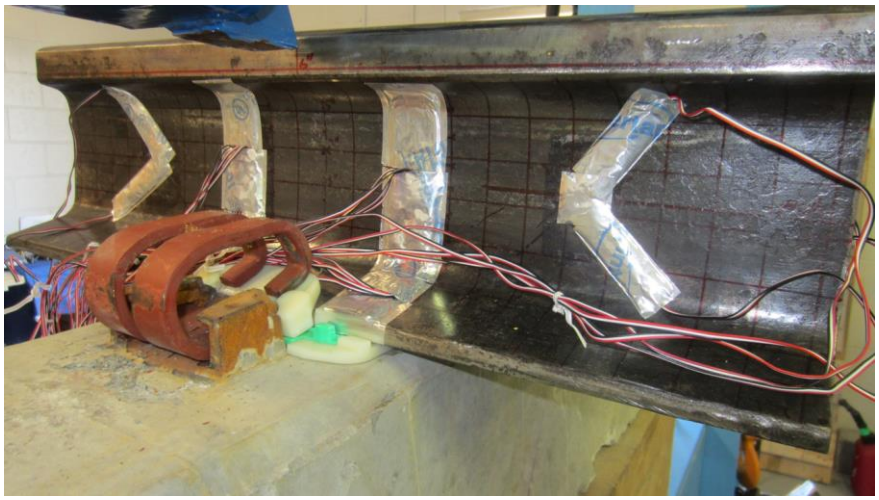

Figure 3.13 Strain Gauges Installed on Rail

3.4.1.2 Crosstie Internal Strain Measurement

Internal crosstie strains were measured to understand the compression behavior of the crosstie beneath the rail seat area (**Figure 3.14**). Embedment strain gauges were used to measure vertical deformation below rail seat from which vertical reaction forces and internal pressure distributions could be known. The gauges were mounted to a steel mesh and fixed to the pre-stressing strands before concrete was poured. Wires were secured in a wire box and released after the concrete had hardened.

Figure 3.14 Mesh to Hold Embedment Crosstie Strain Gauges Prior to Concrete Being Poured

3.4.1.3 External Crosstie Strain Measurement

External crosstie strains were measured to understand the bending and compression behavior of the crosstie under loading. Concrete surface gauges were applied at multiple locations on the surface of the crosstie oriented longitudinally to measure bending moments (**Figure 3.15**).

Gauges were also applied on the surface of the crosstie below the rail seats oriented vertically to measure vertical rail seat stress distribution.

Figure 3.15 External Crosstie Strains

3.4.1.4 Fastening Clip Strain Measurement

Fastening clip strains were measured to understand the behavior of the clip and change in clamping force under the applied wheel loads. Strain gauges were used to measure clip deformation and were applied on specific locations on the inner and outer surfaces of a clip perpendicular to the rail (**Figure 3.16**).

Figure 3.16 Strain Gauges on Clip

3.4.1.5 Fastening Shoulder Strain Measurement

Lateral forces entering the shoulder were directly measured to understand the forces passing through the insulator post as well as to further define the lateral load path. Strain gauges were installed on both surfaces of a steel beam. The material of shoulder face was grounded down to meet the same thickness of the steel beam instrumented with strain gauges prior to the test, and then the beam was inserted between the remaining part of the shoulder and rail base (**Figure 3.17**). The installation first required removing the clips and rail pad assembly from the rail seat. Next, the shoulder face was grounded away. To complete the process before data acquisition, the steel beam, the new rail pad assemblies, the insulators, and the clips were installed. The structural testing and the associated data analysis with the instrumented shoulder beam insert was cooperated with Brent Williams (Williams et al 2014).

Figure 3.17 Strain Gauges Installed on Shoulder Prior to Clip Application

3.4.2 Displacement Measurement

The global and relative displacements of the crosstie and fastening systems were measured with potentiometers. Displacement measurement was obtained to know the structural deformation and system stiffness. Combining the strain and displacement measurements, the deformation map of a component could be generated.

3.4.2.1 Global Displacement Measurement

Global displacements of the crosstie were measured with linear potentiometers, which were clamped tightly onto rods driven into the subgrade (**Figure 3.18**).

Figure 3.18 Global Crosstie Displacement Measured by Potentiometers Mounted on Rods

3.4.2.2 Relative Displacement Measurement

The displacements of fastening systems relative to a crosstie were measured by linear potentiometers mounted on the crosstie. Aluminum fixtures were used to hold potentiometers as shown in **Figure 3.19**. Lateral displacements of the rail web and the rail base, vertical displacements of the rail base on both of field and gauge sides, and rail pad assembly displacements were measured.

Figure 3.19 Aluminum Fixture for Potentiometer Placement

3.4.3 Rail Seat Pressure Distribution Measurement

MBTSS (Section 3.3.3) was installed below rail seats to measure the distribution of the reaction force onto the concrete rail seat surface. The structural testing with the MBTSS and associated data analysis was prepared by Matthew Greve (Greve et al 2015). As shown in **Figure 3.20**, the MBTSS was installed between the abrasion frame (bottom layer of the pad assembly) and the concrete surface. The installation and removal of MBTSS sheet was accomplished by temporarily raising the rail to a height (about an inch) adequate for accurately placing and removing the sensor. For large-scale multi-crosstie experiments, the fastening clips directly above the rail seat installed with MBTSS and the nearest two pairs of clips from both sides were removed prior to the sensor installation and removal.

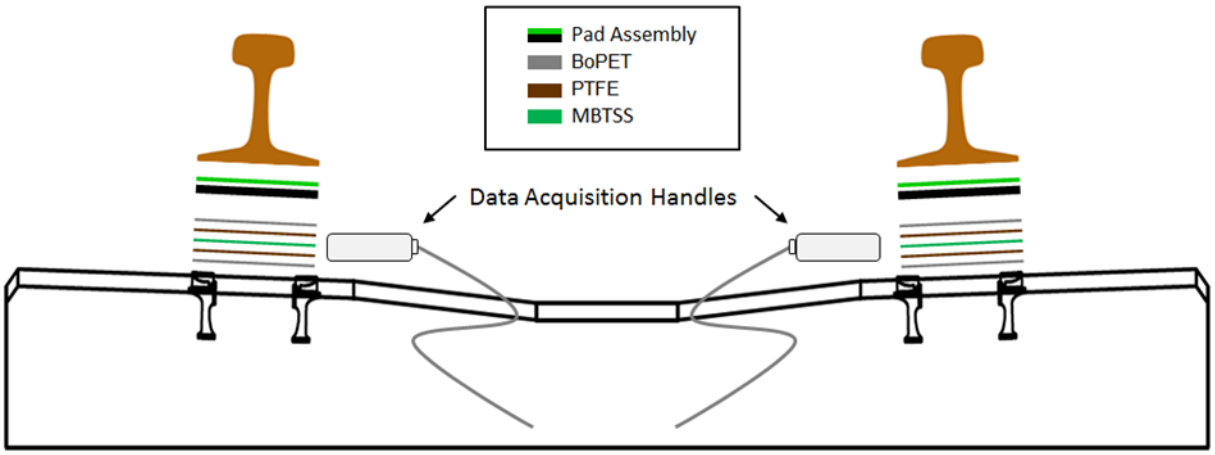

a)

b)

Figure 3.20 a) Profile View of MBTSS Installation on Crosstie b) Plan View of MBTSS Installation on Crosstie

3.5 Various Force Calculation Methodology

Various forces (moments) which including vertical and lateral wheel loads, rail seat vertical reaction force, lateral reaction force transferred through shoulder, clamping force and crosstie

bending moment were measured indirectly. As stated in Section 3.4.1, strain measurements were taken from various locations, with conducting necessary calibration and calculation, the forces (moments) can be obtained. The following sections will describe the methodology used in the calculations for finding force values from the strain measurements.

3.5.1 Vertical Wheel Load (on the Rail) Measurement

Vertical wheel load was measured to quantify the actual load entering the rail head. Chevron strain gauge patterns were installed on both sides of rail 6 inches apart centered in the crib at a height coincide the rail's neutral axis (**Figure 3.21**).

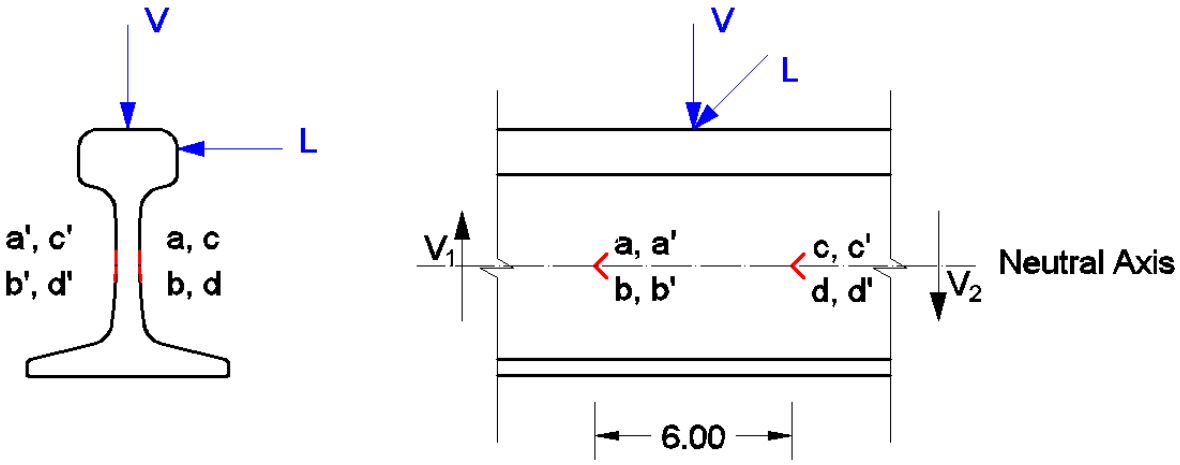

Figure 3.21 Strain Gauge Pattern for Vertical Wheel Load Measurement

Theoretically the following equations could be used to calculate the vertical wheel load V:

$$V = V_1 - V_2$$

$$V_1 = \frac{EIt}{(1+\nu)Q}\varepsilon_1, \qquad V_2 = \frac{EIt}{(1+\nu)Q}\varepsilon_2$$

$$\varepsilon_1 = (\varepsilon_a - \varepsilon_b + \varepsilon_{a'} - \varepsilon_{b'})/4, \qquad \varepsilon_2 = (\varepsilon_c - \varepsilon_d + \varepsilon_{c'} - \varepsilon_{d'})/4$$

$$V = \frac{EIt}{(1+\nu)Q}(\varepsilon_1 - \varepsilon_2) = x_V \cdot (\varepsilon_1 - \varepsilon_2)$$

Where,

$V\ and\ L$ are the vertical and lateral applied wheel loads

$\varepsilon_a, \varepsilon_b, \varepsilon_c, \varepsilon_d$ are strain measurements taken from the front face of the rail

$\varepsilon_{a'}, \varepsilon_{b'}, \varepsilon_{c'}, \varepsilon_{d'}$ are strain measurements taken from the back face of the rail

$V_1\ and\ V_2$ are shear forces left or right beyond the strain gauge patterns

E is the elastic modulus of steel

ν is the Poisson's ratio of steel

t is the thickness of the rail at neutral axis

Q is the static moment of the cross-sectional area of the rail

I is the moment of inertia of the cross-sectional area of the rail

x_v is the gauge factor for the vertical wheel load

As shown in **Figure 3.22**, the eight strain gauges measuring the shear strain are connected into a Wheatstone bridge to obtain $(\varepsilon_1 - \varepsilon_2)$.

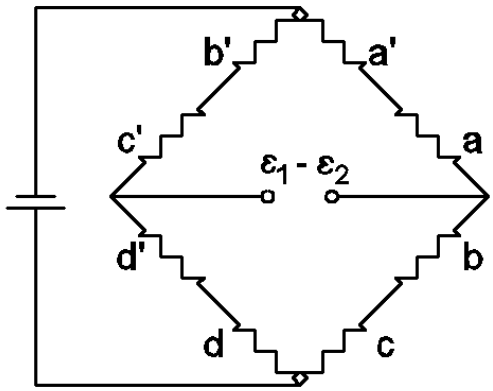

Figure 3.22 Wheatstone Bridge Used to Connect the Strain Gauges to Calculate the Vertical Wheel Load

Considering the accuracy of the strain gauge installation, a known load measured by a load cell was used to calibrate each strain bridge.

3.5.2 Lateral Wheel Loads (on the Rail) Measurement

Similar as the vertical wheel load, lateral wheel load was measured to quantify the actual load going through the rail head. Two methods of measuring the lateral wheel load were designed, one was to measure the shear strain in the crib by using a similar Chevron pattern over the rail base (**Figure 3.23**); the other one was to measure the bending strain with a full Wheatstone bridge over the rail seat (**Figure 3.24**).

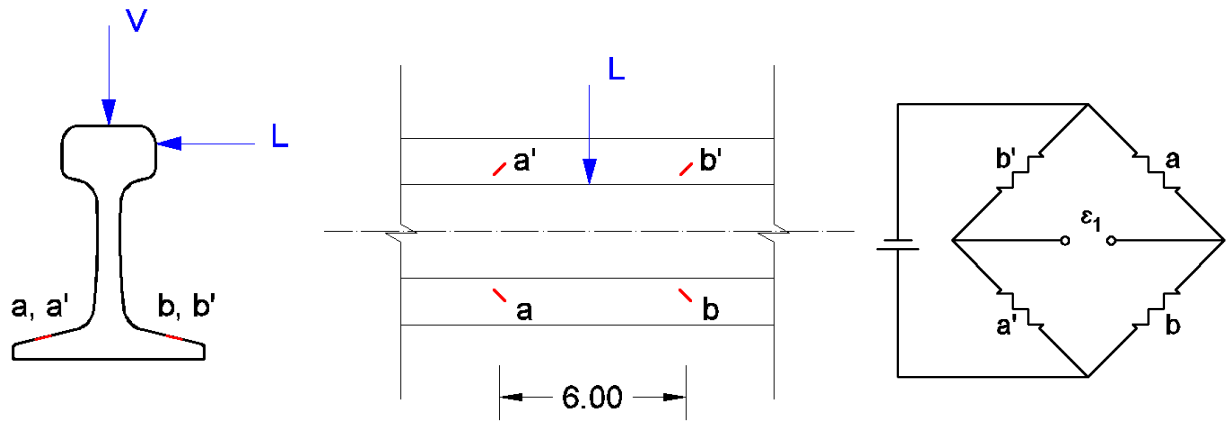

a) **b)** **c)**

Figure 3.23 First Iteration of Strain Gauge Pattern for Lateral Wheel Load Measurement

a) Cross-sectional Elevation View b) Plan View c) Full bridge connection for strain gauges

For the first method, four strain gauges cosisted two pairs of Chevron pattern gauges that were six inches apart and centered at in the crib on the top surface of rail base. The theoretical calculation of lateral force is quite similar to the methodology stated in Section 3.5.1, and calibration is also required.

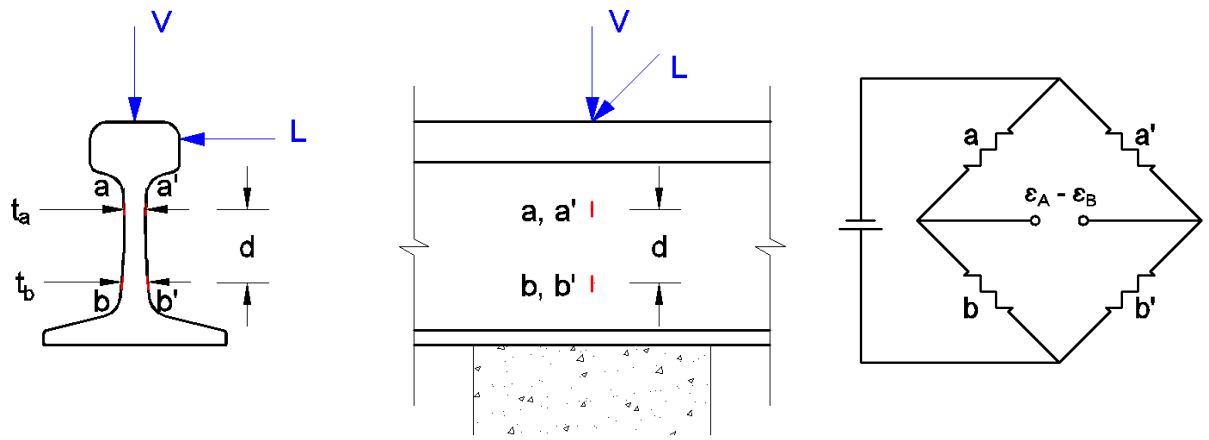

a) **b)** **c)**

Figure 3.24 Second Iteration of Strain Gauge Pattern for Lateral Wheel Load Measurement

a) Cross-sectional Elevation View b) Elevation View c) Full bridge connection

For the second method, two strain gauges were installed on each side of the rail centered above the rail seat. The following equations are used to calculate the lateral wheel load:

$$\varepsilon_A = (\varepsilon_a - \varepsilon_{a'})/2$$
$$\varepsilon_B = (\varepsilon_b - \varepsilon_{b'})/2$$
$$L = \frac{EI_a\varepsilon_A}{t_a d} - \frac{EI_b\varepsilon_B}{t_b d} \approx x_L(\varepsilon_A - \varepsilon_B)$$

Where,

V and L are the vertical and lateral applied wheel loads

$\varepsilon_a, \varepsilon_b$ are strain measurements taken from the front face of the rail

$\varepsilon_{a'}, \varepsilon_{b'}$ are strain measurements taken from the back face of the rail

E is the elastic modulus of steel

t is the thickness of the rail at the location of strain gauge

I is the moment of inertia of the cross-sectional area of the rail at the location of strain gauge

x_L is the gauge factor for the lateral wheel load

Considering the accuracy of the strain gauge installation, a calibrated load cell was used to monitor applied load and calibrate the strain bridge.

3.5.3 Rail Seat Vertical Reaction Calculation Methodology

As stated in Section 3.4.1.2, concrete embedment strain gauges were used to measure the vertical strain internal of concrete below rail seats. Internal crosstie strains were measured 2 inches – which was the depth to the center of the embedment strain gauges – below the concrete surface of the rail seat. Four embedment strain gauges were installed during crosstie manufacturing in a 2 by 2 pattern as shown in **Figure 3.25**.

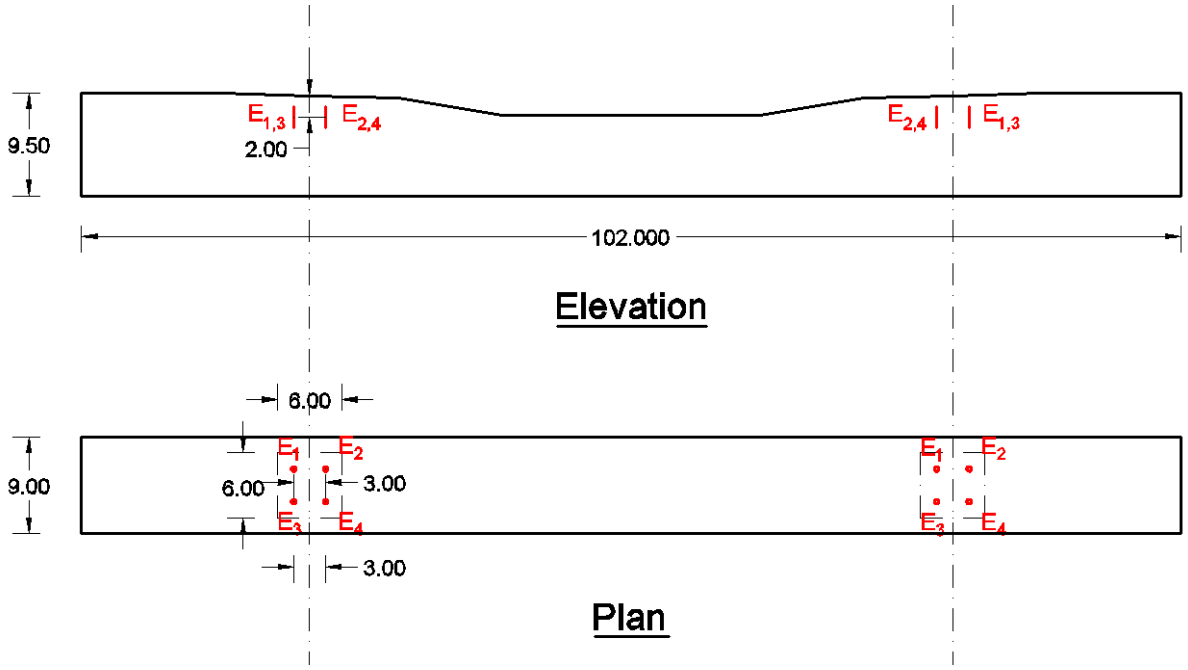

Figure 3.25 Elevation and Plan View of Concrete Crosstie Installed with Embedment Strain Gauges

To obtain the rail seat vertical reaction force using the compressive strain output from these embedment gauges, the following equation is used:

$$V_{tie}(kips) = e_{AVG} \cdot E_c \cdot A \cdot Q_1 \cdot Q_2 \cdot Q_3$$

Where,

V_{tie} is the vertical rail seat reaction force

e_{AVG} is the average strain recorded from the four embedment sensors

E_c is the elastic modulus of the concrete material

A is the area of rail seat

Q_1 is the correction factor for bearing area in concrete at the height of embedment strain gauges

Q_2 is the correction factor for loading eccentricity

Q_3 is the correction factor for support length below concrete crosstie

Q_2 can be calculated using the following equation:

$$Q_2 = 1 - \alpha(e_{DIFF} / e_{DIFF\_MAX})$$
$$e_{DIFF} = (e_1 + e_3)/2 - (e_2 + e_4)/2$$

(e_{DIFF} is taken when the loading width is 1.5 inches at field side of rail seat, α is the amplification factor calculated from calibration)

Q_1, Q_2, Q_3 were obtained through laboratory calibration. Q_1 was measured with no loading eccentricity and Q_3 was standardized as 1 for 6-inch support width. Q_3 was calculated with no loading eccentricity and varying support widths. Q_2 was calculated with various loading eccentricity and standardized support width (6-inch).

3.5.4 Shoulder Lateral Reaction Calculation Methodology

Lateral reaction forces were measured with a full-bridge strain gauge pattern to understand the forces passing through the insulator post as well as to further define the lateral load path. As described in Section 3.4.2.5, a steel beam instrumented with strain gauges was used to replace the material grounded off from the fastening shoulder face. Four strain measurements were taken from both the top and bottom surfaces of the fastening shoulder beam insert (**Figure 3.26**). Strain gauges were adhered to the steel beam. Strains measured on the steel beam induced from lateral loads were resolved into forces using calibration curves generated on the uniaxial loading machine.

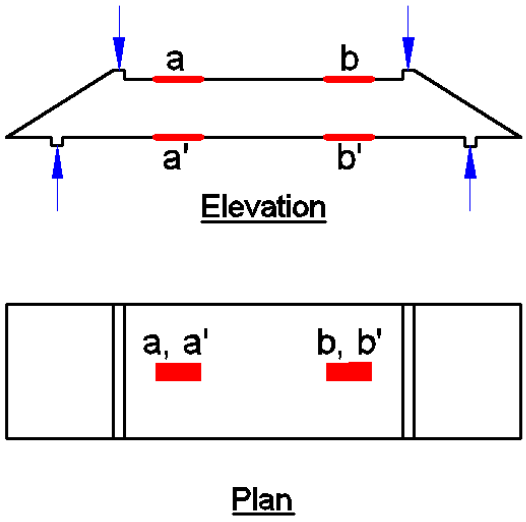

Figure 3.26 Elevation and Plan View of Fastening Shoulder Beam Insert Installed with Strain Gauges

3.5.5 Fastening Clamping Force Calculation Methodology

Strain measured from fastening clips were used in clamping force calculations. A Safelok I type clip was designed to apply 2.375 kips initial clamping force in the vertical direction normally to the rail seat. The 14.2° angle of the rail base from the rail seat plane results in 2.5 kips of clamping force applied normal to the top surface of rail base. The tangential component of clamping force was unknown due to both the direction and magnitude being dependent on the installation procedure. Prior to clip installation, strain gauges were placed on both gauge side and field side clips. The initial applied and reaction forces are shown in **Figure 3.27**.

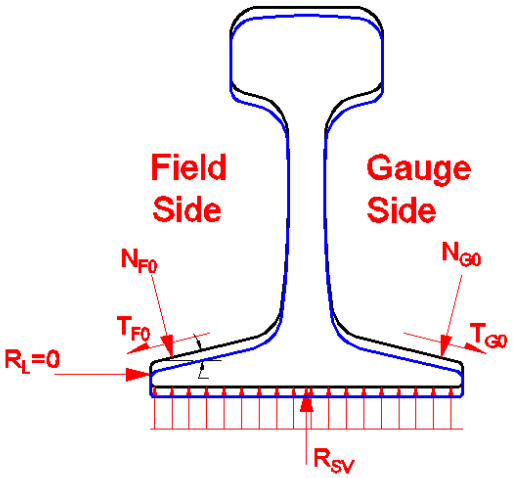

Figure 3.27 Initial Free Body Diagram (after Clip Installation)

Where,

$N_{F0/G0}$: Normal component of clamping force (right after installation) at field/gauge side

$T_{F0/G0}$: Tangential component of clamping force (right after installation) at field/gauge side

R_{SV}: Rail seat reaction force

R_L: Lateral reaction from shoulder face

Three types of strain gauge patterns were used to study the behavior of clips. Strain gauges were installed at multiple locations on the inner and outer surfaces of a clip for clamping force calculations.

Figure 3.28 shows the first iteration, in which seven strain gauges were placed along each leg of the clip. The distance between adjacent gauges was one inch. To protect the gauges during installation, gauges 1-3 were placed on the inner surface of the clip while gauges 4-7 were placed on the outer surface. To compensate for torsional deformation and uneven loading, strain

gauges were installed at the same locations on both legs. The clamping force applied by each leg was then calculated and summed to obtain the total force applied to the clip. The distance from the center of each strain gauge, d_i, and the relevant angle, φ_i, were used to locate each gauge. A numerical program was developed to

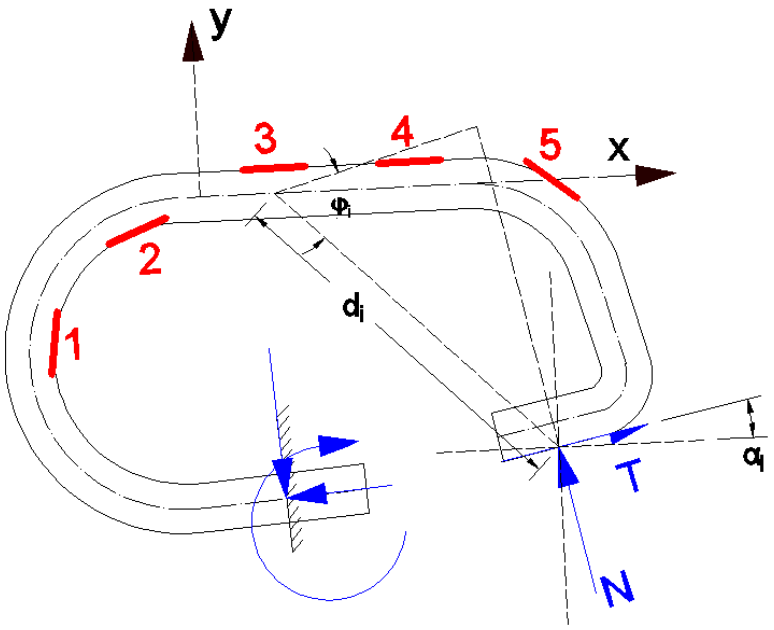

Figure 3.28 First Iteration of Strain Gauge Orientation on Instrumented Clips

For the second iteration, three pairs of stain gauges were placed on both inner and outer surfaces of the clip to determine the bending moment (**Figure 3.29**). Strain gauges were installed on both legs of a clip to compensate for torsional behavior and uneven leg load.

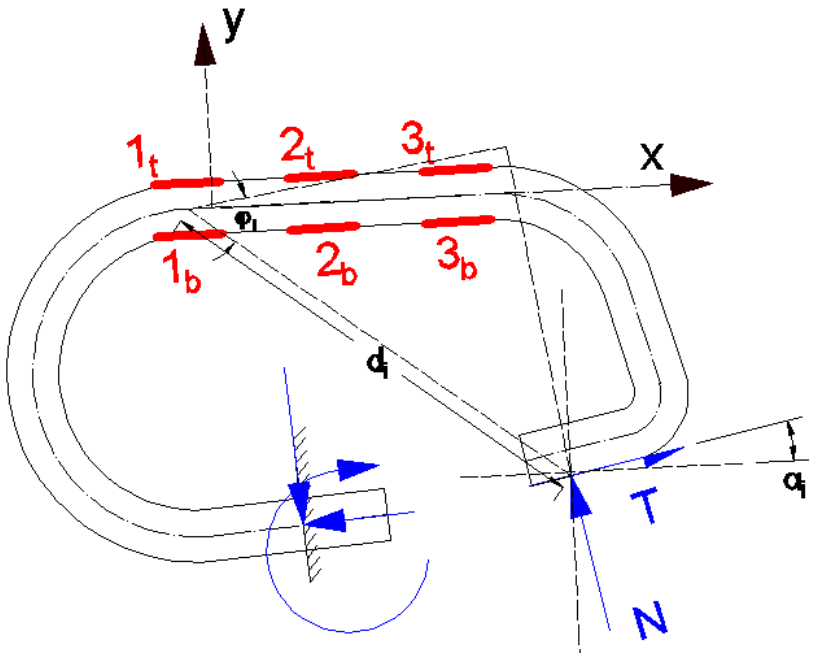

Figure 3.29 Second Iteration of Strain Gauge Orientation on Instrumented Clips

The third iteration is a simplified version of the second one. As shown in **Figure 3.30**, only one pair of strain gauges was installed on each leg.

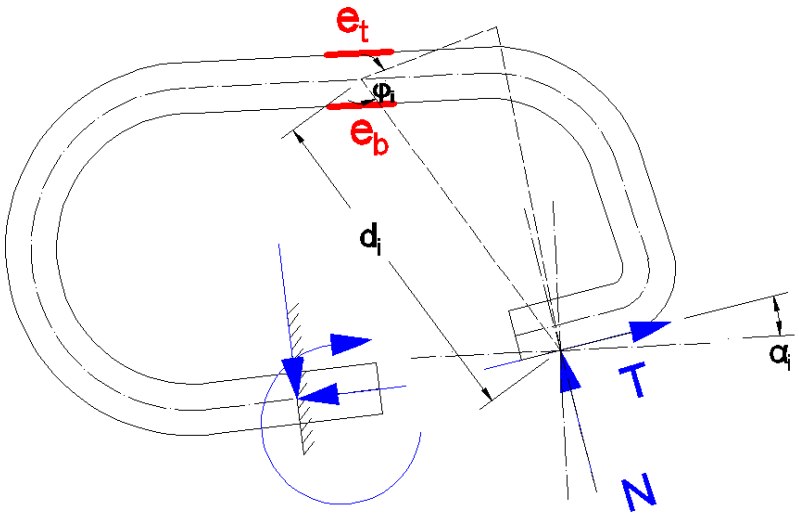

Figure 3.30 Third Iteration of Strain Gauge Orientation on Instrumented Clips

To measure the clamping force, one pair of instrumented clips were installed on one rail seat (on both field and gauge sides). Theoretically, any combination of the two strains read from the same leg of a clip can be used to calculate the normal and tangential forces applied at each clip tip. Linear elastic theory and the free body diagram as shown in **Figure 3.31**.

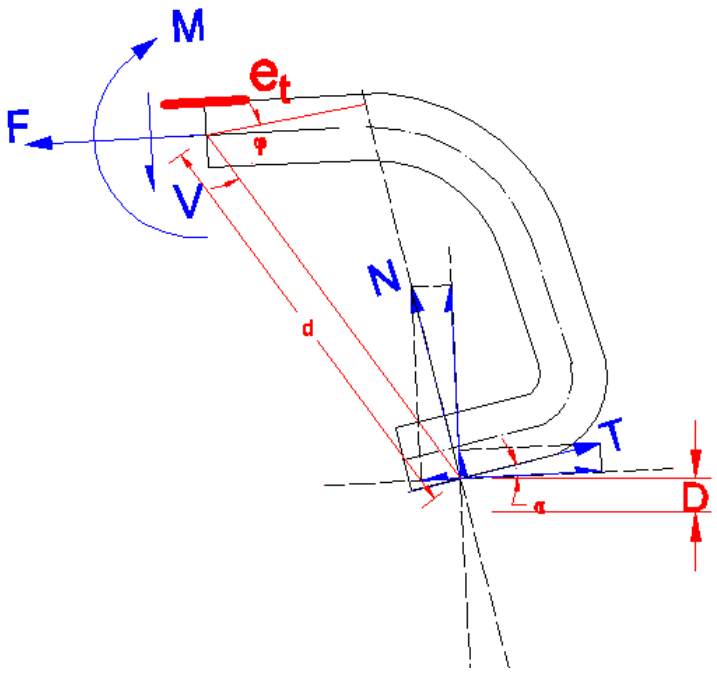

Figure 3.31 Free Body Diagram of Clip

The equations used to address the normal and tangential forces are written below:

$$N = \frac{a_{22} \cdot e_t - a_{12} \cdot e_b}{a_{11} \cdot a_{22} - a_{12} \cdot a_{21}}$$

$$T = \frac{-a_{21} \cdot e_t + a_{11} \cdot e_b}{a_{11} \cdot a_{22} - a_{12} \cdot a_{21}}$$

where,

$$a_{11} = \frac{-d \cdot A \cdot (t/2) \cdot \cos\varphi - I \cdot \sin\alpha}{E \cdot A \cdot I},$$

$$a_{12} = \frac{-d \cdot A \cdot (t/2) \cdot \sin\varphi + I \cdot \cos\alpha}{E \cdot A \cdot I}$$

$$a_{21} = \frac{d \cdot A \cdot (t/2) \cdot \cos\varphi - I \cdot \sin\alpha}{E \cdot A \cdot I},$$

$$a_{22} = \frac{d \cdot A \cdot (t/2) \cdot \cos\varphi + I \cdot \sin\alpha}{E \cdot A \cdot I}$$

E is elastic modulus of the steel used for the clips; A is area of the cross-section of each toe; I is the moment of inertia of the cross-section of each toe.

However, as the dimensions of the clip were not far greater than the length of the strain gauge used in the test, the strain reading could easily be affected by the hand installation of the gauges. To obtain an accurate result, all the five strain measurements needed to be utilized to find the actual clamping force applied to each toe of the clip. To achieve this goal, a Matlab program was developed to search for the N and T that best matching these five strain measurements.

The calculation of clamping force from the second iteration of strain gauge pattern is similar to the first iteration.

Considering the limitation of the number of channels that were available in tests, an alternative way of measuring the clamping force was developed with the third iteration of strain gauge pattern. Linear elastic analysis was used in clips behavior analysis. The contact point

between the clip tip and the insulator is assumed to be 0.3 inch from the edge, which agreed with findings from preliminary finite-element analysis

To deal with large amount of data, it is impossible to use the numerical program described above to calculate the increment of clamping force. However, as one vertical displacement measurement (from potentiometer) was recorded from gauge side rail base, the increment of clamping force can be obtained by combing the clip deformation and the clip tip deflection.

The change of normal and tangential forces can be calculated using the equations below:

$$\Delta N = D \cdot (1250 lbs / 0.289 in)$$

$$\Delta T = \left(\frac{-e_t + e_b}{2} - \frac{\Delta N d (t/2)\cos\varphi}{EI}\right) \cdot \frac{EI}{d(t/2)\sin\varphi}$$

Where,

ΔN is the change of normal force N

ΔT is the change of tangential force T

D is the vertical rail base deflection

The assumptions used for calculation are listed below:

1) The normal component of clamping force (N_F and N_G) can be expressed by $\Delta N = kD$ (in linear range), where k is the clip opening stiffness, which can be obtained from the manufacturer manual and FEM analysis, or from simple component testing. For Amsted RPS UAB 2000 clips, k is designed to be 8650 lbf/in, and the initial clamping force (normal component) is 2500 lbf.

2) Displacement vertically to the clip toe can be expressed by the vertical deflection D_F and D_G relative to the crosstie measured at the tip of the rail base. As the inclination of rail base is 14.2°, cos(14.2°)=0.97~1, it is reasonable to use the vertical displacement relative to tie to the displacement vertical to top surface of rail base or the clip toe.

3) When the tangential component of the clamping force is greater than the maximum static friction force, which means the friction cannot hold the clip toe from sliding, there is a relative movement between the clip toe and the rail along the rail base. The vertical component of the sliding relative to the crosstie is assumed to be negligible compared to the vertical deflection at rail base.

4) The rail base remained straight, which has been examined in the laboratory experimentation. The curvature at rail base was negligible.

3.5.6 Crosstie Bending Moment Calculation Methodology

Crosstie bending moments were determined from the external strain measured longitudinally of crossties. Two strain gauge patterns were developed as shown in **Figure 3.32** and **Figure 3.33**.

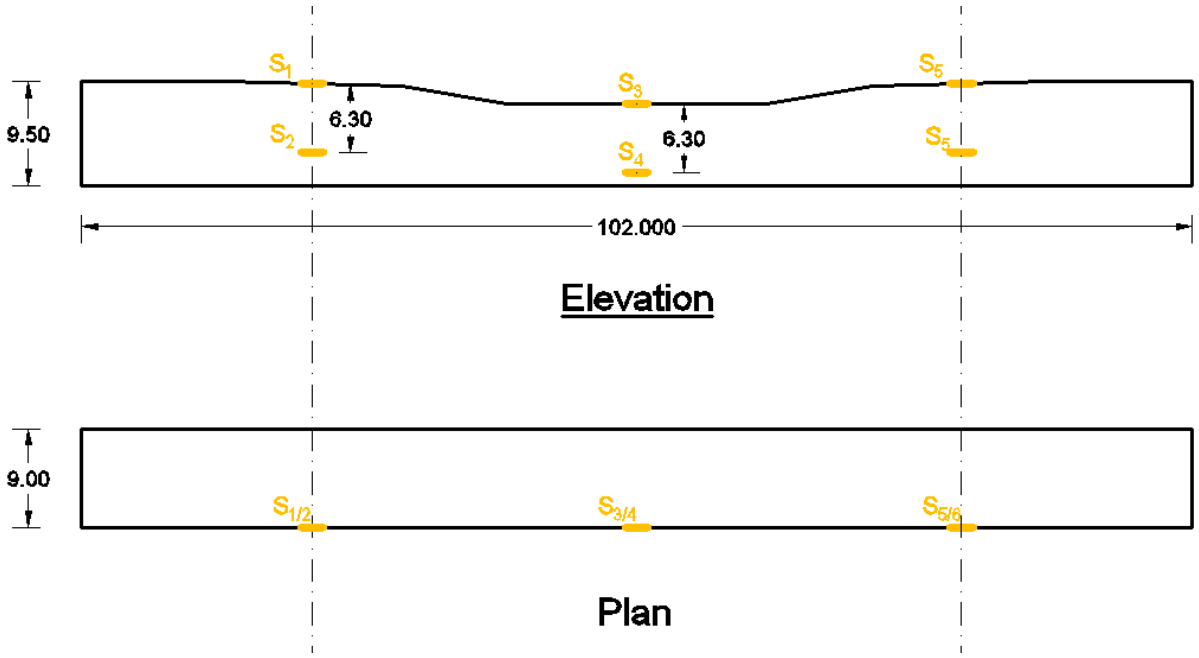

Figure 3.32 First Iteration of Strain Gauge Orientation on Instrumented Crossties

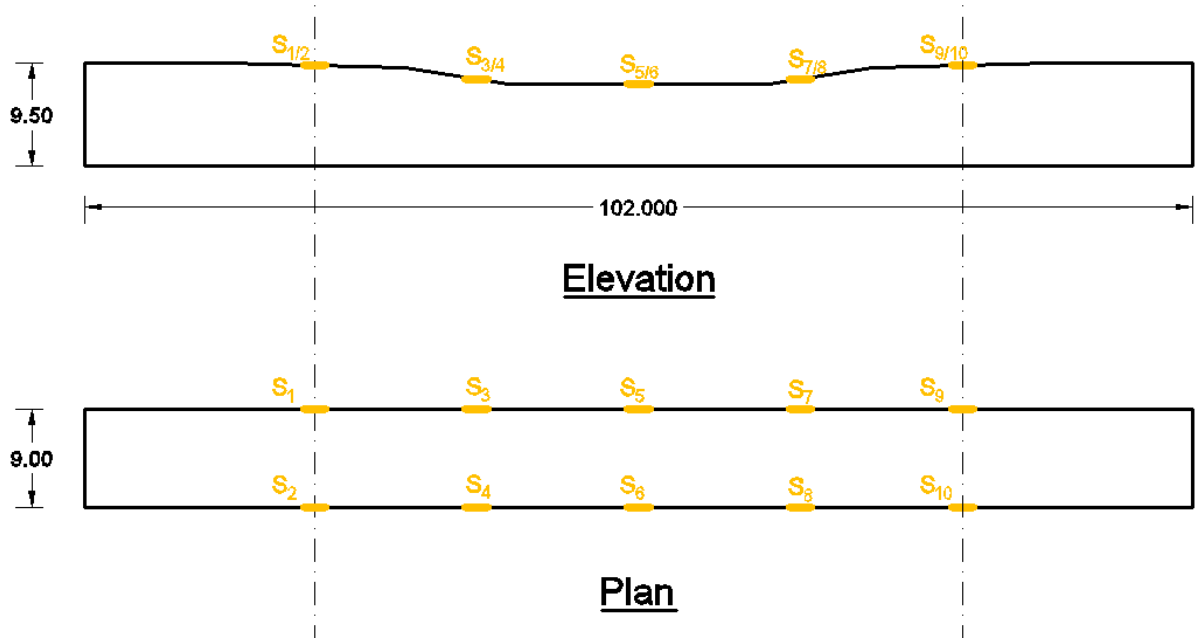

Figure 3.33 Second Iteration of Strain Gauge Orientation on Instrumented Crossties

For the first iteration (**Figure 3.32**), a pair of strain gauges was installed on the crosstie below each rail seat and the tie center. Within each strain gauge pair, the upper gauge was

installed at the narrow inclined surface at the top of concrete crosstie, the other was 6 inches below the upper one.

The following equations show the calculation to obtain the bending moments at each real seat as well as at concrete crosstie center.

$$M(railseat1) = (e_{S2} - e_{S1})E_c I_{12} / d$$
$$M(center) = (e_{S4} - e_{S3})E_c I_{34} / d$$
$$M(railseat2) = (e_{S6} - e_{S5})E_c I_{56} / d$$

Where,

e_{S1}~e_{S6} are the strains recorded from concrete surface strain gauges S_1~S_6 (See **Figure 3.32**).

E_c is the elastic modulus of concrete material

I_{12}~I_{56} are the moment of inertia of the concrete cross section at the location of each strain gauges pair

d is the vertical distance between the two strain gauges in each pair

For the second iteration (**Figure 3.33**), a pair of strain gauges was applied on both of the top corners of a crosstie at five locations: both rail seat centers, crosstie center and both mid points between crosstie center and rail seat centers. The calculation is similar as the first iteration.

3.6 Material-Level Experimental Plan

Material tests were done to validate the properties provided by the manufacturers. It is necessary to run materials-level because boundary conditions, creeping or shrinkage may also affect material behavior in reality.

3.6.1 Compressive Stiffness of Polyurethane and Nylon 6/6

For a Safelok I type fastening system, the rail pad made by polyurethane was used for load attenuation underneath the rail. The abrasion plate made by Nylon 6/6 was placed between the rail pad and concrete. Although material properties were provided by the material supplier, it was unclear whether or not the material properties were altered during the manufacturing process and loading application. To obtain the compressive stiffness of the rail pad and the abrasion plate, static uniaxial compression tests of both materials were conducted on the uniaxial loading machine (Section 3.2.1). The material testing and data analysis were prepared by Zhe Chen and Moochul Shin (Chen et al 2014).

Through the compression tests, the Young's modulus and the yielding strength of the polyurethane and nylon 6/6 were determined. Uniform compressive load was applied in the vertical direction on the entire area of the testing specimens. The magnitude of the applied load and center deflection of the specimen were output from the loading machine. Two circular specimens were cut from a polyurethane rail pad and a nylon 6/6 abrasion frame. The diameters for each were 5 inches and 2 inches (**Figure 3.34**). To reduce frictions, Teflon was sprayed over both top and bottom surfaces of the testing specimens.

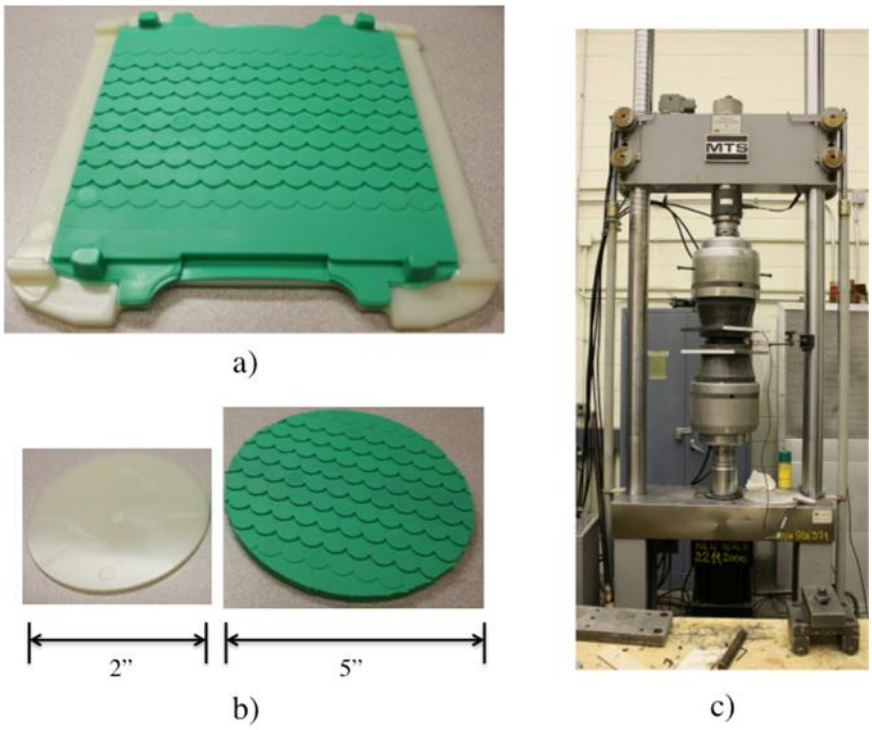

Figure 3.34 a) Rail Pad and Abrasion Plate b) Specimen of Rail Pad (Polyurethane) and Abrasion Plate (Nylon 6/6) Used in Compression Test c) Uniaxial Loading Machine

Figure 3.35 summarizes the result of compression test of rail pad and abrasion plate specimens. During the compressive experiment, no significant inelastic behavior was observed within the normal design rail seat load (40 kips). And therefore the compressive load was further increased until reaching the capacity of the loading machine.

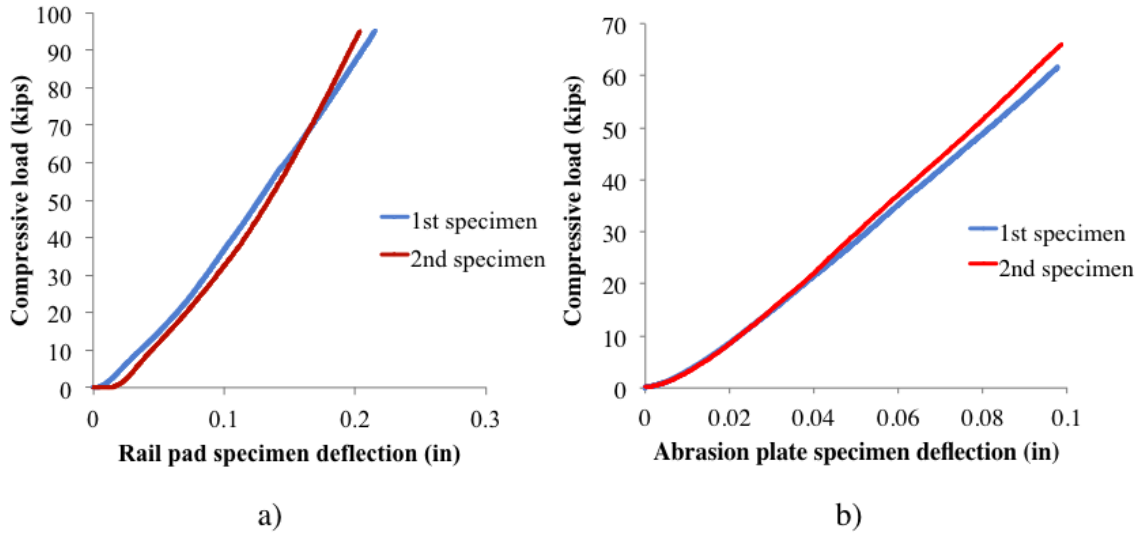

Figure 3.35 The Relationship Between Compressive Load and Specimen Deflection of Rail Pad and Abrasion Plate Specimens (Prepared by Zhe Chen and Moochul Shin)

It can be observed that the specimens remained elastic through the compression test, and inelastic behavior was not found. It should be specially noted that the expansion of both materials was significant (dark area surrounding the test specimens in **Figure 3.36**). And during the unloading process the specimens contracted back to the original size. Because Teflon was sprayed on both top and bottom surfaces of each specimen, low frictions were anticipated (no more than 10%). However, this is different from the actual boundary conditions existing in the rail pad assembly system. For detailed discussion, see Section 3.7.2.

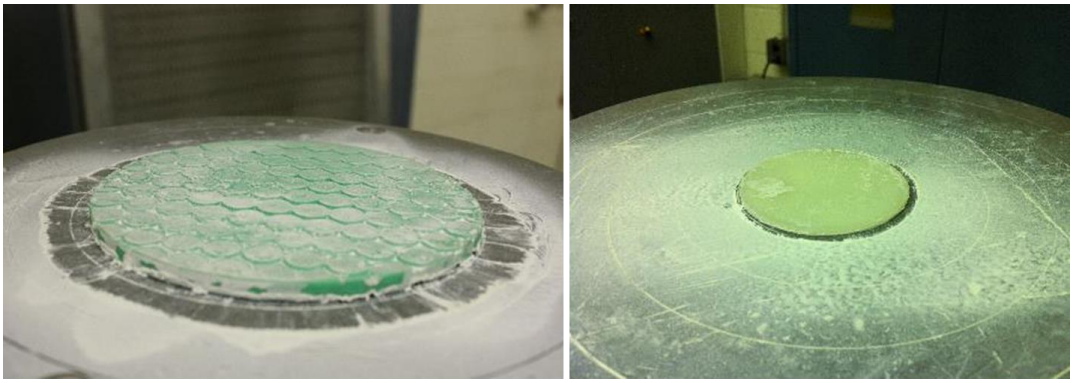

Figure 3.36 Specimens of Rail Pad and Abrasion Plate After Compression Test (Prepared by Zhe Chen and Moochul Shin)

The comparison between material properties from the suppliers and from tests is shown in **Table 3.1**. The elastic modulus of rail pad (polyurethane) was 26.4% lower than that provided by material supplier. The elastic modulus of abrasion plate (nylon 6/6) was only 5.3% of the given value, more experimental validation is needed in future. Considering the thickness of the abrasion is 0.055 inch and of 23.3% of the thickness of rail pad, and its elastic modulus is much greater (even from the laboratory material tests), the uncertainty of its material properties won't interfere the system behavior too much (see discussion in Section 4.2.3.1).

Table 3.1 Comparison of Material Properties from Compression Test Result and from Material Suppliers

Component	Test result		Material supplier information	
	Young's modulus (psi)	Yielding strength (psi)	Young's modulus (psi)	Yielding strength (psi)
Abrasion plate	23258	-	440000	12000
Rail pad	5520	-	7500	1900

3.6.2 Concrete Strength and Modulus

The concrete strength and elastic modulus were measured from concrete core compression cylinder testing. Cores were drilled and then used to obtain the concrete cylinder samples from a crosstie cast at the same time with the specimens used for other laboratory testing. Six concrete cylinder cores were prepared, the diameter for each specimen was 3 inches, and the length was 4.5 inches. To measure the compressive strain during the test, three concrete surface strain gauges were installed in the vertical direction of each cylinder. Uniaxial compressive loading machine was used to apply a uniform compressive load to each cylinder. Resin cap was cast on top and bottom surfaces of each cylinder to reduce friction. **Figure 3.37** shows the uniaxial compressive loading machine and the concrete core specimen with resin cap and the strain gauges. The geometry of the specimens, design of compression test, and material properties from the material supplier are summarized in **Table 3.2**.

a) **b)**

Figure 3.37 a) Uniaxial Compressive Loading Machine b) Specimen of Concrete Core with Three Concrete Surface Strain Gauges

Table 3.2 Design of Experiment and the Material Property from Manufacturer

Component	Design of experiment				Material property from manufacturer	
	Diameter (in)	Height (in)	Crushing load (kips)	Load rate (kips/min)	Young's Modulus (ksi)	Ultimate Strength (ksi)
Concrete Core	3	4.5	>49.5	10	4500	>7

The concrete strength and elastic modulus were also provided by the crosstie manufacturer. The average strength f′c and Young's modulus Ec obtained from the LB Foster concrete ties tests are shown in **Table 3.3**.

Table 3.3 Concrete Properties Measured from Concrete Core

	f′c (psi)	Ec (psi)
1 days	--	3.68×106
7 days	--	4.00×106
28 days	11,730	4.26×106

The concrete strength f′c at 1 year was founded as 11,000 psi, which was 6.2% lower than its 28 days strength. The slightly low strength could be due to the small sampling size. The Young's modulus was found to be 4.50×10^6 psi, which was 5.6% greater than its 28 days modulus. The tensile strength (cracking stress) of concrete was not measured directly but can be obtained using the equation recommended by ACI 318 as shown below:

$$f't = 7.5\sqrt{f'c} = 7.5\sqrt{11{,}000} = 787\text{psi}$$

The material properties obtained from the concrete cylinder core test were used in the analysis of concrete crossties.

3.7 Component-Level Experimental Plan

3.7.1 Rail Bending Behavior Experiment

The purpose of the rail bending behavior experiment was to understand the bending behavior of the rail under loading conditions representative of field loading conditions. In addition, the concept of using the rail as a load cell to measure forces going into the crosstie and fastening system was evaluated.

The uniaxial loading machine (Section 3.2.1) was used to apply static vertical loads to a 24-inch wide rail section. The rail was tested as a simply supported beam. Eight strain gauges were installed on the rail web, with four on each side (**Figure 3.38**). A static load was applied at the center of the rail section up to 35,000 lbf. Strains recorded from the experiment were compared with calculations applying linear-elastic beam theory for validation purposes.

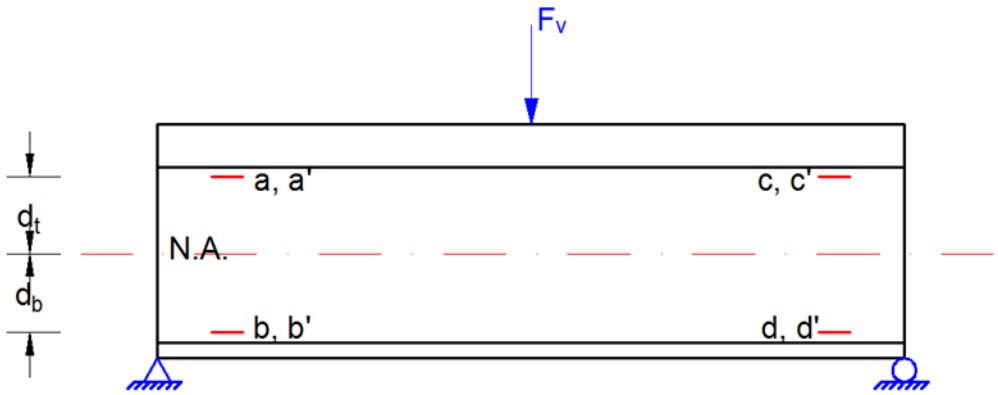

Figure 3.38 Detail Drawing of Rail Bending Experiment

The strain measurements recorded from the test under various center positive loadings were compared to the analytical strain values obtained by applying Euler-Bernoulli beam theory (**Figure 3.39**). In **Figure 3.39**, the experimental and analytical strain measured from the upper and lower gauges were labeled as "e_t" and "e_b". The average strain measured from a, a', c and c' was used as "e_t (experimental)"; and the average strain measured from b, b', d and d' from the same figure was used as "e_b (experimental)". The results show that, the experimental strain matched with the analytical strain very well, the maximum error for the top and bottom strain was only 0.8% and 0.3%. The results also revealed that, the rail strain remained linear under the static loading up tp 32.5 kips. And it can also be found that the straight plane assumption made in Euler-Bernoulli beam theory can be applied to rail at 2.5 inches away from

the supports (the lateral distance from the strain gauges to the supports). As a conclusion, under the static loadings being applied, the rail deformed elastically, and the bending strain was measureable using strain gauges, and the errors were acceptable.

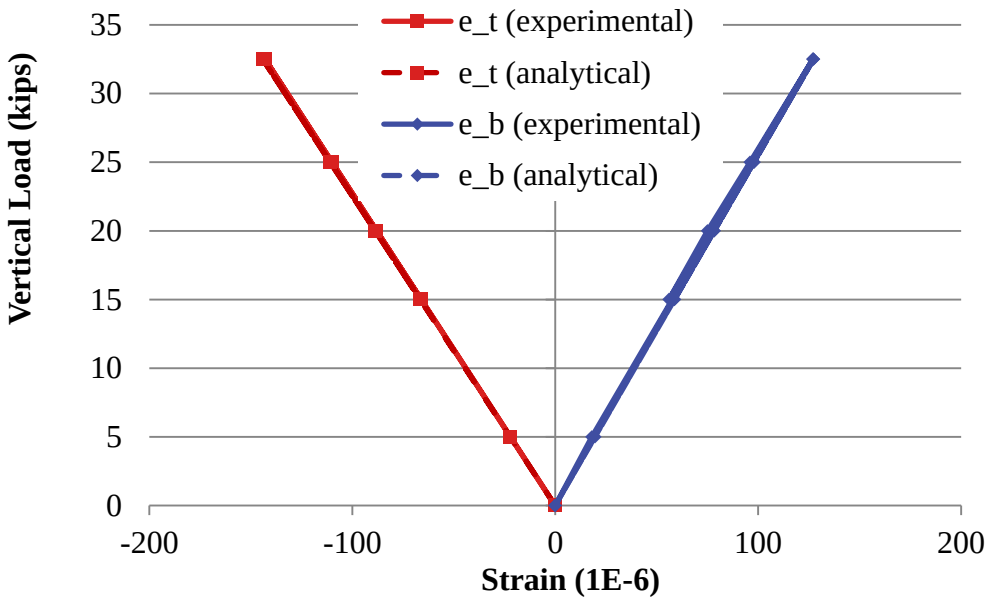

Figure 3.39 Experimental and Analytical Strain Measurements Under Center-Positive Bending Test

3.7.2 Rail Pad Assembly Stiffness Experiment

The friction-free compressive stiffness experiment for polyurethane (rail pad) and Nylon 6/6 (abrasion frame) was described in Section 3.6.1. However, the confinement caused by the friction forces at rail base – rail pad, rail pad – abrasion frame and abrasion frame – concrete interfaces need to be known. The purpose of the rail pad assembly stiffness experiment was to determine the compression deflection of the rail pad and abrasion frame under certain rail seat loads while putting into the track system, and thus to calculate the stiffness.

The STT was used to apply static vertical loads to the rail seat. A 1-inch thick steel plate was placed between the STT loading head and the rail pad. Four potentiometers were mounted onto the STT frame to measure the deflections from the four corners of the steel plate (**Figure 3.40**). A static 40 kips evenly distributed load was applied vertically over the entire rail seat.

Compression deflections and rail pad assembly stiffness were compared with the friction-free polyurethane and Nylon 6/6 stiffness.

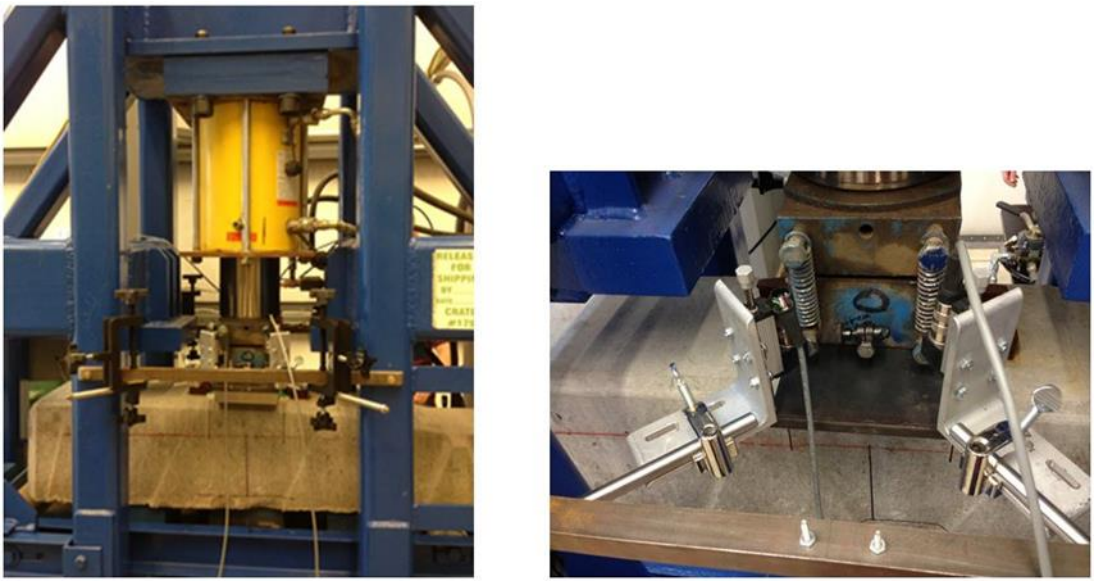

Figure 3.40 a) Vertical rail seat load applied by STT b) Rail pad assembly deflection measured by potentiometers

Because the nominal elastic modulus of polyurethane (7500 psi) is known to be far less than that of nylon 6/6 (440,000 psi), and the thickness of pad (0.236 inch) is about 4 times greater than the thickness of abrasion plate (0.06 inch), the compression deformation of the abrasion plate can be considered as negligible. To eliminate the compression of concrete included in the deflection measurements, the test was repeated with no polyurethane pad or

nylon frame. The deflection due to concrete compression can thus be subtracted. Both tests were repeated of 3 times, the average results were used.

Comparison of the pad deflection and stiffness from the nominal material properties and assembly test is shown in **Table 3.4**. It could be found that, due to the confinement provided by frictions between top and bottom interfaces, the compression deflection of the rail pad was only 34% of the deflection calculated using its nominal Young's modulus. This result revealed that the effect of the friction confinement was great. It also suggested that in the design and analysis, the assembly stiffness of the pad should be used instead of its Young's elastic modulus.

Table 3.4 Comparison between Nominal Material Properties and Assembly Test Result

Component	Nominal properties		Assembly test result	
	Young's modulus (psi)	Deflection at 40 kips rail seat load (in)	Stiffness (psi)	Deflection at 40 kips rail seat load (in)
Rail pad	7,500	0.035	21,850	0.012

3.7.3 Concrete Crosstie Behavior Experiment

The internal and external strain of a concrete crosstie was measured and analyzed to validate the concrete elastic modulus, to determine the location of the neutral axis of the crosstie and to clarify the vertical load path through the crosstie from the rail seat to the crosstie's support. The effect of varying support conditions on the load path in the crosstie was studied.

Embedment strain gauges were installed below the rail seat area of a concrete crosstie. Vertically-oriented surface strain gauges were installed in three layers to study the bearing area at various heights below the rail seat as well as the load path in the crosstie. Concrete surface gauges were also placed in the longitudinal direction, parallel to the crosstie, to quantify the

bending moments in the crosstie at the rail seat and center line of the crosstie. The dimensions of the crosstie and locations of strain gauges are labeled in **Figure 3.41**.

Labels of gauges:

E_1-E_8: Embedment strain gauges

S_{L1}-S_{L6}: Surface gauges in longitudinal direction of concrete tie

S_{V1}-S_{V10}: Surface gauges in vertical direction

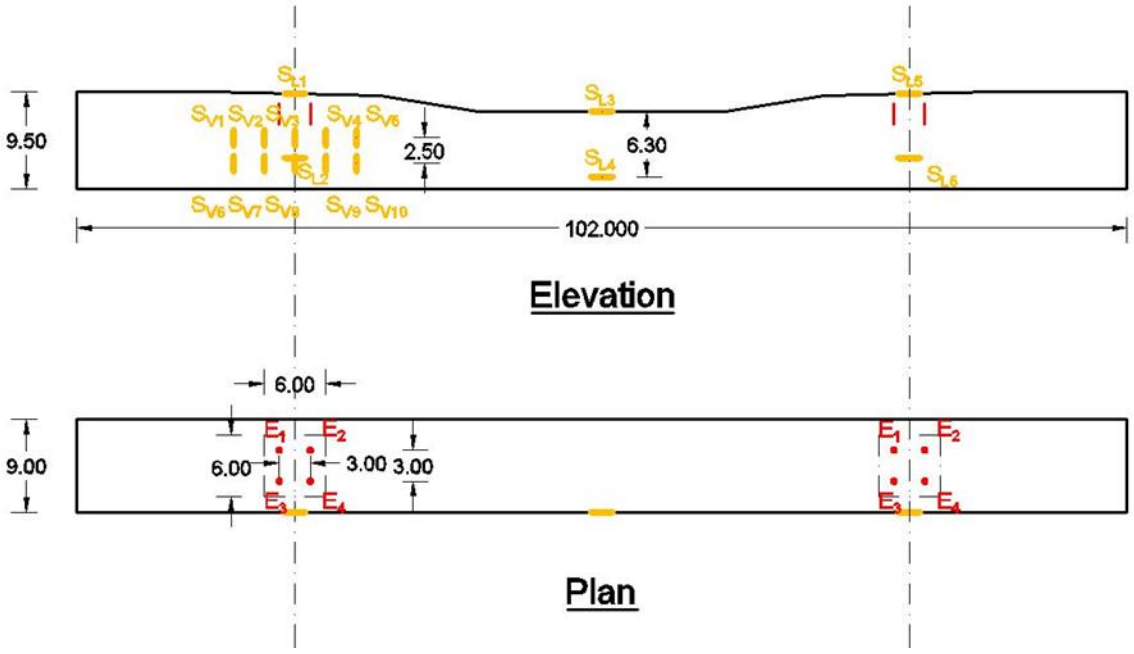

Figure 3.41 Dimensions of Crosstie and Location of Strain Gauges

3.7.3.1 Center-Positive Bending Test

Center-positive bending tests were conducted with static loads provided by the STT (Section 3.2.4). The bottom surface of each rail seat was supported by a two inch wide rubber pad at the center of the rail seat oriented perpendicular to the crosstie (**Figure 3.42**). A vertical static load was applied at the center of the top surface of the crosstie. The vertical load started at zero and increased by 1,000 lbf increment for each step up to 5,000 lbf (**Figure 3.43**).

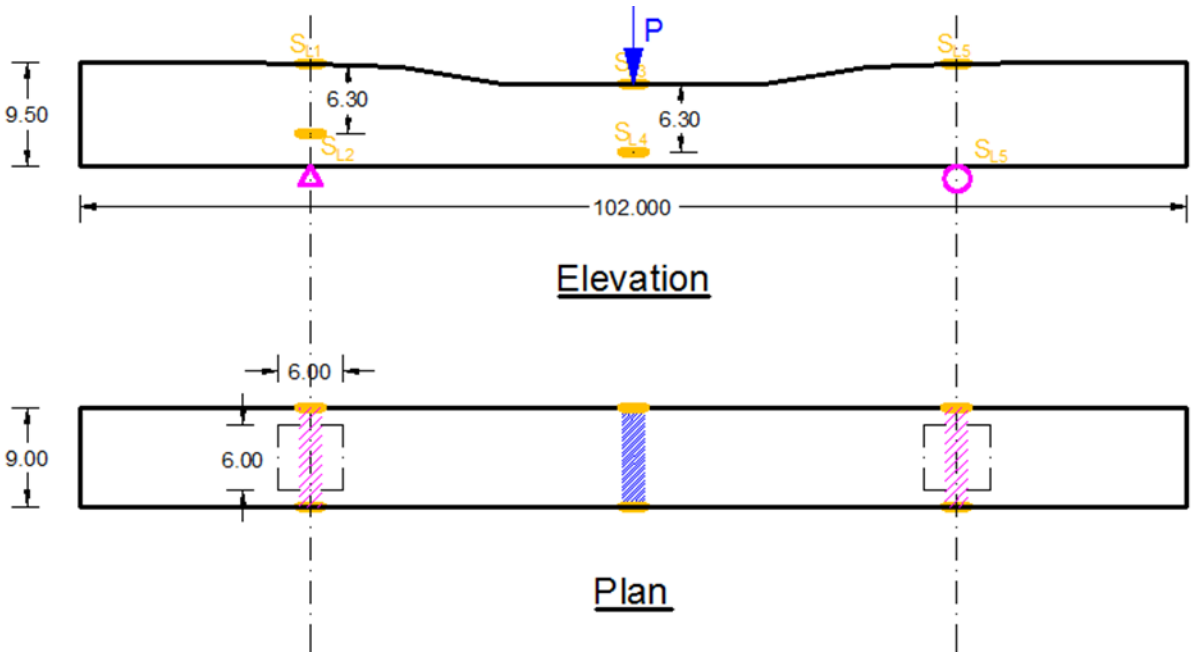

Figure 3.42 Load and Support Conditions for Center-Positive Bending Test

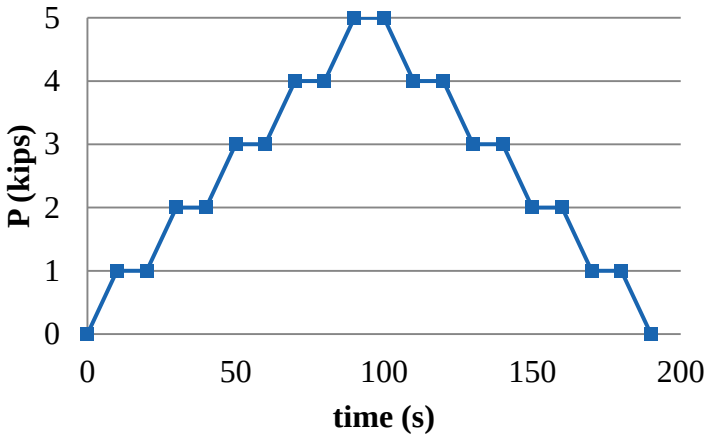

Figure 3.43 Loading Rate for Center-Positive Bending Test

3.7.3.2 Rail Seat Compression Test

Rail seat compression tests were conducted with the same instrumented crosstie. Static vertical load was applied with the STT at the rail seat at one end of the crosstie while the other end of the crosstie was supported by a roller. The vertical load started at zero and increased by 25,000 lbf increments for each step up to 50,000 lbf (**Figure 3.44**). The length of the loading head was six inches, measured perpendicular to the crosstie. The width of the loading head, measured parallel to the crosstie was an independent variable in this experiment, with three cases: six inches, three inches and 1.5 inches (**Figure 3.45** – **Figure 3.53**). The support was distributed evenly across the full width of the tie. The support length, also an independent variable, was tested with three cases: 6 inches, 12 inches and 18 inches centered about the center line of rail seat (**Figure 3.45** – **Figure 3.53**). A 1-inch rubber pad was used for the loading and 0.75-inch plywood pad was used for support contact to prevent damage to the crosstie.

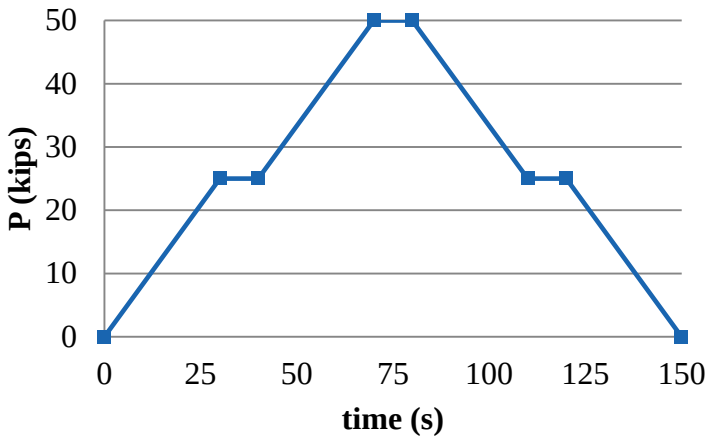

Figure 3.44 Loading Rate for Rail Seat Compression Test

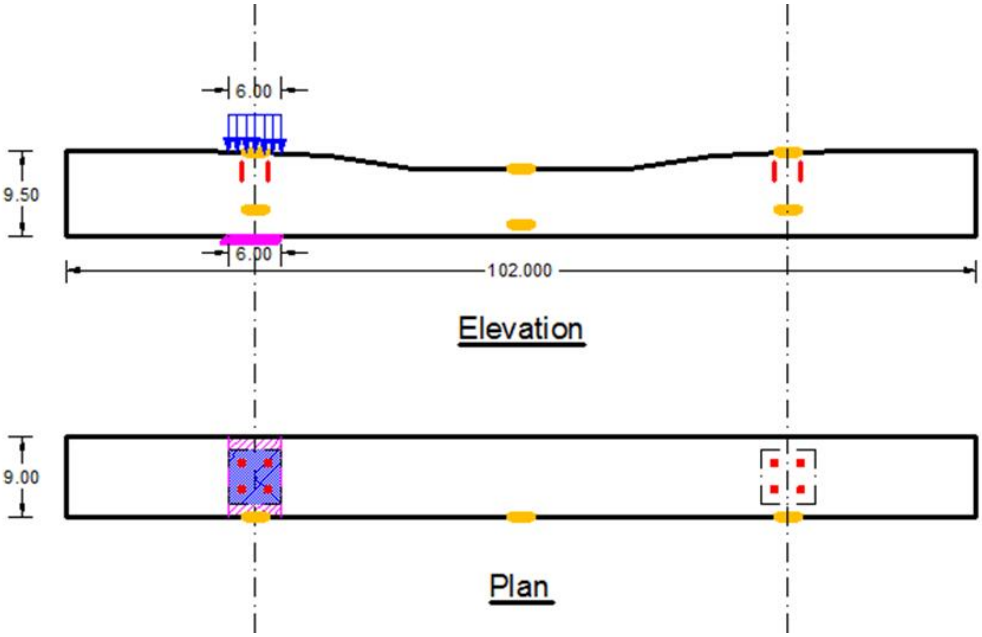

Figure 3.45 Load and Support Conditions for Rail Seat Compression Test – Loading Head Width: 6", Support Width: 6"

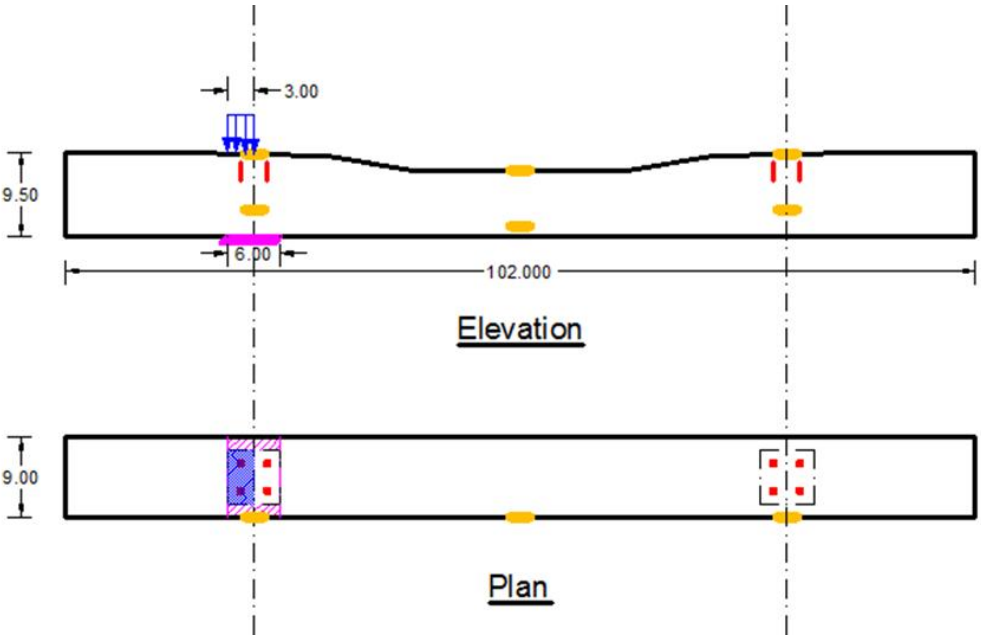

Figure 3.46 Load and Support Conditions for Rail Seat Compression Test – Loading Head Width: 3", Support Width: 6"

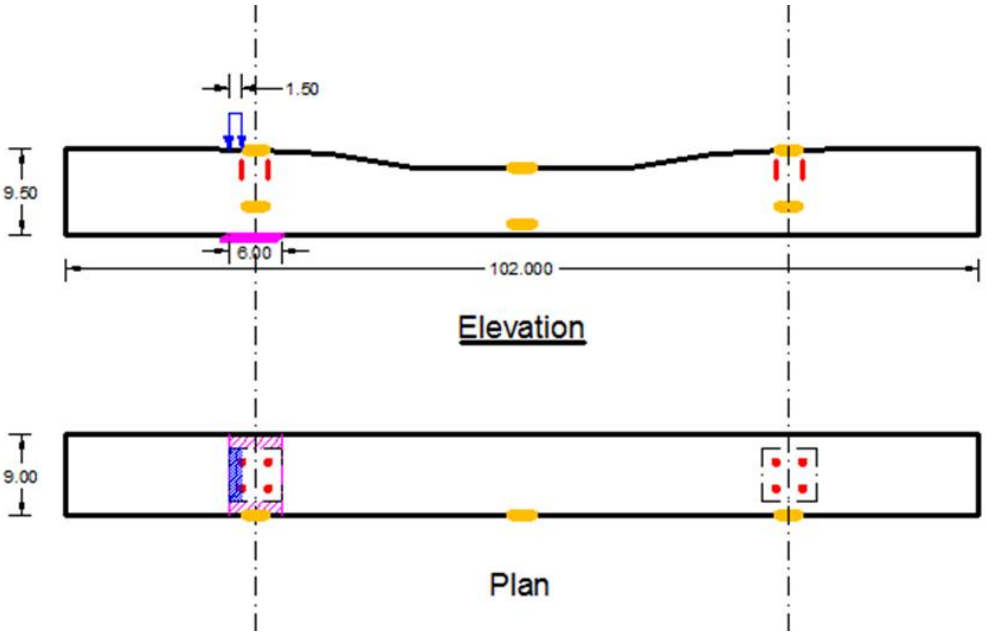

Figure 3.47 Load and Support Conditions for Rail Seat Compression Test – Loading Head Width: 1.5", Support Width: 6"

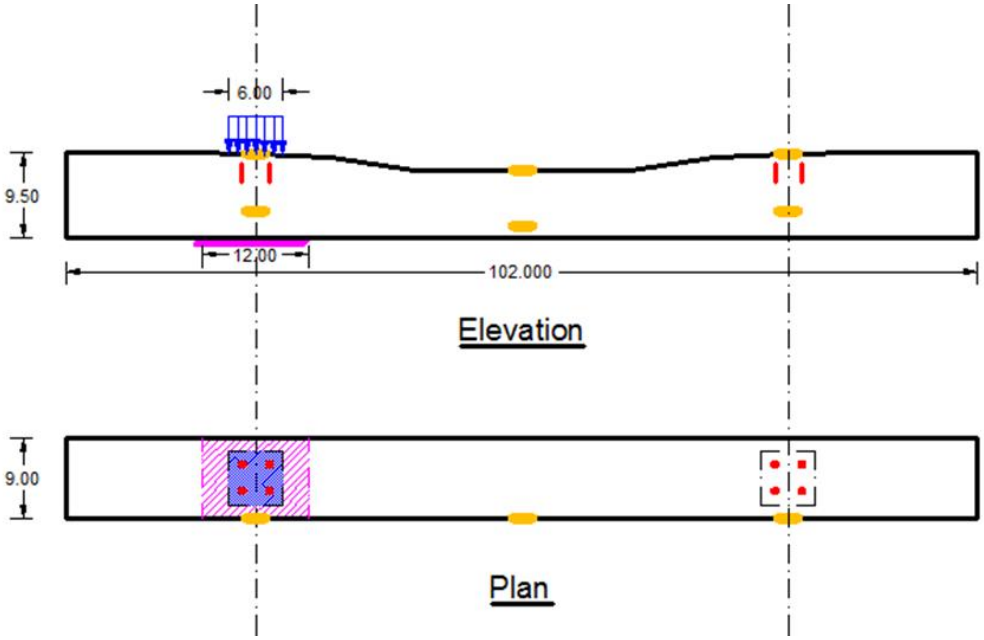

Figure 3.48 Load and Support Conditions for Rail Seat Compression Test – Loading Head Width: 6", Support Width: 12"

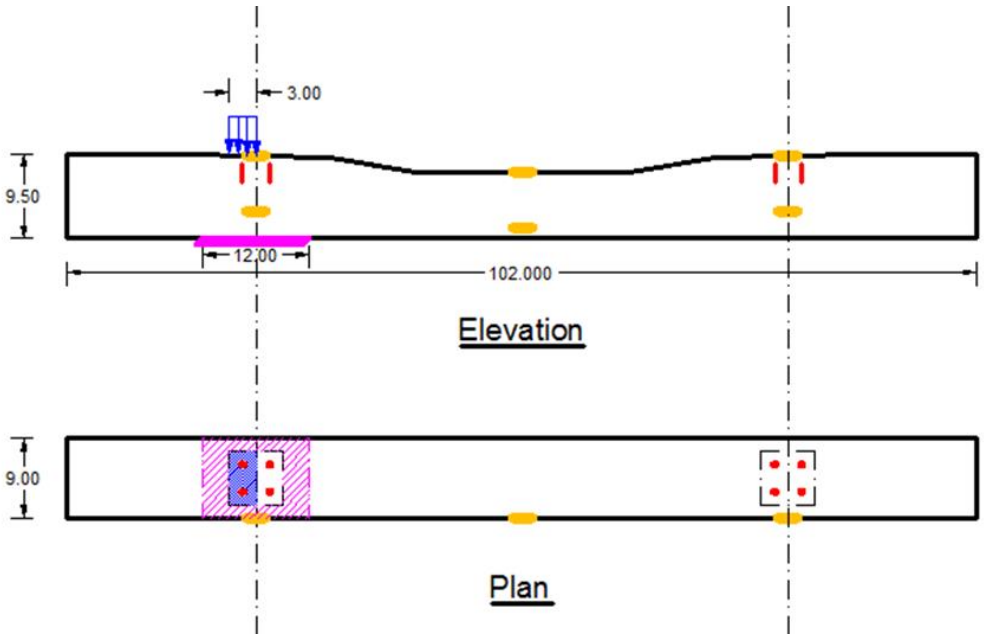

Figure 3.49 Load and Support Conditions for Rail Seat Compression Test – Loading Head Width: 3", Support Width: 12"

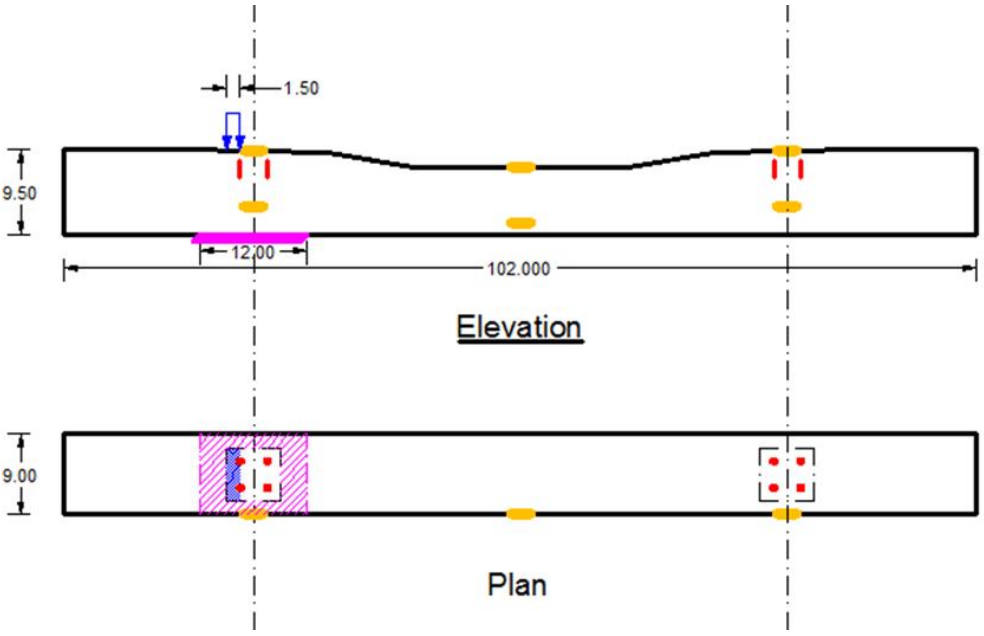

Figure 3.50 Load and Support Conditions for Rail Seat Compression Test – Loading Head Width: 1.5", Support Width: 12"

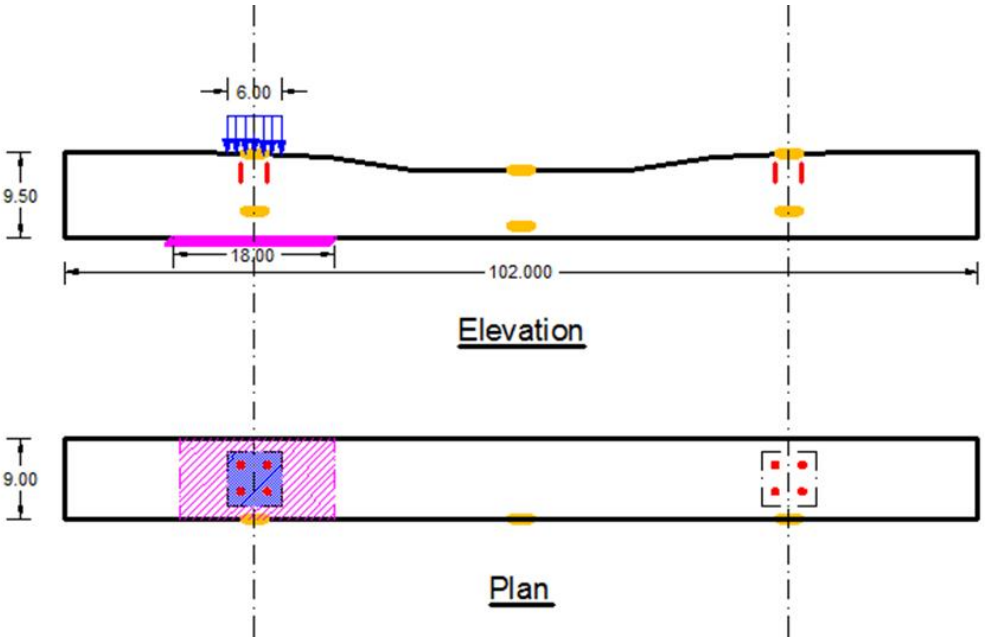

Figure 3.51 Load and Support Conditions for Rail Seat Compression Test – Loading Head Width: 6", Support Width: 18"

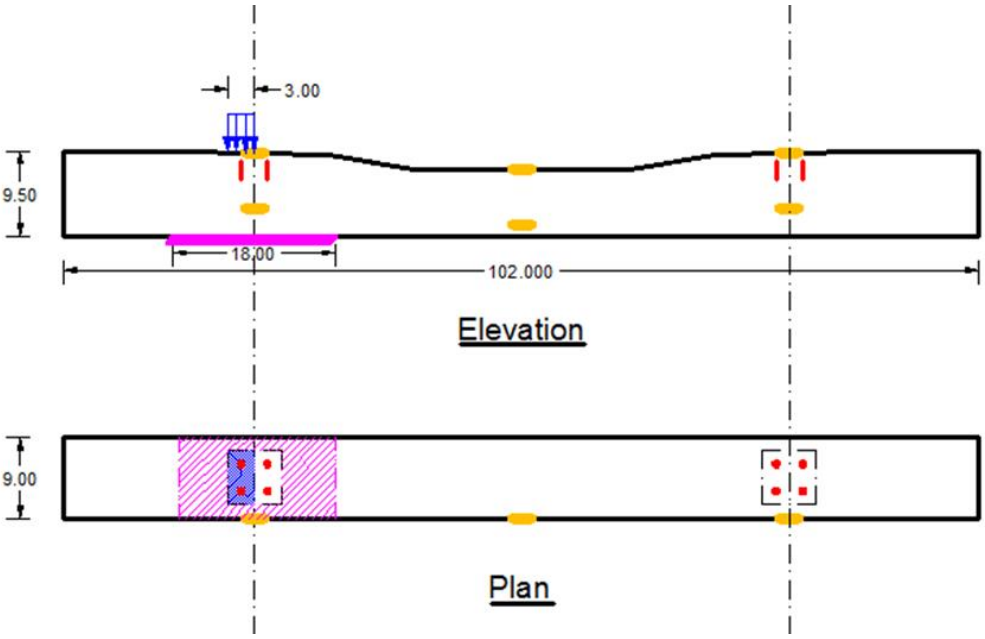

Figure 3.52 Load and Support Conditions for Rail Seat Compression Test – Loading Head Width: 3", Support Width: 18"

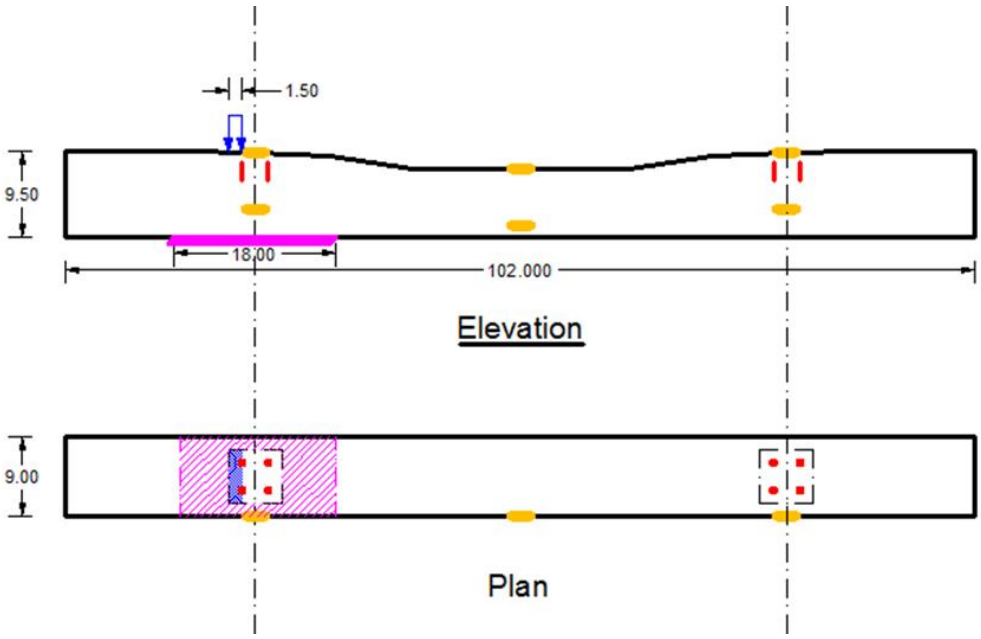

Figure 3.53 Load and Support Conditions for Rail Seat Compression Test – Loading Head Width: 1.5", Support Width: 18"

3.8 System-Level Experimental Plan

The purpose of the full-scale concrete crosstie and fastening system loading experiment was to map the vertical and lateral load paths through the rail, fastening system, and crosstie, to validate the finite element model (FEM) and to compare system-level results with current track design standards.

The applied wheel load, rail seat vertical reaction, lateral reaction at the shoulder (lateral friction force going to rail seat can be calculated consequently), and clamping force (normal and tangential components) were all considered to map the load path. Some of these forces were measured directly (e.g. wheel load, rail seat vertical reaction), however, some forces were obtained indirectly by analyzing data recorded during testing (e.g. clamping force). **Figure 3.54** shows the applied forces (vertical and lateral components of wheel load) and reactions on the rail

as well as the original and deformed shape of the rail cross-section where:

F_V: Vertical component of wheel load (applied load), kips

F_L: Lateral component of wheel load (applied load), kips

R_{SV}: Vertical rail seat reaction (1/3 the width of the distributed load from field side), kips

R_{SL}: Lateral rail seat reaction (center of the distributed load), kips

R_L: Lateral reaction entering shoulder, kips

N_F: Normal component of clamping force at field side, lbf

T_F: Tangential component of clamping force at field side, lbf

N_G: Normal component of clamping force at gauge side, lbf

T_G: Tangential component of clamping force at gauge side, lbf

D_{VF}: Vertical displacement at rail base at field side, in.

D_{VG}: Vertical displacement at rail base at gauge side, in.

D_{LH}: Lateral displacement at rail head, in.

D_{LW}: Lateral displacement at rail web, in.

D_{LB}: Lateral displacement at rail base, in.

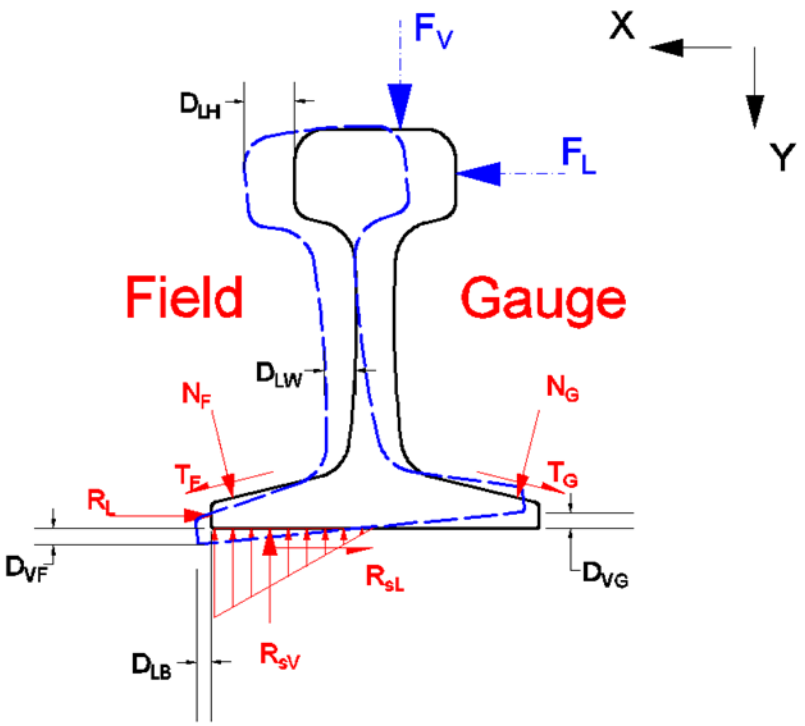

Figure 3.54 Idealized Load Path Through Rail

The positive position for all the forces and displacements in the lateral (X) direction is pointing to the field side, no matter which side of crosstie the rail locates. The positive direction for the vertical (Y) direction is pointing downward perpendicularly to the rail seat.

The global displacements of a concrete crosstie and positive directions are given in **Figure 3.55**.

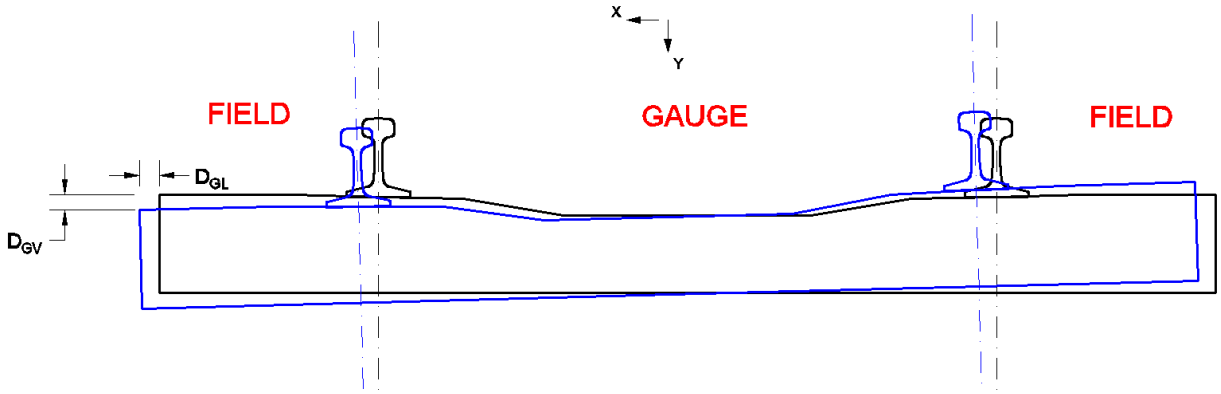

Figure 3.55 Undeformed/deformed Shape of a Concrete Crosstie

D_{GL}: Global lateral displacement of a crosstie, in.

D_{GV}: Global vertical displacement of a crosstie, in.

The positive position for the global lateral displacement (X) is pointing to the near side of the track. The positive direction for the global vertical displacement (Y) is pointing downward perpendicularly to the crosstie centroid axis.

Five full-scale testing facilities were utilized to provide the loading and boundary conditions in the system-level experiments, which including three in laboratory: SLTM (Section 3.2.2), PLTM (Section 3.2.3) and FSTLS (Section 3.2.5); and two in the field: RTT (Section 3.2.7) and HTL (Section 3.2.8).

3.8.1 Static Single-crosstie and Fastening System Test on the SLTM

A single concrete crosstie was placed on 0.75-inch thick plywood pad. Three loading conditions were applied and tested separately: lateral load, vertical load and a combination of lateral and vertical loads with fixed or various lateral-to-vertical load ratios (L/V). Lateral loads were applied to the rail web using the PTLF (**Figure 3.56 (a)**) or to the rail head using the GRMS. Lateral loads were applied up to a maximum of 5 kips. Vertical loads were applied to the center

of the rail by rotating the blue loading head of 90 degree. The combination of lateral and vertical loads with a variable L/V was achieved by applying a lateral force using PTLF initially, and held on this lateral force, then applying a vertical load to the center of the rail section at one side of the crosstie by rotating the loading frame of 90° (**Figure 3.56 (b)**). Vertical loads were applied up to a maximum of 40 kips to each rail. The combination of lateral and vertical loads with a fixed L/V was applied by placing the loading head over both of the rails (**Figure 3.2**). Vertical loads were applied up to a maximum of 40 kips to each rail in conjunction with lateral loads at a constant L/V of 0.5.

a) **b)**

Figure 3.56 a) Lateral Force Applied by the GRMS b) Lateral and Vertical Forces Applied by PTLF and SLTM Loading Head

When the SLTM loading head was used to apply the fixed combination of lateral and vertical forces, the L/V was designed to be 0.5. The real L/V was validated through measuring the actual lateral force from the strain gauge bridges on the rail while recording the total vertical force applied to both rails from the load cell above the loading head.

The lateral load measurement was described in Section 3.5.2 and **Figure 3.24**. Because the curvature designed at wheel-rail contact area of both the SLTM loading head and the GRMS are following the standard wheel profile, the GRMS (Section 3.2.5) was used to calibrate the full bridges by applying a 3 kips lateral load to each rail.

To form the rail strain gauge bridges used to measure the applied lateral force, four installed strain gauge pairs (refer to **Figure 3.13** Strain Gauges Installed on Rail, one strip of strain gauges at each side of a clip) from **Figure 3.58** were selected: the strain gauges at location #5 and #9 consisted one bridge, and the strain gauges at location #6 and #8 consisted another bridge. The validation of the designed L/V is shown in **Figure 3.57**, in which a full cycle of loading was applied. The solid green line is for the design lateral force. The dashed blue and red lines are the lateral force calculated from the two strain gauge bridges. At the beginning, the SLTM loading head pushed both rails towards field sides. When the lateral force reached approximately 3 kips, it started to apply the lateral and vertical force simultaneously. The actual applied lateral force and the design lateral force converged when the vertical applied force was 38 kips, and the error was 5.5%.

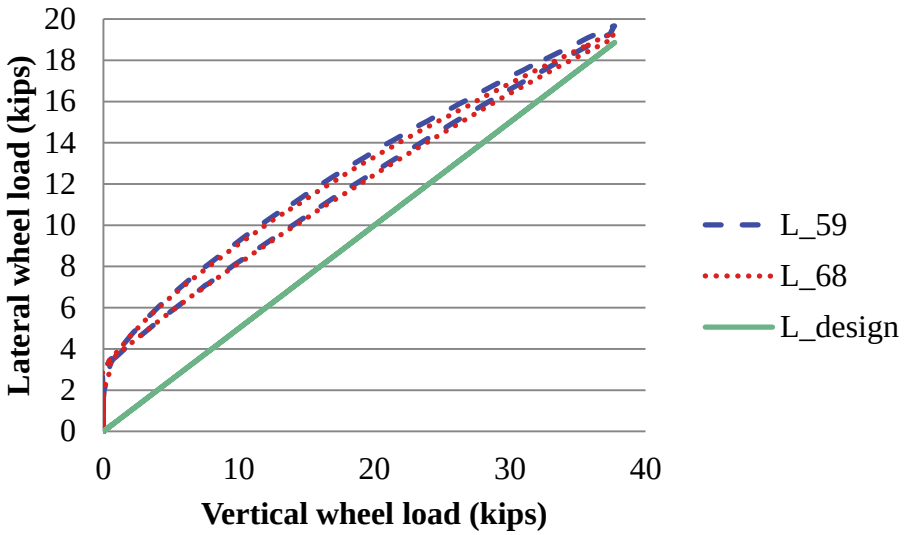

Figure 3.57 Lateral Applied Load Measurement

Rail deformation, rail relative deflection, crosstie global deflection and change of clamping force were measured in the single-crosstie with the fastening system experiment.

Rail deformation was measured through strain gauges installed in strips on each side of the 24-inch rail section. To eliminate the effect of out-of-plane bending and torsion, on each side of the rail, two strips of strain gauges were installed (**Figure 3.13** Strain Gauges Installed on Rail). Three pairs of strain gauges were placed along the rail base and the other seven pairs were installed on rail web. The distance between adjacent strain gauges was 0.625 inches (**Figure 3.58**).

Rail movements relative to the crosstie D_{VF}, D_{VG} and D_{LH} as shown in **Figure 3.54** were also measured. One lateral potentiometer was placed at the center line of the rail seat parallel to the crosstie and 0.5 inches below the rail head to measure the lateral displacement D_{LH} facing the field side. Four more potentiometers were placed at the rail base 0.5 inches from the outer most

edge of the rail base and three inches apart from the centerline of the crosstie on each side of the rail (**Figure 3.59**).

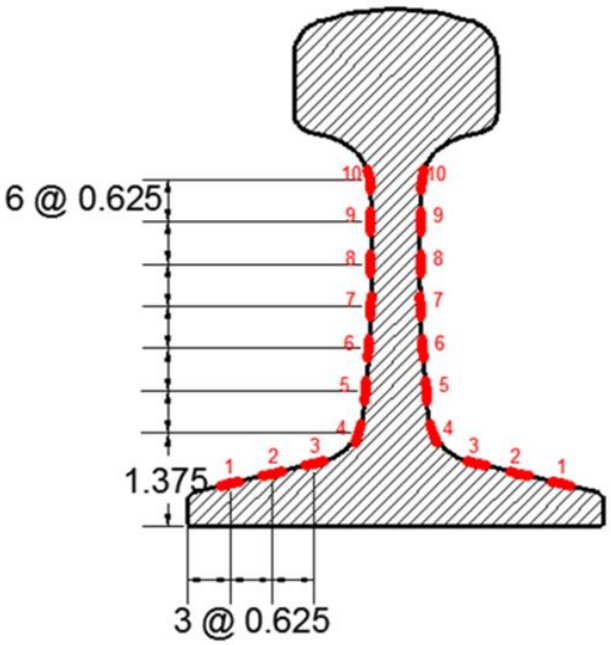

Figure 3.58 Strain Gauge Locations on Rail Web and Base

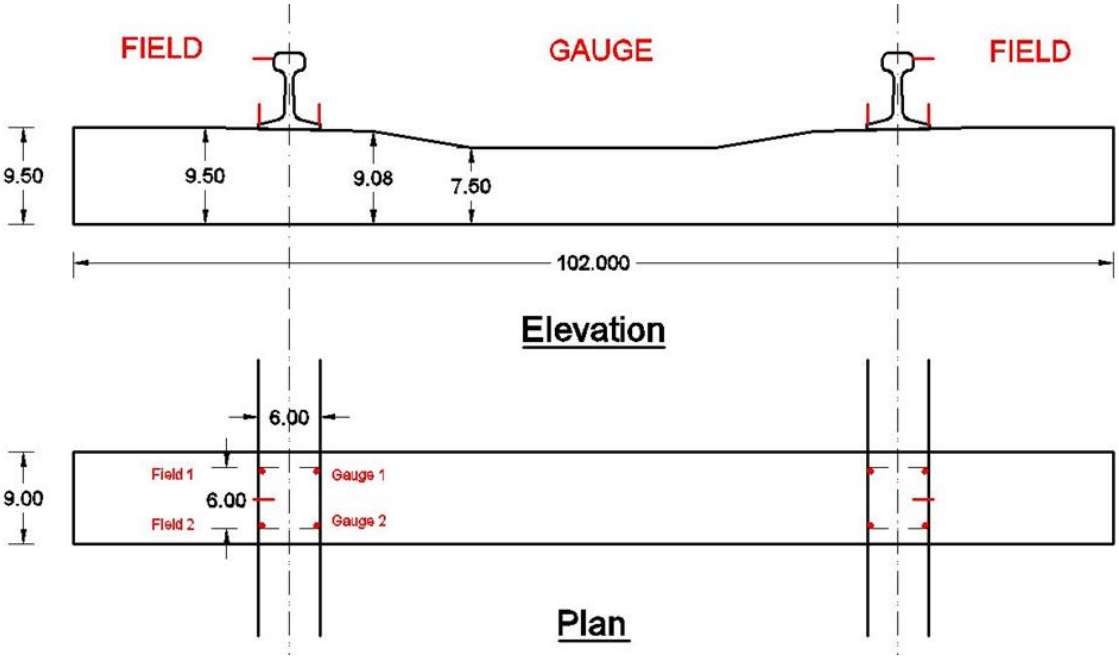

Figure 3.59 Rail Relative Deflection Measurements

For crosstie global displacement measurements, three vertically-oriented potentiometers were attached to the bottom chord of the loading frame to capture the vertical deflections under various loading cases; one horizontally-oriented potentiometer was installed at each end of the crosstie to measure the crosstie movement in the lateral direction. In **Figure 3.60**, "Tie L_1" and "Tie L_2" show the locations of potentiometers to measure the lateral displacements. "Tie V_1", "Tie V_2" and "Tie V_3" show the locations of potentiometers to measure vertical crosstie deflections below each rail seat and the center.

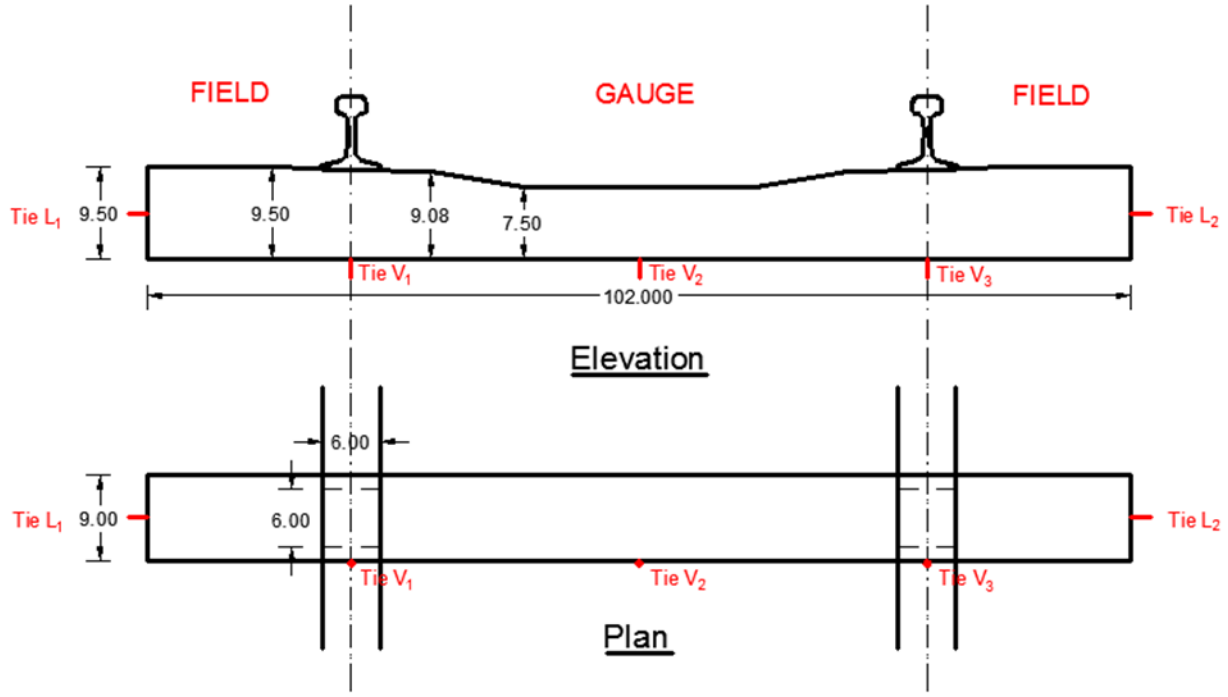

Figure 3.60 Crosstie Global Displacement Measurements

The first method of strain gauge patterns as stated in Section 3.5.5 was used to measure the change of clamping force.

3.8.2 Single-crosstie and Fastening System Test on the PLTM

A single concrete crosstie with one 24-inch section of rail and fastening system were placed on the PLTM (Section 3.2.3) testing frame as shown in **Figure 3.3**. Both ends of the crosstie were tightened to the foundation plate so there was no relative movement between the crosstie and the testing frame. Vertical loads were applied up to a maximum of 40 kips at a constant rate in conjunction with lateral loads at constant lateral-to-vertical (L/V) ratios of 0.1, 0.2, 0.3, 0.4, 0.5, and 0.6. For the dynamic testing through PLTM, rail deformation, clip deformation were measured.

3.8.3 Multi-crosstie and Fastening System Test on the TLS

Eleven concrete crossties with two sections of rail and fastening system were placed on the track bed of the TLS facility (Section 3.2.5). With the TLS, a vertical wheel load up to 40 kips was applied by two actuators to both sides of the testing wheel set simultaneously. And 10 kips, 20 kips, 30 kips and 40 kips static vertical wheel loads were applied in conjunction with lateral wheel loads at lateral-to-vertical (L/V) ratios of 0.1, 0.2, 0.3, 0.4, 0.5, and 0.6 (**Figure 3.61**). Each test was run at various locations on the TLS with five fastening system conditions: (1) all fastening system components installed; (2) one field side clip removed directly beneath the point of loading; (3) one field side clip and one field side insulator removed directly beneath the point of loading; (4) three field side clips removed centered about the point of loading; and (5) three field side clips and three field side insulators removed centered about the point of loading. Rail seat reaction force, rail relative deflection, crosstie global deflection and crosstie bending moment were output from tests. The rail bridges were calibrated prior to the tests using GRMS. The structural testing was cooperated with the UIUC RAILTEC group, the data analysis was

cooperated with Brent Williams (Williams et al, 2014) and Matthew Greve (Greve et al, 2014). The full instrumentation map is shown in **Figure 3.62**.

Because the using of the MBTSS might reduce the frictions between rail base and concrete surface significantly, two rounds of replicated testing were completed. The first round was with no MBTSS, the second round was with all MBTSS installed at rail seats 4 – 8.

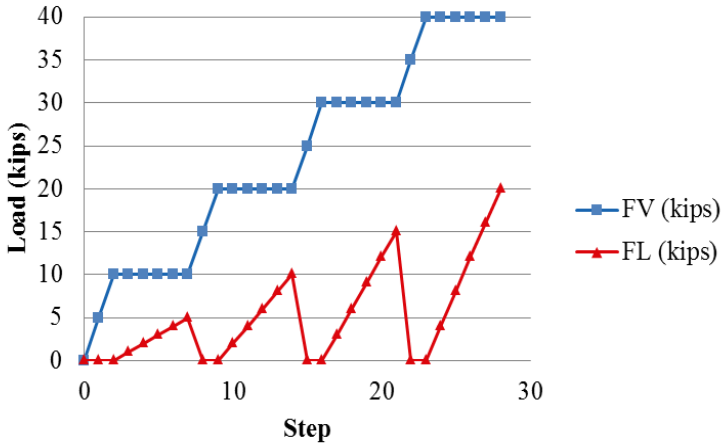

Figure 3.61 Loading Step with the FSLTS

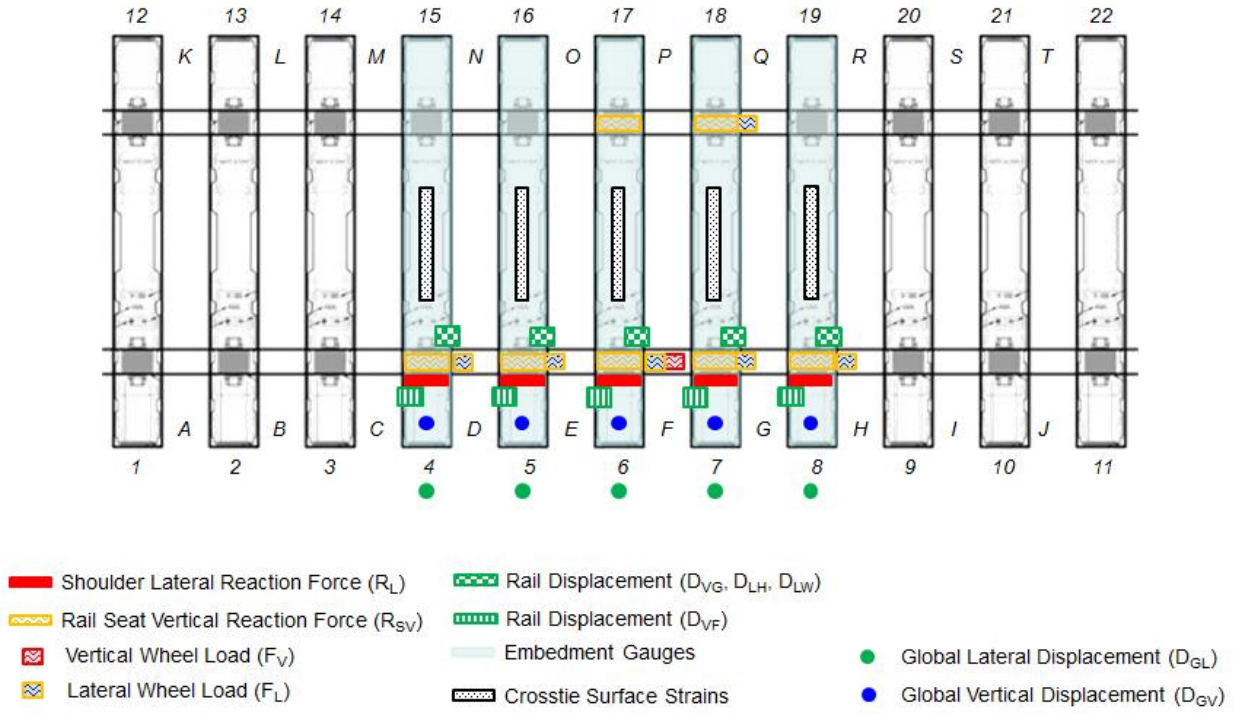

Figure 3.62 Instrumentation Map with the TLS

3.8.4 Full-Scale Field Experiment

Two sections of track were investigated at the Transportation Technology Center in Pueblo, CO as in July 2012 and May 2013. One section was a segment of the tangent track at the RTT (Section 3.2.7) while the other was a part of a curved segment at the HTL (Section 3.2.8) with a curvature of approximately five degrees (5°). One uniform testing procedure was used for both of the RTT and HTL sections. The static loading procedure was referred to **Figure 3.61**. For dynamic tests, two consists of passenger and freight train series rolled across the instrumented section with various speeds. The running speed of each test is shown in **Table 3.5**, respectively.

Table 3.5 Speed of Passenger and Freight Train series at RTT and HTL

	RTT		HTL	
Speed (mph)	Passenger	Freight	Passenger	Freight
2	×	×	×	×
15	×	×	×	×
30	×	×	×	×
45	×	×	×	×
60	×	×	×	
70	×	×		
80	×			
90	×			
105	×			

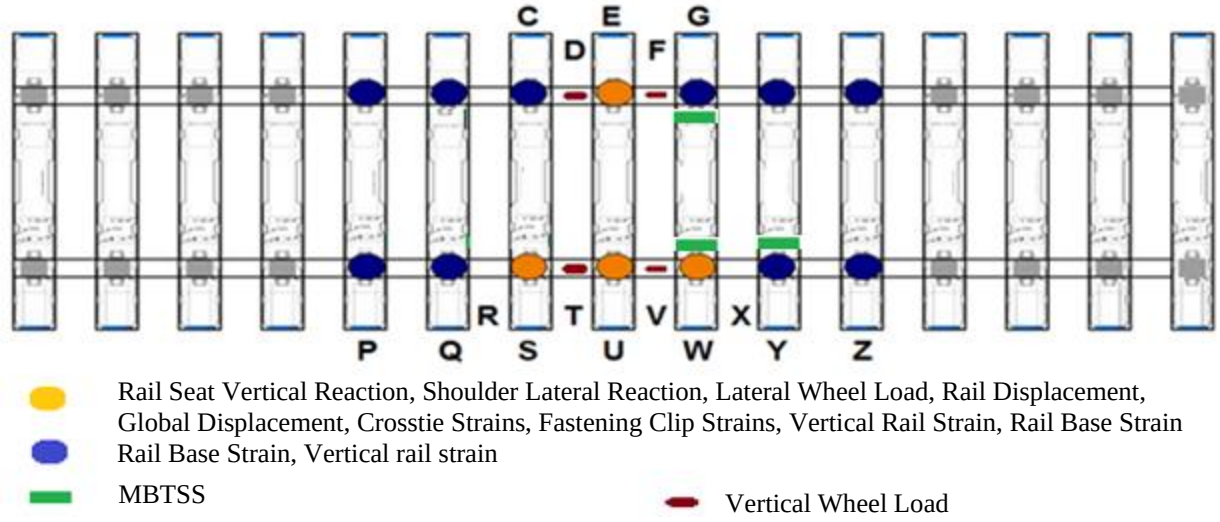

Figure 3.63 Locations of Fully (Orange) and Partially (Blue) Instrumented Crossties

There were two levels of instrumentation densities that were deployed at each of the two locations. A dense set of instrumentation was deployed on three adjacent rail seats and the opposite rail seat of the center crosstie (labeled orange in **Figure 3.63**). Additional rail seats in the section were partially instrumented with vertical strain gauges on the rail (labeled blue in **Figure 3.63**). The detailed instrumentation map employed during field experimentation is given in **Figure 3.64**.

Additional wheel load measurements were taken by TTC personnel using an instrumented wheel set (IWS). These results were used to supplement the data analysis. The structural testing was cooperated with the UIUC RAILTEC group, the data analysis was cooperated with Justin Grasse (Grasse et al, 2014), Kartik Manda, Brent Williams and Matthew Greve.

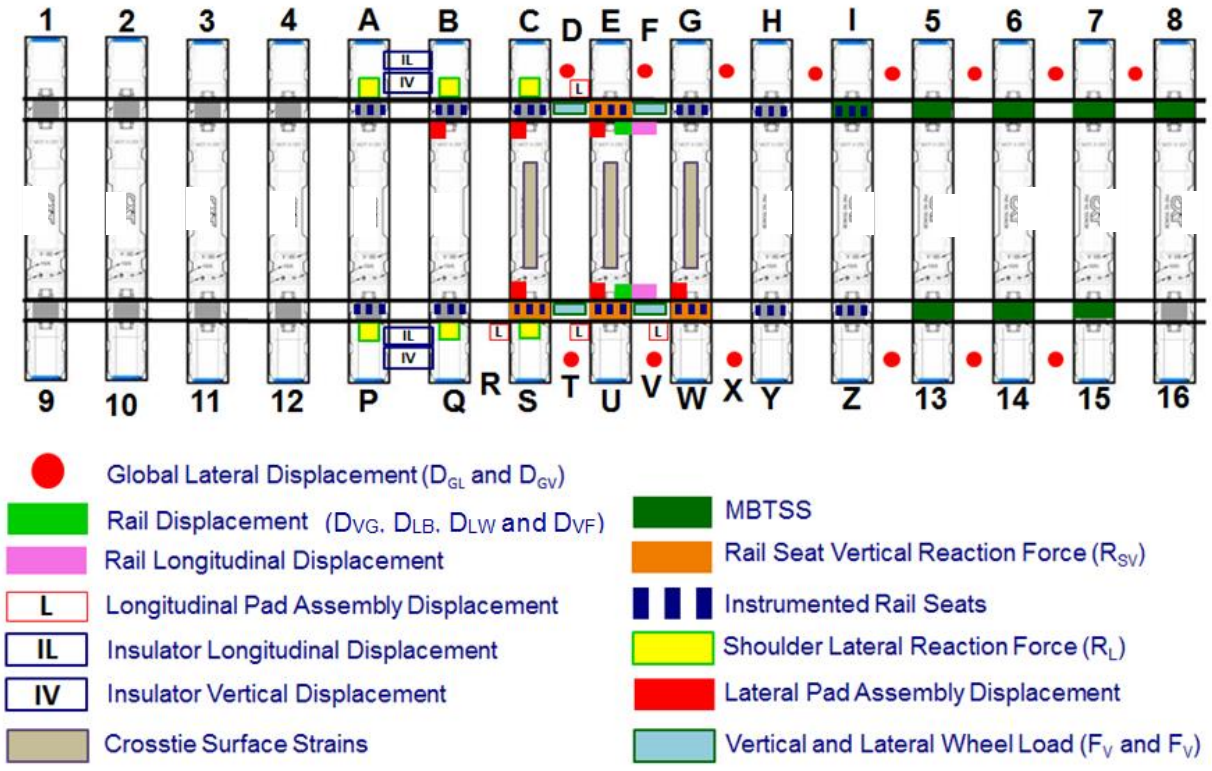

Figure 3.64 Locations of all Instrumentation Technologies Used During May 2013

4. Load Path Analysis

An evaluation of loads and stresses within the track structures is used to determine and quantify the load transfer path. Loads will be transferred by physical contact between various component parts, which including wheel and rail, rail and insulator, insulator and clip, rail and pad, pad and concrete, concrete and ballast. The study provided new insight into the load path going through rail, fastening system and concrete crosstie. Mapping of the vertical and lateral load path under static and dynamic loading environment are studied in this chapter. The free body diagram of a section of rail and fastening system, the notations of forces and displacements, as well as the positive directions are standardized and shown in **Figure 3.54**. The global displacements of a concrete crosstie and positive directions are given in **Figure 3.55**.

The load path analysis is developed in two major sections: under static and dynamic loading. As described in Chapter 3, single-crosstie and multi-crosstie laboratory experiments as well as full-scale field experiments were used to provide evidence.

In this chapter, the field data analysis was cooperated with Justin Grasse (Grasse et al 2014) and Kartik Manda; the lateral force transferred through the should was cooperated with Brent Williams (Williams et al 2014); the rail seat pressure distribution was prepared by Matthew Greve (Greve et al 2014).

4.1 Wheel Load Demand

Wheel load demand was studied first to design the applied loads for the laboratory and field experiments. The vertical and lateral wheel loads in this report are defined as the vertical and lateral components of the wheel-rail contact force, no matter what contact conditions are (**Figure 4.1**).

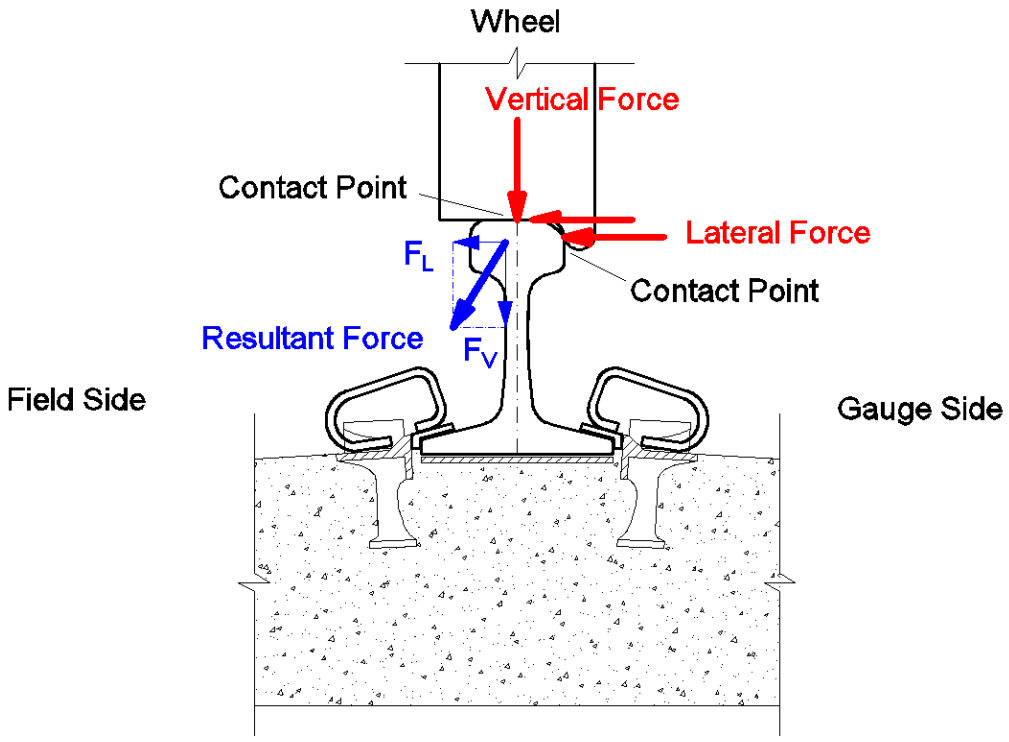

Figure 4.1 Applied Wheel Load Definition

4.1.1 Vertical Wheel Load Measured from Field Experiment

Vertical wheel load used in this chapter is defined as the vertical component of the resultant wheel load acting on the head of rail (**Figure 4.1)**. Nominal wheel load is used to define the static wheel load applied by the weight of the railcars. The vertical load of the wheel on the rail often deviates depending on train speed and track curvature. Vertical wheel loads can far exceed nominal wheel loads in extreme cases, which are called impact loads. The impact loads are primarily due to irregular wheel profile which allows for little damping of the track structure.

Vertical loads in field testing at TTC were measured from a freight consist and a passenger consist with known car weights. The freight train consisted of cars weighing 263 kips, 286 kips and 315 kips with nominal wheel loads of 33 kips, 36 kips and 39 kips respectively

excluding locomotive. The passenger train consisted of cars weighing 87 kips with nominal wheel loads of 11 kips excluding locomotive.

On the tangent track (RTT), the median vertical loads from the freight consist were approximately 35 kips (**Figure 4.2**), with almost negligible correlation between the average vertical wheel loads and train speeds. However in general, there was an increase in maximum loads from increased vehicle speed; and the vertical wheel loads were found distributed in a wider range under higher speeds. It is also observed that the recorded vertical wheel load can be as high as 60 kips with a speed of only 30 mph, which was highly possible due to the impact load caused by the wheel with a flat spot installed to one car on purpose. Because the vertical wheel load was recorded only when the wheel hit the center of vertical rail bridges, and the chance that the flat spot hit the center of vertical rail bridges was very low, the impact loads were only found in very few time histories. And thus, it is premature to draw a relationship between the maximum vertical wheel load and the train running speed at this stage.

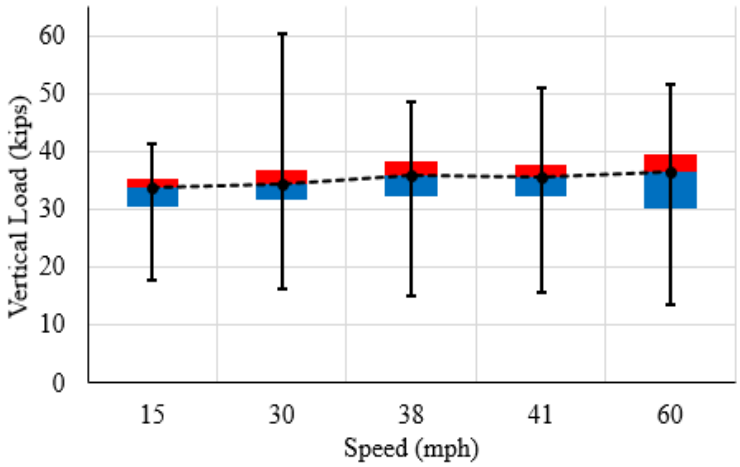

Figure 4.2 Vertical Wheel Loads Imparted by Freight Consist on Tangent Track (RTT)

Similar results were found from data recorded under passenger consists. The median vertical loads from passenger consist on tangent track did not deviate much from the nominal wheel loads, which were all about 11 – 12 kips (**Figure 4.3**). Even though there was no flat wheel used for passenger consist, the dynamic amplification can be greater than for freight consist: at 90 mph, the measured vertical wheel load can be as high as 2.5 times the nominal wheel load. Approximately 3% of the vertical loads measured exceeded 1.5 times the nominal wheel load, and 0.5% of the loads exceeded 2.5 times the nominal wheel load from eighteen train passes on tangent track with their speeds varied from 2 mph to 102 mph.

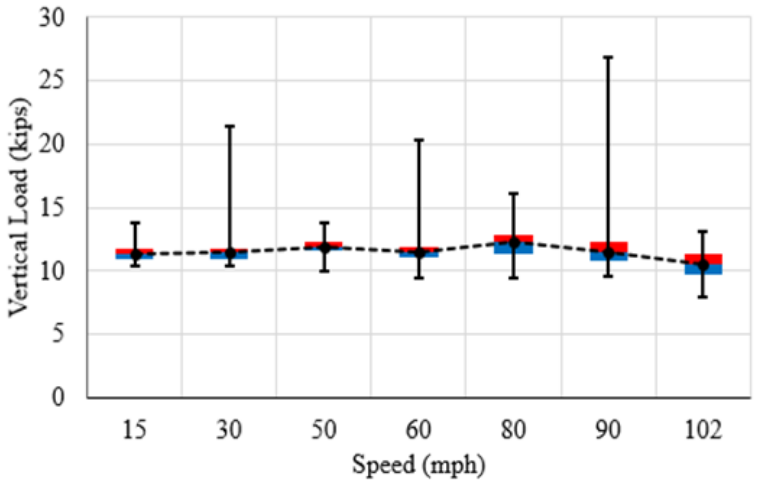

Figure 4.3 Vertical Wheel Loads Imparted by Passenger Consist on Tangent Track (RTT)

The vertical wheel loads measured on the curved testing track (HTL) were found to be highly dependent on curve radius and train speeds (**Figure 4.4**). Under static or low-speed cases, a bigger fraction of axle load was supported by the low rail; due to centrifugal forces acting on the body of the vehicle, the load shared by the high rail increased with the increase of train speed. At 45 mph, about 67% of axle load transferred to the high rail, and 33% of axle load went through the low rail. If summing up the wheel load measured from high rail and from low rail, it

reaches about twice as much of the average wheel load measured from the tangent track (RTT), which is similar to the axle load under static case.

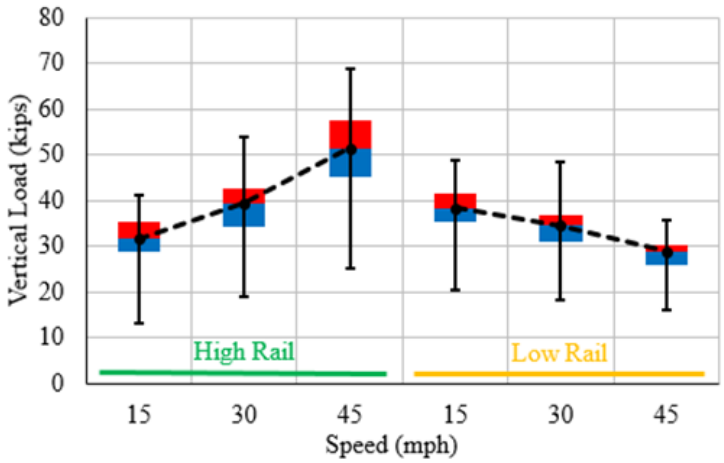

Figure 4.4 Vertical Wheel Loads Imparted by Freight Consist on Curved Track (HTL)

The measured wheel load provided the range of vertical load input that can be used in the laboratory experiments. The observations stated above suggest that there might be a benefit of treating tangent and curved sections of track separately in design. This could include using specialized track components or practices to compensate for the increase of loading demands at the high rail of the curved track sections. In addition, the decrease of vertical wheel load at the low rail for a lower speed doesn't necessarily suggest it is "safer", the lateral applied wheel load which described in the next section should be combined into analysis.

4.1.2 Lateral Wheel Load Measured from Field Experiment

Lateral load is defined as the lateral component of the resultant wheel load acting on the head of the rail (**Figure 4.1**). The lateral demands are influenced mainly by curve radius, train speed, wheel-rail interface and suspension characteristics of the trucks. In particular, lateral loads apply large bending moments to the rail, which requires rotational restraint from the fastening system.

Due to the nature of the lateral rail bridges used in the field experiments (Section 3.5.2), the measured lateral wheel load was contributed by two parts: the lateral load going through the wheel flange and rail contact, and the lateral component of the load going through the wheel rim and rail contact.

On the tangent testing track (RTT), most axles imposed modest outward (towards the field side) lateral loads to the rail. Over 75% of the outward lateral loads from freight runs were below 3.5 kips, and one in about forty axles imparted approximately a 6 kips lateral load. The inward lateral load was usually found to be negligible. Similar as vertical wheel loads, on tangent track, the correlation between lateral wheel loads and train speeds were also found to be negligible.

On the curved testing track (HTL), the lateral loads were found to be much greater and strongly correlated with train speeds. On the high rail, there was a positive correlation between lateral and vertical wheel loads (**Figure 4.5**); and the low rail showed a slight negative correlation between lateral and vertical wheel loads (**Figure 4.6**).

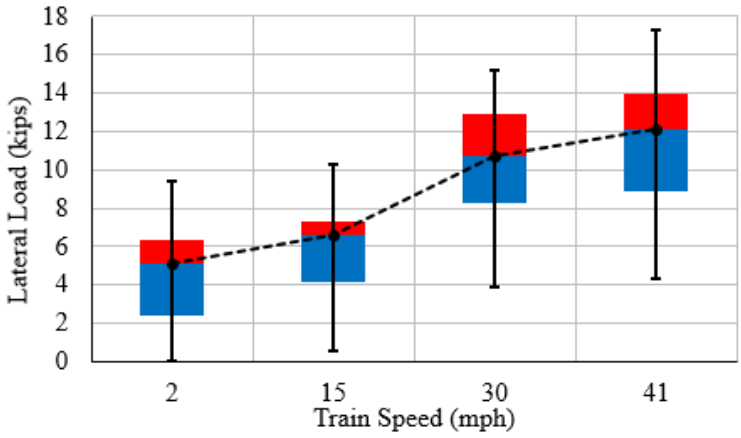

Figure 4.5 Lateral Wheel Loads Imparted by Freight Consist on the High Rail

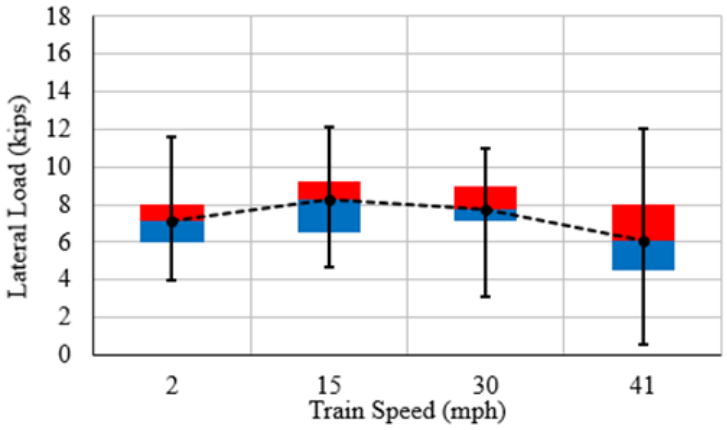

Figure 4.6 Lateral Wheel Loads Imparted by Freight Consist on the Low Rail

As shown in **Figure 4.5**, the median lateral loads measured from the freight consist on the high rail was about 5 kips with the speed of 2 mph, which increased to 12 mph with the speed of 41 mph. Correspondingly, the median measured lateral force applied to the low rail was 7 kips for 2 mph, and dropped slightly to 6 kips for 41 mph (**Figure 4.6**). The differences in magnitude of lateral demands on each track type suggest that there should be significantly higher lateral loading demands on a curved than a tangent track considered in design.

4.1.3 Demand of L/V Regard to Track Curvature

To design the input ratio of lateral versus vertical applied wheel load (L/V), the dependency of lateral loads on vertical loads was analyzed (**Figure 4.7**) using the data recorded from the HTL. The trend lines show the correlation between the lateral and vertical wheel loads on the high and low rail. For the high rail, the L/V varied from 0 to 39% with the maximum value took place at 15 mph when the vertical force was 36 kips; for the low rail, the L/V varied from 0 to 56% with the maximum value took place at 45 mph when the vertical force was 25 kips.

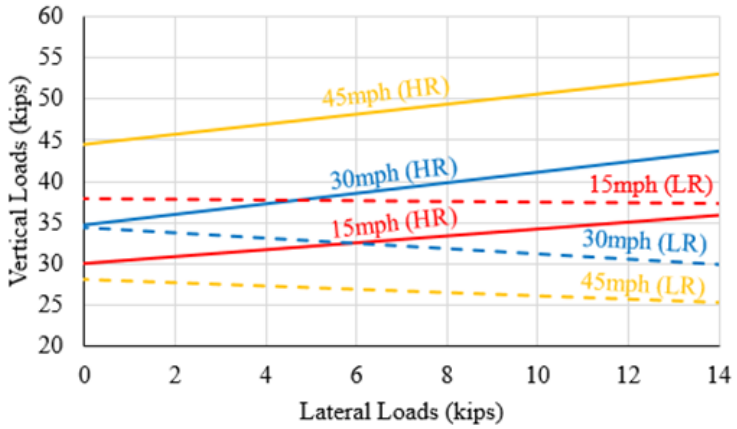

Figure 4.7 Correlation Between Lateral and Vertical Axle Loads on Curved Track

It should be noticed that, sometimes, the L/V ratio reached a very high value with a low vertical wheel load. So the L/V as well as the magnitude of loads should be combined to design the critical loading case. Based on the findings stated above, for the static testing in the laboratory and field, 10 kips, 20 kips, 30 kips and 40 kips vertical wheel loads were applied in conjunction with lateral loads at L/V ratios of 0.1, 0.2, 0.3, 0.4 and 0.5.

4.2 Vertical Load Path Under Static Loading

In this report, the full load path is discussed in two parts: the load path under the vertical and lateral wheel load respectively. In both sections, the analysis is based on the results from the single-crosstie system with the STT and the SLTM, the multi-crosstie system with the TLS and the full-scale multi-crosstie field experiments.

4.2.1 Vertical Load Path in Single-crosstie and Fastening System

The study of the vertical load path under static loading in single-crosstie and fastening system refers to the experiment with the STT and the SLTM.

With the STT, internal and external strains below the tested rail seat were studied to understand the vertical load path going through the concrete (Section 4.2.1.1). A single concrete crosstie instrumented with embedment and surface strain gauges was tested with varying loading and support conditions (Section 3.7.3).

With the SLTM, the performance of rail, crosstie and fastening system were studied, in which including the deformation of rail, the displacements of rail and crosstie, the rail seat reaction force and the change of clamping force (Section 4.2.1.2 – 4.2.1.6). The designed vertical wheel loads were applied; a full-scale crosstie and fastening system was placed on a plywood pad which was used to simplify the ballast support in the field.

4.2.1.1 Concrete Compressive Strain Below Rail Seat Under Various Loading and Support Conditions

The deformation of concrete below rail seat and the compression load flow was studied with the STT. The instrumented rail seat was centralized to the loading and support frame (**Figure 4.8**). Data output from embedment strain gauges E_1 to E_4 and surface strain gauges S_{V1} to S_{V10} was used for load path analysis (see **Figure 3.41**). The four concrete embedment strain gauges E_1 to E_4 were installed 2 inches (measured from the center of each gauge) below the surface of the rail seat before casting. Surface strain gauges S_{V1} to S_{V5} were installed 5 inches above the bottom, and surface strain gauges S_{V1} to S_{V10} were 2.5 inches above the bottom.

Figure 4.8 Vertical Rail Seat Loading Applied by STT

The compressive strains measured below the rail seat were used to validate the effective load distribution assumption made in UIC 713 (2002). The assumed support condition is shown in **Figure 4.9 (a)** (or Figure 1a in UIC 713). The effective load distribution and lever arm defined in UIC 713 are shown in **Figure 4.9 (b)** (or Figure 2 in UIC 713). The effective width of the reaction force distribution was derived from the rail seat width and the crosstie depth, and the assumed distribution angle was 45°.

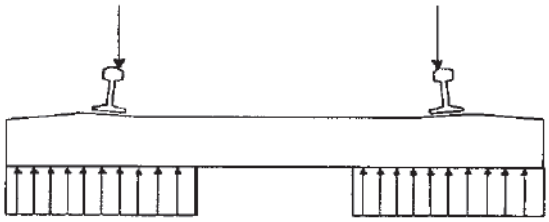

a)

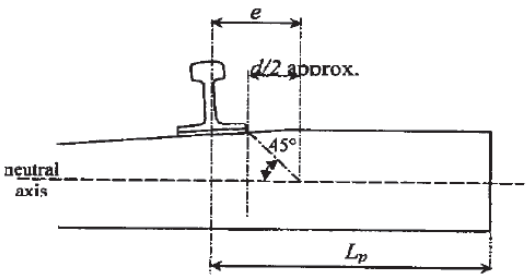

b)

Figure 4.9 Support Condition and Calculation Methodology Used in UIC 713 for a) Crosstie Reaction Distribution for Newly Tamped Track and b) Assumed Load Distribution and Lever Arm Derivation for Rail Seat Bending

Using the STT, three support conditions with different support widths were evaluated (Section 3.7.3.2 in the Laboratory Experimentation Plan). The vertical strain measured from the crosstie side surface below the rail seat is shown in **Figures 4.10 – 4.15** for the three loading and three support conditions. The x-axis represents the distance from the location of the strain measurement to the center of the rail seat. **Figure 4.10**, **Figure 4.12** and **Figure 4.14** show the strain measured 5 inches above the bottom surface of the crosstie (S_{V1} – S_{V5} in **Figure 3.41**). **Figure 4.11**, **Figure 4.13** and **Figure 4.15** show the strain measured from 2.5 inches above the bottom surface (S_{V6} – S_{V10} in **Figure 3.41**).

By comparing the three unique support conditions, a wider support led to slightly lower compressive strains when there was no eccentricity for the rail seat loadings. When the support width and the loading width were both 6 inches, the center strain at a point 5 inches above the bottom surface of the crosstie was -157 ms (“6″ × 6″” in **Figure 4.10**). The center strain at the same height was -111 ms for the 12-inch support with a 6-inch loading width (“12″ × 6″” in

Figure 4.12), and -105 ms for the 18-inch support with a 6-inch loading width ("18″ × 6″" in **Figure 4.14**). The support width also had a large effect on the strain measured 2.5 inches above the bottom of crosstie. The strain measured from 2.5 inches above the bottom at the center line of the rail seat was -130 ms ("6″ × 6″" in **Figure 4.11**), -110 ms ("12″ × 6″" in **Figure 4.13**) and -61 ms ("18″ × 6″" in **Figure 4.15**) for the three cases. These results show that the bottom of the crosstie sees significantly lower compressive strain values due to a bigger bearing width.

When eccentric loading was applied to the rail seat, the peak of the measured strain diagram drifted from the centerline of the rail seat toward the side with eccentric loading (field side in this test). For example, when the support width was 18 inches, and the rail seat load was applied with a large eccentricity (**Figure 4.14** and **Figure 4.15**, case "18″ × 1.5″"), the peak of the distributed strain below the rail seat drifted towards the field side. Based on this result, the common assumption of evenly distributed crosstie reaction forces used for crosstie design may not be valid. Additionally, as shown in these data, the 45° assumption found in UIC 713 may not be accurate under some loading scenarios.

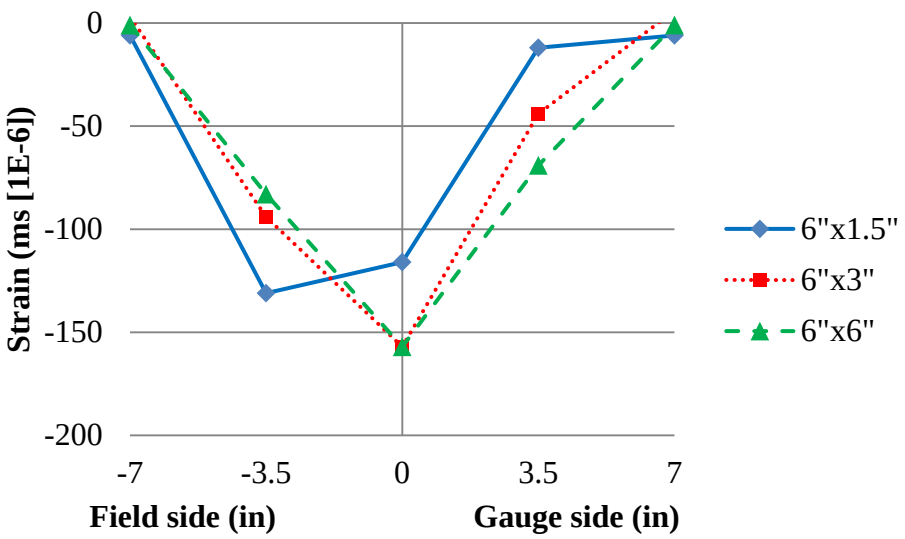

Figure 4.10 Compressive Strain Distribution 5 Inches Above the Crosstie Bottom

(Support Width = 6")

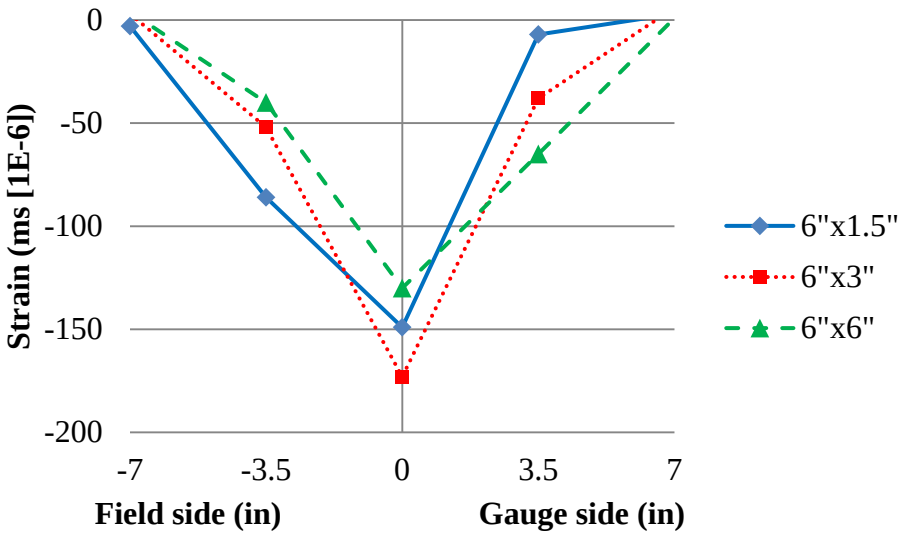

Figure 4.11 Compressive Strain Distribution 2.5 Inches Above the Crosstie Bottom

(Support Width = 6")

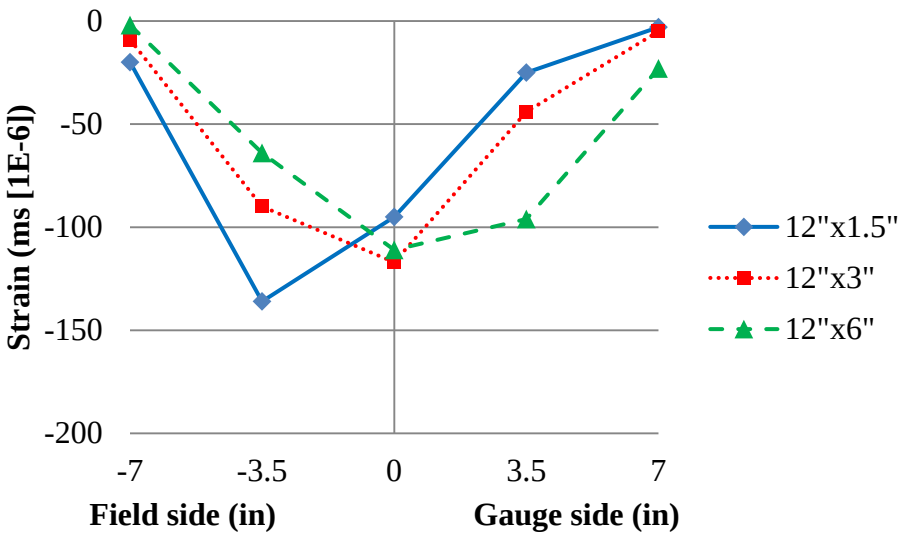

Figure 4.12 Compressive Strain Distribution 5 Inches Above the Crosstie Bottom

(Support Width = 12”)

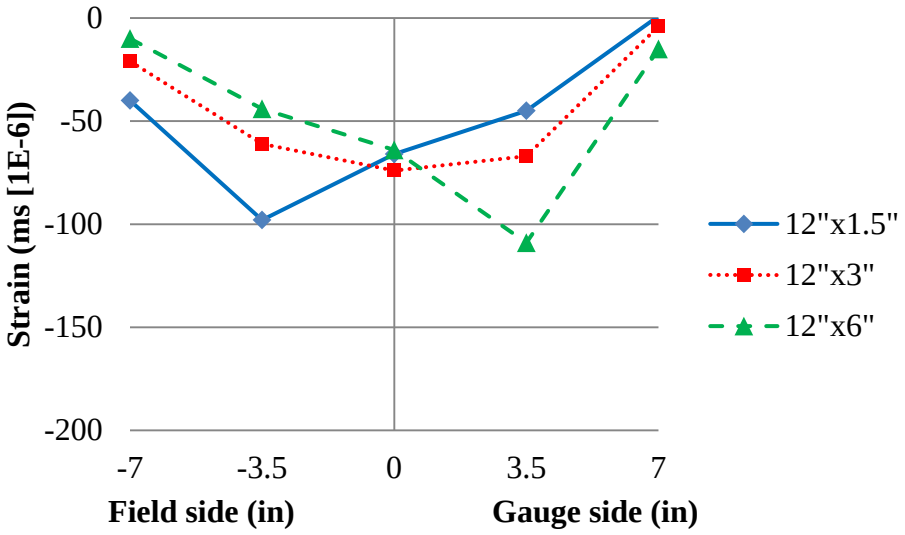

Figure 4.13 Compressive Strain Distribution 2.5 Inches Above the Crosstie Bottom

(Support Width = 12”)

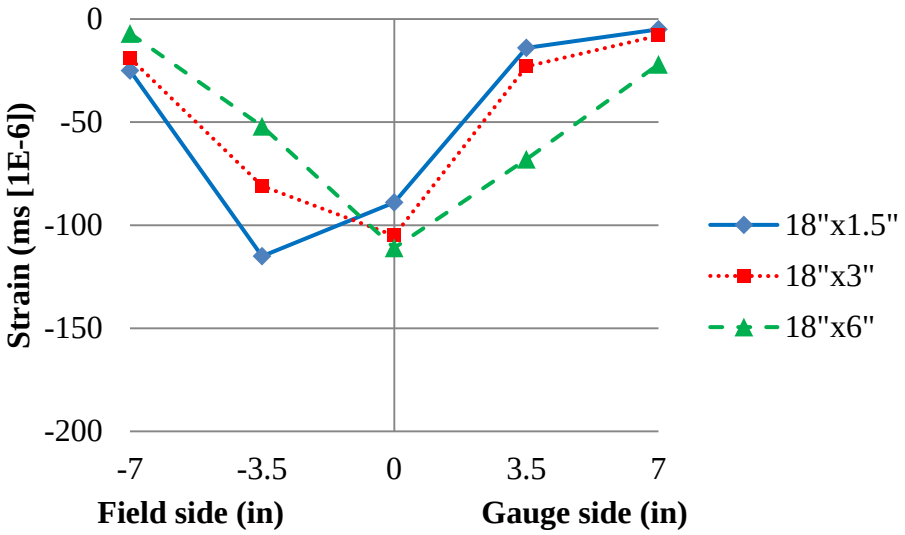

Figure 4.14 Compressive Strain Distribution 5 Inches Above the Crosstie Bottom

(Support Width = 18")

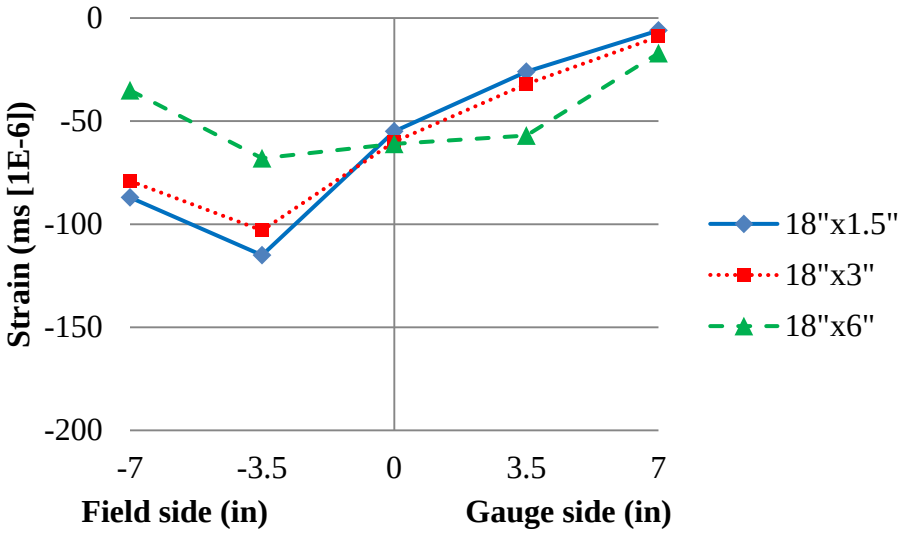

Figure 4.15 Compressive Strain Distribution 2.5 Inches Above the Crosstie Bottom

(Support Width = 18")

The internal compressive strain measured from the embedment strain gauges is shown in **Figures 4.16** – **Figure 4.18** for the three cases of support conditions. The internal strain

distribution agreed with the concrete surface strain measurements where the maximum strain was measured on the field side of the rail seat under eccentric loads. Using the cases shown in **Figure 4.16** as an example (6 inch support width), the internal compressive strain was measured as -146 ms and -150 ms from the field and gauge sides when there was no loading eccentricity (case of "6" × "6"). The measured internal compressive strain was -327 ms and -33 ms from the field and gauge side when the largest eccentricity was applied (case of "6" × 1.5"").

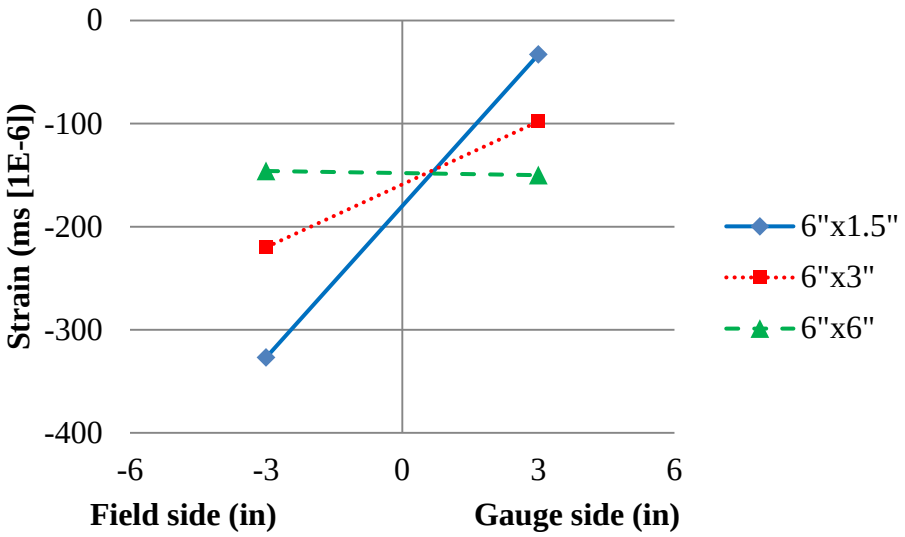

Figure 4.16 Compressive Strain Measured From Embedment Strain Gauges

(Support Width = 6")

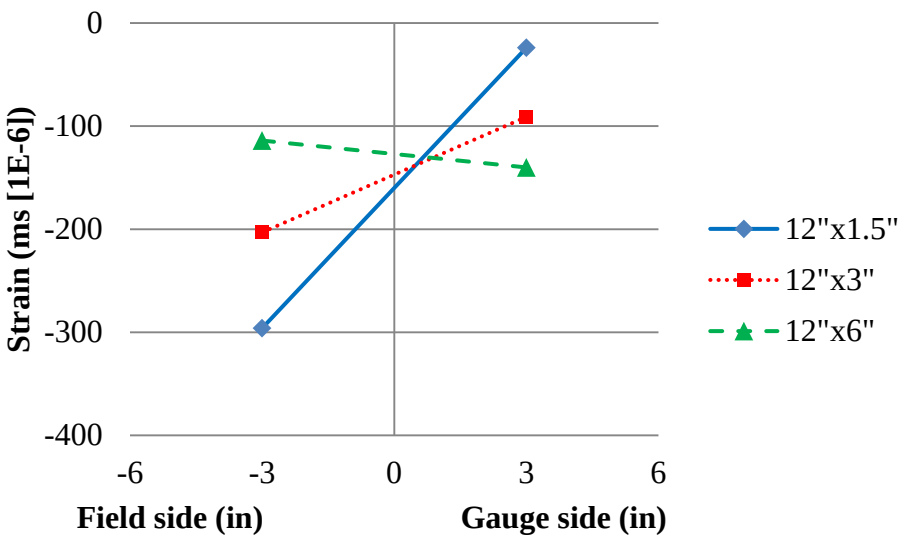

Figure 4.17 Compressive Strain Measured From Embedment Strain Gauges

(Support Width = 12”)

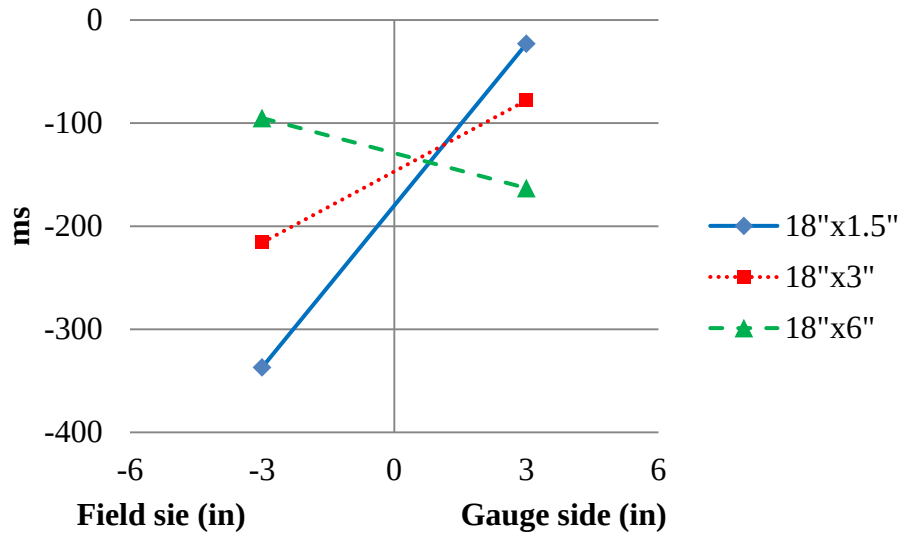

Figure 4.18 Compressive Strain Measured From Embedment Strain Gauges

(Support Width = 18”)

In conclusion, the methodology provided in UIC 713 to calculate the design bending moment needs to be modified to accommodate eccentric loadings, such as those that have been

found common on heavy-axle freight infrastructure where high L/V ratios are present. More research is needed to include various cases of loading and support conditions in a revised approach to crosstie flexural design.

4.2.1.2 Rail Deformation

Single crosstie and fastening system was tested using the SLTM with vertical loads only to validate the vertical load path. The vertical load was applied by rotating the loading head of 90 degree (**Figure 3.56 (b)** with no PTLF), which was centralized with the rail. The rail strain measured from the field and gauge side rail is shown in **Figure 4.19** and **Figure 4.20**. It can be found that the strains measured at the same height of rail from field side and gauge side were not the same as imagined, although all in compression (negative strain). The possible reason is the 1:40 inclination of rail seat made the applied vertical force wasn't exact perpendicular to the rail seat.

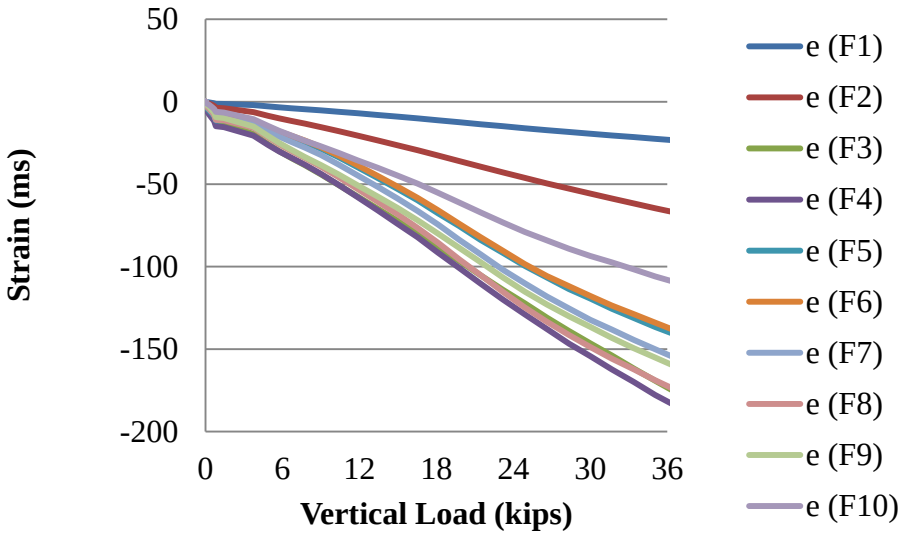

Figure 4.19 Strain Measured from Rail Under Vertical Load (Field Side)

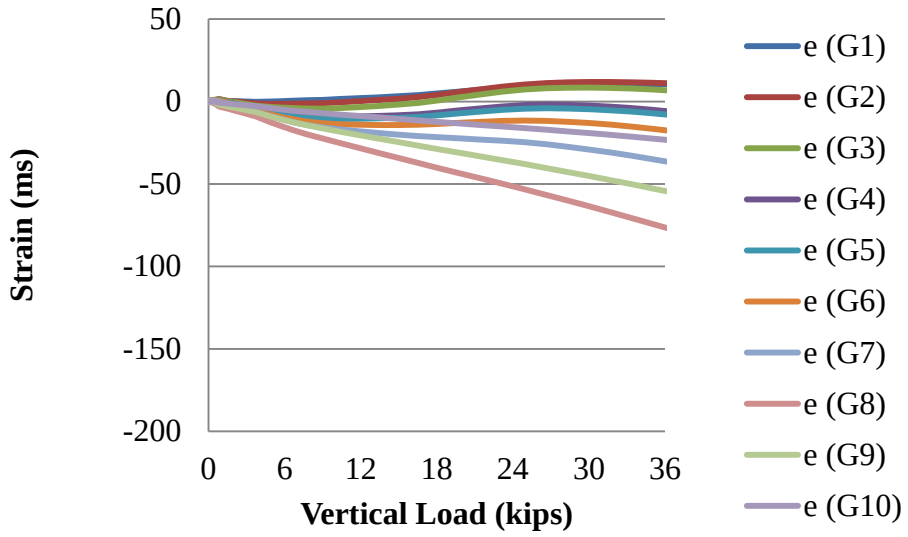

Figure 4.20 Strain Measured From Rail Under Vertical Load (Gauge Side)

Because only vertical load was applied to the center of the rail section, the field and gauge side was in a symmetric condition. And thus the averaged strains measured from the two sides of the rail was examined and given in **Figure 4.21**. In general, the linearity of all the strain measurements was pretty good. The strain measured from the top surface of rail base (Gauge 1 – 3) was all negative, in other words, the rail base was bent up due to the distributed rail seat reactions. The average strain measured from rail web (Gauge 4 – 10) varied in a narrow band from -64 ms (gauge 10) to -126 ms (gauge 8) under the vertical load of 36 kips. Theoretically, the vertical rail seat load (if unknown) can be calculated using these compressive strain measurements. However, these strains couldn't be used directly by multiplying the cross-sectional area and the Young's modulus, because the shear flow through the rail was unclear (**Figure 4.22**).

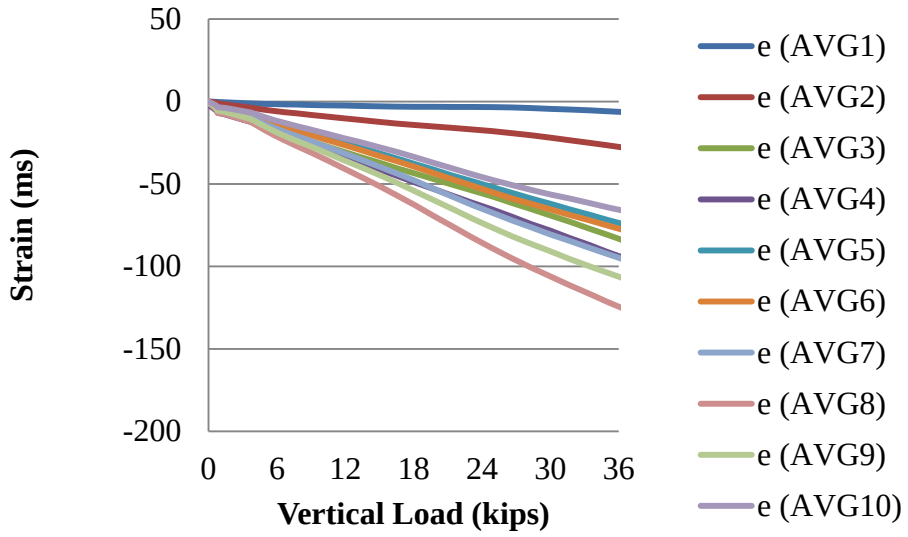

Figure 4.21 Average Strain Measured from Rail Under Vertical Load

The equation given below was used to calculate the vertical applied load:

$$F_V = eA_{eqv}E = etb_{eqv}E$$

Where e is the average compressive strain from gauge pair 4 to 10, A_{eqv} is the equivalent bearing area corresponding to the location of each strain measurement, b_{eqv} is the equivalent bearing width, t is the thickness of rail web at each location, and E is the Young's modulus of steel.

The calculated equivalent width b_{eqv} at each location is shown in **Table 4.1**. The shear flow is shown in **Figure 4.22**.

Table 4.1 Equivalent Width at Each Strain Measurement (inch)

b_{eqv} 4	b_{eqv} 5	b_{eqv} 6	b_{eqv} 7	b_{eqv} 8	b_{eqv} 9	b_{eqv} 10
11.8	15.1	14.4	11.7	8.9	10.5	17.0

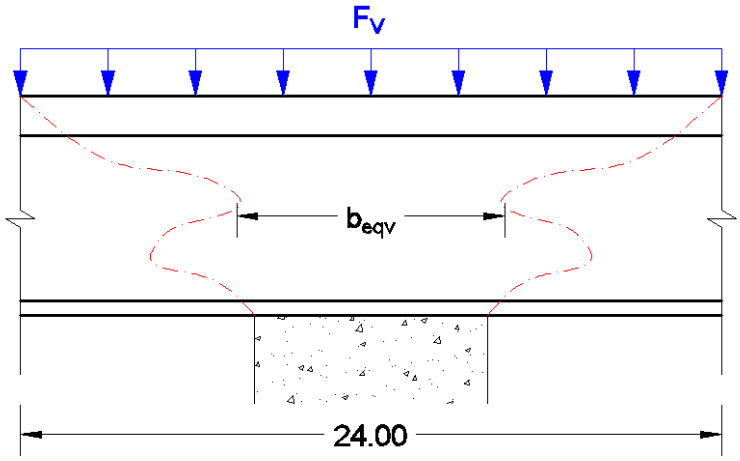

Figure 4.22 Shear Flow in Rail Under Vertical Load

4.2.1.3 Rail Deflection

Same as Section 4.2.1.2, rail deflections were recorded under various vertical loads with no lateral load applied with the SLTM. As shown in **Figure 4.23**, the vertical rail base deflections at field and gauge side as well as the lateral rail head deflection were measured by potentiometers (Section 3.8.1).

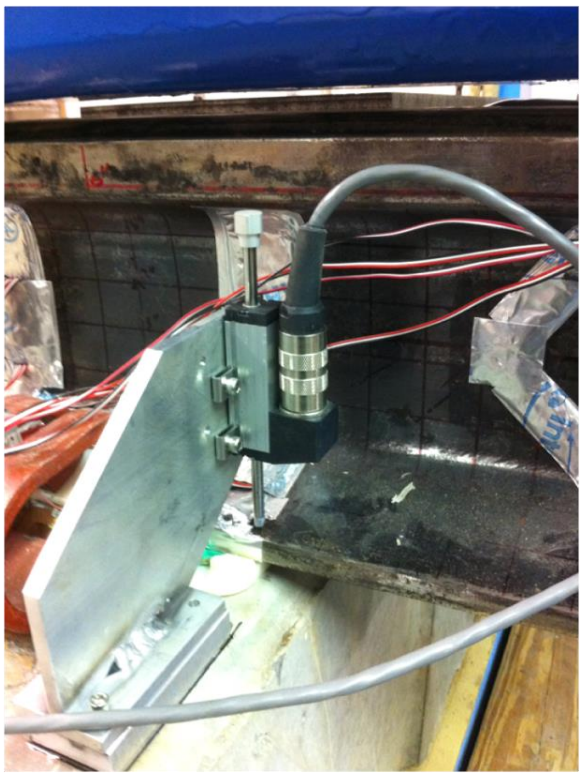

Figure 4.23 Potentiometers and Aluminum Fixture Used to Measure Rail Seat Vertical Displacement

The average vertical deflection from the field and gauge side of rail is shown in **Figure 4.24**. From the plot, it can be found the deflections measured from each side of rail was almost symmetric, the maximum deflection was 0.011 inch (under 36 kips vertical load). In addition, the rail base deflection was almost linear corresponding to the applied vertical load. This result can be compared with the rail pad assembly test (Section 3.7.2). The average vertical deflection recorded from rail pad assembly test was 0.012 inch under 40 kips wheel load, which agreed the result found from **Figure 4.24**.

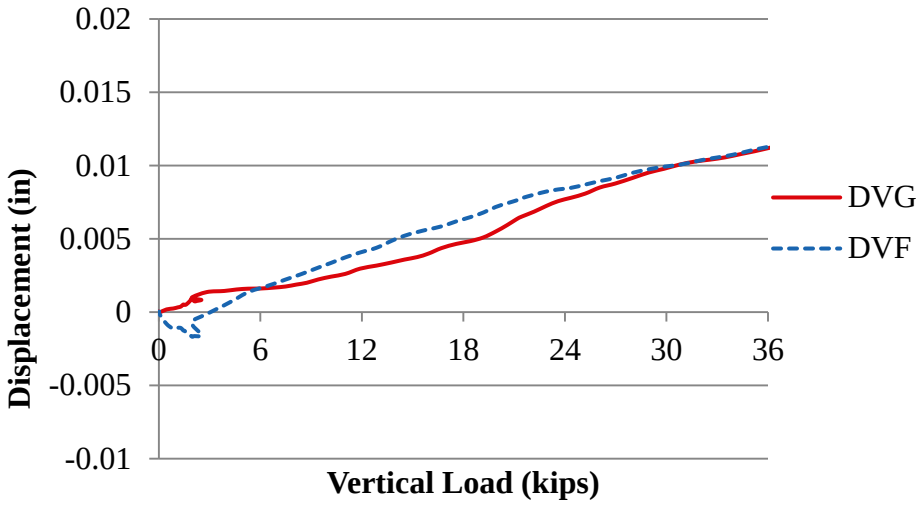

Figure 4.24 Rail Base Vertical Deflection at Gauge and Field Side Under Various Vertical Loads

Rail deflections can also be used to calculate the rail seat vertical reaction force. For a single-crosstie and fastening system, the vertical rail seat reaction is exactly the vertical applied load. If this methodology has been validated through this test, it also can be expanded into a multi-crosstie system or the field. And thus, one more way of measuring the rail seat reaction force would be available. To calculate the rail seat reactions from the rail base deflection measurements, two assumptions were made:

1) The rail base movement can be treated as rigid body motion (i.e. the rail base remains plane or the deformation remains linear in both of the direction along the crosstie and in the direction along the rail).

2) The distributed rail seat reaction can be expressed by a linear function, $FV = kAD_{avg}/t$, where k is the polyurethane pad assembly stiffness, which was obtained from

Section 3.7.2. A is the distributed area, D_{avg} is the average vertical deflection in the rail seat reaction area, and t is the thickness of the pad (0.236 inch).

To verify the above assumptions, the curvature at rail base was calculated from the strain measurements at the rail base. Strain gauges #1 - #3 in Section 4.2.1.2 at both of the field and gauge side were used for this analysis. The deflected shape of the rail base is shown in **Figure 4.25**. The x-axis shows the distance to the field side edge of the rail ("0" is for the field side edge, and "6" is for the gauge side). The "rigid deflection" was generated by drawing a line between the average displacement measurements from the field side and the gauge side. Considering the curvature of rail base due to bending, the rigid deflection needed to be corrected to better present the true deformation of the rail base. The "corrected deflection" was the real deflection of the rail base calculated using both the displacement and strain measurements. From **Figure 4.25**, it can be seen that the rail base curvature did exist; however the curvature can be neglected comparing with the rigid body motion of displacement when calculating the rail seat vertical reactions. The maximum error was 0.00021 inch or 1.9% that found at the center.

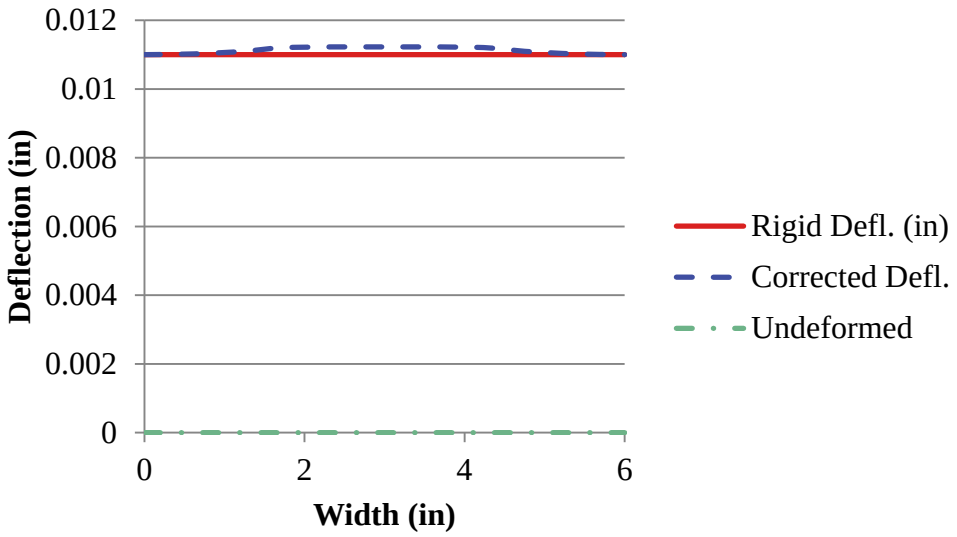

Figure 4.25 Deformed Shape of Rail Base (FV=36 Kips)

Using the measured rail base deflection and the pad assembly stiffness (**Table 3.4**), the rail seat reaction force can be calculated as 36.7 kips, which was 1.9% higher than the vertical applied load.

To clarify the vertical load path, the change of clamping force also needs to be considered, because the magnitude of the vertical applied load should be equivalent to the rail seat reaction force plus the change of clamping force. Similarly as used in calculating the rail seat reaction, $N=k_cD$ was used, where k_c is the clip stiffness, which was determined by the manufacturer to be 8.65 kips/in, and D is the vertical deflection at 0 and 6 inches from **Figure 4.27** for the field and gauge side clips.

The vertical rail base deflection is due to both the compression of polyurethane pad and the compression of the nylon 6/6 abrasion plate. The properties of these two layers of material between the rail and the concrete crosstie are shown in **Table 4.2**.

Table 4.2 Properties of the Rail Pad and Abrasion Plate

Component	Material	Thickness (in)	Assembly stiffness (ksi)
Rail pad	Polyurethane	0.236	21.9
Abrasion plate	Nylon 6/6	0.055	439

To compare the rail base deflection contributed by the rail pad and the abrasion plate, the following equation is used:

$$\frac{\Delta t_{pad}}{\Delta t_{frame}} = \frac{E_{frame}}{E_{pad}} \cdot \frac{t_{pad}}{t_{frame}} = \frac{439}{21.9} \cdot \frac{0.236}{0.055} = 86.0$$

Where *t* is the thickness of the component and *E* is the stiffness. The deflection of the abrasion plate was significantly smaller than the deflection of the rail pad, and could be

neglected. In other words, the rail base deflection measured from the test can be roughly assumed as the rail pad vertical deflection. To calculate the rail seat vertical loading by utilizing the rail base vertical deflection measurements, the equation stated in assumption 2 was used.

Based on the above discussion, the change of clamping force at each side of rail was 95 lbf, which was only 4.0% decrease from the initial clamping force.

4.2.1.4 Crosstie Displacement

Three vertical and two lateral displacement measurements were recorded (**Figure 3.60**). In the vertical load path section (4.2.1), the vertical force was only applied to one rail. Under this circumstance, the crosstie deflections were not representative to calculate the vertical stiffness. And therefore, the data of crosstie displacements is not displaced here.

4.2.1.5 Change of Clamping Force

The change of clamping force was found to be really small (below 100 lbf) that can be ignored in the vertical load path analysis, for details see Chapter 7.

4.2.2 Vertical Load Path in Multi-crosstie and Fastening System in Laboratory Experiment

In multi-crosstie system, the vertical load path analysis is consisted by the vertical load application, vertical reaction force of each rail seat directly below and adjacent to the wheel, lateral load going through shoulder and frictions between rail and concrete, as well as rail and crosstie displacements. Experiments of multi-crosstie and fastening system were operated with the TLS, the instrumentation map is shown in **Figure 3.62**.

4.2.2.1 Vertical Wheel Load Application

With the TLS, vertical wheel loads up to 40 kips were applied by two actuators to both sides of the axle **(Figure 4.26)**. It was assumed that the vertical load was applied symmetrically to both sides of the axle, in the other words, the same loading conditions were applied to each rail. In reality, there might a negligible error of the vertical load transferred to each wheel which dependent on the contact condition and geometric dimensions between each actuator and wheel set.

Figure 4.26 Test Set-up with the TLS

Due to the uncertainty on the wheel and rail contact conditions, even with no load applied (by the hydraulic jack) in the lateral direction, the lateral component of the applied load (F_L) might not be zero. The lateral component of wheel load was recorded by the second iteration of lateral rail bridge (**Figure 3.24**) installed on the near rail above each instrumented rail seat (4 –

8). The measured lateral load (F_L) associated with 0 – 40 kips vertical load application above each rail seat is shown in **Figure 4.27**. The recorded data suggests that the lateral load (F_L) due to the 40 kips applied vertical load can be as great as 11.6 kips (crosstie 8-19), all pushing the rail towards the field side. In the following analysis, gap was demonstrated between concrete and ballast below rail seats 6 and 8. The irregularity of the track structure due to the unbounded rail seats might be a possible reason that high lateral loads were observed at these two rail seats.

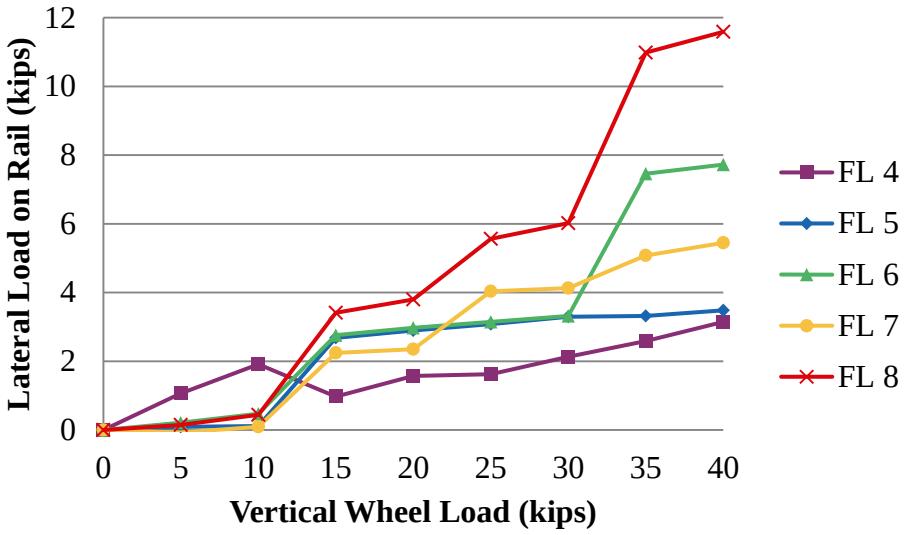

Figure 4.27 Measured Lateral Loads under Vertical Load Application

4.2.2.2 Rail Seat Vertical Reaction Load

To measure the vertical load transfer from rail to each rail seat, two ways of instrumentation were used. The first method was stated in Section 3.5.3 using embedment strain gauges: by analyzing the internal concrete strain, the vertical reaction forces were calculated. Laboratory calibration was applied to obtain the correction factors used in equation:

$$V(kips) = e_{AVG} \cdot E_c \cdot A \cdot Q_1 \cdot Q_2 \cdot Q_3$$

The correction factors used for the instrumented rail seats E, S, U and W at the TLS are listed in **Table 4.3**.

Table 4.3 Correction Factors Used for Rail Seats 4 – 8 and 17 at the TLS

Rail Seat	4	5	6	7	8	17
Q_1	2.075	2.075	2.075	2.075	2.075	2.075
Q_2 (α)	0.175	0.5	0.175	0.175	0.25	0.175
Q_3	1	1	1.15	0.9	1.15	1.15
e_{DIFF_MAX} (E-6)	600	400	600	200	600	400

The second method was to use the rail bridge (with a shape of Chevron pattern) as described in Section 3.5.1. One pair of Chevron patterns was placed 2 inches away from the side surface of each crosstie, the reading from the Wheatstone bridge stands for the change of shear force between the two Chevron patterns, i.e. when the crosstie is directly below the wheel set, the output is the difference between the wheel load and rail seat vertical reaction force; when the crosstie was adjacent to the wheel set, the output force was exactly the rail seat reaction.

When static vertical wheel load was the only force applied by the two vertical actuators, the wheel-rail contact point located almost directly over the center line of a rail seat, and therefore the loading eccentricity was negligible. **Figure 4.28** shows the vertical rail seat reaction forces (R_{SV}) measured from the six rail seats by embedment strain gauges, which including rail seats 4 – 8 below the near rail and rail seat 17 from the center crosstie below the far rail. **Figure 4.29** shows the rail seat loads measured from the same rail seats by the rail vertical bridges. The results shown in these two figures reveal that the rail seat loads measured from the two ways of instrumentation agreed very well. The error was found no more than 2.2

kips (at rail seat 5) when the applied vertical wheel load was 40 kips. **Figure 4.28** and **Figure 4.29** also agree that rail seats 6 and 8 were not engaged at all, even when 40 kips vertical wheel load was directly applied over these two rail seats, the reaction forces were no more than 1 kip. The rest four rail seats behaved normally and similarly to each other. Between 18.7 kips (rail seat 5) to 24.8 kips (rail seat 4) vertical load was transferred to each rail seat, which takes 46.8% to 62.0% of the applied vertical wheel load. In addition, the rail seat reaction force grew linearly with the vertical wheel load, which suggests that the bottom surface of these four rail seats fully contacted with the ballast from beginning.

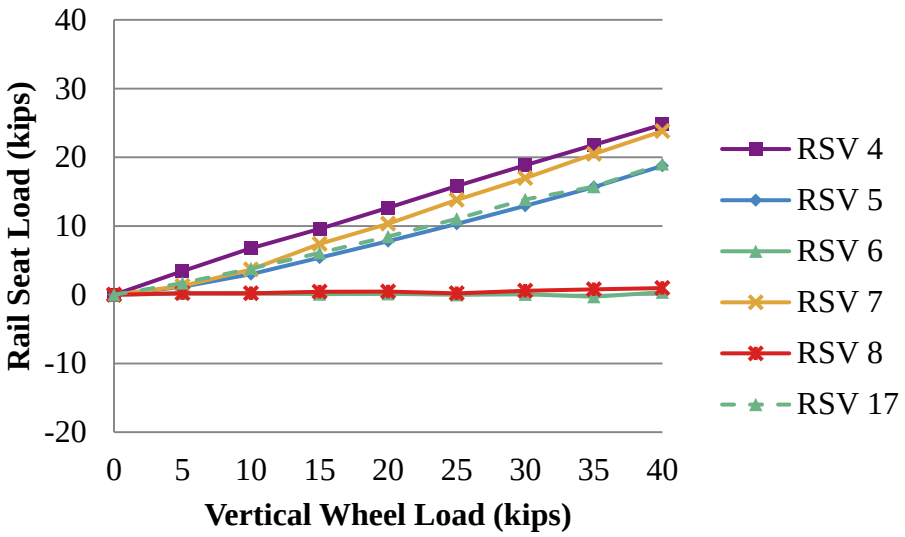

Figure 4.28 Reaction Load for Rail Seat Directly below the Wheel Set Measured by Embedment Strain Gauges (L=0 kips)

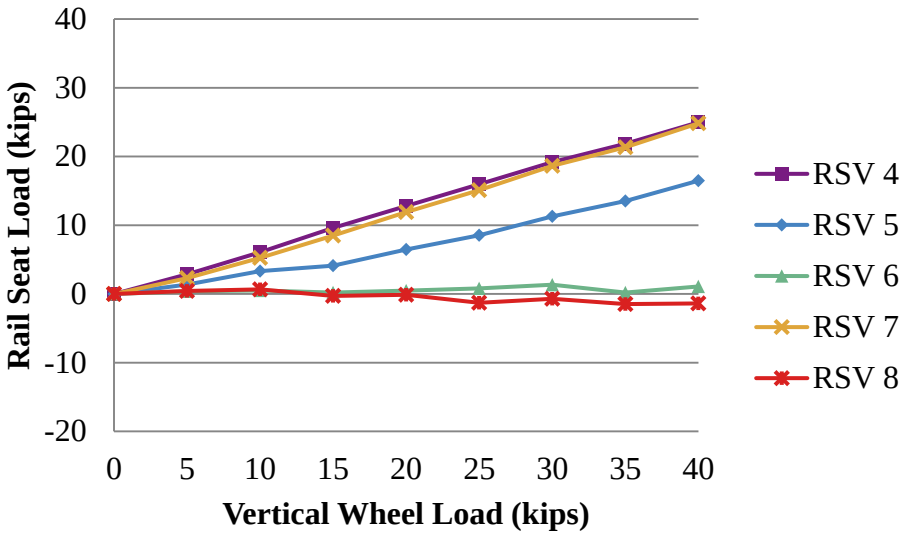

Figure 4.29 Reaction Load for Rail Seat Directly below the Wheel Set Measured by Rail Vertical Bridges (L=0 kips)

For the second round of repeated testing, to understand the rail seat pressure distribution, the MBTSS was installed at rail seats 4 to 8. To install the MBTSS sensors, rail clips were removed from rail seats 2 to 9, and the rail was jacked up. During this process, the support conditions below a few rail seats were found changed. The reaction force of each rail seat directly below the wheel set measured after the MBTSS installation is shown in **Figure 4.30**. Comparing the results shown in **Figure 4.28** and **Figure 4.30** (the first and second round of the repeated testing), it can be found that the reaction force of the four fully engaged rail seats remained almost the same, which supported 19.7 kips to 26.2 kips or 49.3% to 65.5% of the vertical wheel load. After the rail was jacked up and clips replacement, rail seat 6 turned to be partially engaged: when a small wheel load was applied, more load transferred to the adjacent rail seats (only 1.5 kips directly to rail seat 6 under 10 kips wheel load). With a greater wheel load being applied, a large percentage of the vertical force went through the rail seat directly below the wheel (13.9 kips directly to rail seat 6 under 40 kips wheel load). In other words, the

initial gap between the concrete crosstie and ballast still existed, and a minimum vertical load was needed to close up the gap gradually.

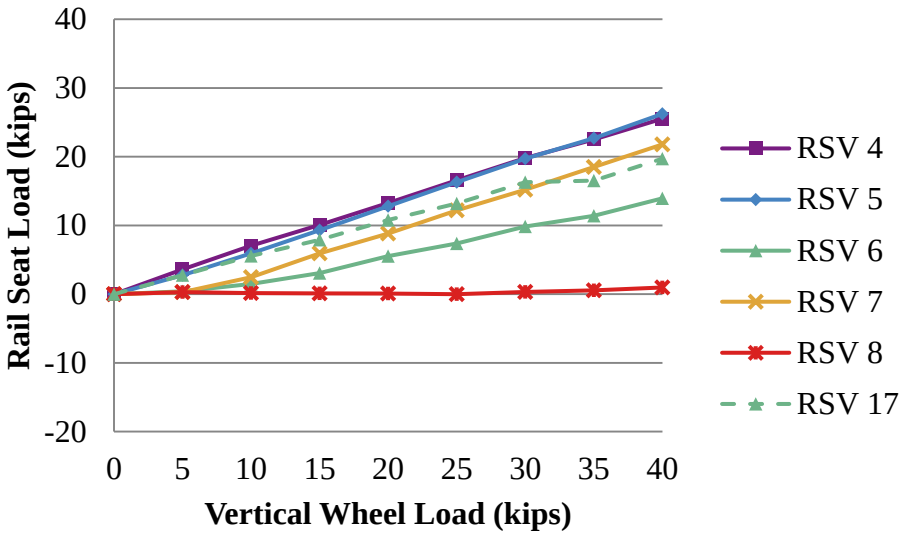

Figure 4.30 Reaction Load for Rail Seat Directly Below the Wheel Set Measured by Embedment Strain Gauges After the MBTSS Installation (L=0 kips)

The gap between crosstie and ballast at rail seat 6 and 8 was observable by bare eyes before the clips were installed. As shown in **Figure 4.31**, about 0.5 inch gap was found between rail base and concrete when no clips were in place. Assuming the rail was straight and rigid, the gap was due to the irregularity of the ballast support. After all the clips had been installed, rail seats 6 and 8 were lifted up due to the pair of 2.5 kips clamping force, and the gap between the rail and concrete vanished; however, a new gap formed between concrete and ballast at the same time (**Figure 4.32**).

Gap Between Rail Base and Concrete at Rail Seat 6 and 8 Prior to the Clip Installation

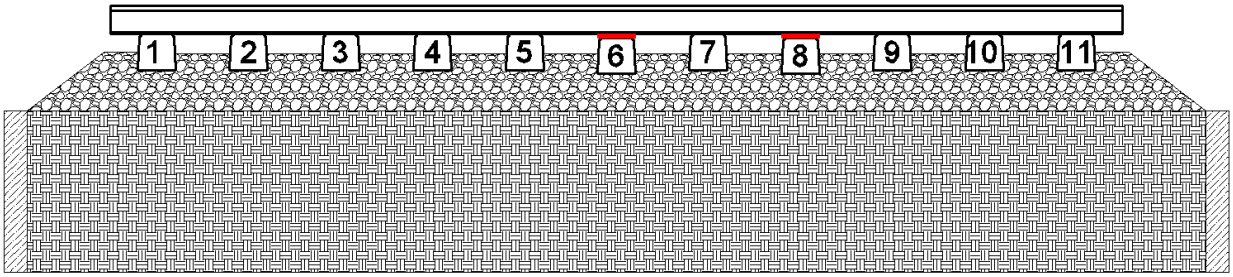

Figure 4.31 Gap Between Rail Base and Concrete at Rail Seats 6 and 8 Prior to the Clip Installation

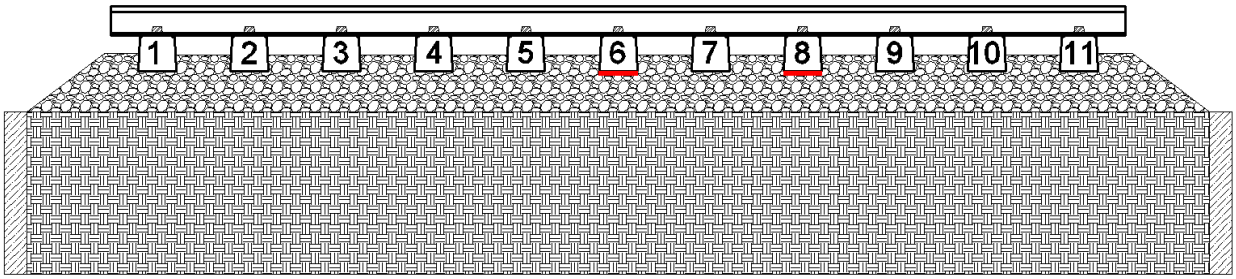

Figure 4.32 Gap Between Concrete and Ballast at Rail Seats 6 and 8 After the Clip Installation

The distribution of rail seat reaction force can validate the gap theory mentioned above (**Figure 4.33**). **Figure 4.33** shows that rail seat 5, which located one crosstie spacing left of rail seat 6, provided the greatest reaction force although the wheelset was above rail seat 6. When the vertical wheel load was 10 kips, the reaction force measured from rail seat 6 was 1.5 kips or 15.0%, and 6.1 kips or 61.0% for rail seat 5. With a greater wheel load being applied, the reaction force at rail seat 6 grew at the same rate with its adjacent rail seat 5 and 7. When 40 kip vertical wheel load was applied, 13.9 kips or 34.8% load was supported by rail seat 6; for rail seat 5, it was 16.3 kips, which is percentage decrease of 40.8%.

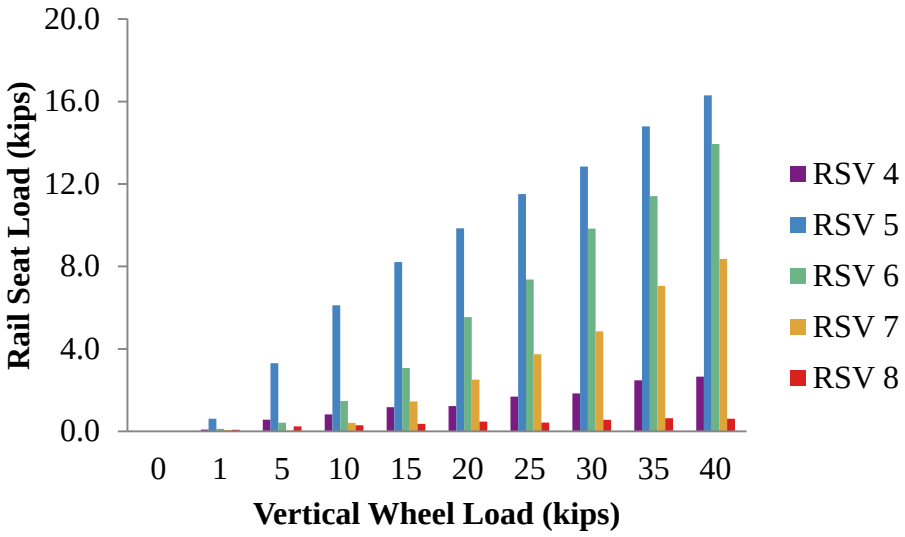

Figure 4.33 Distribution of Rail Seat Reaction Load Measured by Embedment Strain Gauges After the MBTSS Installation (L=0 kips)

4.2.2.3 Rail Seat Pressure Distribution

The deformation of each rail seat can be measured using the method discussed in Section 4.2.1.3. However as only four displacements as well as a few strain measurements were taken, some details must be neglected. To study the pressure distribution over an entire rail seat, the MBTSS was utilized. When only vertical wheel load was applied perfectly to the center of each rail seat, evenly compression was expected.

4.2.2.4 Lateral Load Going Through Shoulder

As discussed in Section 4.2.2.1, depending on the contact condition between wheel and rail, lateral component of the applied load might not be neglected even if no lateral force was directly applied to the axle. Consequently, the lateral force transferred to each shoulder might exist. **Figure 4.34** shows the lateral load going through each shoulder (R_L) when the wheel set was placed directly above that crosstie. In general, the load going through the shoulder was small,

which was no more than 2.3 kips from the recorded data. The rest of the lateral applied load was balanced by the frictions between the rail base and concrete. It is also noticed that the lateral force going through should 4 was a negative one, which suggests that after the clip installation, the initial force was not zero. And due to the applied wheel load, the contact force between the side surface of the rail base and shoulder face at rail seat 4 decreased.

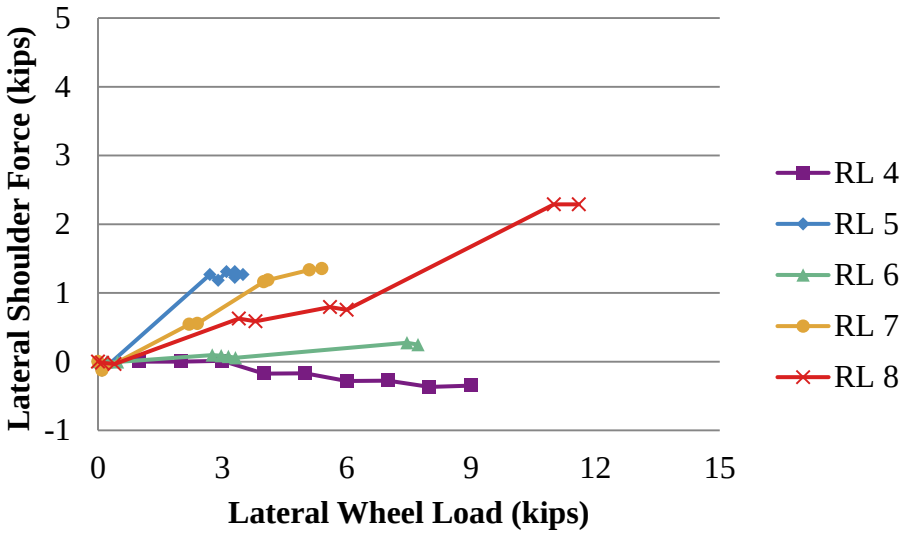

Figure 4.34 Lateral Load Going Through Shoulder under Vertical Wheel Load Directly Applied over Each Crosstie

4.2.2.5 Rail Relative Deflections

To reduce the number of sensors, only one potentiometer was placed on gauge/field side of each rail seat (see Section 3.8.3 for details). Vertical rail base deflections measured from field (D_{VF}) and gauge side (D_{VG}) are shown in **Figure 4.35** and **Figure 4.36**. Ideally, if the vertical wheel load was applied at the center line of the rail, the gauge side and field side vertical deflections should be close. However, from **Figure 4.35** and **Figure 4.36**, almost all the field side deflections were positive (pointing downward) and gauge side deflections were negative

(pointing upward). Two possible reasons may result in this uneven deflection observed from displacement measurements. First, the existence of lateral component of the applied load (F_L) caused the rail rotation; secondly, the rail base vertical deflections were measured only from one side of each rail seat, the initial skewing of a crosstie may affect the vertical load transfer. In addition, the vertical deflection under the vertical applied load was very small (no more than 0.02 inch), and much smaller than the deflections caused by the lateral applied load, the imperfections of the test set up may affect the accuracy.

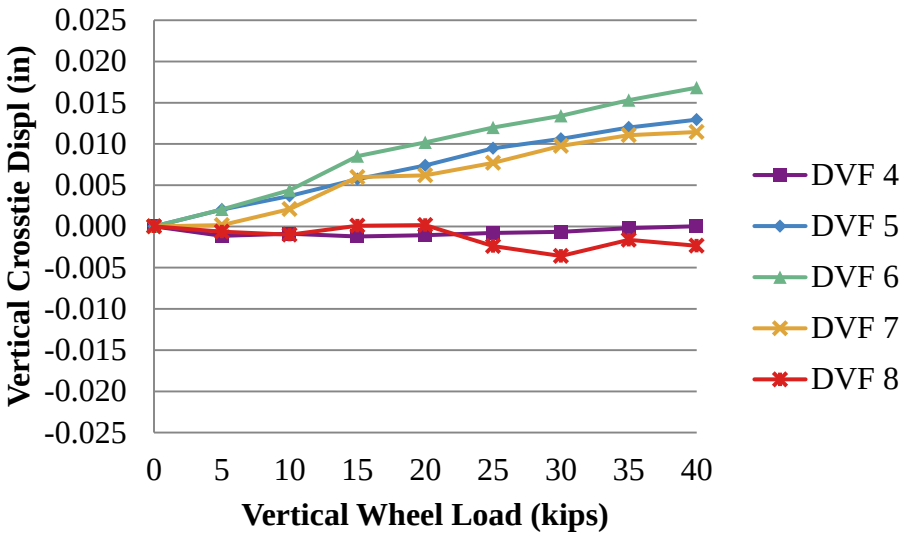

Figure 4.35 Rail Base Vertical Deflections at Field Side Under Vertical Wheel Load Directly Applied over Each Crosstie

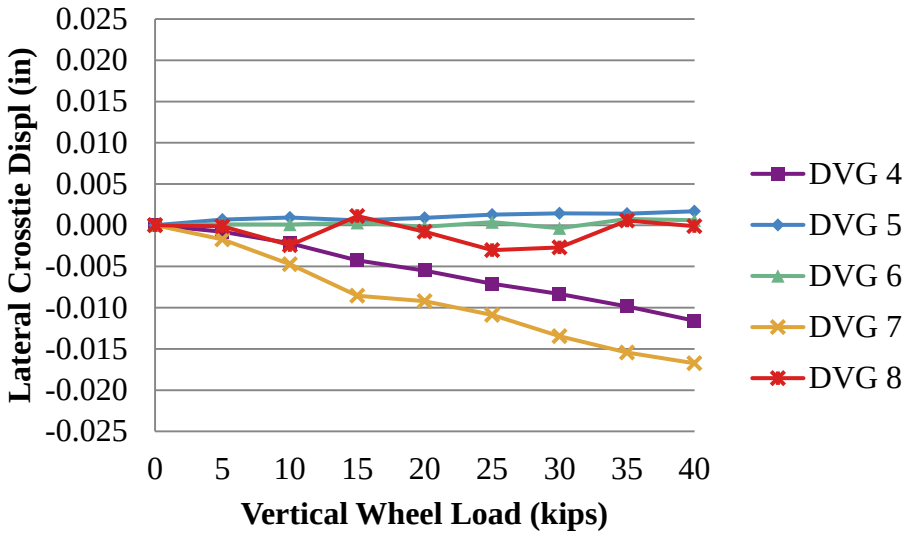

Figure 4.36 Rail Base Vertical Deflections at Gauge Side under Vertical Wheel Load Directly Applied over Each Crosstie

The lateral deflections measured from rail web (D_{LW}) and rail base (D_{LB}) were also very small (**Figure 4.37** and **Figure 4.38**) with no significant value observed at any location.

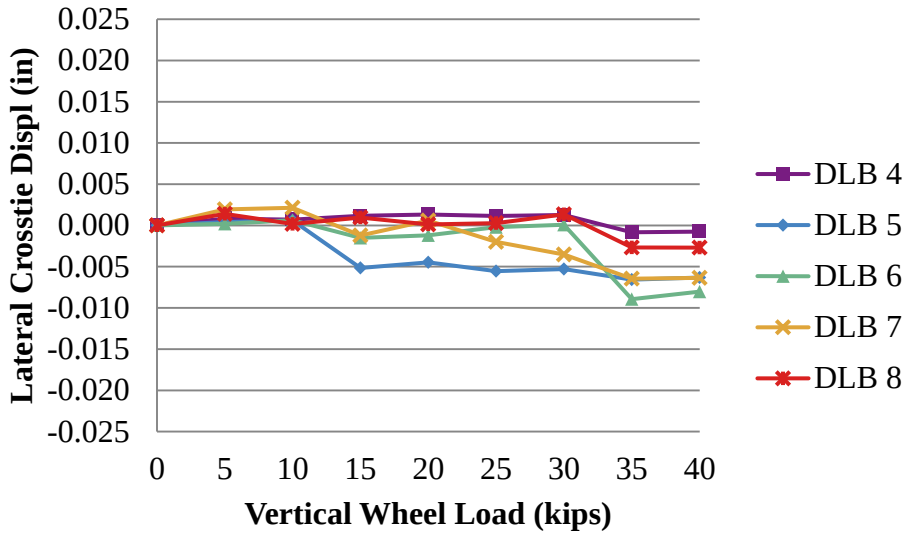

Figure 4.37 Rail Base Lateral Deflections at Gauge Side Under Vertical Wheel Load Directly Applied over Each Crosstie

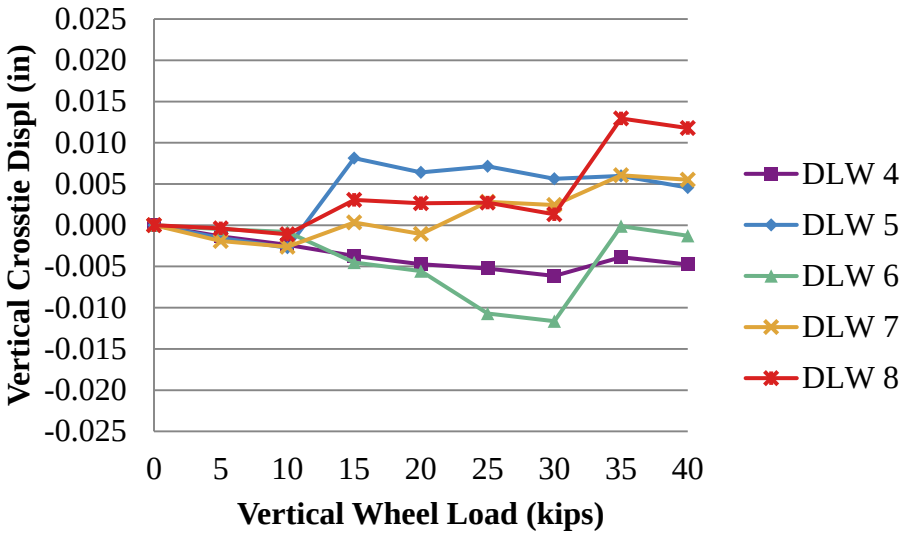

Figure 4.38 Rail Web Lateral Deflections at Gauge Side Under Vertical Wheel Load Directly Applied over Each Crosstie

4.2.2.6 Crosstie Global Displacements

Vertical (D_{GV}) and lateral (D_{GL}) crosstie global displacements were measured from the near end of each crosstie (**Figure 4.39 and Figure 4.40**). The deflections (both in vertical and lateral directions) measured from crosstie 6-17 and 8-19 were found greater than the others, although no rail seat reaction force was recorded. This observation implied that the rail seat load doesn't necessarily correlate with crosstie global vertical displacement. The large deflections were resulted by the poor support conditions below these two rail seats. When a 40 kip vertical wheel load was applied, the vertical crosstie displacement varied between 0.030 inch (crosstie 4-15) and 0.134 inch (crosstie 8-19). The crosstie lateral displacements were found all pointing to the field side, which ranged from 0.008 inch (crosstie 4-15) to 0.057 inch (crosstie 8-19).

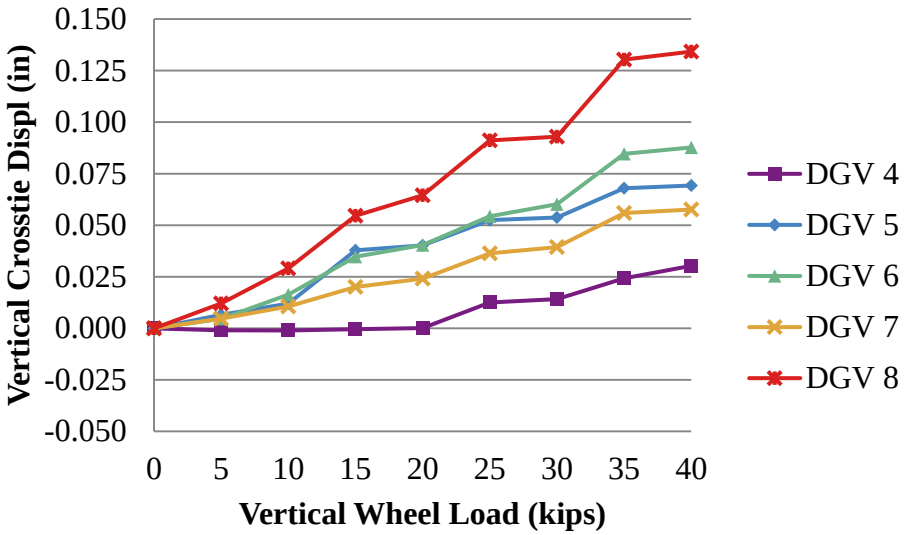

Figure 4.39 Crosstie Vertical Deflection Under Vertical Wheel Load Directly Applied over Each Crosstie

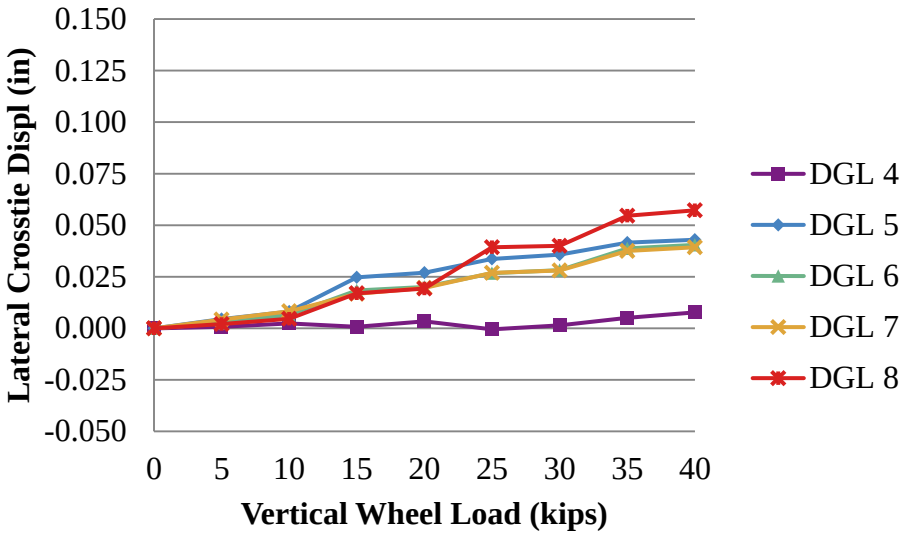

Figure 4.40 Crosstie Lateral Deflection Under Vertical Wheel Load Directly Applied over Each Crosstie

4.2.3 Vertical Load Path in Full-scale Field Experiment

Full-scale field experiments were operated at the RTT and the HTL located at the TTCI, CO (**Figure 4.41**). Because static loads in both vertical and lateral directions were applied by actuators installed on TLV, the testing results were not affected by the track curvature or super elevation. Under this condition, tests operated at the HTL can be treated as duplicated tests operated at the RTT.

Figure 4.41 Full-scale Field Test Set-up at RTT, TTC

4.2.3.1 Vertical Wheel Load Application

Vertical loads with the same magnitude were applied to both rails (**Figure 4.42**). The loads were directly output from load cells installed on the hydraulic actuators instead of the rail bridges used in dynamic field tests. However, it couldn't be guaranteed that the wheel load was perfectly centralized to the rail. White paint was sprayed over the top surface of rail head, when the wheel was removed, the contact patch could be found (**Figure 4.42**). In general, the contact was found closer to the gauge side. It should also be clarified that, the dark area with no paint shown in

Figure 4.42 was due to the effect of overlying multiple loading cases, which including the loading in both vertical and lateral directions. Because of the frictions and contact angle between wheel and rail, as well as the potential eccentricity in vertical load application, small amount of lateral load F_L might be applied.

For both the tangent track (RTT) and the curved track (HTL), static wheel loads were applied over each instrumented rail seat as well as over the center of crib between each pair of instrumented rail seats. In 2012 testing, the data was zeroed for embedment and surface strain gauges at 5 kips vertical load. Under this situation, the 5 kips vertical applied load should be taken as a pre-loading, and all rail seat loadings recorded in 2012 increased from 5 kips.

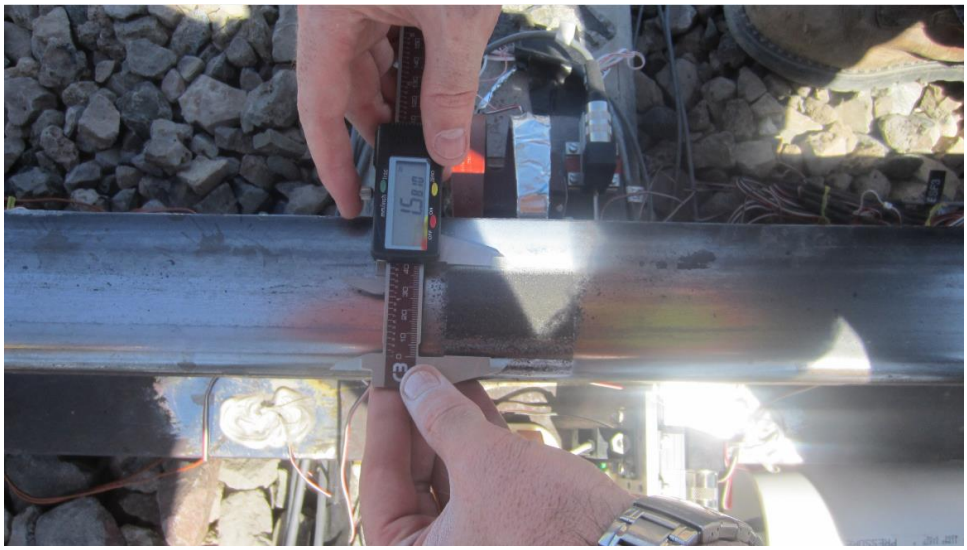

Figure 4.42 Rail-wheel Contact Patch Shown on White Paint

Figure 4.43 Vertical Wheel Load Applied by Hydraulic Actuators

4.2.3.2 Rail Seat Vertical Reaction Load

Same as used in multi-crosstie laboratory experiments (Section 4.2.2.2), both embedment strain gauges (Section 3.5.3) and vertical rail bridges (Section 3.5.1) were used to measure the vertical load transfer from rail to each rail seat.

Laboratory calibration was applied to obtain the correction factors used in equation:

$$V(kips) = e_{AVG} \cdot E_c \cdot A \cdot Q_1 \cdot Q_2 \cdot Q_3$$

In September 2013, Crosstie CS, EU, GW were removed from the RTT and shipped to University of Illinois. The calibration work for these three crossties was done and the correction factors were obtained as shown in **Table 4.4**.

Table 4.4 Correction Factors Used for Rail Seats E, S, U and W at the RTT

Rail Seat	E	S	U	W
Q_1	2.075	2.075	2.075	2.075
Q_2 (α)	0.175	0.175	0.175	0.175
Q_3	1	1	1	1
e_{DIFF_MAX} (E-6)	600	400	400	400

However, none of the crossties at the HTL had a chance to be calibrated in the laboratory. And therefore, the averages of the correction factors of all the crossties calibrated in the laboratory were used for crossties from the HTL. The correction factors for rail seats E, S, U and W at the HTL are listed in **Table 4.5**.

Table 4.5 Correction Factors Used for Rail Seats E, S, U and W at the HTL

Rail Seat	E	S	U	W
Q_1	2.075	2.075	2.075	2.075
Q_2 (α)	0.175	0.175	0.175	0.175
Q_3	1.15	1.15	1.15	1.15
e_{DIFF_MAX} (E-6)	400	400	400	400

Based on the analysis from laboratory experiments (Section 4.2.2.2), the rail seat directly below the wheel set is hypothesized to support a constant ratio of vertical load, i.e. the rail seat load is expected to grow proportionally with the increasing of wheel load if the track foundation was perfect linear elastic. However, the vertical load supported by each adjacent rail seat is expected to be highly dependent on the vertical stiffness of the track and support conditions from ballast, and therefore it is highly variable. To explore the attenuation of all the rail seat reactions, data collected from these embedment strain gauges were analyzed to calculate each vertical rail seat load below the loading axle.

Figure 4.44 and **Figure 4.45** show the vertical rail seat loads under 0 - 40 kips vertical wheel load, when the TLV was directly above each rail seat.

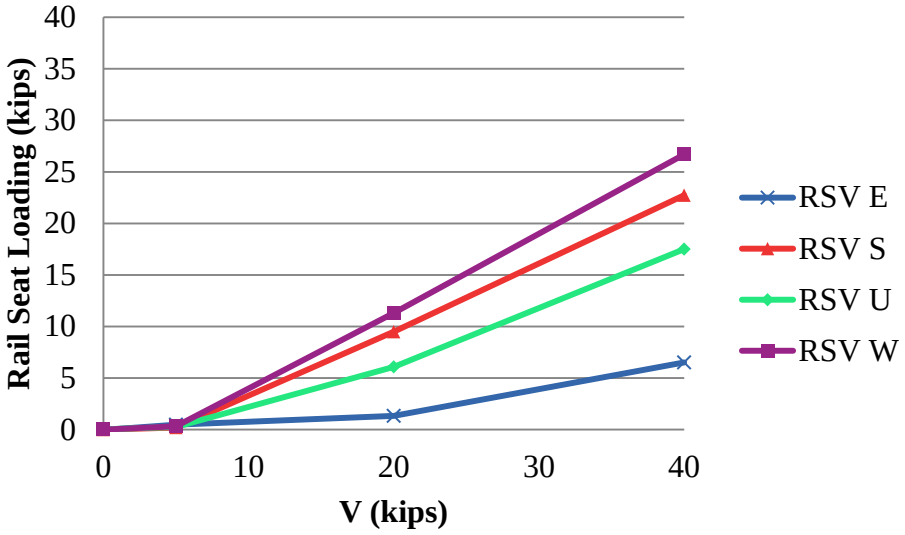

Figure 4.44 Rail Seat Loading Under Various Vertical Wheel Loads at the RTT (2012)

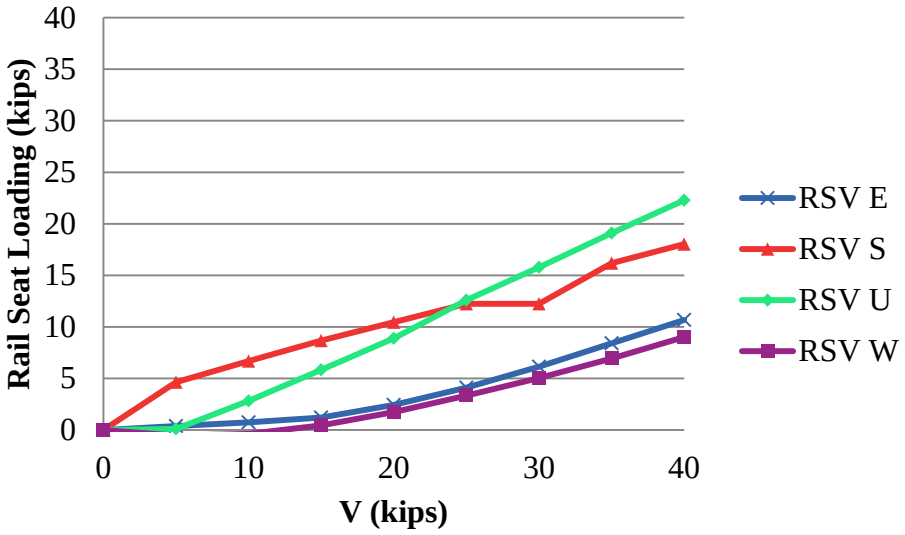

Figure 4.45 Rail Seat Loading Under Various Vertical Wheel Loads at the RTT (2013)

Both **Figure 4.44** and **Figure 4.45** show a large variation in rail seat loadings under a certain vertical wheel load. In the testing conducted at RTT in 2012 (**Figure 4.44**), under a 40

kip vertical wheel load, the rail seat loads varied from 6.5 kips to 26.7 kips, or 16% and 67% of the wheel load. For the data collected from 2013 testing which is shown in **Figure 4.45**, it can be found that the rail seat loads varied from 9.0 kips to 22.3 kips, or 22% and 56 % of the vertical wheel load. A smaller loading interval (5 kips) was used in 2013 testing (**Figure 4.45).** For all the four rail seats in 2013 testings, the increment of rail seat loading was all about constant for each loading step when the wheel load was above 15 kips. This finding suggests that the ballast reaction increased almost linearly after the wheel load (or rail seat load) researched a threshold. For rail seat S, which recorded the highest vertical loading when the wheel load was below 20 kips, its slope decreased and turned close to constant after 5 kips wheel load being applied. As for rail seat E and W, which recorded much lower rail seat loading, the reaction forces were very low until the vertical loading reached 15 kips. Rail seats E and W showed very similar curves, suggesting a similar vertical stiffness (similar ballast contact and compaction) under these two rail seats. Combining all this information, it reveals that rail seat E, U and W was hanging initially, in other words, a gap existed between the crosstie and ballast prior to the wheel load being applied. It also suggests, a vertical wheel load is needed to close up such this gap, and the ballast reaction would start to increase linearly afterwards.

Although fewer data points were collected in 2012 testing, there is a similar trend between the 2012 and 2013 testing: widely varying rail seat reactions were found from different rail seats; and some rail seats were only partially engaged or hanging over the ballast. By comparing the rail seat load recorded from the same rail seat in 2012 and 2013 (**Figure 4.44** and **Figure 4.45**), it can be concluded that the reaction force might have changed significantly dependent on the change of support conditions within that year. For example, under a 40 kips wheel load, the rail seat load recorded from rail seat W was 26.7 kips in 2012 and 9.0 kips in

2013. This shows the drastic effect that support conditions have on rail seat loading; although crossties, spacing, rail seat, and vertical load were all the same, the rail seat loading could decrease as much as 66% in one year, merely due to a change in support conditions.

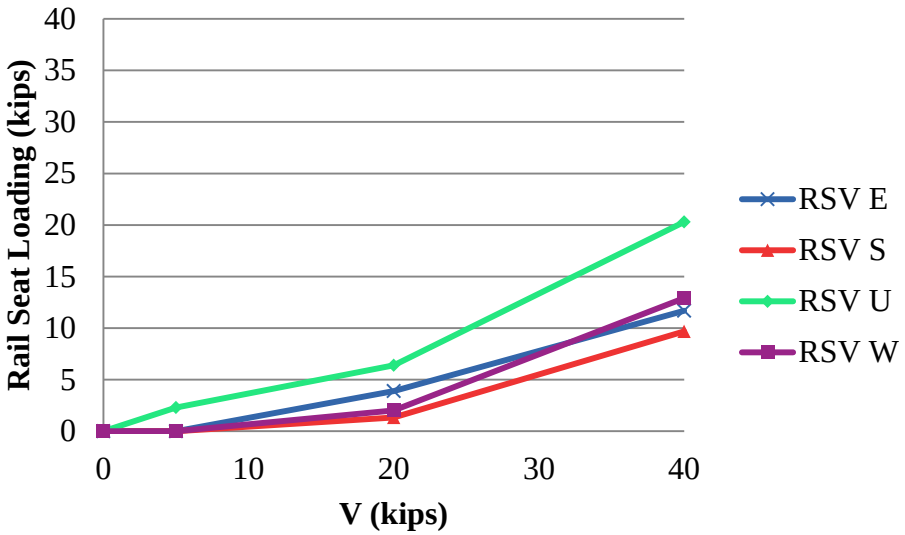

Figure 4.46 Rail Seat Loading Under Various Vertical Wheel Loads at the HTL (2012)

As shown in **Figure 4.46**, evidence was also provided for the existing of hanging ties at a curved section (the HTL). Clearly, the portion of the wheel load supported by each rail seat was much lower when the applied wheel load was below 20 kips. That suggests a preload of about 20 kips was required to initiate a full reaction from the ballast. This also illustrates how the distribution of rail seat load would be affected by its support conditions. If the crosstie placed directly below the wheel set hangs, the crossties located one or more tie-spacing away must provide higher reaction forces to compensate.

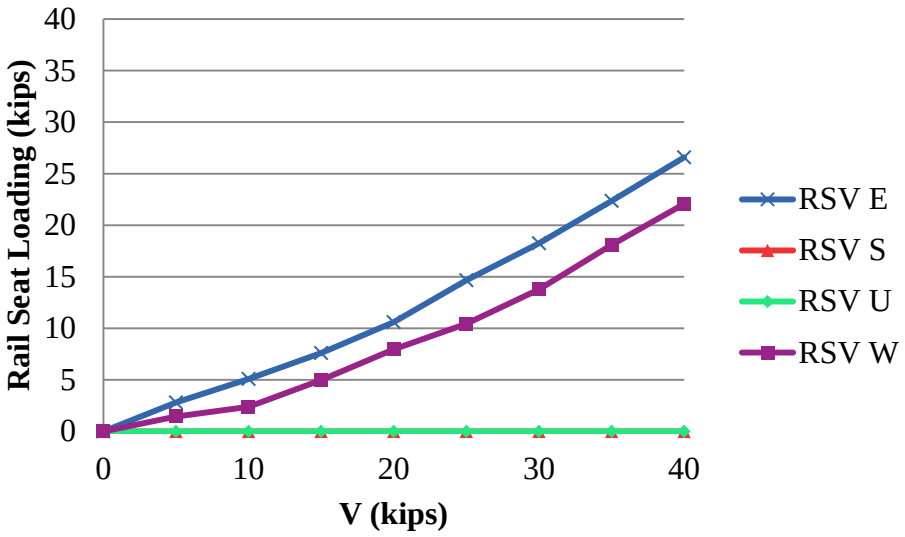

Figure 4.47 Rail Seat Loading Under Various Vertical Wheel Loads at the HTL (2013)

The support conditions for a hanging tie might be improved by re-tamping the track. **Figure 4.47** shows the rail seat loading measured from the same testing section at HTL one year later (2013), after the track was re-tamped. The sensors below the rail seats S and U were damaged and did not give proper reading, but the vertical reaction forces measured from the remaining two rail seats increased immediately upon application of wheel load and took a significantly higher portion of the wheel load.

The support conditions can also be reflected in the distribution of rail seat reaction force. With all proper supports directly below the wheel set and one crosstie spacing adjacent to it, about 50% of vertical load was beard by the middle rail seat; and about 25% flew to each rail seat next to it **(Figure 4.48)**. If one rail seat was supported weakly (hanging tie), more load would transfer to other rail seats (**Figure 4.49**). Because only three rail seats were instrumented in the field experiments, a portion of load might be supported by rail seats located two or more crosstie spacing away. However, this rail seat load distribution only applies to the case subjected

to the track stiffness at the TTC; and how much the foundation modulus could affect the load distribution is upon further study.

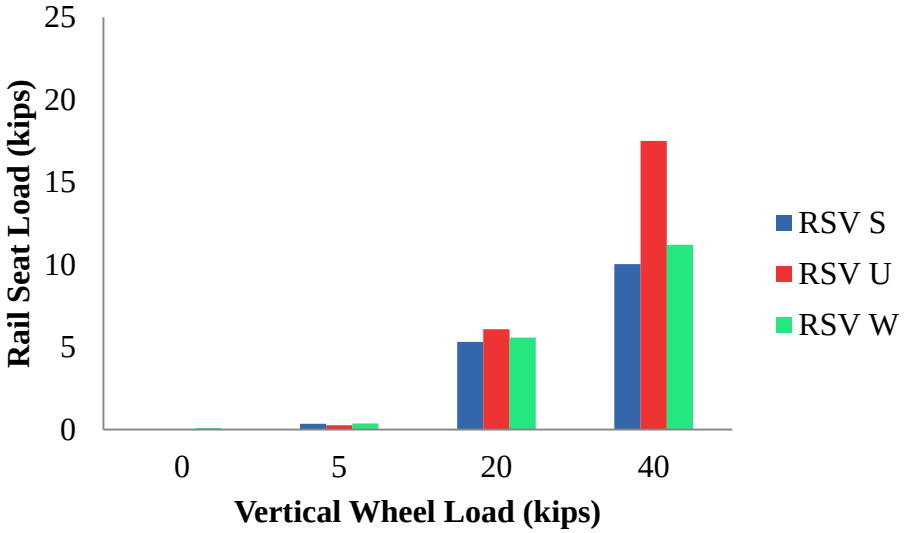

Figure 4.48 Distribution of Rail Seat Loading Under Various Vertical Wheel Loads Applied over Crosstie EU at the RTT (2012)

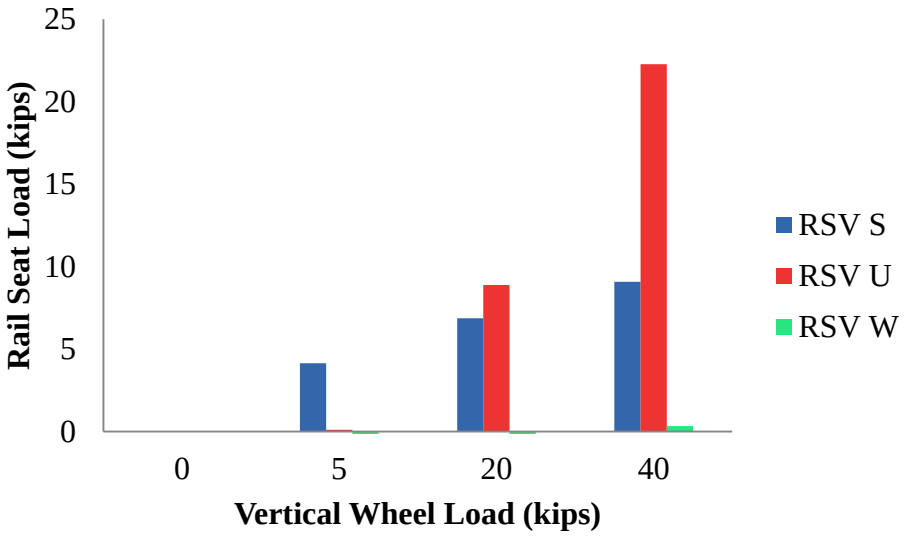

Figure 4.49 Distribution of Rail Seat Loading Under Various Vertical Wheel Loads Applied over Crosstie EU at the RTT (2013)

From these results, the hypothesis that rail seat load grows proportionally with increasing wheel load can be restated as: once adequate contact was made with the ballast, the rail seat loading increased in a nearly linear manner. This loading increase is highly dependent on support conditions however, as ballast contact and stiffness are primarily responsible for the changes in rail seat loading.

4.2.3.3 Rail Seat Pressure Distribution

When insignificant lateral force was applied to the top of the rail, the distribution of rail seat pressure was found evenly distributed through MBTSS (Greve et al, 2014).

4.2.3.4 Lateral Force Going Through Shoulder

Due to the small amount of lateral load (F_L) when vertical load was being applied, very small lateral force was found transferred through the shoulder. Except rail seat E at the HTL, the lateral shoulder reaction measured from all other rail seats were found lower than 100 lbf under 40 kips vertical load (Williams et al, 2014).

4.2.3.4 Rail Relative Deflections

While assuming the rail displaced as a rigid body, the three displacement measurements should depend on the actual lateral force (F_L) applied to each rail and the vertical load transferred to each rail seat (R_{SV}). Because of initial imperfection, loading eccentricity and lateral load (F_L), the vertical rail displacement may not increase linearly (**Figure 4.50**).

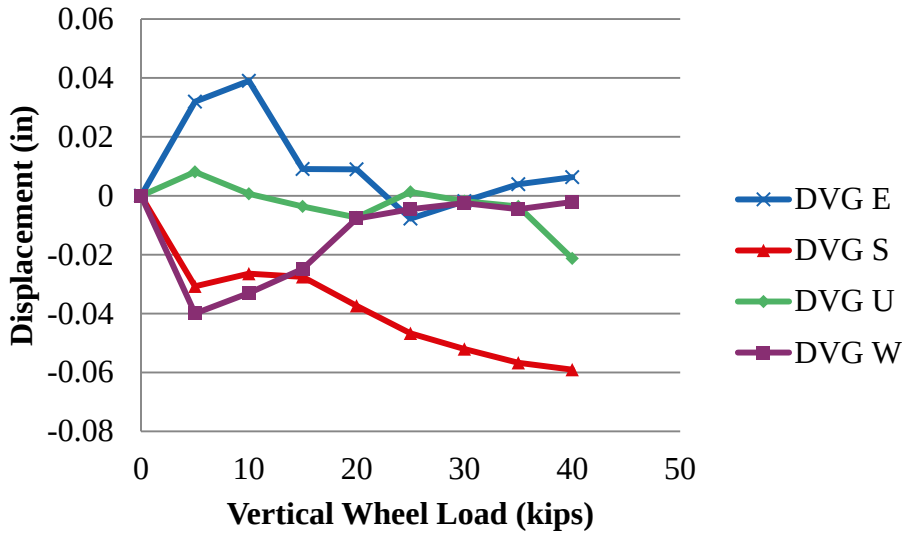

Figure 4.50 Gauge Side Rail Base Vertical Displacement Under Various Vertical Wheel Loads at the HTL (2012)

Ideally, no lateral displacements were expected at rail base or rail web. The variation was brought by the interference factors given above. Fortunately, this interference might be negligible depending on the required accuracy. The variation was found no greater than 0.015 inch for rail web lateral displacement, and no greater than 0.002 inch for rail base lateral displacement.

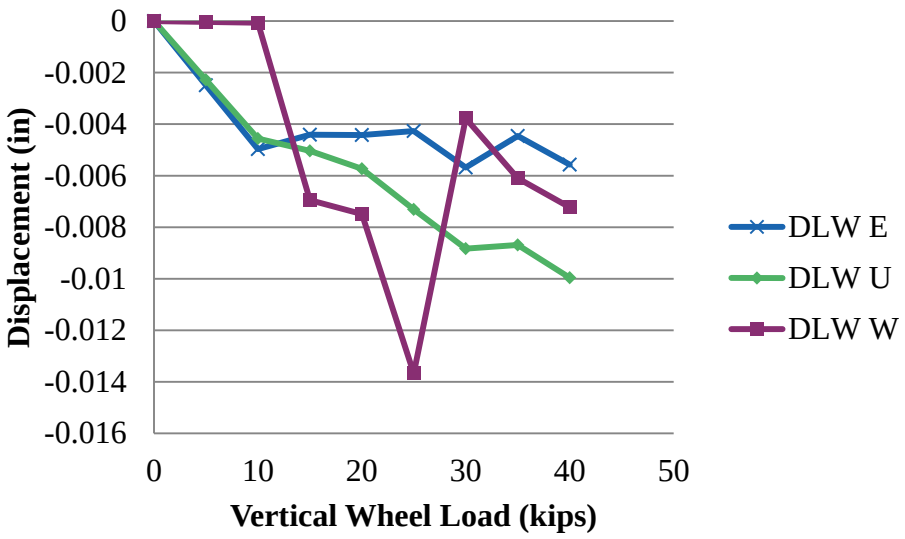

Figure 4.51 Gauge Side Rail Web Lateral Displacement Under Various Vertical Wheel Loads at the HTL (2012)

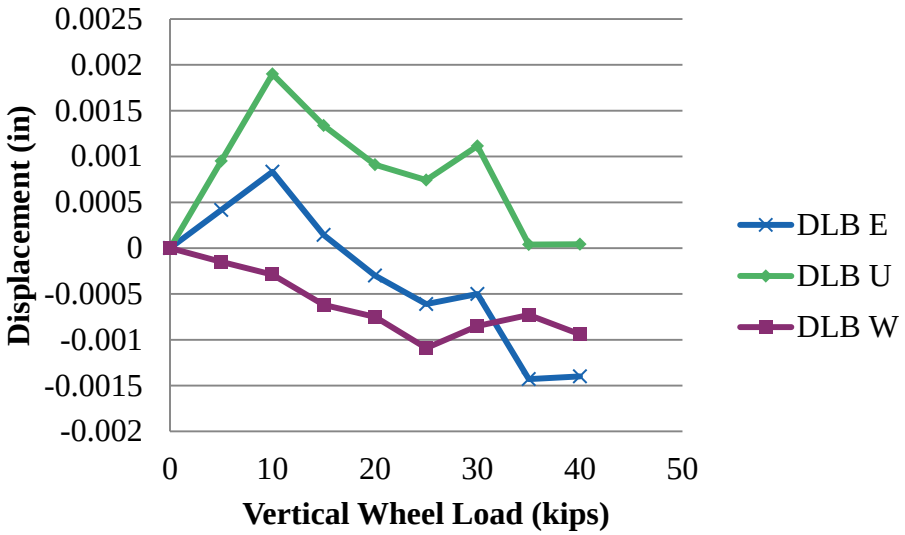

Figure 4.52 Gauge Side Rail Base Lateral Displacement Under Various Vertical Wheel Loads at the HTL (2012)

4.2.3.5 Crosstie Global Displacement

Concrete crosstie global vertical deflection was found increasing almost linearly corresponding to the vertical wheel load (F_V) when the initial gap between concrete crosstie and ballast was fully closed. However, the strain hardening behavior is important to note, as it impacts the magnitude of loads that are carried by individual rail seats and dictates how load is transferred to adjacent crossties (also discussed in Section 4.2.2.2). This is shown through the hinge point in **Figure 4.53**. The crosstie global lateral deflection was found to be negligible.

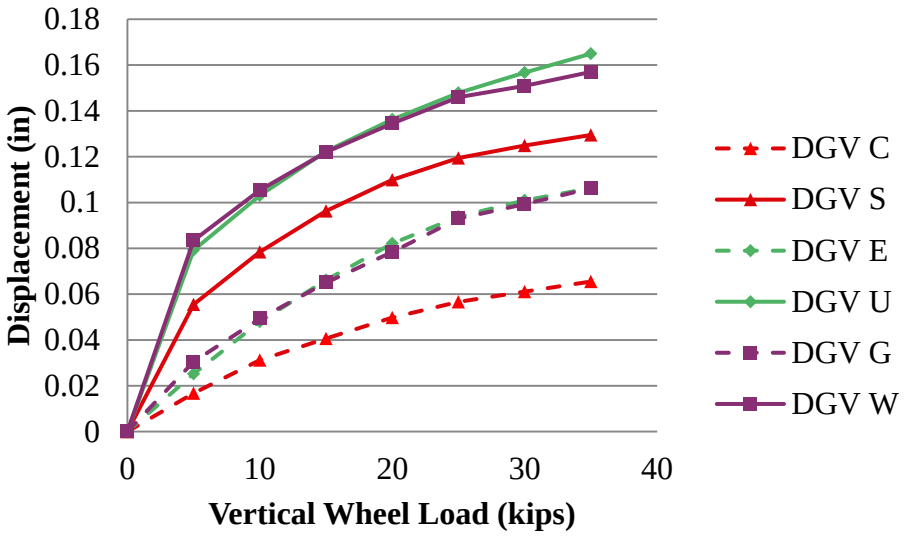

Figure 4.53 Crosstie Global Vertical Displacement Under Various Vertical Wheel Loads at the HTL (2013)

4.3 Lateral Load Path Under Static Loading

Same as the static vertical load path, this section is divided into three parts: lateral load path in single crosstie and fastening system, in multi-crosstie laboratory, and field experiments. Because in reality the lateral wheel load couldn't stand alone, the lateral wheel load was sometimes

applied associated with a certain vertical wheel load. In multi-crosstie laboratory and field experiments, the L/V was limited below 0.6.

4.3.1 Lateral Load Path in Single-crosstie and Fastening System

The study of the Lateral load path under static loading in single-crosstie and fastening system refers to the experiment with the SLTM (Section 3.8.1).

With the SLTM, the performance of rail, crosstie and fastening system was studied under a constant vertical load with various lateral applied loads. Two loading conditions were examined; 0 – 3 kips lateral load applied to both rails by the PTLF (at web), and GRMS (at head); 0 – 36 kips vertical with a fixed ratio (0.5) of lateral loading applied by the SLTM loading head. With the PTLF and the SLTM loading head, the applied load was read and output digitally; with the GRMS, a dial gauge was used to read load applied by a hydraulic jack. The deformation of rail, the displacements of rail and crosstie, the rail seat reaction force, the shoulder face reaction force and the change of clamping force were all measured to map the full lateral load path.

4.3.1.1 Rail Deformation

For the first loading case described in Section 4.3.1, only the lateral load was applied to the rail web by the PTLF or to the rail head by the GRMS. With the PTLF, because the lateral load was applied 3 inches below the top of rail head, only the strain measurements below the contact point were valid and presented in **Figure 4.54** and **Figure 4.55**.

Due to the bending moment created by the lateral force applied on the rail web, the rail web surface at the field side was predicted in compression (negative strain), and the rail web surface at gauge side was in tension (positive strain), which agrees with the finding from **Figure**

4.54 and Figure 4.55. The bending action at rail base is affected by rail seat reaction force and clamping forces, which is the reason that the strain measured from field and gauge side rail base was not really symmetric as from rail web.

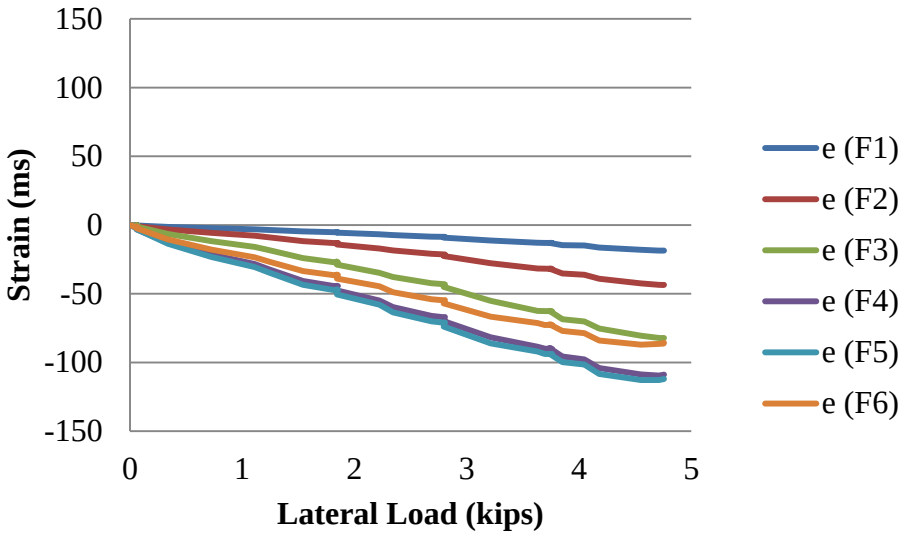

Figure 4.54 Strain Measured from Rail Under Lateral Load (Field Side)

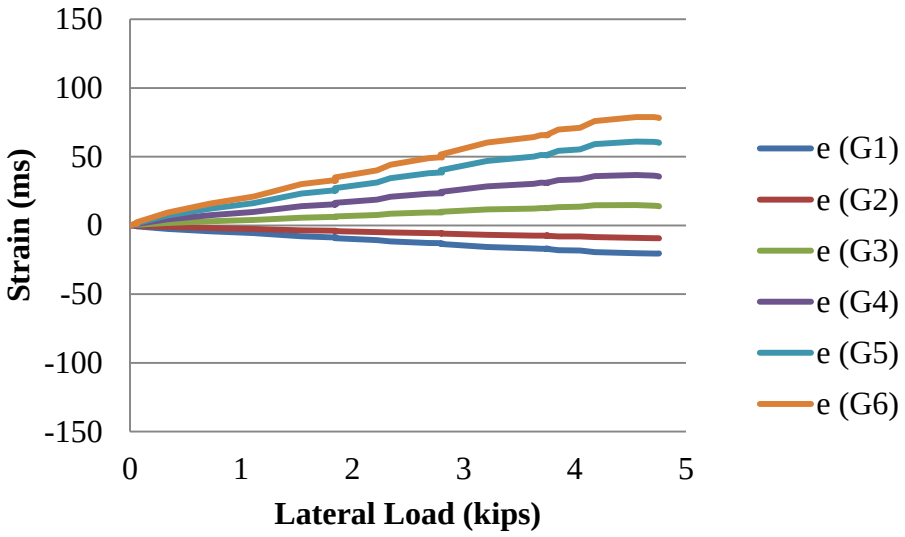

Figure 4.55 Strain Measured from Rail Under Lateral Load (Gauge Side)

As to the second loading case (0 -36 kips vertical force with 0.5 as L/V applied by the SLTM), strains measured from field and gauge side rail are shown in **Figure 4.56** and **Figure 4.57**. The strain measurements were used to calculate the curvature of rail and generate the deformation map of the rail cross-section (see Section 4.3.1.2). When the vertical applied load was very small (below 1 kip), the strain recorded from almost all the gauges increased tremendously. This due to the special loading profile using the SLTM loading head (**Figure 3.57**); at the beginning, the loading head only pushed both rail towards the field side with no vertical load being applied.

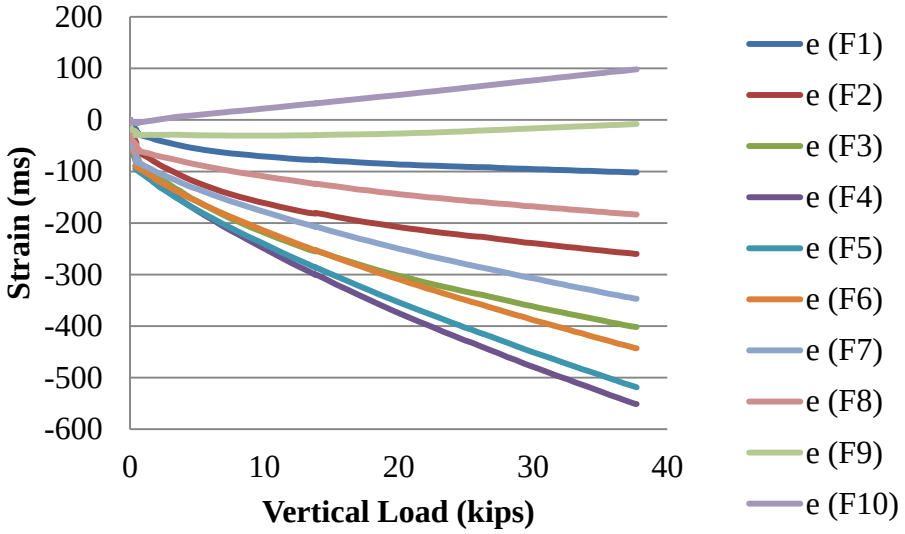

Figure 4.56 Strain Measured from Rail Under Simulated Wheel Load (Field Side)

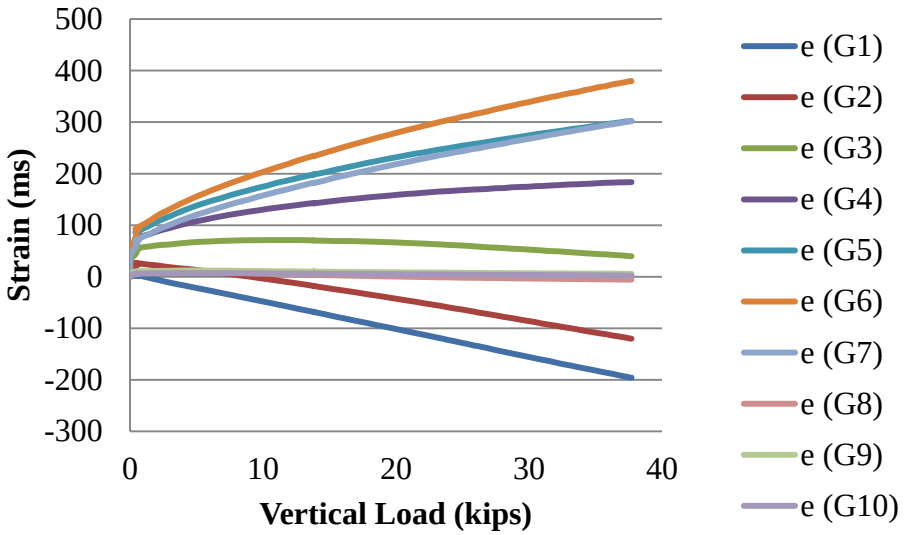

Figure 4.57 Strain Measured from Rail Under Simulated Wheel Load (Gauge Side)

4.3.1.2 Rail Relative Deflection

Same as Section 4.3.1.2, the single-crosstie and fastening system was tested with the SLTM under two loading scenarios. With lateral force applied to the center of rail web with the PTLF, the average of the two vertical rail base deflections measured from the field and gauge side as well as the rail head lateral deflection are shown in **Figure 4.58**. Under 3 kips lateral load, the gauge side rail base was lifted up significantly (0.026 inch with 3 kips lateral load); the field side rail base dipped down slightly (-0.004 inch with 3 kips lateral load); the rail head was pushed towards the field side to 0.021 inch. Strong non-linearity was found in these displacement measurements when the applied lateral load was greater than 1 kip and lower than 3 kips.

When 3 kips lateral load was applied to the rail head with the GRMS, bigger deflections were found due to bigger applied moments. The rail base vertical deflections at gauge and field side were 0.105 inch and -0.008 inch; the rail head lateral deflection increased dramatically to 0.153 inch.

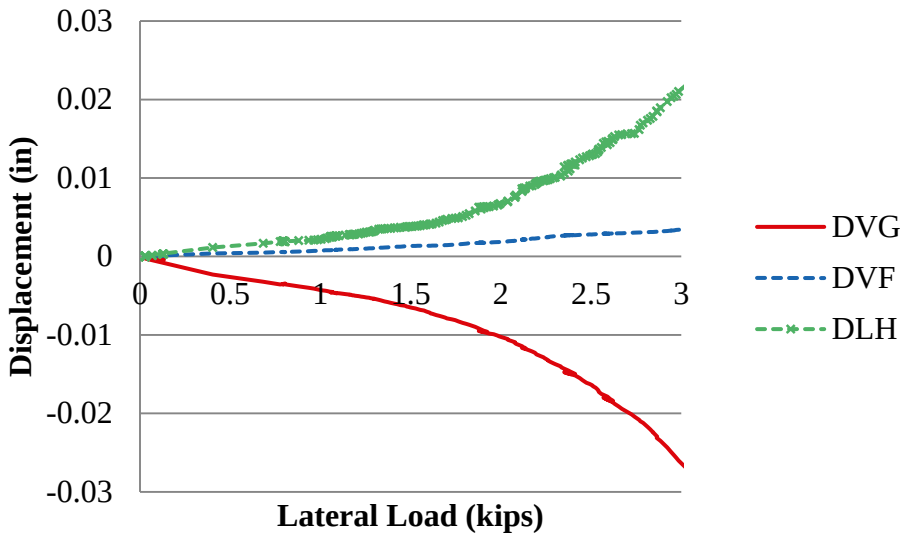

Figure 4.58 Rail Relative Deflections under Various Lateral Loads Applied by the PTLF

For static loading cases with a fixed L/V ratio of 0.5 applied by the SLTM loading head, the three deflection measurements are shown in **Figure 4.59**, which suggests that the maximum deflections were almost reached when the vertical applied force was really small (below 1 kips). This strange behavior was due to the nature of the SLTM loading head discussed in Section 3.8.1. As shown in **Figure 3.57**, the fixed gauge loading head applied up to 3 kips lateral force with almost no vertical load to both rails at the very beginning, then the lateral and vertical applied load started to increase simultaneously with a ratio approximately equal to its design value (0.5). **Figure 4.59** also reveals that the lateral applied load plays a big role in rail deflections, and how much the rail movement is affected by the vertical load applied at the same time is upon to be discovered in the testings with various L/V ratios (Section 4.3.2.2)

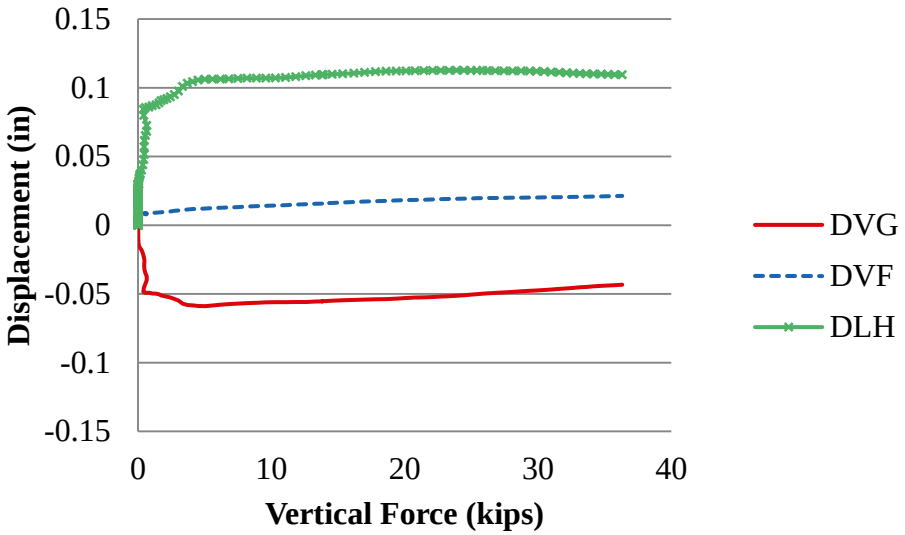

Figure 4.59 Rail Relative Deflections Under Various Loads with Fixed L/V (0.5) Applied by the SLTM Loading Head

Combining the rail deformation (strain) measured from both sides of rail with the three displacement measurements, the deformed shape of the rail cross-section was generated. **Figure 4.60** shows the deformation map of rail cross-section under the second loading case. For better visualization purpose, an amplification factor of 5 was used in this plot, generated with MATLAB using linear elastic theory. In **Figure 4.60**, the blue line shows the un-deformed shape and the red line shows the deformed shape of the rail cross-section. As the wheel load was not applied at the centerline of the rail base, "double curvature" can be seen at the rail web. The first curvature was found at the transition area between the rail head and the rail web due to the moment created by the eccentric loading. The second curvature was referred in the middle of the web due to the lateral force applied to the rail head.

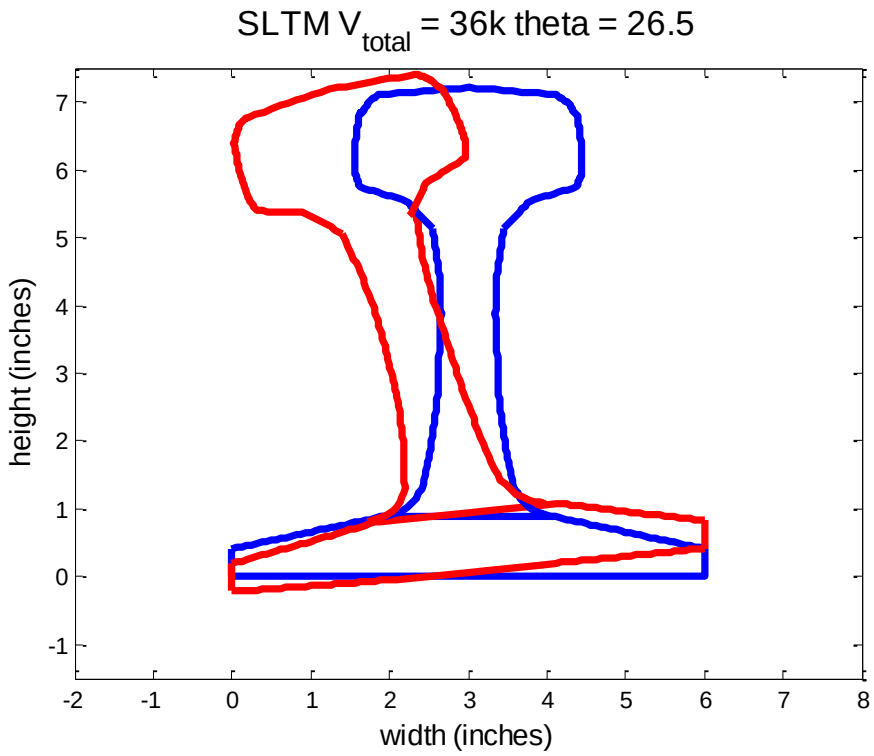

Figure 4.60 Deformed Shape of Rail Cross Section (L=18 kips, V=36 kips)

Similarly as discussed in Section 4.2.1.2, the rail base curvature was also calculated and shown in **Figure 4.61**. The x-axis shows the distance to the field side edge of the rail ("0" is for the field side edge, and "6" is for the gauge side). The "rigid deflection" was generated by drawing a line between the average displacement measurements from the field side and the gauge side.

Based on the two assumptions stated before in Section 4.2.1.3, a linearly distributed pressure from rail pad was expected. When the load applied to the rail was with the L/V of 0.5**,** the gauge side rail base saw uplift. During uplifting of the gauge side rail base, there was no reaction force in the area of the pad losing contact with rail. The gap between the bottom surface of rail base and the rail pad is shown in the load path map in **Figure 3.54**.

To validate such assumptions, the curvature at rail base was calculated from the strain measurements at the rail base. Strain gauges #1 - #3 in Section 4.2.1.2 at both of the field and gauge side were used for this analysis. From **Figure 4.61**, it can be seen that the rigid deflection of the rail base was close to the real (corrected) deflection. The maximum error was found at 1.875 inches from the field side edge, which was 0.00078 inches or 1.2% of the total deflection. And therefore, it is comfortable to use the rigid body movement as the deformation of rail base for simple, because the bending of the rail base was negligible and the rigid body assumption held. Similarly, when only lateral force was applied to either rail head or web, the curvature was found to be negligible.

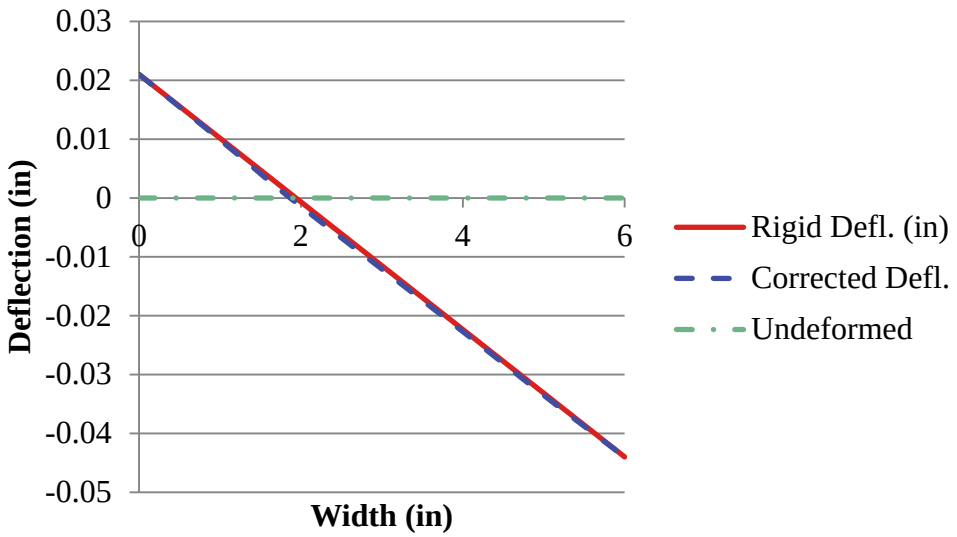

Figure 4.61 Deformed Shape of Rail Base (F_L=18 kips F_V=36 kips)

The change of the clamping forces at both the field and gauge sides was calculated using $N=k_cD$, where k_c is the clip stiffness, which was determined by the manufacturer to be 8.65 kips/in, and D is the vertical deflection at 0 and 6 inches from **Figure 4.59** for the field and gauge side clips.

For the two loading cases, the comparison of the applied rail seat vertical load, the calculated rail seat reaction force, and the calculated change of the clamping force are shown in **Table 4.6**. The magnitude of the change of the clamping force was much smaller than the vertical rail seat load (no more than 1.2%). When comparing the applied load with the calculated reaction force, the change of the clamping force could be neglected.

Table 4.6 Comparison of the Applied Load and the Calculated Reaction Force

Loading Case	Applied rail seat load (kips)	Rail seat reaction force (kips)	Δ clamping force (field side) (kips)	Δ clamping force (gauge side) (kips)
1 (PTLF)	0	0.7	-0.03	0.22
1 (GRMS)	0	0.11	-0.07	0.91
2	36	33.4	-0.18	0.38

Under loading case 2, when 36 kips vertical with 18 kips lateral load was applied, the calculated rail seat reaction force was 33.4 kips using the above theory, for which the error was 7.2%. This conclusion reveals that the rail base deflections can be used to calculate the vertical rail seat reaction force under static loading. But all the rail base vertical deflections measured from the four corners should be used, because uneven compression of rail pad may have been experienced.

4.3.1.3 Crosstie Global Displacement

Crosstie global displacements were measured by potentiometers in both vertical and lateral directions (**Figure 3.60**). Three vertical potentiometers were placed below rail seats and crosstie center; two lateral potentiometers were placed at both ends of the crosstie.

Three loading cases were examined (Section 3.8.1) and rail deflections are presented in **Table 4.7**.

Table 4.7 Crosstie Global Displacements for Various Loading Cases

Loading	Case 1		Case 1		Case 2	
	Lateral load		Lateral Load		Lateral & Vertical Load	
	L	V	L	V	L	V
	PTLF	--	GRMS	--	Overhead frame	Overhead frame
	3 kips	--	3 kips	--	18 kips	36 kips
D_{V1} (in)*	--		--		-0.027	
D_{V2} (in)*	0.003		0.028		0	
D_{V3} (in)*	--		--		-0.042	
D_{L1} (in)**	-0.001		-0.001		0.052	
D_{L2} (in)**	0.004		0.023		0.048	

* positive pointing downward, negative pointing upward

** positive pointing towards field side

With reference to Case 1 with the GRMS in **Table 4.7**, it can be found that under 3 kips lateral load applied to both rail heads, the elongation of the crosstie was 0.024 inch, which was about 0.02% of the crosstie length. Due to the bending action caused by the eccentric lateral loading, the crosstie center was raised up, the vertical deflection was 0.028 inch. It should also be noticed that, vertical deflections of the crosstie could also be affected by the stiffness of the support (ply-wood pad with the SLTM testing), the value should rather be used to qualify than quantify the crosstie deformation. With reference to Case 2, when 36 kips vertical and 18 kips lateral load applied to rail head on both sides, the elongation of the crosstie was 0.1 inch, which was about 0.1% of the crosstie length.

Because a plywood pad was used as support, the measured crosstie vertical deflections were mostly contributed by the compression of the wood pad. The stiffness of the plywood could be much different than that of the ballast, and thus, the crosstie displacement couldn't be used for comparison.

4.3.1.4 Change of Clamping Force

The change of clamping force was found to be really small that can be ignored to the vertical load path, for details see Chapter 5.

4.3.2 Lateral Load Path in Multi-crosstie and Fastening System in Laboratory Experiment

In multi-crosstie system, the lateral load path analysis is consisted by the lateral load application, how the lateral load affects the reaction force of each contact surface, as well as rail and crosstie displacements. Experiments of multiple-crosstie and fastening system were operated with the TLS, the instrumentation map is shown as **Figure 3.62**.

4.3.2.1 Lateral Wheel Load Application

With the TLS, lateral axle loads up to 24 kips were applied in conjunction with certain vertical loads (Section 3.8.3) by a hydraulic pump to the center of the axle **(Figure 4.26)**. Because of the uncertainty of wheel-rail contact conditions and frictions between surfaces, the actual lateral force going through each rail needed to be measured. Lateral loads (F_L) were measured by strain gauge bridges shown in **Figure 3.24**. As discussed in Section 4.2.2.1, the lateral component of the vertically applied axle load may also contribute to the force measured from the rail bridge. The lateral load measured from each instrumented rail seat at the near rail is shown in **Figure 4.62**. The greatest lateral load was found over rail seat 4, which was even higher than the load

applied by the hydraulic pump. The lateral load going through the other four locations was found varying in a narrow bend, from 11.4 kips (rail seat 5) to 17.9 kips (rail seat 7).

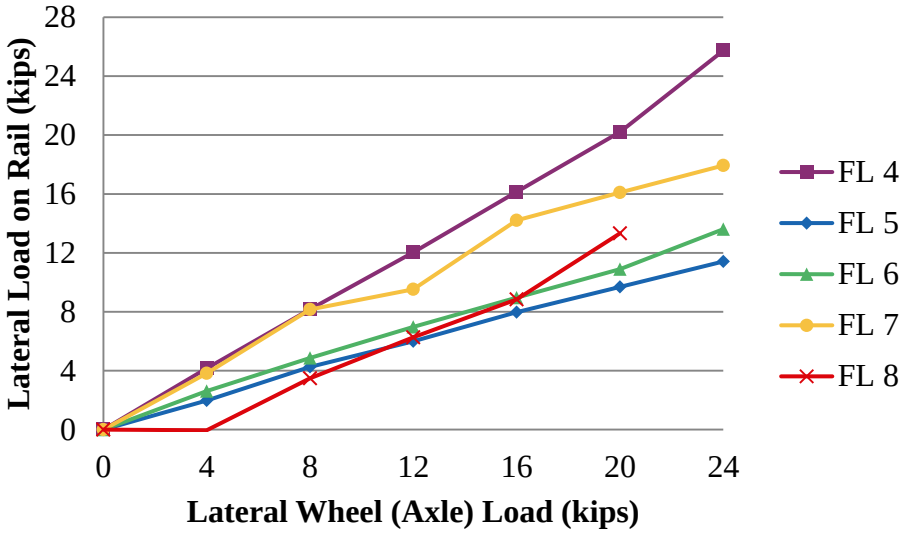

Figure 4.62 Lateral Component of the Wheel Load Applied Above Each Crosstie (V=40 kips, L=0 – 24 kips)

4.3.2.2 Rail Seat Reaction Load

As used in Section 4.2.2.2, embedment strain gauges installed 2 inches below the rail seats and vertical rail bridges installed on the rail were used to measure the reaction force of each rail seat. Under a certain vertical load, the change of rail seat reaction force was found very small corresponding to various lateral loads. **Figure 4.63** gives an example of the rail seat reaction forces under 40 kips vertical and 0 – 24 kips lateral forces. The maximum change was found at rail seat 17, which dropped from 19 kips (with no lateral force) to 13.5 kips (with 24 kips lateral force).b The change of reaction forces measured from the other rail seats was found no more than 2.5 kips.

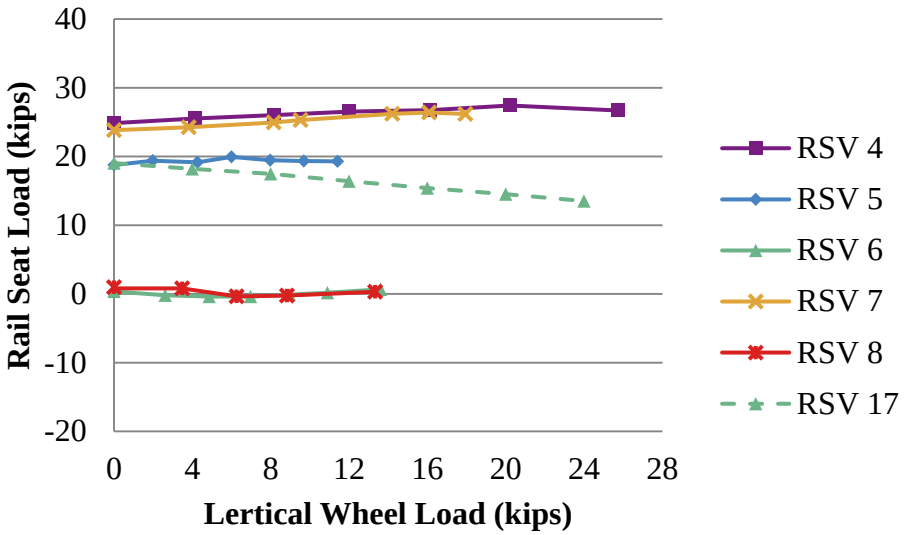

Figure 4.63 Reaction Load for Rail Seat Directly Below the Wheel Set Measured by Embedment Strain Gauges (V=40 kips)

4.3.2.3 Rail Seat Pressure Distribution

This section presents the distribution of rail seat pressure recorded by the MBTSS (Greve et al 2014). **Figure 4.64** compares the qualitative effect of the ratio of lateral load to vertical load. It is very obvious that the rail seat pressure tend to shift towards the field side when increasing the lateral wheel load. And the maximum pressure was found approximately 0.5 inch from the edge at field side, with a magnitude of 6,000 psi when the L/V ratio was 0.5.

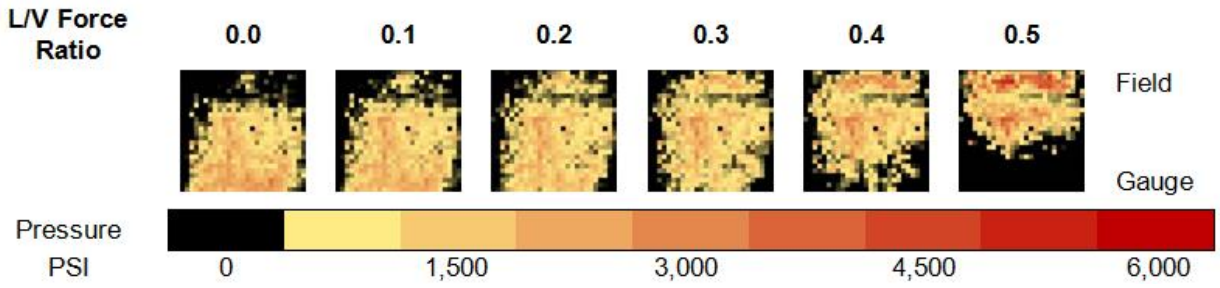

Figure 4.64 Comparison of Rail Seat Pressure Distributions (V=30 kips) (Prepared by Matthew Greve)

4.3.2.4 Lateral Load Going Through Shoulder

The lateral load applied to each rail head was balanced by the shoulder face lateral reaction and rail seat friction force. The lateral force going through each shoulder was directly measured (Section 3.5.4). **Figure 4.65** shows the lateral load going through each shoulder when the wheel set was placed directly above that crosstie. Generally, a small portion of lateral force was found flowing through the shoulder, which was between 11% (at rail seat 6) and 28% (at rail seat 5). Except the field side shoulder at rail seat 5, the shoulder lateral reaction force increased smoothly corresponding to the growth of lateral wheel load. The discontinuity shown in the curve for the shoulder at rail seat 5 was possibly due to the relative movement between wheel and rail as well as between rail and concrete, which was observed during the loading process.

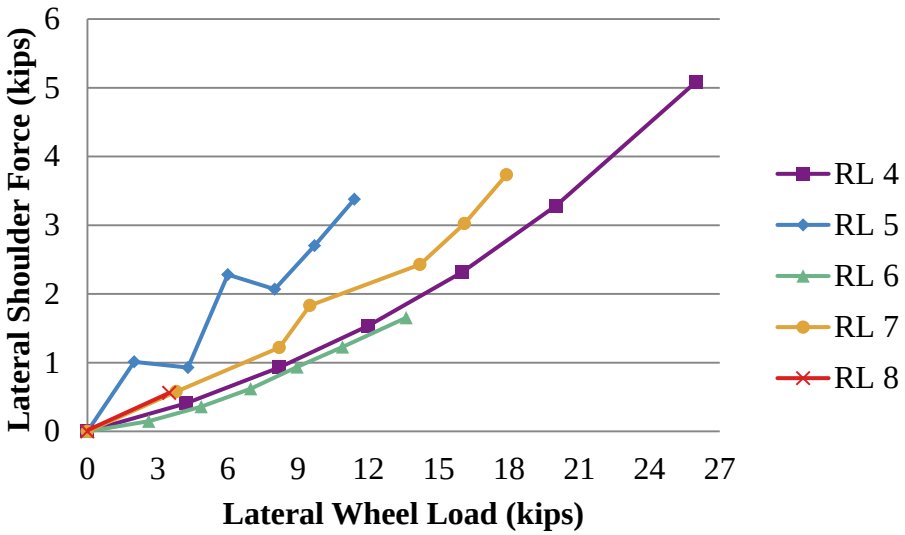

Figure 4.65 Change of Lateral Load Going Through Shoulder Under 40 kips Vertical and Various Lateral Load Directly Applied over Each Crosstie

Under a known lateral applied load, the distribution of shoulder lateral reaction force is given in **Figure 4.66**. 40 kips vertical load was applied by actuator to each rail, while the lateral load was being applied gradually. As discussed before, because of the poor support below rail seat 6, the lateral load transferred through the shoulder of this rail seat was even lower than its adjacent rail seat (rail seat 7). The total lateral force went through all the five instrumented shoulder (data from shoulder beam insert located at rail seat 4 was lost, however, the lateral force transferred at two crosstie spacing away was usually found small) was also shown in **Figure 4.66**. When 14 kips lateral force was applied above the center crosstie 6-17, the total force flowing through the five instrumented shoulders was found as 5.4 kips (38.6%). The rest 8.6 kips load was balanced by the frictions between rail and concrete.

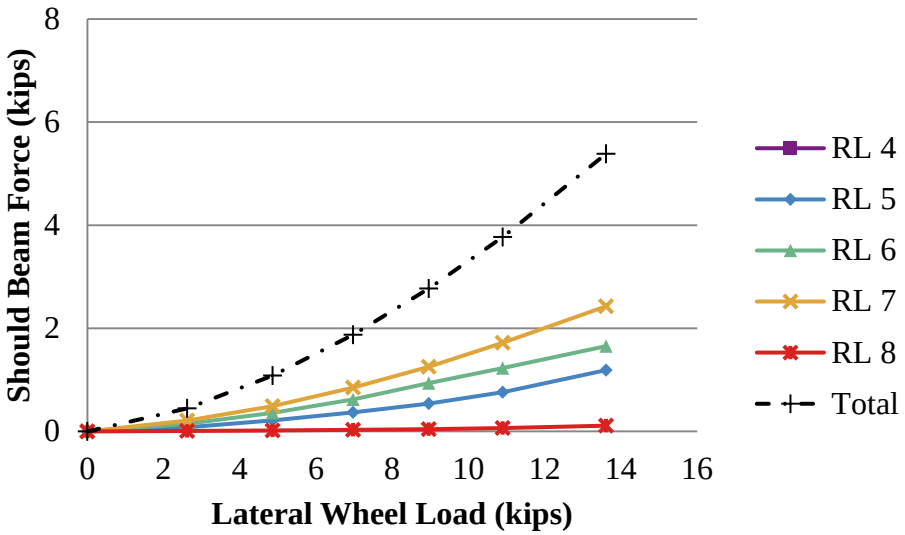

Figure 4.66 Change of Lateral Load Going Through Each Shoulder Under 40 kips Vertical and Various Lateral Load Applied over Crosstie 6-17

4.3.2.5 Rail Relative Deflections

When a lateral load was applied over a certain vertical load, both the vertical and lateral rail deflections were affected. When the lateral load was pushing the rail head towards the field side, it is equivalent to move this lateral force to the rail rotation center and apply a moment which is obtained by multiplying the force with the distance. Because of this action, the rail movement can be treated as the superposition of a lateral translation and a rigid body motion of rotation (the compression deformation and bending curvature of rail can be negligible based on discussion in Section 4.2.2.5). This is also demonstrated by the vertical rail base deflections measured from field and gauge side shown in **Figure 4.67** and **Figure 4.68**.

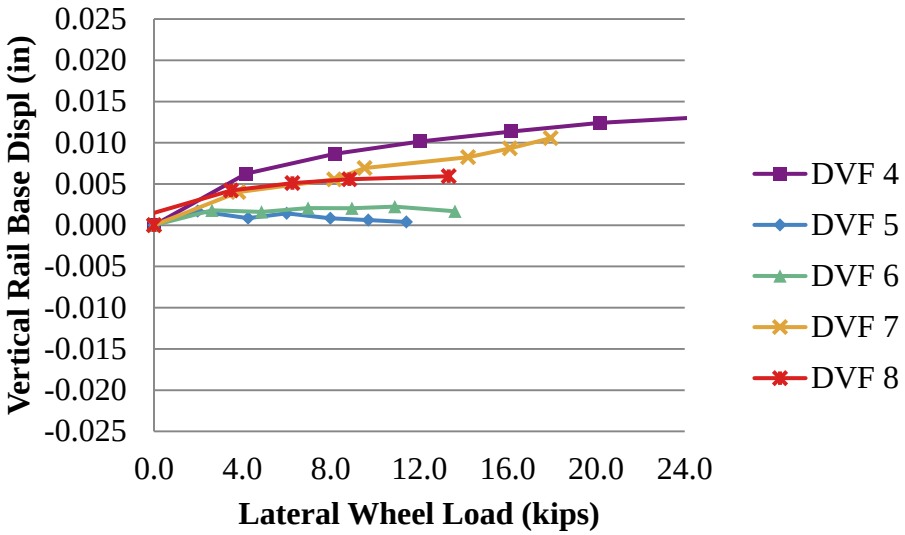

Figure 4.67 Rail Base Vertical Deflections at Field Side Under 40 kips Vertical and Various Lateral Wheel Load Directly Applied over Each Crosstie

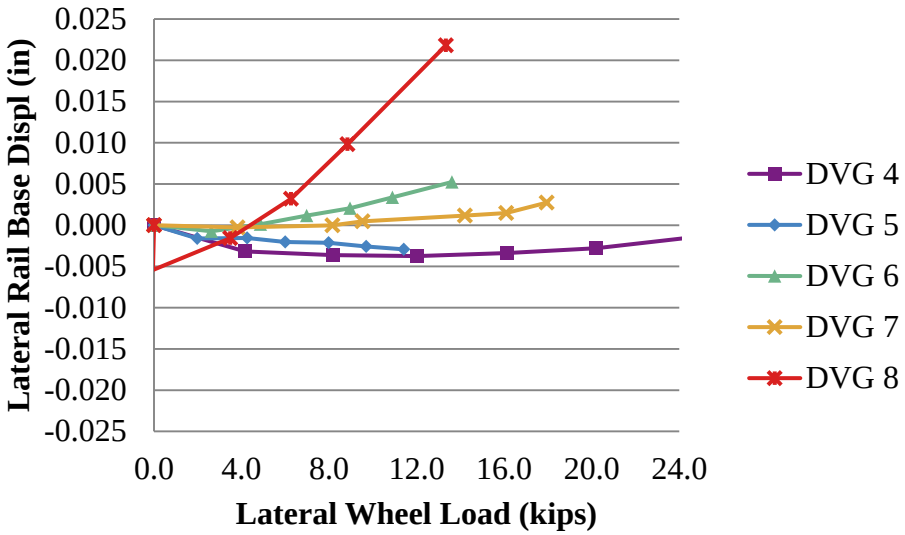

Figure 4.68 Rail Base Vertical Deflections at Gauge Side Under 40 kips Vertical and Various Lateral Wheel Load Directly Applied over Each Crosstie

The lateral deflections measured from rail web and rail base were also very small (**Figure 4.69** and **Figure 4.70**). It was found that the lateral deflections measured from both rail base and

web were pointing toward field side. In addition, the lateral web deflections were slightly higher than the lateral base deflections. For example, with maximum lateral load (26 kips), the lateral deflection measured from rail base at rail seat 4 was 0.025 inch, while the value measured from rail web at the same location was 0.033 inch. The higher value measured from the rail web was resulted by the rail rotation.

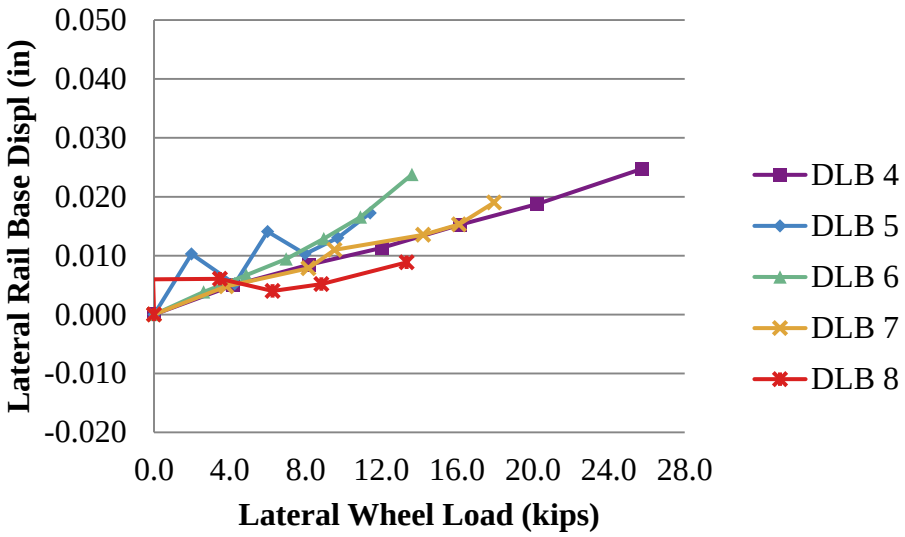

Figure 4.69 Rail Base Lateral Deflections at Gauge Side Under 40 kips Vertical and Various Lateral Wheel Load Directly Applied over Each Crosstie

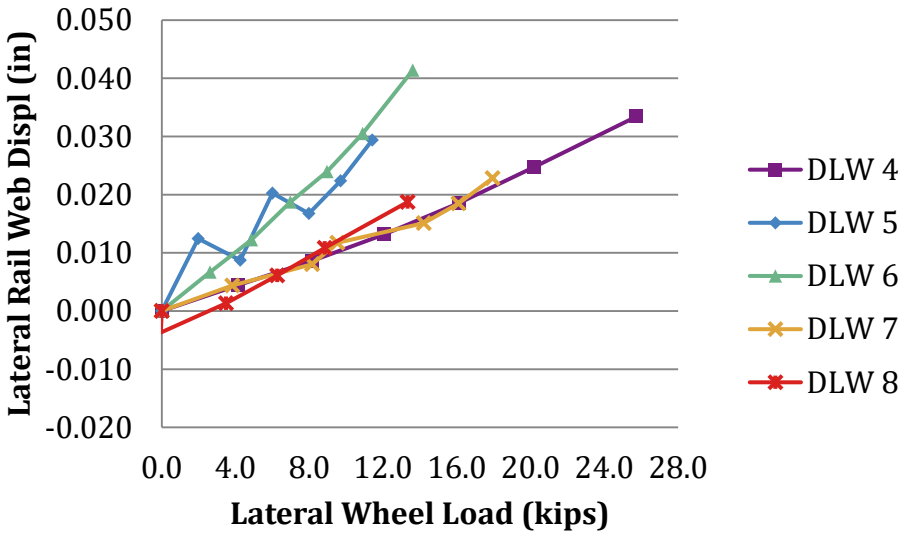

Figure 4.70 Rail Web Lateral Deflections at Gauge Side Under 40 kips Vertical and Various Lateral Wheel Load Directly Applied over Each Crosstie

4.3.2.6 Crosstie Global Displacements

Vertical and Lateral crosstie global displacements are shown in **Figure 4.71 and Figure 4.72**. The existence of lateral force resulted in all the crossties dipping downward and shifting towards the near side globally.

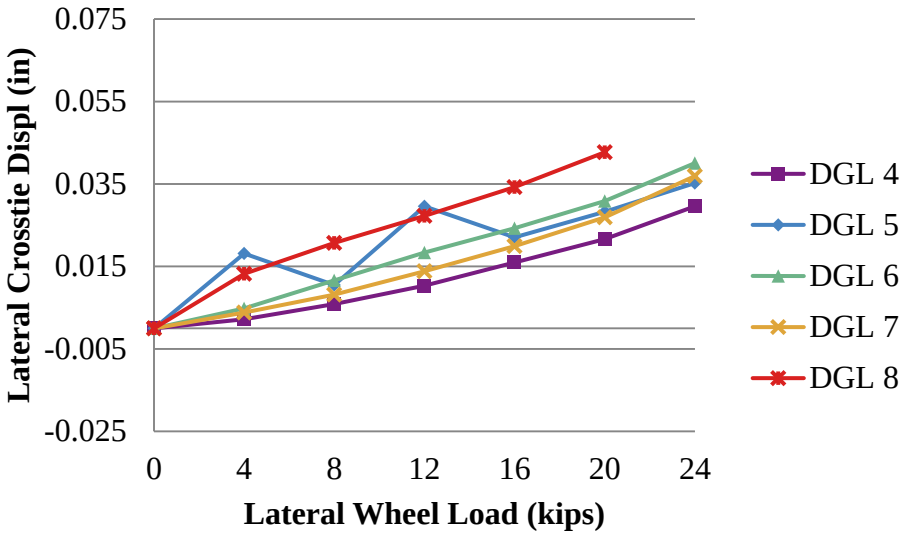

Figure 4.71 Vertical Crosstie Global Displacements Under 40 kips Vertical and Various Lateral Wheel Load Directly Applied over Each Crosstie

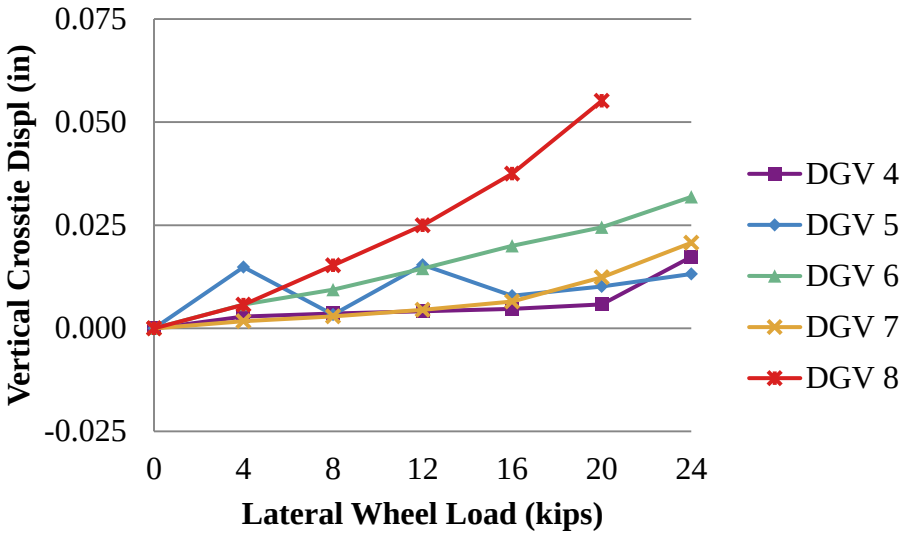

Figure 4.72 Lateral Crosstie Global Displacements Under 40 kips Vertical and Various Lateral Wheel Load Directly Applied over Each Crosstie

4.3.2.7 Change of Clamping Force

The change of clamping force will be discussed in detail in Chapter 5.

4.3.3 Lateral Load Path in Full-Scale Field Experiment

Full-scale field experiments were operated in RTT and HTL in the TTC, CO (**Figure 4.41**). Because static loading in both vertical and lateral directions were applied by actuators installed on the TLV, the test results were not affected by the track curvature or super elevation. In this condition, tests operated at HTL can be treated as duplicated tests at RTT.

4.3.3.1 Lateral Wheel Load Application

Lateral loads with the same magnitude were applied to both rails (**Figure 4.73**), which were directly output from load cells installed on the hydraulic actuators instead of rail bridges. The actuators providing lateral load to the wheel is circled in the figure. For both tangent track (RTT) and curved track (HTL), static wheel loads were applied over each instrumented rail seat as well as over the center of crib between each pair of instrumented rail seats. In 2012 testing, the data was zeroed for all sensors at 5 kips vertical load. Under this situation, the 5 kips vertical applied load should be taken as a pre-loading, and all rail seat loadings recorded in 2012 increased from 5 kips.

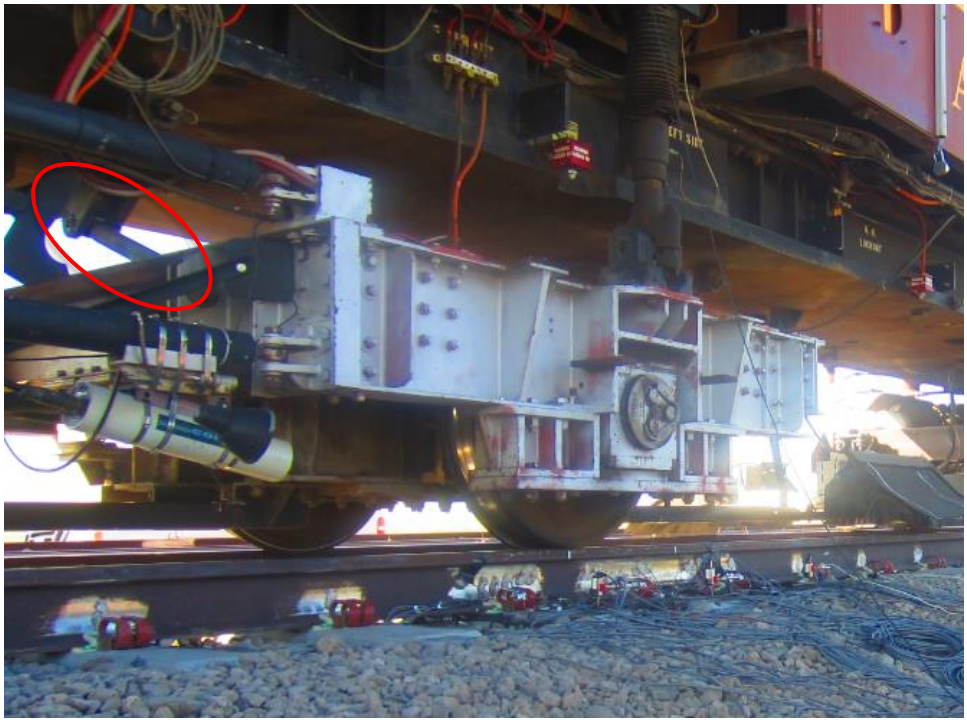

Figure 4.73 Lateral Wheel Load Applied by Hydraulic Actuators

4.3.3.2 Rail Seat Vertical Reaction Load

Same as used in multi-crosstie laboratory experiments (Section 4.2.2.1), both embedment strain gauges (Section 3.5.3) and vertical rail bridges (Section 3.5.1) were used to measure the vertical load transfer from rail to each rail seat.

To examine the influence of the lateral wheel load on rail seat loading, only vertical load was applied gradually at the beginning; and once the vertical wheel load reached 40 kips, it was held constant and the lateral wheel load was increased till 20 kips. **Figure 4.74** and **Figure 4.75** show the change of rail seat loading under 40 kips vertical load with various lateral forces.

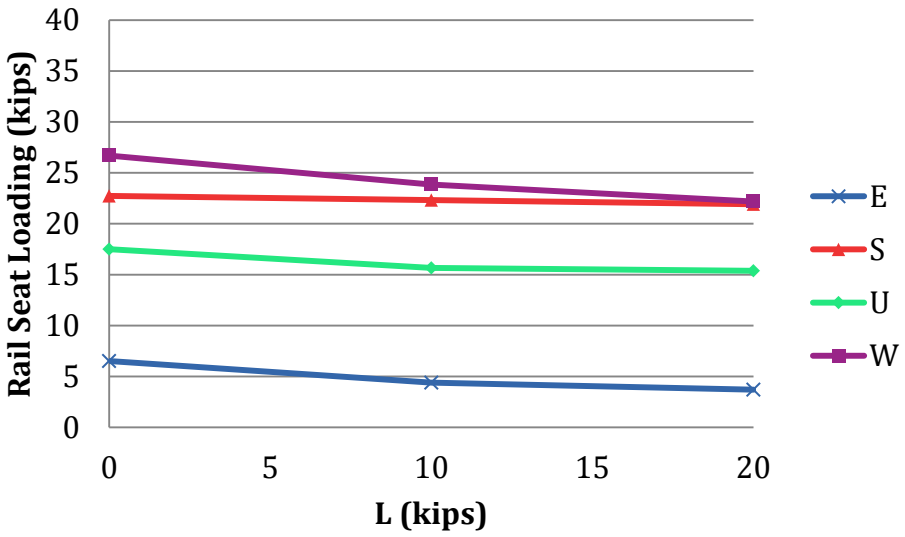

Figure 4.74 Rail Seat Loading Under Various Lateral Wheel Loads at RTT (2012)

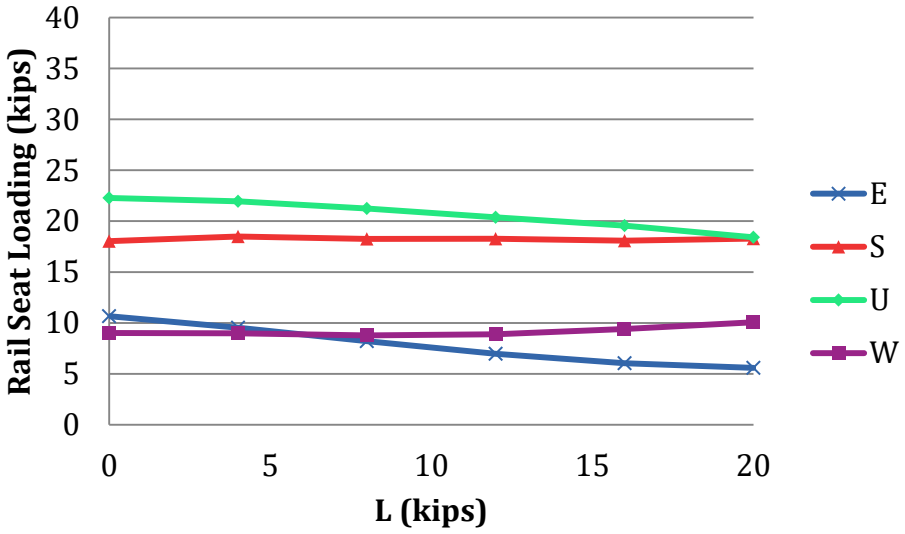

Figure 4.75 Rail Seat Loading Under Various Lateral Wheel Loads at RTT (2013)

Figure 4.74 and **Figure 4.75** reveal the rail seat loading was not significantly affected by lateral wheel load. In 2012 testing (**Figure 4.74**), the greatest variation took place at rail seat W, which was 26.7 kips with 0 kips lateral load, and 22.2 kips with 20 kips lateral load. In 2013 testing (**Figure 4.75**), the greatest variation took place at rail seat E, which was 11.9 kips with 0

kips lateral load and 6.2 kips with 20 kips lateral load. Some rail seats, for example rail seat S and W in 2013, experienced an almost constant reaction force when lateral force was applied.

From the analysis of the HTL data, similar trends were seen, with lateral load application resulting in a slight decrease in rail seat loading. The greatest change took place at rail seat U in 2012 testing, which decreased from 19.4 kips to 13.8 kips; for all other rail seats, the change was below 3 kips.

Figure 4.76 and Figure 4.77 show the distribution of vertical force over three adjacent rail seats below the wheel set (when wheel was placed above crosstie EU) due to 40 kips vertical load with various lateral forces.

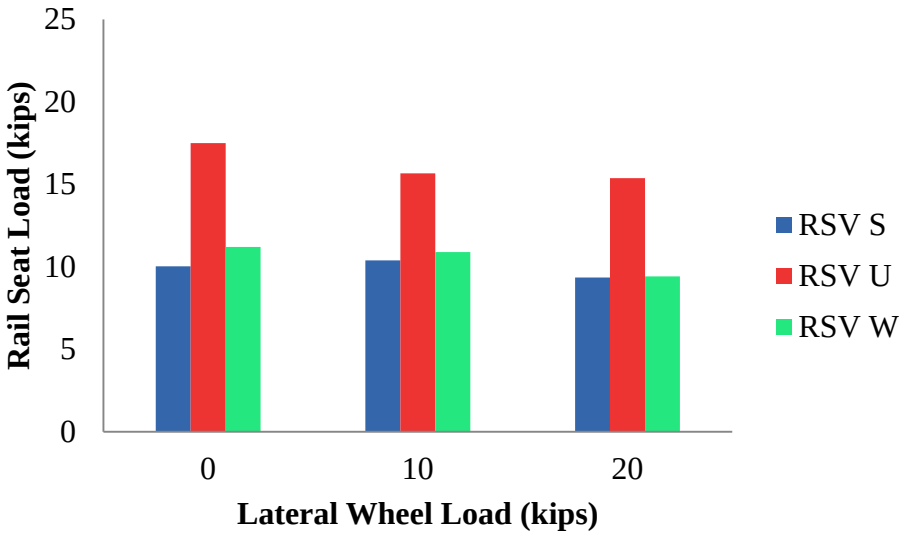

Figure 4.76 Rail Seat Load Distribution Under Various Lateral Wheel Loads Applied over Crosstie EU at RTT (2012)

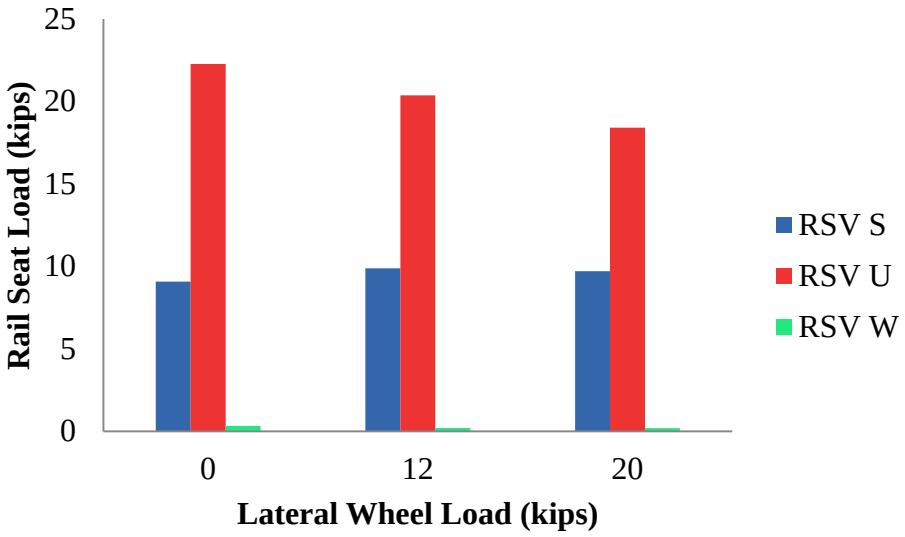

Figure 4.77 Rail Seat Load Distribution Under Various Lateral Wheel Loads Applied over Crosstie EU at RTT (2013)

There is a trend found from both figures that rail seat loading which was measured directly under the wheel set slightly decreasing with increasing lateral load. Comparing the testing results from 2012 and 2013, it could be found, when one of the adjacent rail seat below wheel set was not fully engaged, more load was transferred to the rail seat immediately below it. When all the three rail seats below the wheel were fully engaged (**Figure 4.76**), the summation of vertical reaction forces was about 40 kips which was equivalent to the vertical applied load; when one of the three rail seat was not engaged (rail seat W in **Figure 4.77**), the summation of vertical reaction forces was barely over 30 kips, which can be deduced that some force was transferred to rail seat beyond one crosstie spacing away.

Ultimately, these results cannot speak decisively about the distribution of rail seat load for all kinds of track conditions. It supports the conclusion that lateral load ultimately does not drastically affect rail seat loading, and thus the current statement in AREMA that 50% of vertical load is transferred to the rail seat is reasonable when all the three rail seats below the wheel were

fully supported, regardless of the presence of lateral load. Since only three ties were instrumented there is not a definitive answer to the width of the lateral load distribution amongst ties. However, this data again illustrates the extreme importance that support conditions have on load distribution. Rail seats with solid contact would be loaded first, hanging rail seats start taking load after the gap closure. Contact needs to be made with ballast before any load bearing can occur. This is clearly seen from the above discussion, rail seat S gained reaction force from the beginning due to good initial contact with ballast; whereas seat W barely gained any load because it has never been forced into a good contact with ballast (**Figure 4.77**).

4.3.3.3 Rail Seat Pressure Distribution

Lateral wheel load played an important role in rail seat pressure distribution (**Figure 4.78**) (Greve et al 2014). When 40 kips vertical with no lateral load being applied, the rail seat pressure distributed almost evenly over the entire rail seat. Due to increasingly lateral load being applied, **Figure 4.78** shows a clear trend that the rail seat pressure shifted towards the field side. Under 40 kips vertical with 20 kips lateral load it can be observed, that a significant portion of the rail seat was completely unloaded. A concentration of forces on the field side was observed while the gauge side of the rail seat was not engaged. By counting the area with pressure distributed overt it, only 58% of the rail seat area was loaded corresponding to the maximum lateral load (20 kips).

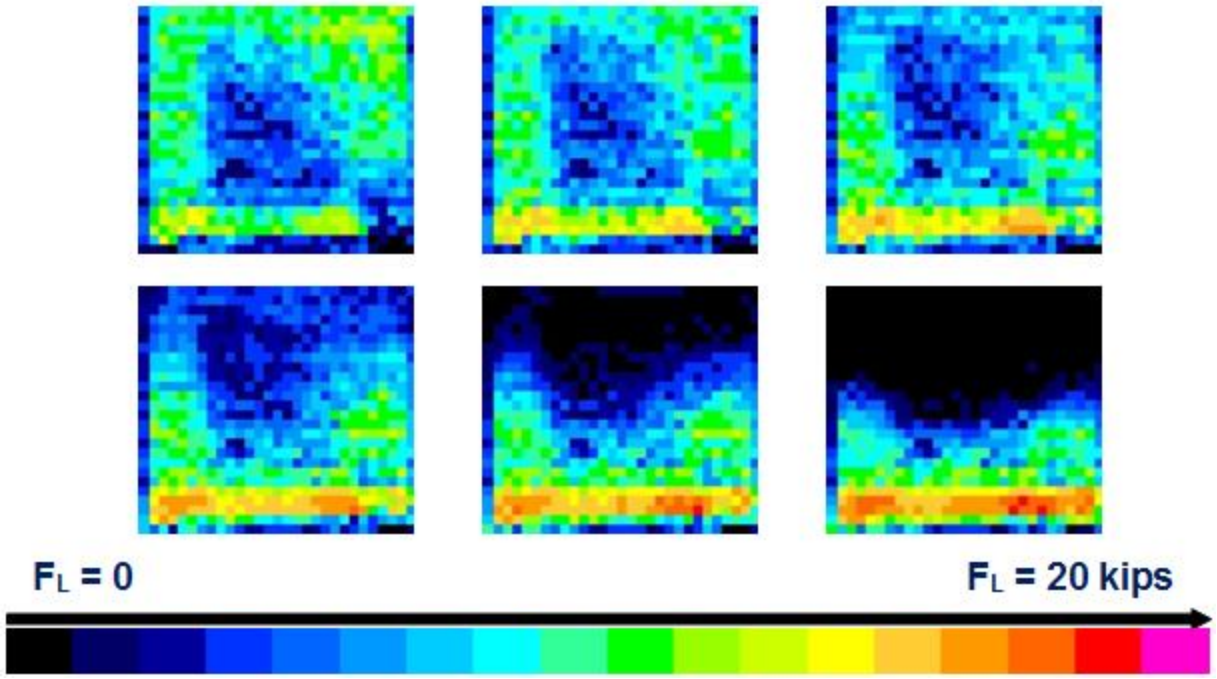

Figure 4.78 Rail Seat Pressure Distribution Under 40kips Vertical Load and Various Lateral Load (0, 4, 8, 12, 16 and 20kips) (Prepared by Matthew Greve)

4.3.3.4 Lateral Force Going Through Shoulder

Under 40 kips vertical and various lateral applied loads, the change of the measured lateral force transferred to shoulder is shown in **Figure 4.79**. The increasing of rail seat B, C and S was almost linear from the beginning; however, for rail seat E and U, the increasing started to become linear only when the lateral force was above 12 kips. This observation suggests that, there might be an initial gap between the shoulder and insulator or between insulator and rail base, and a certain amount of lateral force is required to close up this gap.

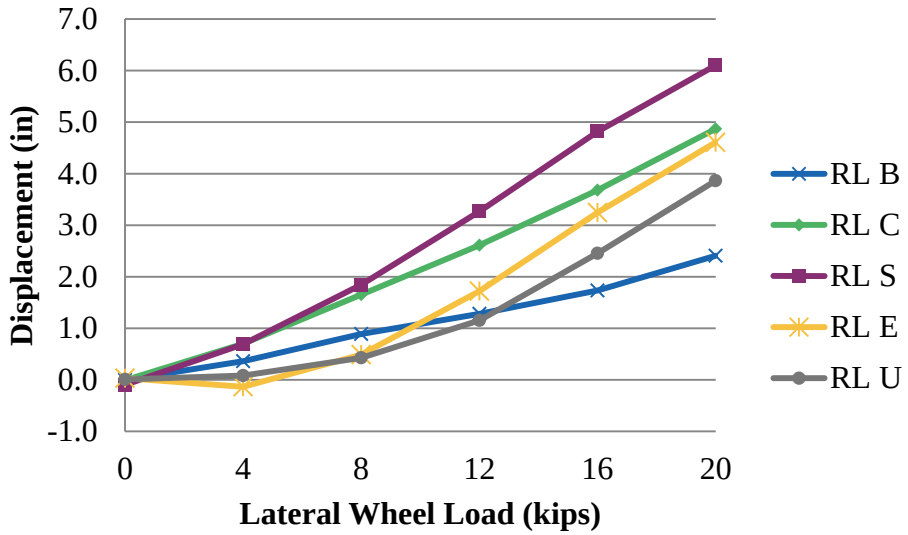

Figure 4.79 Shoulder Lateral Reactions Under Various Lateral Load at RTT (2013)

Figure 4.80 shows the average magnitude of the lateral force measured from the instrumented shoulders under a given lateral wheel loads with a constant 20 kips or 40 kips vertical wheel load applied by the TLV directly over the specified rail seat.

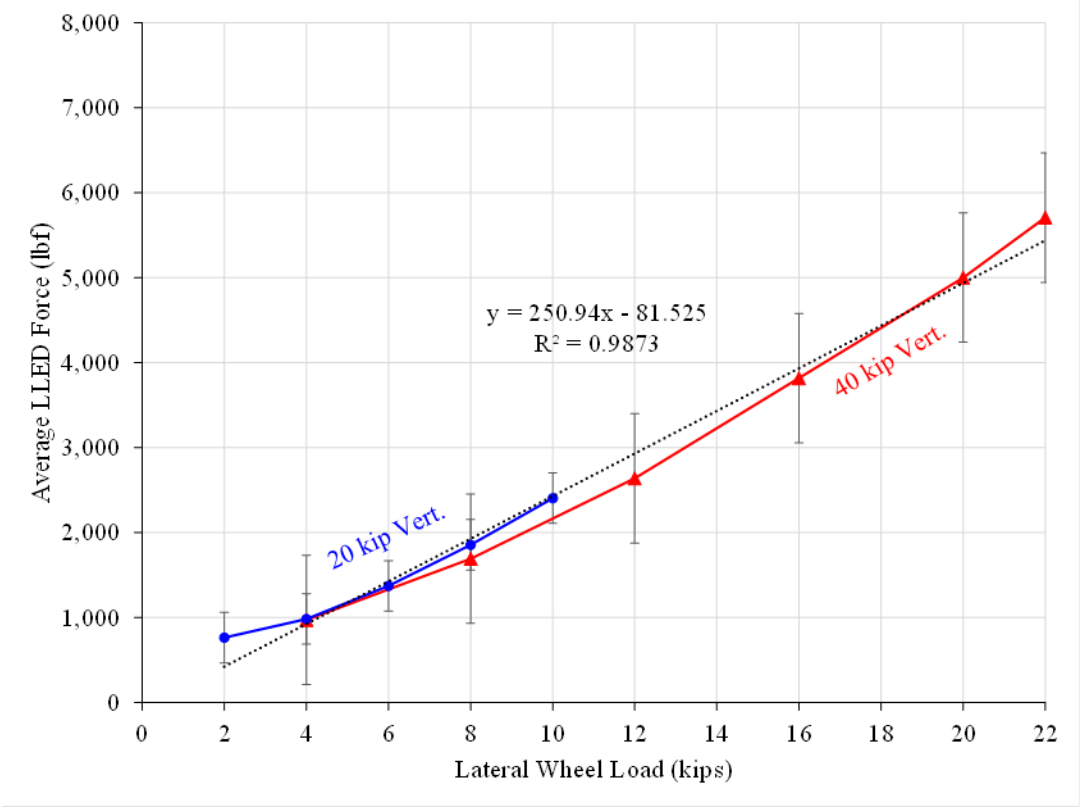

Figure 4.80 Average Shoulder Lateral Reaction Force Under 40 kips Vertical and Various Lateral Loads (Prepared by Brent Williams)

The average shoulder lateral reaction force from static TLV loading was plotted against various lateral wheel loads under a constant 20 kips and 40 kips vertical wheel load to determine the load transfer characteristics of the system (**Figure 4.75**). As lateral wheel loads increased, the average shoulder lateral reaction force on the rail seat directly beneath the point of loading increased linearly. As can be found from the linear trend line, approximately 25% of the lateral applied load was transferred to the shoulder at the loading rail seat. Similar percentage of later load was found transferred to the shoulder under 20 kips and 40 kips vertical load.

From laboratory experiments (Section 4.3.2.4), notable lateral force transferred to shoulder was found from three crossties, which included the crosstie immediately below the

wheel set and two adjacent ones. If we assume it also applied to field environment, it could be roughly concluded as 50% of lateral applied load was balanced by shoulder reaction, and the other 50% was transferred through the frictions (Williams et al, 2014).

4.3.3.5 Rail Relative Deflections

As moving down the load path, the load from the rail base is exerted on the pad assembly below. The pad assembly which is sandwiched between the rail base and rail seat below it, experiences a compressive force. While holding on a certain vertical and increasing the lateral input force, the rail starts to rotate and translate towards the field side. Under a 40 kips vertical load with various lateral loads, the three rail deflections measurements relative to concrete crosstie are shown in **Figure 4.81**, **Figure 4.82** and **Figure 4.83**. For all the four instrumented rail seats, the gauge side rail based was raised up during the lateral load application, which increment varied between 0.009 inch (rail seat U) to 0.020 inch (rail seat E). In addition, a slight strain hardening was found correlated with all the four curves.

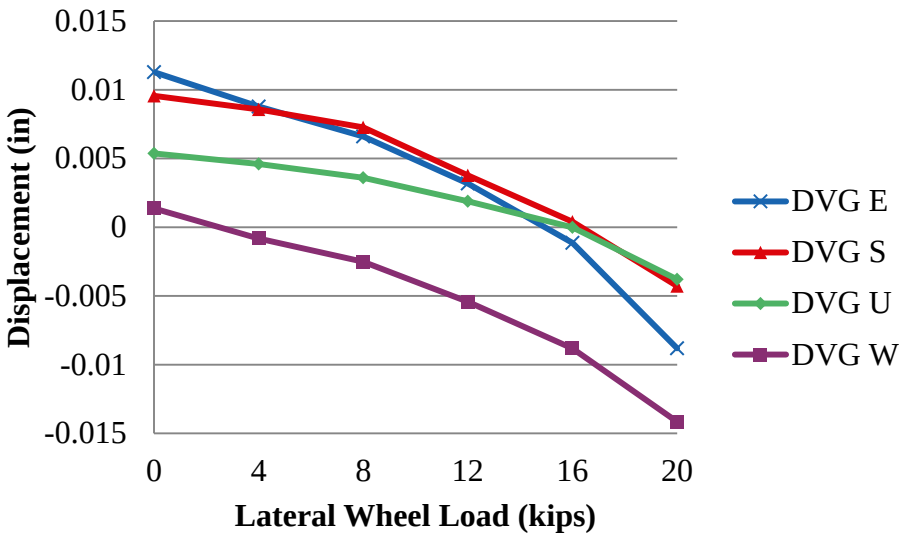

Figure 4.81 Gauge Side Vertical Rail Deflection Under Various Lateral Load at RTT (2013)

The trends shown in lateral deflections measured from rail web (**Figure 4.82**) and rail base (**Figure 4.83**) are very similar: the rail at all the four instrumented locations translated towards the field side, the increment varied in a narrow band under the same lateral applied load. In addition, the lateral deflections at rail web were found greater than at rail base, which was caused by the rail rotation due to the lateral wheel loads.

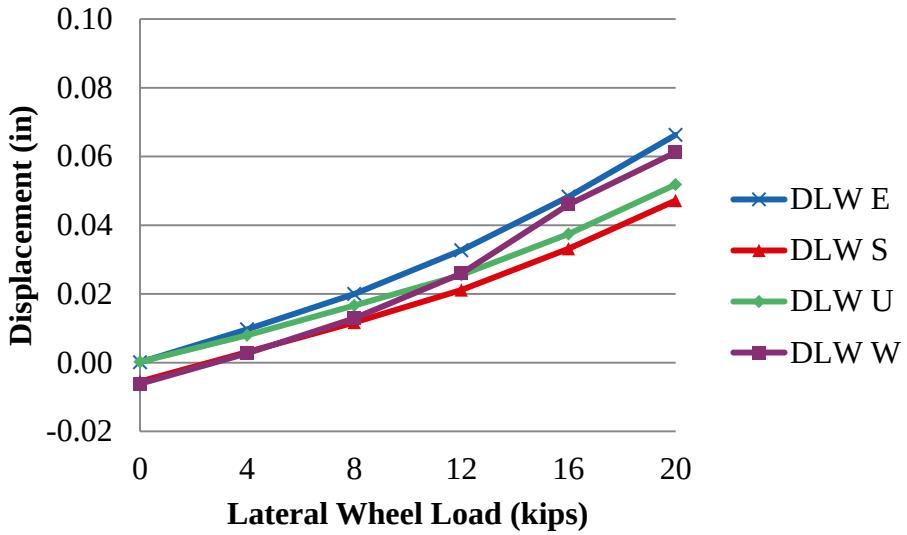

Figure 4.82 Gauge Side Lateral Rail Web Deflection Under Various Lateral Loads at RTT (2013)

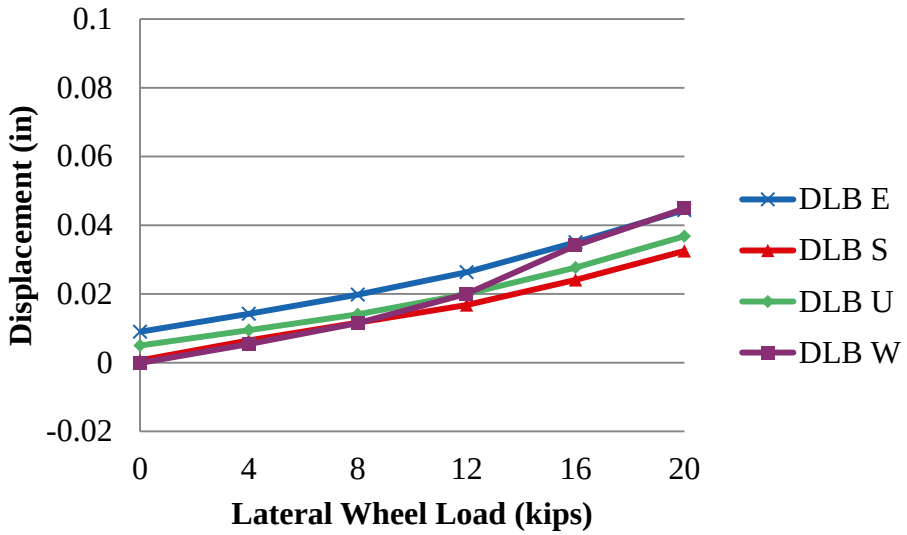

Figure 4.83 Gauge Side Lateral Rail Base Deflection Under Various Lateral Loads at RTT (2013)

4.3.3.6 Crosstie Global Displacement

While holding on 40 kips vertical wheel load and applying the lateral load to both rails gradually, the crosstie global displacements measured from all locations were found increasing slightly (**Figure 4.84**). This was caused by the bending action of crossties under the eccentric lateral load. Due to the elongation of crosstie under the lateral input load (because the lateral wheel load was applied by two lateral actuators both pointing towards the field side), the global lateral displacements were found increased too (**Figure 4.85**). However, this couldn't be used to compare with the dynamic data, because in reality, it is impossible to have notable positive lateral load applied to both rails at the same time.

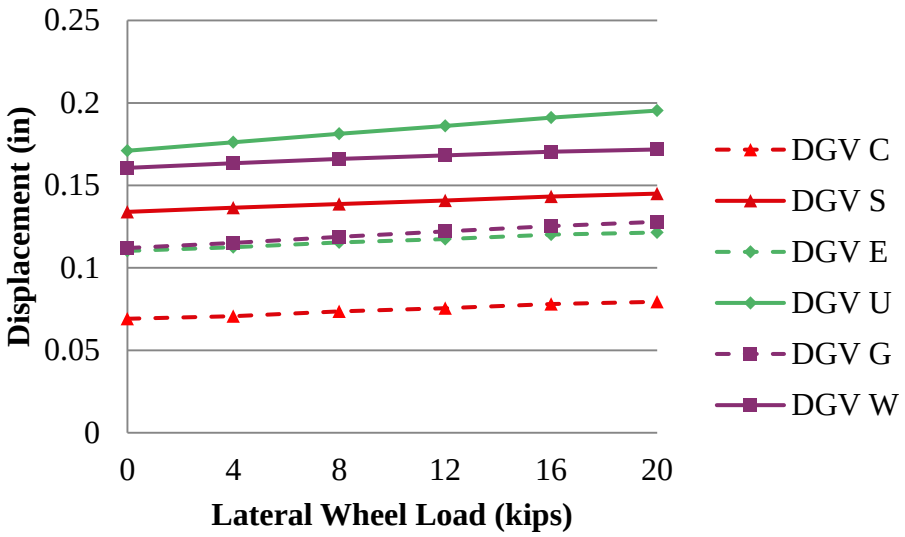

Figure 4.84 Crosstie Global Vertical Displacement Under Various Lateral Loads at HTL (2012)

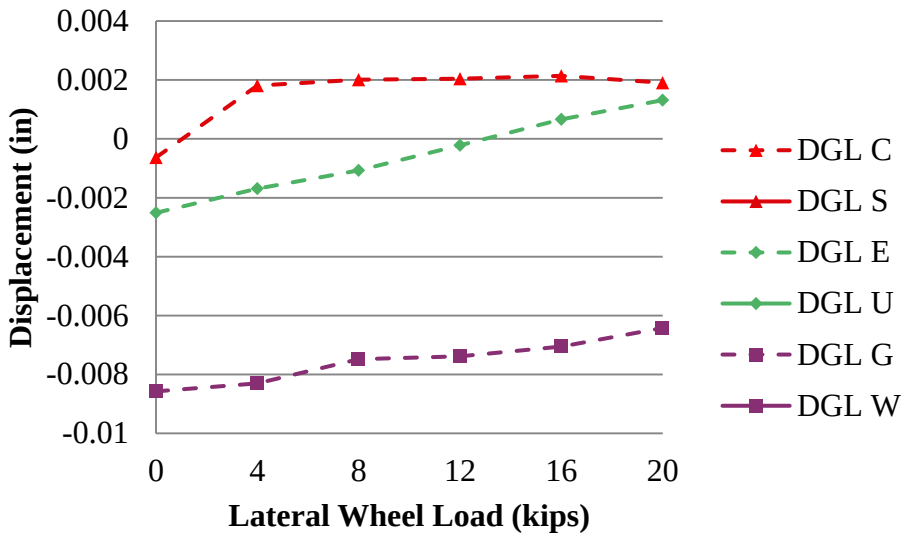

Figure 4.85 Crosstie Global Vertical Displacement under Various Lateral Loads at HTL (2012)

4.4 Vertical Load Path Under Dynamic Loading

Vertical load path under dynamic loading was examined both in laboratory and field experiments. In laboratory, cyclical loading was applied to rail with the TLS. In field testing, the effect of dynamic wheel loads caused by train passage was examined.

4.4.1 Vertical Load Path in Multi-crosstie Laboratory Experiments

In laboratory, under cyclical vertical loading (with 50 loading cycles ranged from 0 to 40 kips), a hysteresis loop was observed for the vertical deflection measurements from both the field and the gauge side (**Figure 4.86**). The area of the loop represents the energy dissipation. **Figure 4.86** presents the hysteresis loop found at vertical rail base displacements, and similar situation was found from other measurements. The energy dissipation found from crosstie global displacement was even more significant (**Figure 4.87**)

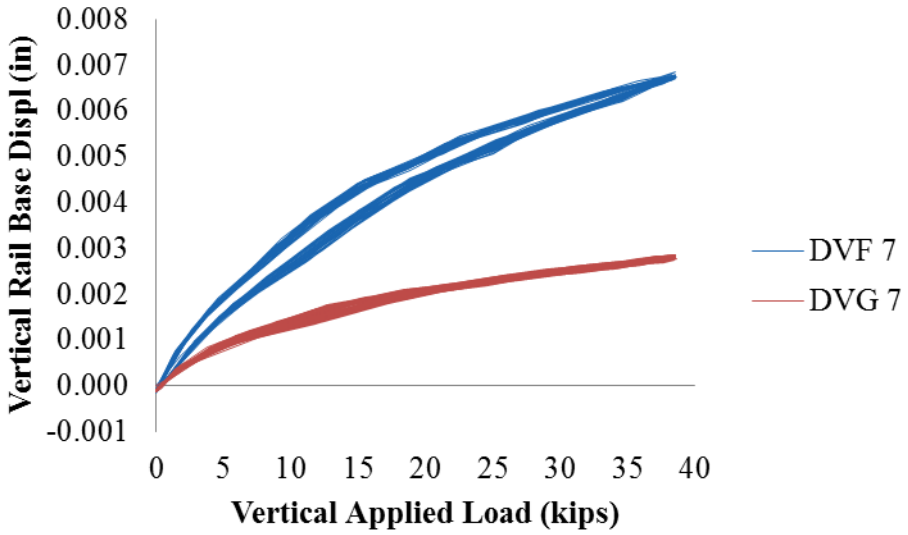

Figure 4.86 Vertical Displacements at Field/Gauge Side Under Cyclical Loading

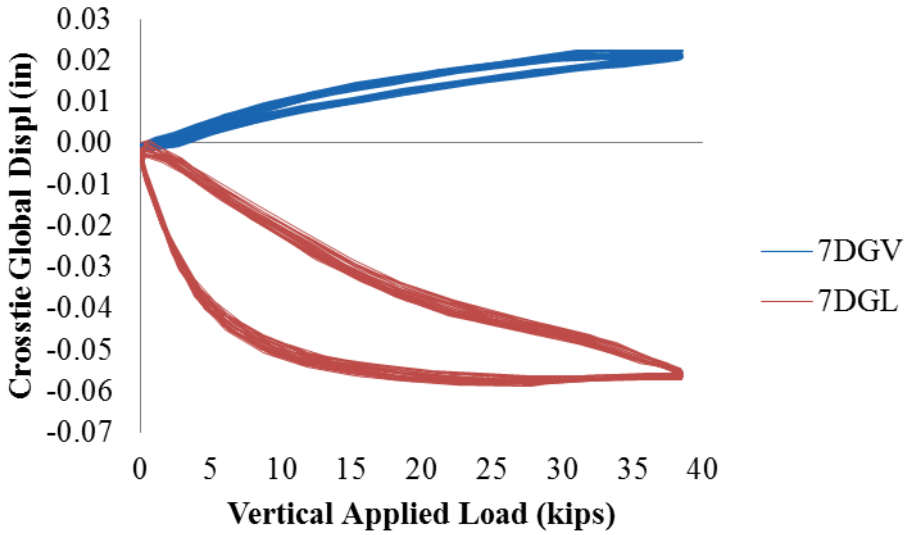

Figure 4.87 Crosstie Global Displacements at Field/Gauge Side Under Cyclical Loading

4.4.2 Vertical Load Path in Full-scale Field Experiments

Under dynamic loading from the passage of the passenger and freight train consists, the rail seat reaction forces are hypothesized to be proportional to the wheel loads. The ratio is expected to be the same as under static wheel load. As the wheel loads were measured from rail strain gauge

bridges (D, F, T, and V in **Figure 3.61**) it was found that they did not match exactly with the true wheel loads when the rail seat reaction forces were measured. Because dynamic wheel-rail interaction is more significant at a higher speed, the variation of the ratio of rail seat load versus vertical wheel load is expected to be greater. Following with the trend of wheel load demand, at the curved track (HTL), the low rail is expected to record a greater reaction force at a lower speed; and the high rail is expected to record a greater reaction force at a higher speed.

4.4.2.1 Under passenger train consist

The passenger train series consisted of one locomotive which weighted 260 kips and nine passenger cars which weighted 87 kips. Train passes were made at speeds of 2, 15, 30, 60, 80, 90 and 105 mph. When each train wheel rolled across the instrumented rail seats E, S, U and W, the vertical wheel load was recorded by rail strain gauge bridges. Rail seat loadings were calculated from the concrete internal strains measured form E, S, U and W. Analyzed from 2012 testing results, the rail seat reaction forces corresponding to the detected wheel load at a low speed (**Figure 4.88**) and a high speed (**Figure 4.89**) are given below.

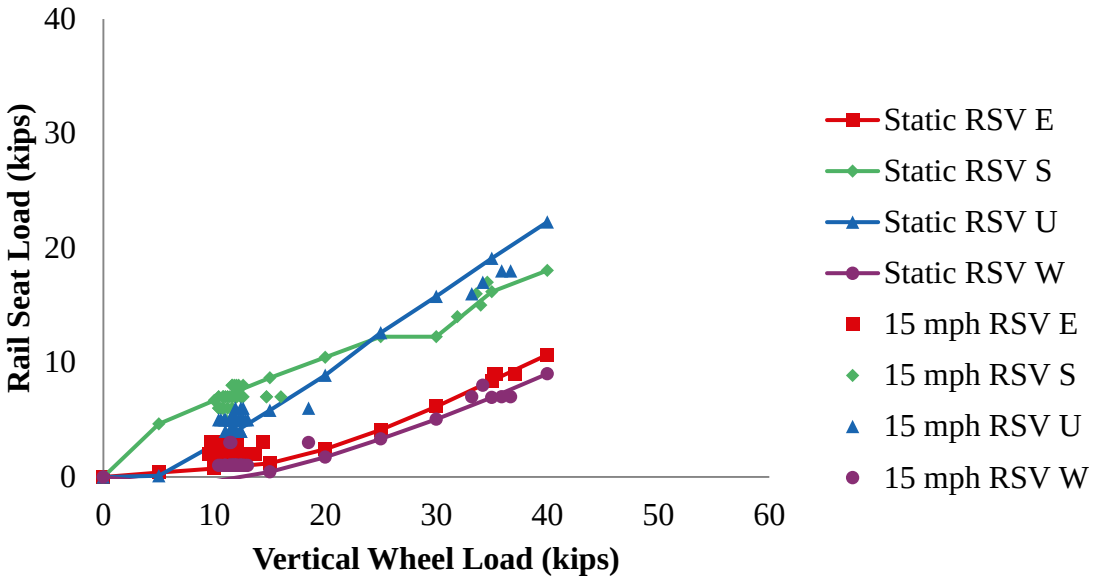

Figure 4.88 RTT, Passenger Train, Speed = 15 mph (2013)

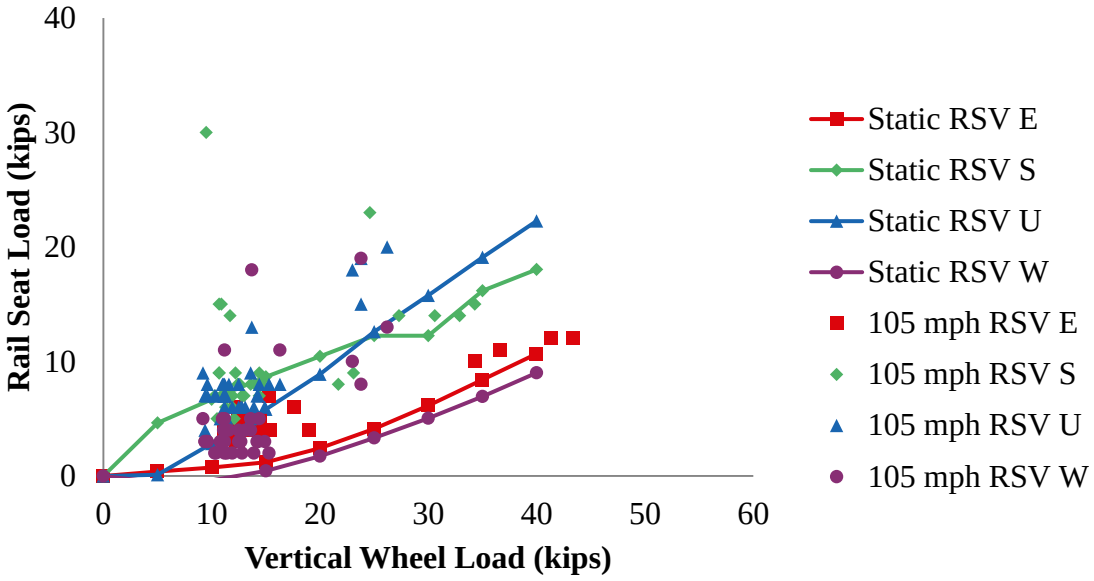

Figure 4.89 RTT, Passenger Train, Speed = 105 mph (2013)

From **Figure 4.87** and **Figure 4.89**, the magnitude of the vertical load measured from different rail seats could be much different dependent on the running speed and the support condition under each specific crosstie. Under a lower speed (15 mph as shown in **Figure 4.88**),

23% to 53% of vertical wheel load was supported by the rail seat directly loaded. The reaction forces measured from the four rail seats increased almost constantly with the rising of wheel loads. Under a much higher speed (105 mph as shown in **Figure 4.89**), each rail seat still tended to afford a similar portion of wheel in average, however the variation was greater; in **Figure 4.89**, some reaction loads measured from rail seat S were far off the trend line. The greater variation was brought by the higher dynamic interactions of wheel, rail, crosstie and ballast at high speed. Comparing **Figure 4.88** with the static loading condition as shown in **Figure 4.45**, it can be found that there is a good match between the static and dynamic loading. Rail seat E and W were always bearing a lower percentage of wheel load. Because locomotives were far heavier than passenger cars (260 kips to 87 kips), a much higher vertical load can be found to be applied to each rail seat when locomotive wheels rolled over. As a conclusion, when the train speed increased, the variation of rail seat loading increased, and this variation may connect to the wheel profile, clamping force or crosstie support conditions.

The variation of the ratio of rail seat loads to wheel loads from HTL testing was found smaller. **Figure 4.90** shows the rail seat reaction forces corresponding to wheel load from 2012 testing at HTL, at a speed of train was 15 mph, which was the same as used for **Figure 4.88**. Clearly, the rail seat loads concentrated in a much narrower band, which varied from 23% to 35% of the vertical wheel loads.

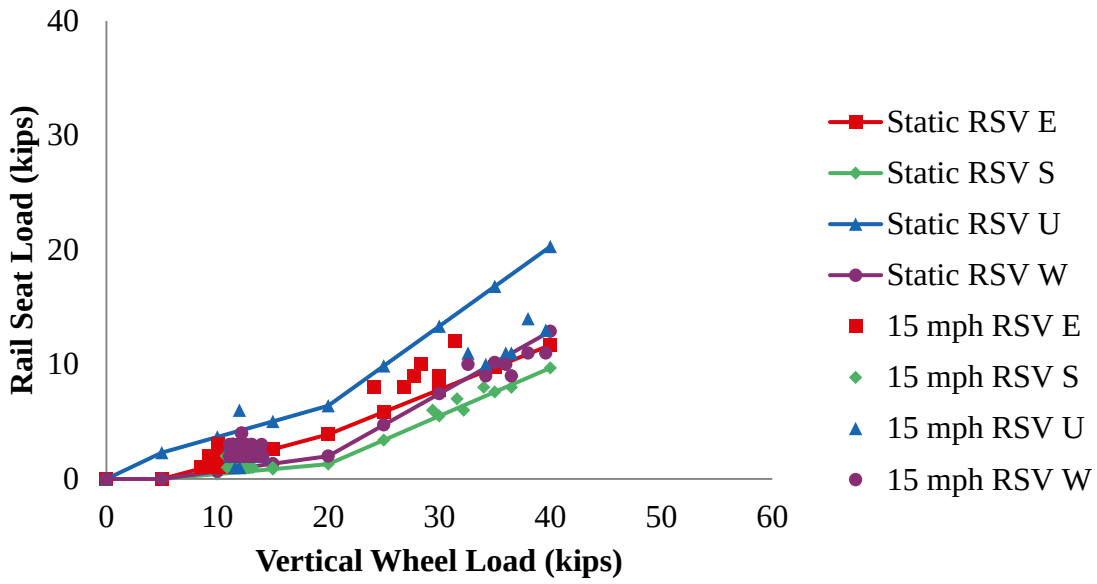

Figure 4.90 HTL, Passenger Train, Speed = 15 mph (2012)

For a higher speed (45 mph) of train running at HTL, the results are shown in **Figure 4.91**. **Figures 4.91** and **Figure 4.90** are very similar, except for a few high loads recorded from rail seat E. It could be found, even though these reaction forces were much higher than others recorded from the same rail seat, they still followed the same proportion, which were 32% of the wheel loads. The comparison of **Figure 4.90** and **Figure 4.91** reveals that, at a higher speed, the rail seat below the high rail (rail seat E) took a greater reaction force; and the rail seat below the low rail (rail seat S, U and W) took a smaller reaction force. The drift of the vertical rail seat reaction force from low rail to high rail was caused by the greater vertical wheel load on the high rail due to the greater centripetal force applied at a higher speed.

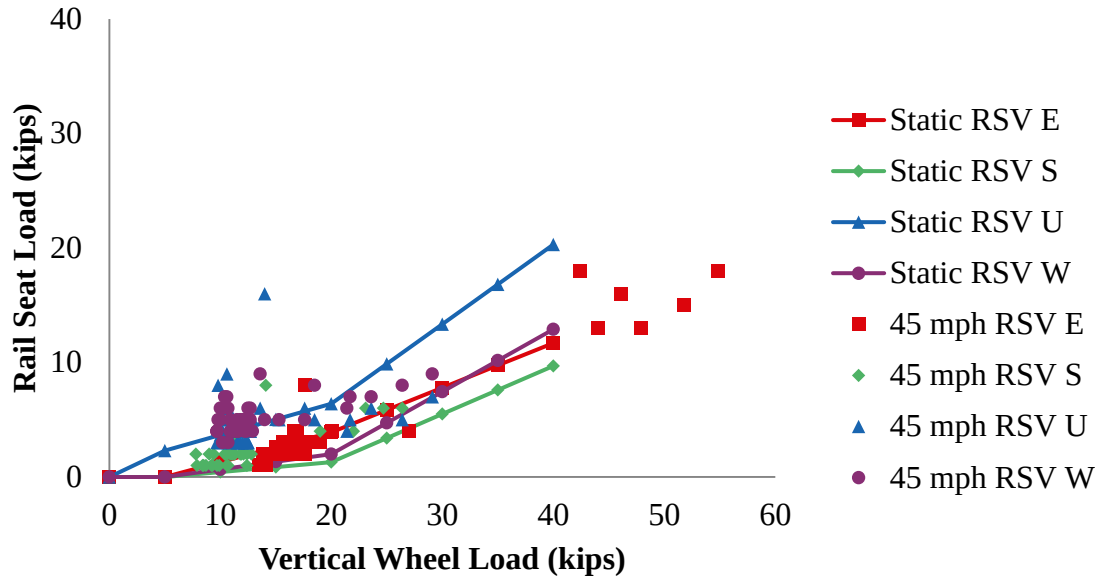

Figure 4.91 HTL, Passenger Train, Speed = 45 mph (2012)

The effect of car weight and speed corresponding to the center rail seats E and U in 2013 testing is shown in **Figure 4.92** and **Figure 4.93**.

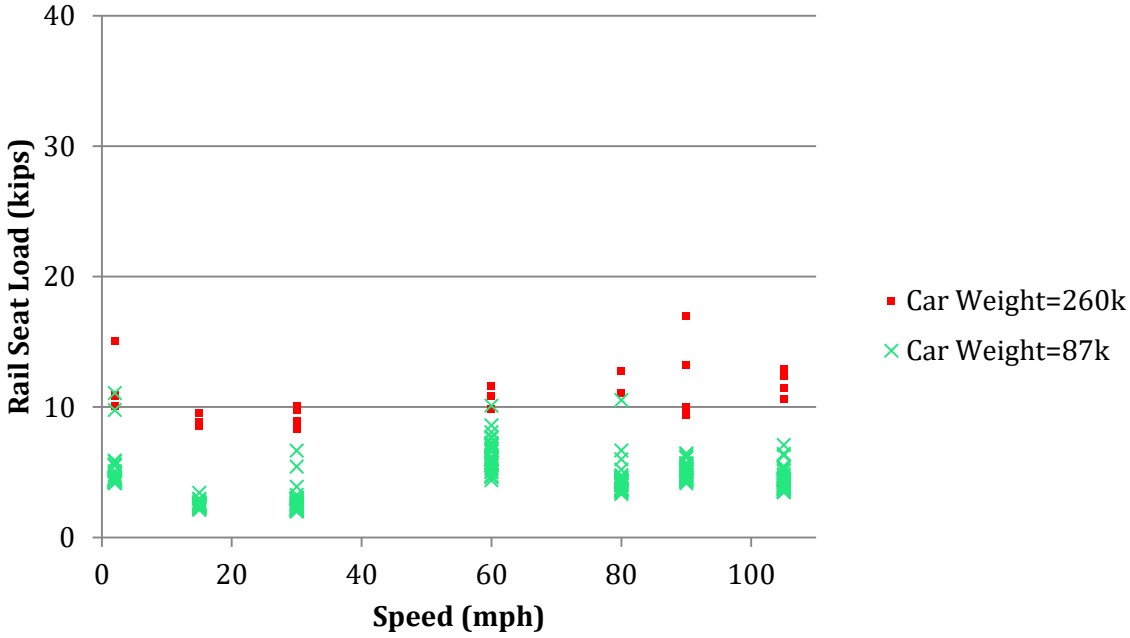

Figure 4.92 RTT, Passenger Train, Rail Seat Loading at E (2013)

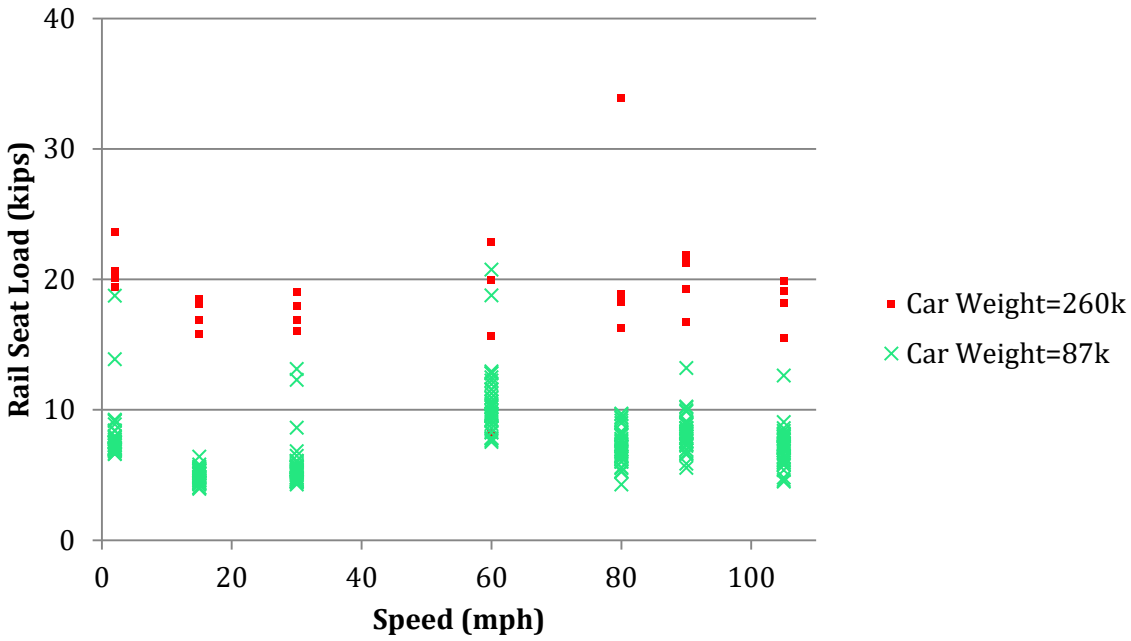

Figure 4.93 RTT, Passenger Train, Rail Seat Loading at U (2013)

From **Figure 4.92** to **Figure 4.93**, generally it could be found, the magnitude of the rail seat loadings weren't affected much by the train speed. However, high speed introduced a larger variation to the rail seat reaction forces, and a much impact force could be recorded.

4.4.2.2 Under freight train consist

The freight train series consisted of one locomotive and ten freight cars with various weights. Train speeds between 2 to 60 mph were used. When each train wheel rolled above the instrumented rail seats E, S, U and W, the vertical wheel load was recorded by rail strain gauge bridges. Rail seat loadings were calculated from the concrete internal strains measured from strain gauges in E, S, U and W. The relationship between wheel load and rail seat load is shown in **Figure 4.94** and **Figure 4.95**, corresponding to the speed of 2 mph and 70 mph respectively.

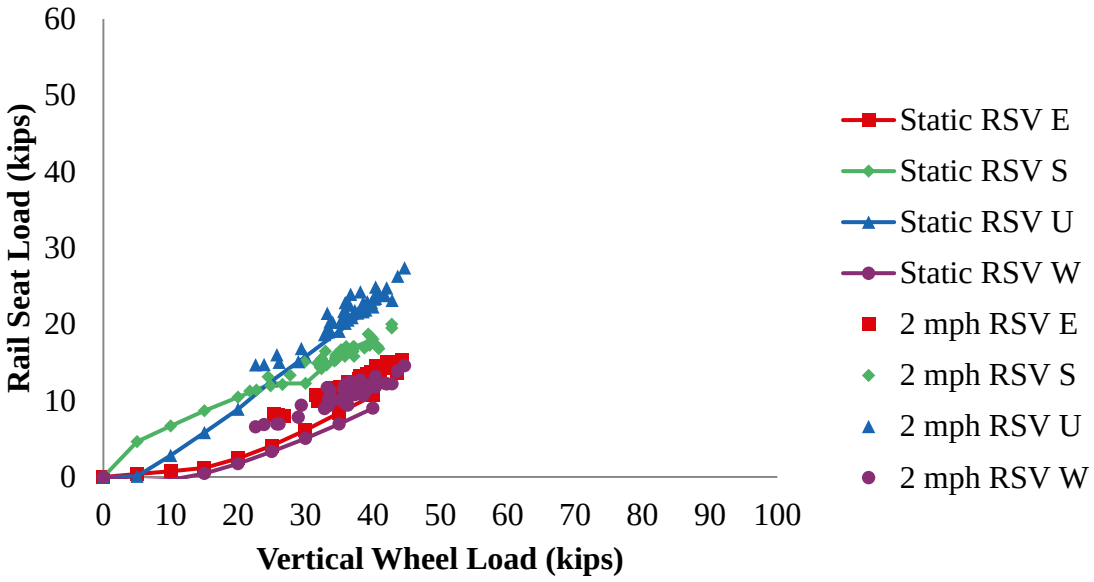

Figure 4.94 RTT, Freight Train, Speed = 2 mph (2013)

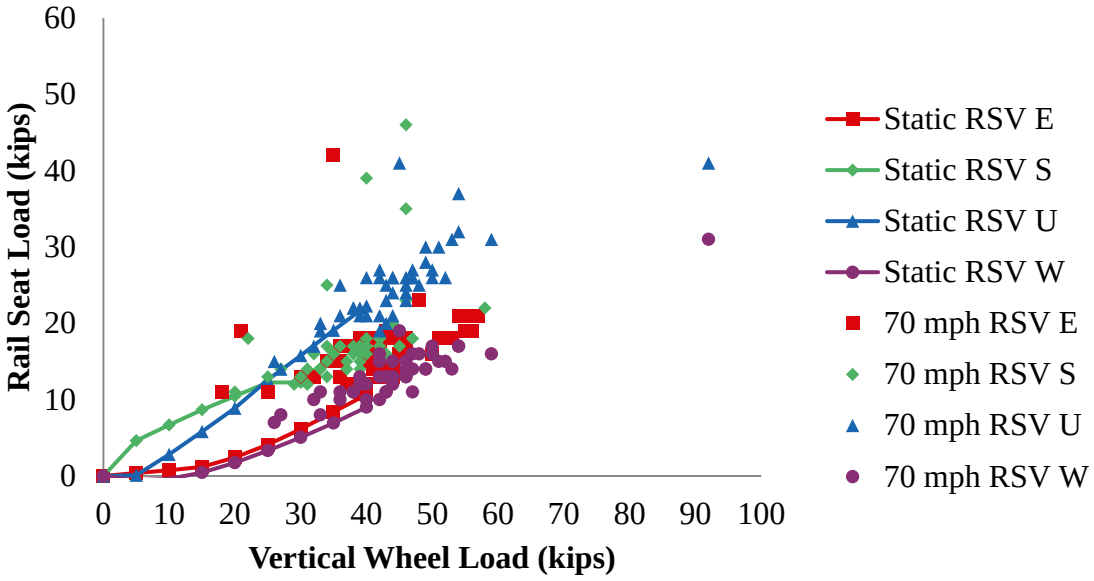

Figure 4.95 RTT, Freight Train, Speed = 70 mph (2013)

The rail seat loading under the freight consist generally showed a similar trend as the passenger consist. From **Figure 4.94** it can be found that the magnitude of the vertical load measured from different rail seats were varying from 30% (rail seat W) to 60% (rail seat U). For

Figure 4.95 the range is from 32% (rail seat W) to 64% (rail seat U) which are pretty similar as found in **Figure 4.94**. The observation agreed with the finding from the passenger consists. The possible reason for the wide band of vertical load shared by each rail seat is the variation of support conditions, as discussed in Section 4.2.3.2. This portion of load sharing agreed from the static testing results in Section 4.2.3.2 and the passenger train testing results in Section 4.4.2.1. A much higher vertical load was found at each rail seat when heavier axles were rolling over the instrumented rail seats. This was consistent with the behavior under passenger trains, when the speed increased, the variation of rail seat loading increased.

Also, as seen in the passenger train data, the variation of the ratio of rail seat loads to wheel loads from HTL was found much smaller. **Figure 4.96** shows the rail seat reaction forces corresponding to wheel load from the 2012 testing at HTL under train speeds of 15 mph. The rail seat loads concentrated in a much narrower band than in RTT testing, which varied from 30% to 45% of the vertical wheel loads.

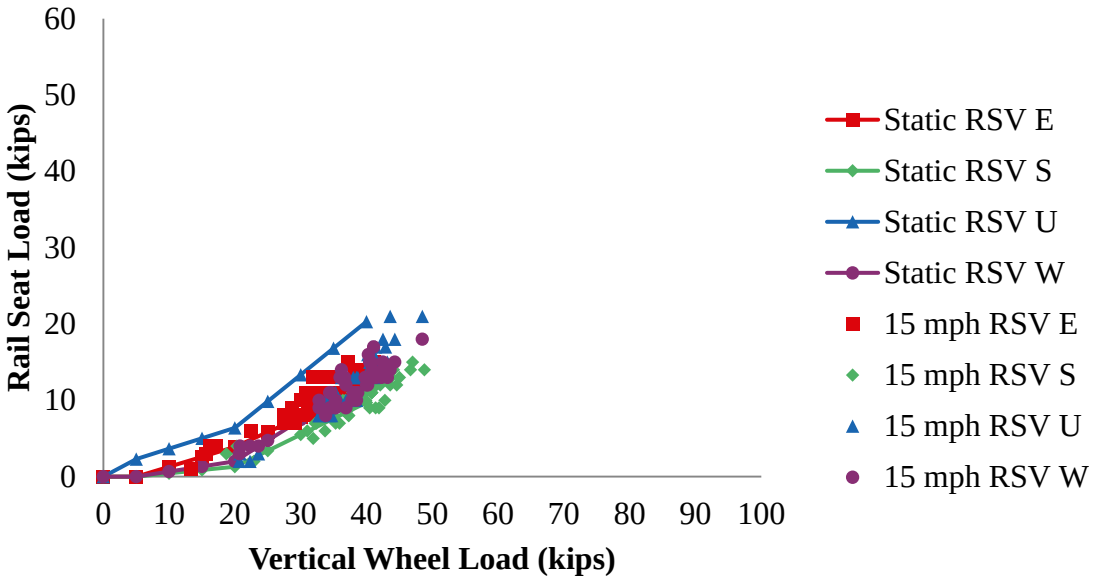

Figure 4.96 HTL, Freight Train, Speed = 15 mph (2012)

The results for a higher speed train run (45 mph) the HTL are shown in **Figure 4.97**. When high wheel loads were recorded from the rail seat E at the high rail, high rail seat load reaction forces were found consequently. The ratio of rail seat load to wheel load remained consistent, regardless of the vertical wheel loads applied. The comparison of **Figure 4.96** and **Figure 4.97** shows a similar result as from the comparison under passenger consists; at a higher speed, the higher centripetal force increased the vertical wheel load on high rail and decreased the vertical wheel load on low rail, but the rail seat reaction forces still followed the constant proportion.

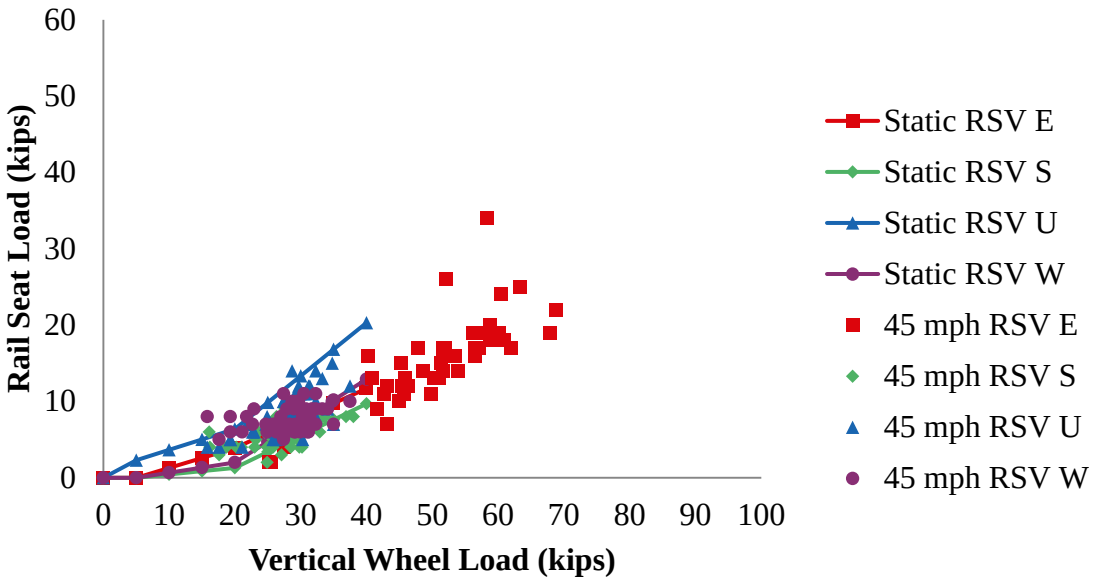

Figure 4.97 HTL, Freight Train, Speed = 45 mph (2012)

The effect of car weight and speed is shown in **Figure 4.98** and **Figure 4.99**. In general, the trend was similar as found in Section 4.4.2.1 for passenger train testing results; the rail seat loadings were not significantly affected by the train speed. However, high speed brought a larger variation to the rail seat loading.

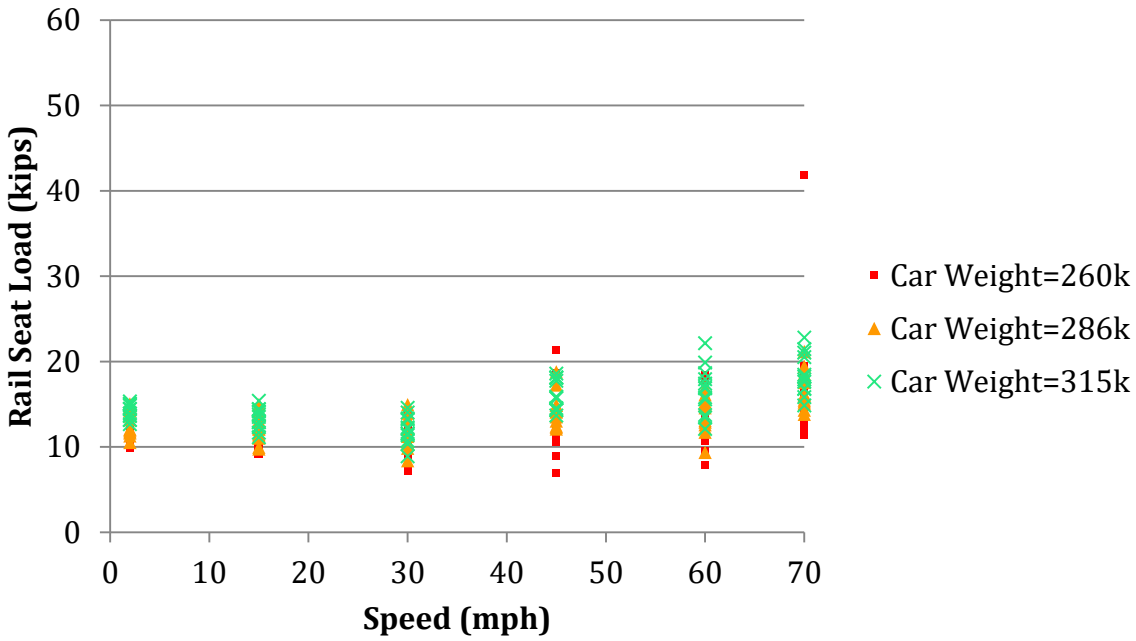

Figure 4.98 RTT, Freight Train, Rail Seat Loading at E (2013)

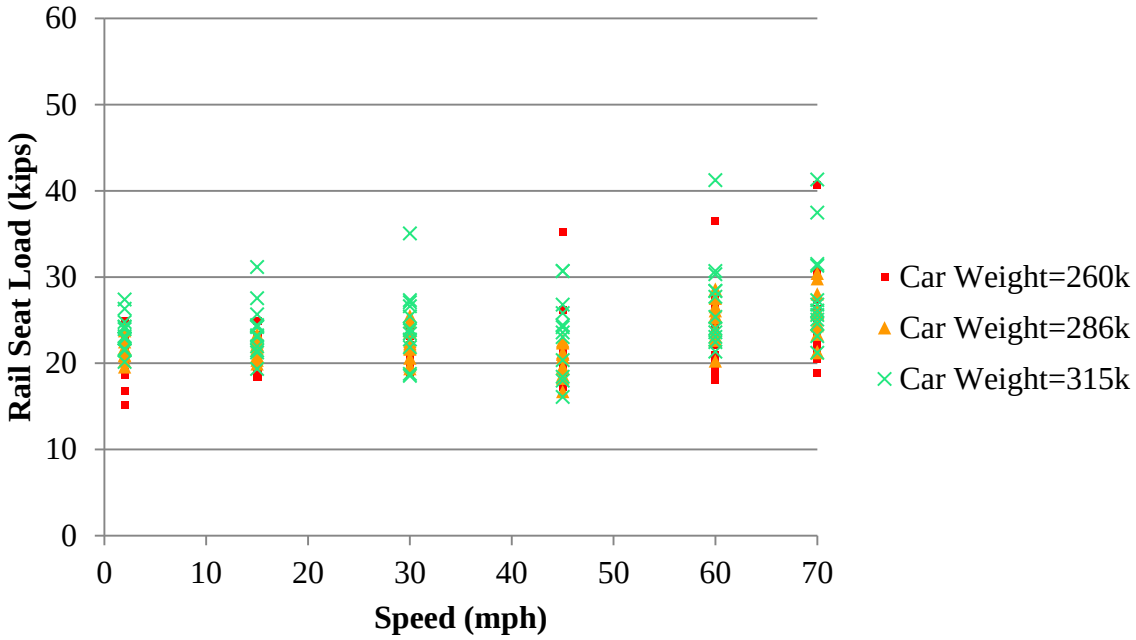

Figure 4.99 RTT, Freight Train, Rail Seat Loading at U (2013)

4.5 Lateral Load Path Under Dynamic Loading

Lateral load path under dynamic loading was examined in both laboratory and field experiments. In laboratory, cyclical loading was applied to rail with the TLS. In field testing, the effect of dynamic wheel loads caused by train passage was examined.

4.5.1 Lateral Load Path in Multi-crosstie Laboratory Experiments

Multi-crosstie laboratory experiments suggests a quite similar lateral load path under dynamic loading as under static loading, and a very good repeatability was found between cycle and cycle.

4.5.2 Lateral Load Path in Full-scale Field Experiments

On tangent track, the shoulder lateral reaction force was found to not be significant. In this section, all dynamic train test data is from rail seat U on the low rail of the HTL test section to maintain a constant location with varying dynamic loading scenarios. The peak shoulder lateral reaction forces from axles of dynamic 315 kips freight car loading were also plotted against the corresponding applied lateral wheel loads under speeds ranging from 2 mph to 45 mph to determine the load transfer characteristics of the system under varying speeds and constant car weight (**Figure 4.100**). As lateral wheel loads increased, the corresponding peak shoulder lateral reaction forces from the axles of a 315K freight car increased linearly. A linear trend line of the peak reaction force data for all data points shows that approximately 350 lbf will be transferred into the shoulder per one kip of lateral wheel load. The data indicate that approximately 35% of the lateral wheel load will be transferred into the shoulder, 10% more than the static loading case, regardless of the magnitude of the lateral wheel load. A variety of factors could have led to the difference in percentage of load transferred to the shoulder. Differences in loading

conditions (i.e. static vs. dynamic) can have an effect on the magnitudes of the applied wheel loads. Differences in track geometry (i.e. tangent vs. curved) will also have an effect on the vehicle-track interaction causing variances in magnitudes of the applied wheel loads.

A linear relationship between the force imparted into the shoulder and applied lateral wheel load shows that a constant percentage of the lateral wheel loads will be transferred to the shoulder throughout the wide range of applied lateral wheel loads that can occur in service.

The lateral reaction force due to 315 kips freight car was found about three times as due to 86 kips passenger car (**Figure 4.101**).

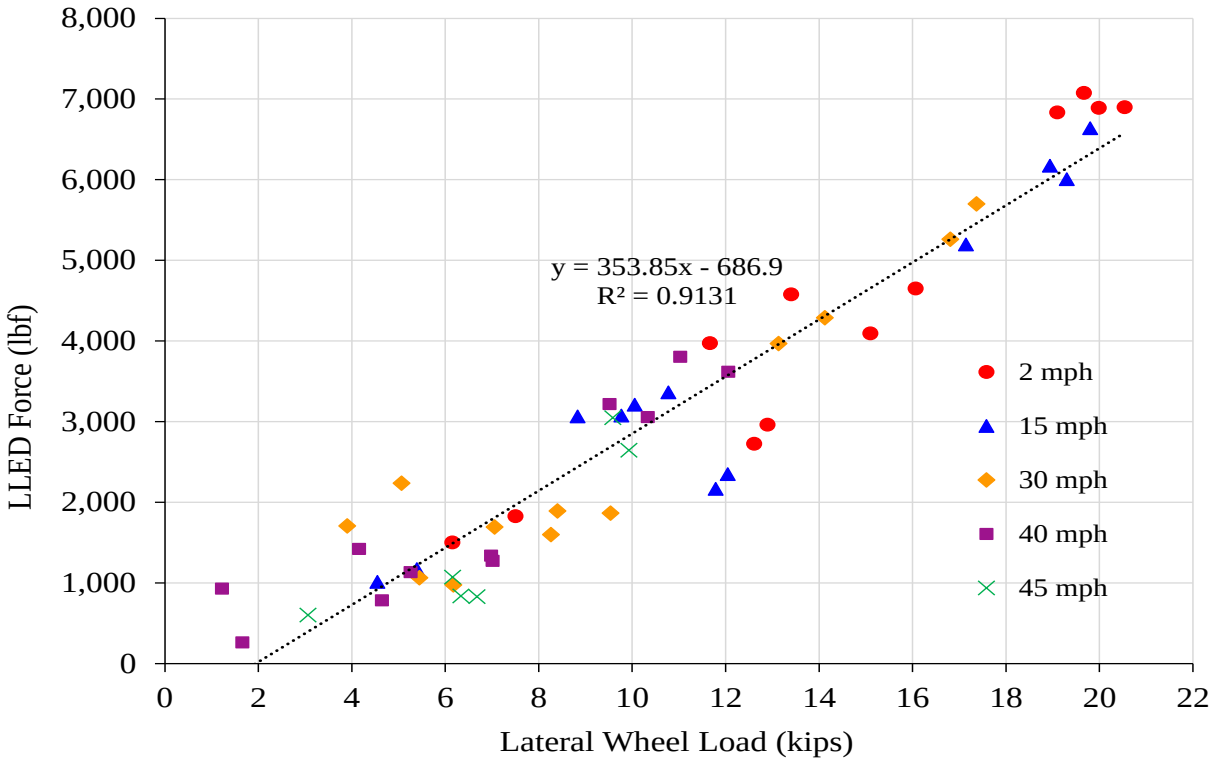

Figure 4.100 Peak Shoulder Lateral Reaction Force (LLED) at Various Speeds – 315K Car, Rail Seat U at HTL (2013) (Prepared by Brent Williams)

All lateral wheel loads from passenger tests were less than 5,000 lbf and all lateral forces measured from shoulders were less than 1,000 lbf. At 15 mph, lateral forces measured from shoulders were 618 lbf for the passenger train while the freight trains yielded 6,637 lbf, more than an order of magnitude difference. The magnitudes from passenger tests were approximately 10 times lower at all speeds. The lower magnitudes indicate that passenger trains impart significantly lower demands on track components compared to freight trains. Although the forces from the freight train were about ten times larger than those from the passenger train, the freight car weights were only approximately 3.7 times heavier than the passenger cars. The disparity shows that there may not be a direct correlation between car weight and lateral forces imparted on the track. The disparity also further shows that freight trains impart much higher forces in the fastening system than passenger trains (Williams et al 2014).

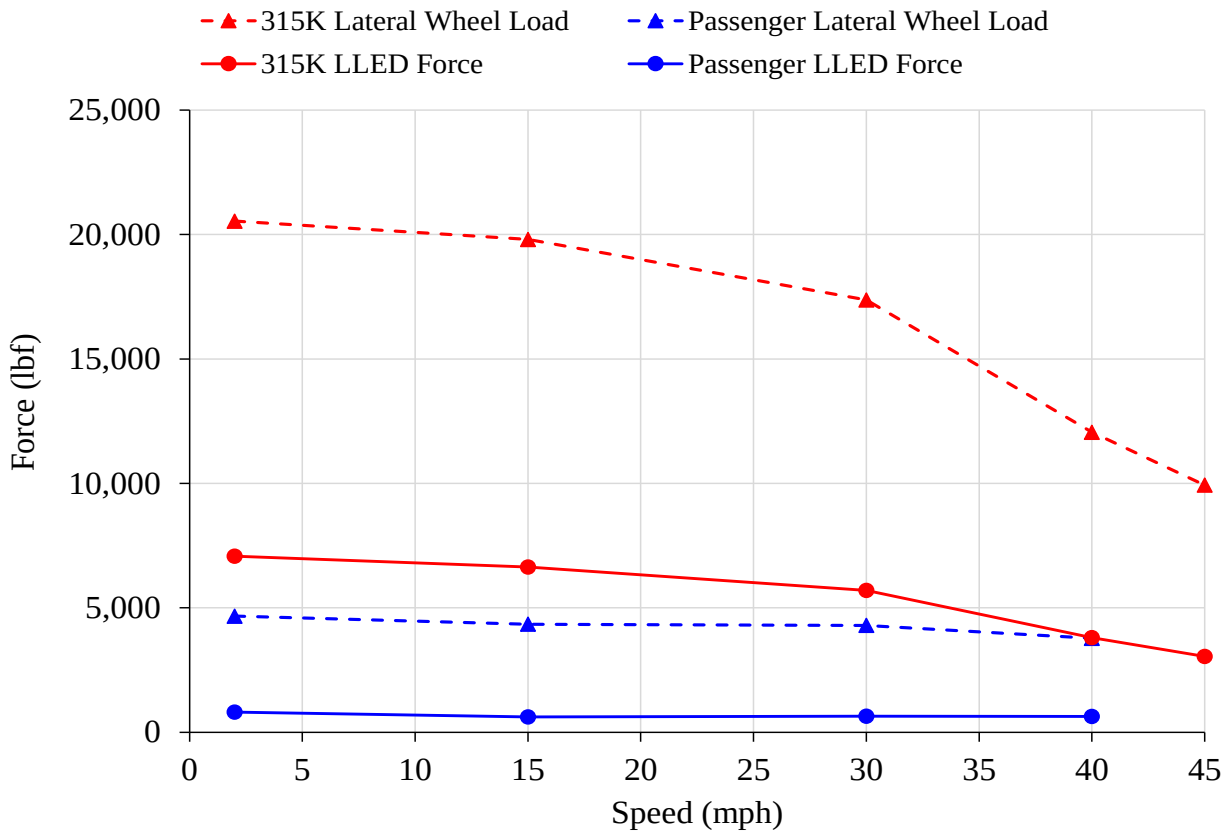

Figure 4.101 Maximum Lateral Wheel Loads and Lateral Shoulder Reaction Forces (LLED) at Speed at HTL (2013) (Prepared by Brent Williams)

5. Evaluation of the Structural Behavior of Rail Clip

There are two primary motivations to study the clamping force. One, it is necessary to know whether or not the change of clamping force under train passage will significantly affect the entire load path. And two, the sufficiency of the current clip design needs to be validated, i.e. the possibility of the clamping force deterioration due to plastic strain. In this research, the performance of Amsted Safelok I type clips (**Figure 5.1**) are examined, which are used extensively in North America on heavy haul railroads, light rail and mass transit systems. This type of spring clips are mounted on non-insulated weld-on shoulders with insulators placed between their tips and rail base.

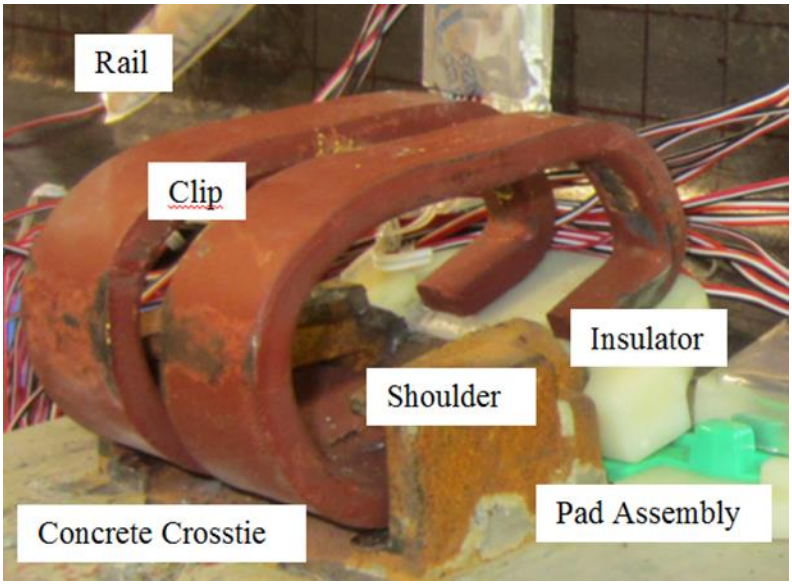

Figure 5.1 Amsted Safelok I Type Rail Clip

The principle objectives of rail clip study were to quantify: i. how the strain within the clip is effected by a change in clamping force; ii. how the clamping force is effected when subjected to static and dynamic wheel loading; iii. the longitudinal length of track in which clamping force is significantly affected by load. To accomplish these goals, instrumentation was developed and deployed to quantify the magnitude and distribution of lateral fastening system forces.

The steel used in this investigation is commercially produced high-strength spring steel with a constitutive relationship shown in **Figure 5.2**. The yielding stress and strain for this material are 183 ksi and 0.007. A strain hardening is expected to happen beyond yielding, the ultimate stress and strain are 202.06 ksi and 0.042, the fracture stress and strain are 183 ksi and 0.092. When unloaded beyond the yielding point, a residual strain is expected with the unloading and reloading curve parallel to the curve within its elastic range, i.e. with the modulus same as its Young's modulus.

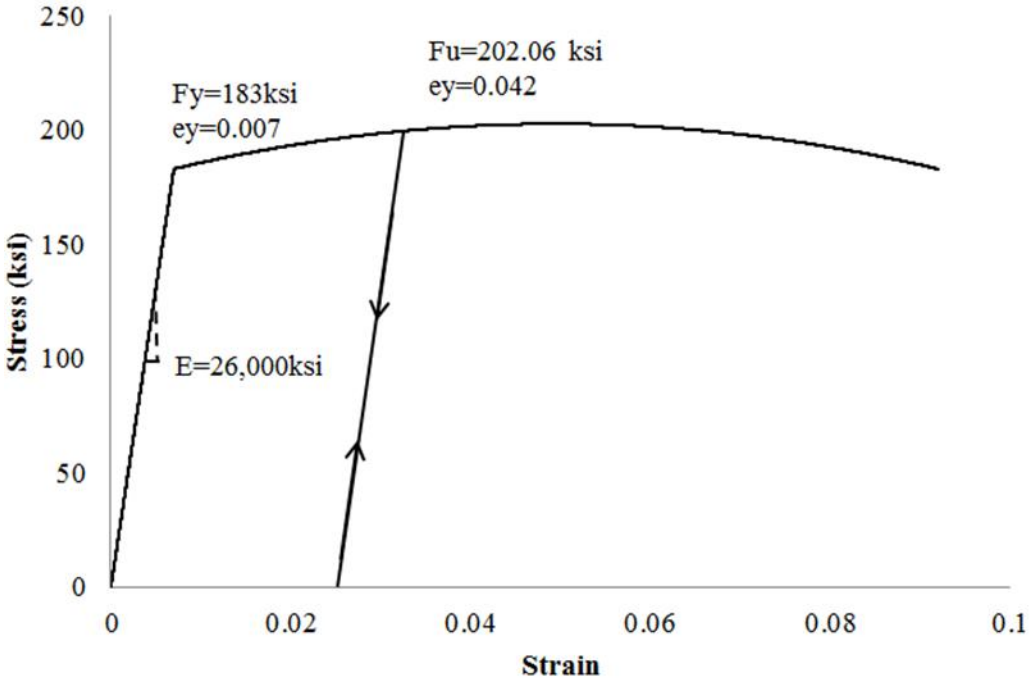

Figure 5.2 Constitutive Model for High-Strength Steel Used for Spring Clips

A pair of properly installed clips at a single rail seat are expected to impose 4750 lbf of clamping force to the rail, with a 0.289 inch predicted clip tip opening. Standard tests were conducted at clip manufacturers to meet the AREMA (2012) requirements (**Figure 5.3**). Lubricants were used between the contact surfaces of clip tip and the base plate to reduce frictions.

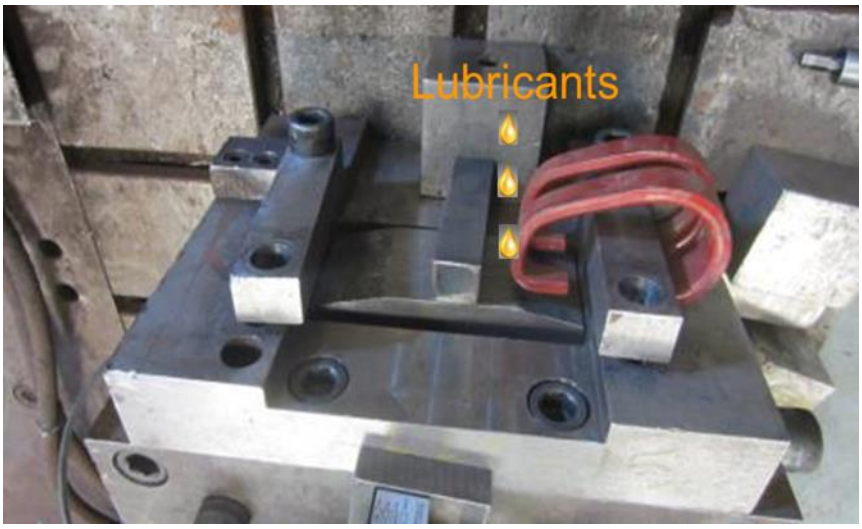

Figure 5.3 Standard Clip Test Required by AREMA (2012)

In order to better characterize the mechanics of the clip, it was determined that the clamping force commonly reported, be broken into its normal and tangential components. The normal component of clamping force is perpendicular to the top of the rail base while the tangential component is parallel to the top of the rail base. These components were defined and presented in **Figure 3.27**. It was found that the rail base thickness and the14.2° angle from the rail seat plane results in 2.45 kips of force applied normally to the top surface of rail base directly after the installation. As no lubricants are used in the field between the clip tip and insulator, the actually tangential force between the contact surfaces exists and is unknown due to both the direction and magnitude being dependent on the installation procedure.

The structural behavior of spring clip is examined in both numerical simulation and field experiments. For numerical calculation, a program was developed with Matlab to find the strain and stress diagram under various combination of normal and tangential forces, the critical zone of a clip, clip opening stiffness as well as the clip inelastic behavior were clarified. From the field experiments, the range of the normal and tangential forces applied to the clip tip was measured due to clip installation and due to train passage, respectively. In the numerical model,

a clip was meshed into 100 beam elements with six degree-of-freedom for each. Because the clip can be treated as a static determinant structure when the applied normal and tangential forces are known, the strain, stress, rotation, and displacement for each arbitrary element can be calculated using the given structural geometry and the material properties.

5.1 Initial Clamping Force Measured from Analysis and Experiments

While the normal force applied to the clip tip immediately after installation is known to be 2450 lbf with 0.289 inch of clip tip opening (under the standard installation procedure), the tangential force is not defined in the design. Both the sign and the magnitude of the tangential component of the clamping force need to be clarified. The numerical program was utilized to find the clip tip opening corresponding to various combinations of normal and tangential forces (**Figure 5.4**).

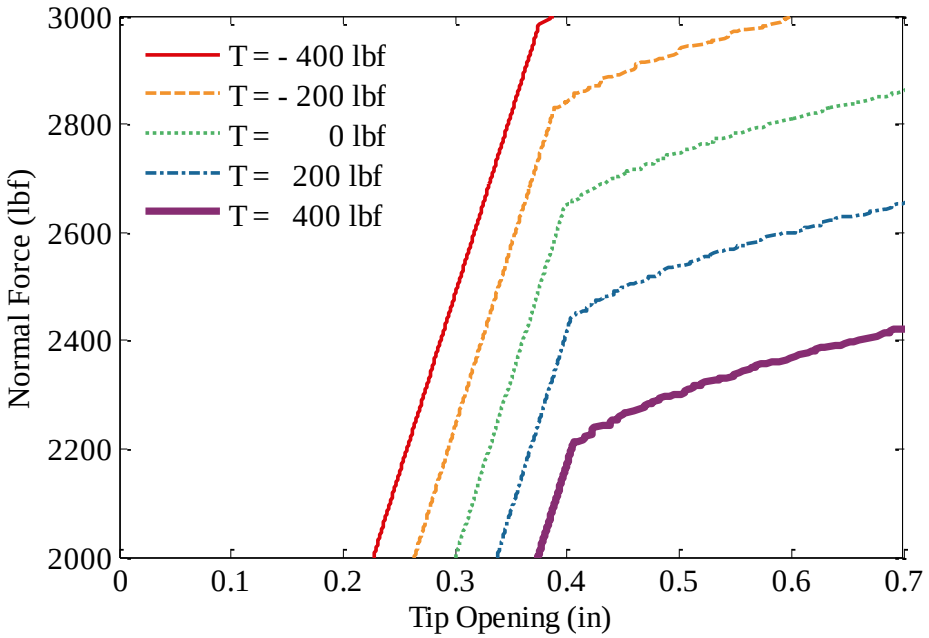

Figure 5.4 Clip Tip Opening Under Various Combination of Normal and Tangential Forces

From **Figure 5.4**, it is found, when the stress level of the entire clip is low (no yielding happens), the opening up of clip remains linearly with the increasing of the normal force. In addition, the

tangential force plays an important role to the clip opening. For example, when there is a 400 lbf tangential force presents, the tip opening is about 0.08 inch wider than with no tangential force. And therefore, the true clamping force applied to the rail by clips couldn't be simply determined by a linear function of clip opening. When yielding limit is surpassed at any location of a clip, the rate for the tip opening turns to be much higher than that in the elastic range. Because of the strain hardening (referred to **Figure 5.2**), the normal force applied by the clip can still increase with the lifting up of its clip, but much more slowly. It should be noticed that, when a constant 400 lbf tangential force applied, the yielding of a clip takes place with a normal force of only 2,250 lbf, which is even lower than the load required in design.

As it is possible to reach yielding when the clip is subjected to a certain combination of normal and tangential force, it is necessary to examine the strain distribution and thus find the critical zone.

Figure 5.5 shows the analytical strain distribution in micro strain along the clip after installation. A 2450 lbf normal force and no tangential force were assumed. Strains at the inner surface and outer surface of the clip were calculated and labeled as shown in **Figure 5.5**, a and b. The difference between the absolute value of strain at the clip inner and outer surface was no more than 100 ms (microstrain), which was due to the axial deformation. The maximum strain was found at the left transition area, which was 6,576 ms at the inner surface and -6,624 ms at the outer surface, both of which were above 90% of the yield strain (7,000 ms). Combing the finding from **Figure 5.5** and **Figure 5.5**, it reveals that the safety margin against plastic deformation of the clip is quite small (below 10%). When the normal or tangential component of the clamping force increases under wheel load, the maximum strain might exceed the yielding limit.

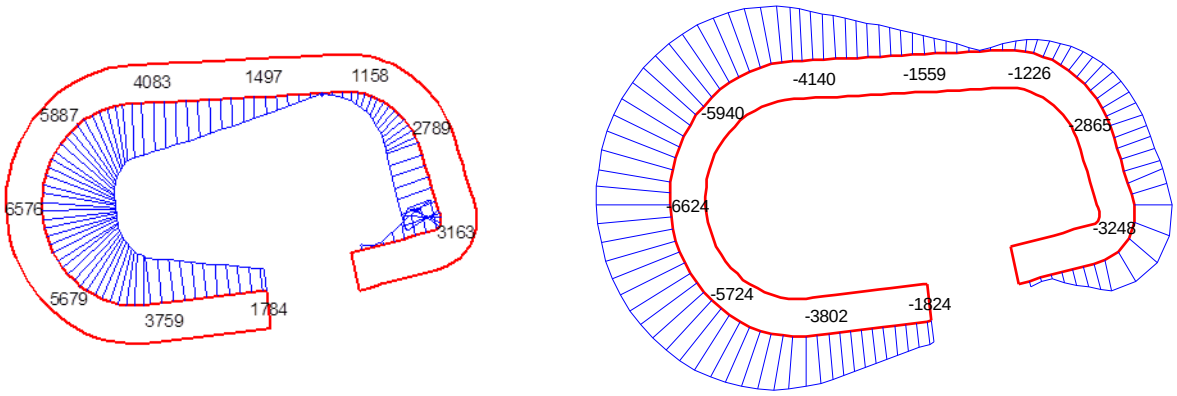

a) b)

N = 2,450 lbf, T = 0

Figure 5.5 Strain Distribution of Inner (Left) and Outer (Right) Surface in Microstrain

Even though the tangential force was not defined in the clip design, evidence of a tangential force exists. **Figure 5.5** shows the strain distribution of the case with 0 tangential force. As a comparison, the actual strain after installation was measured from the instrumented clip (referred to strain gauge pattern shown in **Figure 3.28**), in which five measurements on each toe were taken. Prior to clip installation, strain gauge patterns were placed on both the gauge side and field side of clips with this configuration. The strain recorded from gauge #1 to #5 is listed in Table 5.1 Material Properties of Rail Clip. By analyzing the data read from these strain gauges, initial clamping forces were determined.

Table 5.1 Material Properties of Rail Clip

Manufacturer/Design	Elastic Modulus (E)	Yield Stress (fy)	Yield Strain (ey)
Amsted RPS UAB 2000	23,000 ksi	183 ksi	7,957 ms

The initial stress level on clips was examined through these strain gauges (**Table 5.2**) and compared with the yield stress shown in **Table 5.1**. Another MATLAB program was developed

to calculate the initial clamping force and to plot out the strain diagram. In this program, a single contact point was used to simulate the contact condition between the clip toe and insulator. This contact point was found to be located at 0.3 inches from the edge of the rail clip's toe.

Table 5.2 Initial Strain (ms) After Clip Installation

Gauge #	2	3	4	5	6
Toe 1	6,993	5,510	-3,338	-1,651	-355
Toe 2	6,845	6,378	-3,518	-1,937	-88
Average	6,919	5,944	-3,428	-1,794	-222

An average strain of 6,919 ms was recorded from gauge #2, which fell on the location where the maximum strain was found with the linear elastic analysis (**Figure 5.5** Strain Distribution of Inner (Left) and Outer (Right) Surface in Microstrain). Several replicates were conducted in the laboratory and field testing, all showing similar results.

Theoretically, any combination of the two strain readings from the same leg of a clip can be used to calculate the normal and tangential forces applied at each clip toe. Linear elastic theory was applied for analysis and the methodology was introduced in Section 3.5.5**.** To achieve this goal, a computer program was developed in Matlab to determine the N and T leading to a strain diagram best fit the five strain measurements.

Strain reading output from gauge #1 and #3 were selected to calculate the actual normal and tangential forces using the methodology described before. And the N and T were found to be 2,380 lbf and 400 lbf. The actual normal force was found close to the design value; however, the tangential force was found not negligible. **Figure 5.6** shows the comparison between the strain diagram using the calculated N and T, and the actual strains measured from the test. In **Figure 5.6**, the blue shaded areas express the analytical strain distributions at the inner surface

(left) and outer surface (right) of the clip due to this pair of normal and tangential forces. The strain values are shown in black along the clip body. The red markers and values are for the strains recorded from the test. The error for the maximum strain was found as 62 ms.

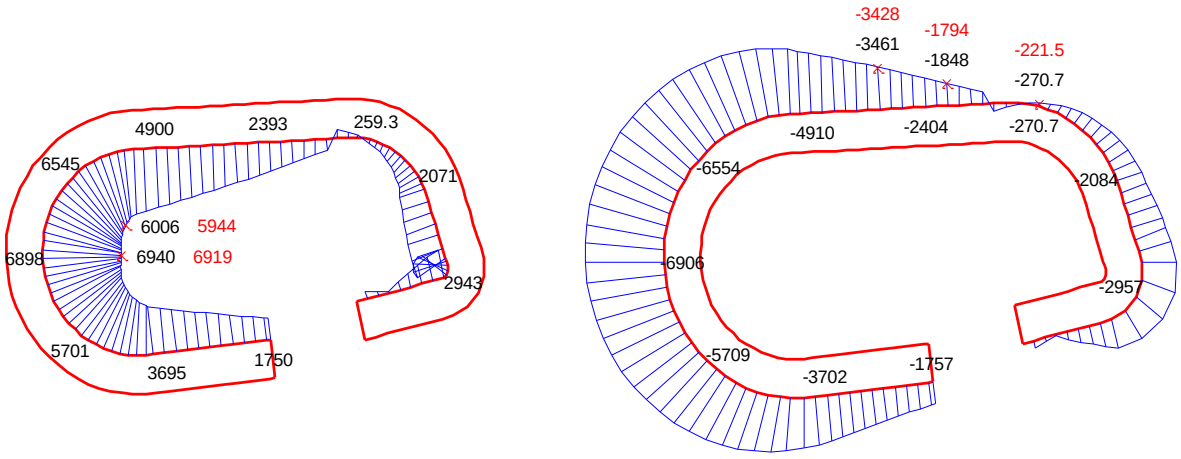

a) b)

N = 2,380 lbf, T = 400 lbf

Figure 5.6 Comparison of Strain (ms) from Theoretical Calculation and Laboratory Measurement

Referring to **Figure 5.5**, the maximum strain found at the clip after installation might surpass 95% of the yield strain of steel. As a small safety margin was left in design, a slight change in normal or tangential force will result in exceeding of the yield limit in clip strain, and thus plastic strain would be expected to occur. Because of the plastic strain, the clip receives a permanent deformation and do not return to its previous geometry after unloading. Therefore, the unexpected plastic strain will case a loss of clamping force. With the help of the numerical program, the examination the highest strain value (tensile/compressive) along the clip corresponding to the normal and tangential forces was output and shown in **Figure 5.7**. It can be found that a positive increment in normal or tangential force will increase the maximum strain on the clip. It can also be found that when the normal force is 2,450 lbf, only about 200 lbf

tangential force is needed to surpass the material yielding limit. This observation provides evidence that the safety margin set in the clip design was small.

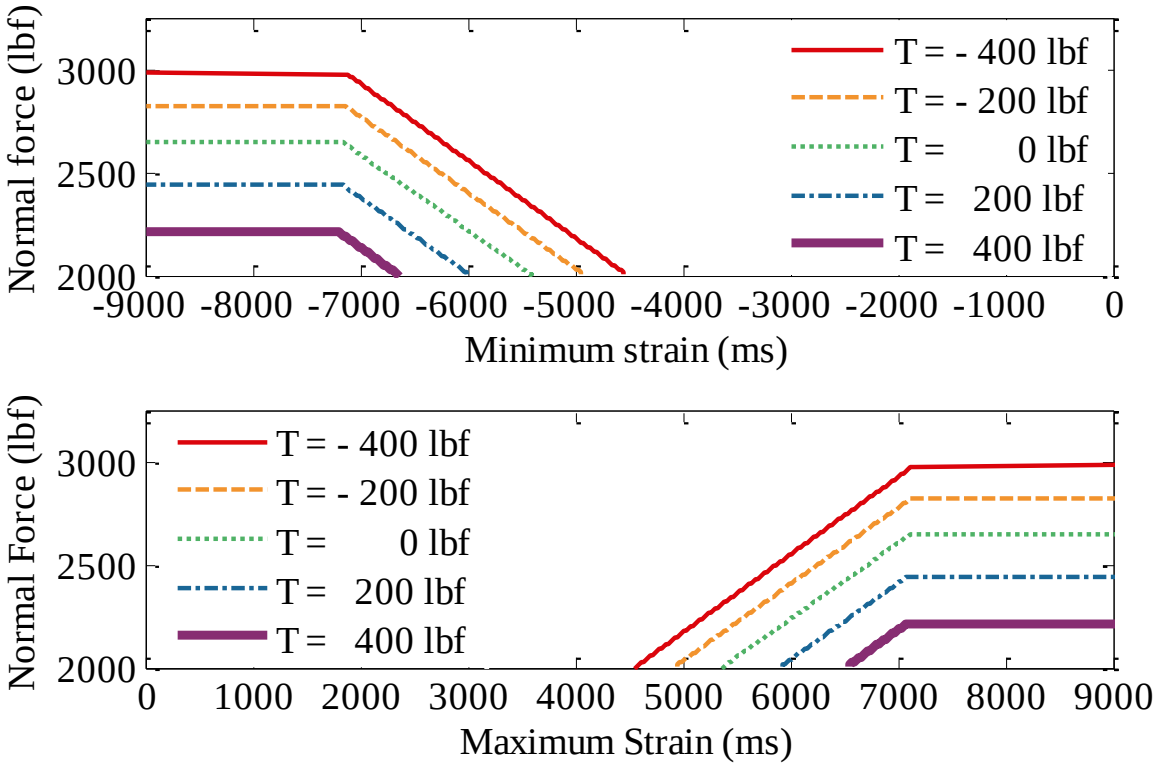

Figure 5.7 a) Minimum Strain (Compressive) on Outer Surface of a Clip Under Various Normal and Tangential Forces; B) Maximum Strain (Tensile) on Inner Surface of a Clip under Various Normal and Tangential Forces

When the extreme value of strain is equivalent to the yielding strain (0.007), the clip reaches its first yielding strength; when the extreme value of stress reaches its peak referring to **Figure 5.5** (with a strain of 0.042), the clip reaches its ultimate capacity. In other words, fracture will take place at the critical zone when the extreme strain value is greater than 0.042. The combinations of normal and tangential forces that will cause clip yielding and failure are presented in **Figure 5.8**.

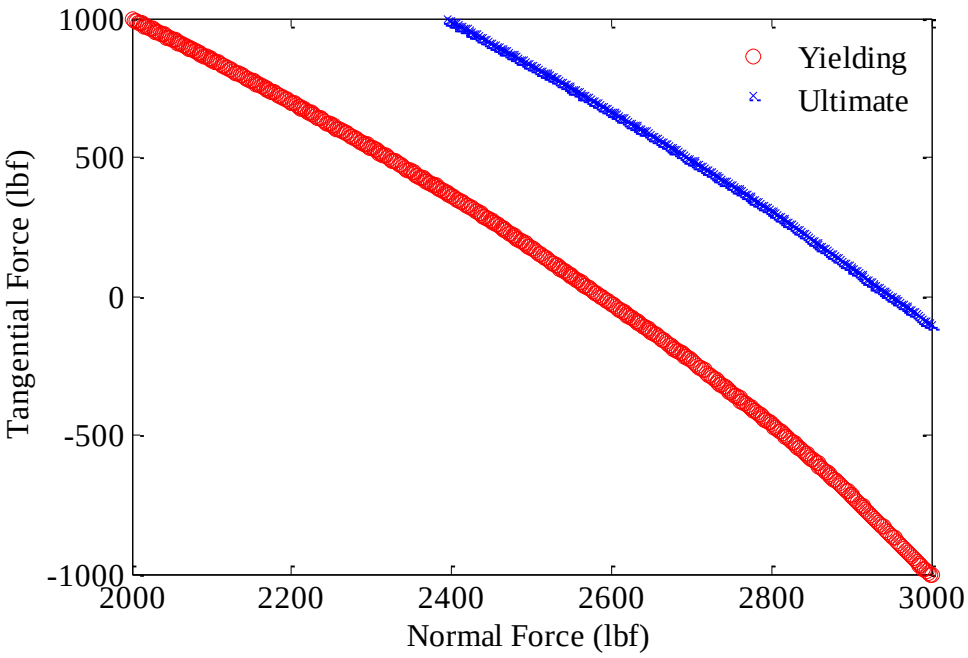

Figure 5.8 Normal and Tangential Force Combinations Causing Clip Yielding and Failure

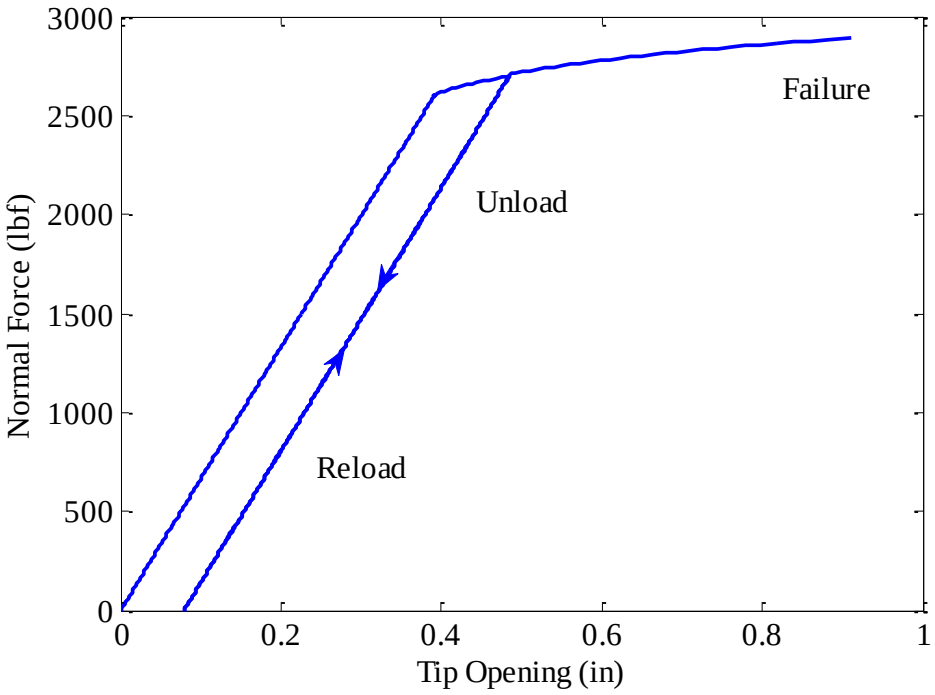

Figure 5.9 Post-yielding Behavior of a Clip (T=0)

Figure 5.10 takes the case of no tangential force as an example to present the post-yielding behavior of a clip. When fully unloaded, a permanent deformation is found which results in the residual tip opening. For the reload process, the normal force provided by the clip increases with the same slop as its first loading cycle; then due to the material strain hardening, the post-yielding curve actually overlap with the original one if subjected with no unloading. This find reveals that, if a clip is loaded beyond yielding point, it couldn't provide the predicted clamping force for the next cycle when the tip opening reaches its design value. In other words, losing of clamping force will happen if subjected to unexpected cyclical tip opening, which is highly

The above observation provides evidence that the safety margin set in the clip design was small. The motivation for measuring the initial clamping forces in the field tests was to find the actual clamping forces applied to clips and to determine if these clamping forces would result in plastic deformation.

In the field experiments, to measure the clip strain and back-calculate the actual clamping forces being applied, one pair of strain gauges were installed on the inner and outer surfaces of each clip toe. The free body diagram of the clip and the locations of the strain gauges are shown in **Figure 5.11**.

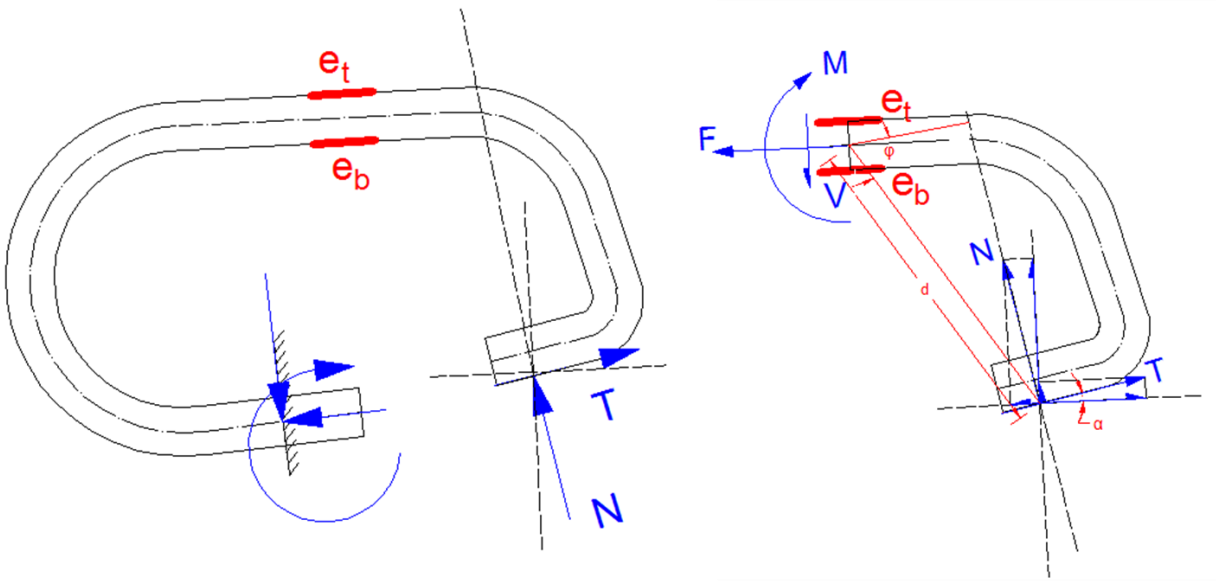

a b

Figure 5.10 Strain Gauge Pattern and Free Body Diagram of the Clip

Again, linear elastic analysis was used in clips to determine the force values. **In Figure 5.10 (b)**, F, M and V are used to show the resultant axial force, bending moment and shear force at the location of the strain gauge pair; N and T are the actual normal and tangential force applied to the clip tip; d, α and φ are the geometric properties. Here, the contact point between the clip tip and the insulator is still assumed to be 0.3 inch from the edge, which agreed with findings from finite-element analysis.

Theoretically, if the normal and tangential components of the clamping force are given, strain at inner and outer surface of the clip e_b and e_t can be found using the following equations (by applying Euler-Bernoulli beam theory):

$$e_t = -\frac{M(t/2)}{EI} + \frac{F}{EA}$$

$$e_b = \frac{M(t/2)}{EI} + \frac{F}{EA}$$

where,

$$M = Nd\cos\varphi + Td\sin\varphi$$

$$F = -N\sin\alpha + T\cos\alpha$$

By running necessary transformations to these equations, the strain measurements can be utilized to calculate the clamping force components N and T. In reality, the dimensions of the clip were not much greater than the length of the strain gauge used in the tests, so the strain reading was easily affected by the hand installation of the gauges. To obtain an accurate result, an alternative way was developed by applying two assumptions:

1) The contact point between the clip tip and the insulator was assumed to be 0.3 inch from the edge;

2) Because a standard clip installation process had been followed, 2,500 lbf normal force was assumed to be applied to each clip.

With these two assumptions, the tangential component of the clamping force could be calculated.

In May 2013 TTCI testing, as stated in the field experimentation plan, instrumented clips were installed at both field and gauge sides of rail-seats E, S U and W for both RTT and HTL (**Figure 3.64**). Before and after the clip installation, the strain values were recorded from each gauge manually using National Instruments Strain Gauge Indicator Box. Clip strains due to the installation process have been subtracted afterwards.

The initial tangential force applied to each clip tip was calculated and shown in **Figure 5.11**, in which the x-axis is the average of the absolute strain value measured from the four strain gauges installed on each clip.

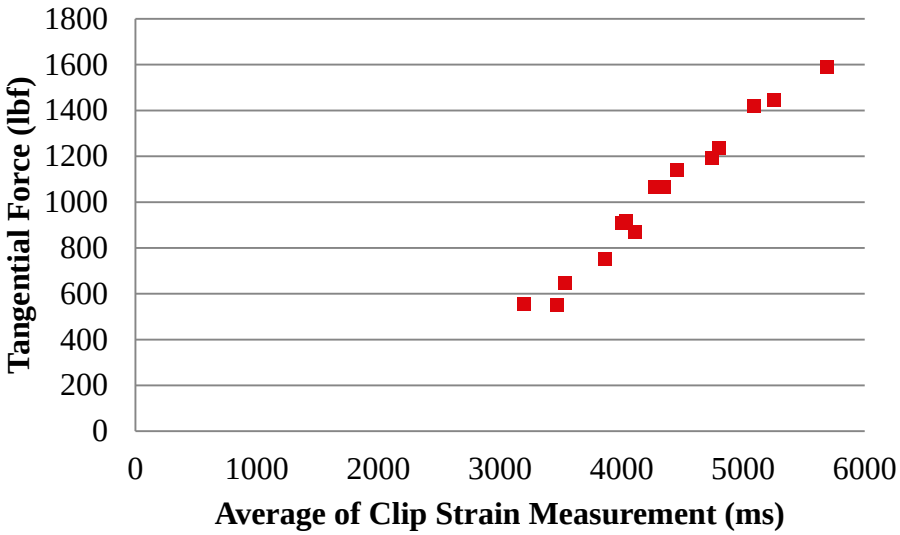

Figure 5.11 Initial Tangential Force Measured at RTT and HTL

From **Figure 5.11**, it was found that the range of the tangential force varied from 551 lbf to 1,588 lbf which was approximately 20% - 60% of the normal force. The maximum tangential force recorded was located at the gauge side of rail seat U at RTT, the maximum tangential and compressive strain under this pair of clamping forces (2500 lbf for normal force, 1588 for tangential force) were calculated as 10,600 ms and -10,500 ms, which were 32% higher than the yielding strain. These observations reveal that the clip design might be inadequate even after the installation.

In addition to the magnitude, the tangential component was found to be always positive, which means after the clip installation process, there was a tangential force pulling the clip tip and holding it in place. It should be noted that the clips tested in this field study were installed

by hand. There is a significant variability in clip strains and forces depending on the installation procedure.

5.2 Change of Clamping Force under Static Wheel Load

The change of the normal and tangential component of clamping force under wheel loads was examined with the SLTM loading frame (**Figure 5.12**). The change of the clamping force of instrumented clips (**Figure 3.28**) was calculated using the methodology developed in Section 5.1.

Figure 5.12 Instrumented Clips Used in SLTM Experimentation

Three loading cases were tested as stated in Section 3.8.1. **Figure 5.13** shows the change of the normal and tangential component of clamping force under a lateral force up to 2 kips applied by PTLF. In general, the change of normal and tangential forces was linear, and corresponded to the increase in the lateral force. When the lateral force was applied, the field

side normal force decreased with the downward movement of the rail base. Also, due to the rail rotation, the gauge side normal force increased with the lifting of the gauge side rail base. When the lateral wheel load was 2 kips, the increment of the gauge side normal force was 66 lbs. The change of all the other forces was less than 25 lbs. Due to the limitation of the lateral load capacity of the single crosstie-rail system with the SLTM, no higher loads were examined. The change of the clamping force under a greater lateral wheel load was discussed in the Field Experimentation Chapter.

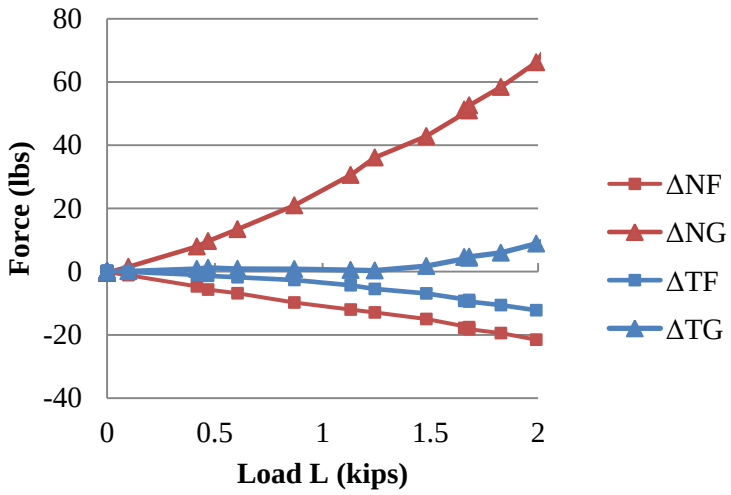

Figure 5.13 Change of Normal and Tangential Forces at Varying Lateral Wheel Loads

With a 2-kip lateral force applied by PTLF, the vertical load was increased to 36 kips (**Figure 5.14)**. Due to the loading eccentricity introduced by the SLTM loading head, the rail section rotated, and the gauge side normal force increased. The change of the gauge side normal force reached 163 lbs, and the change of the field side normal force decreased 73 lbs.

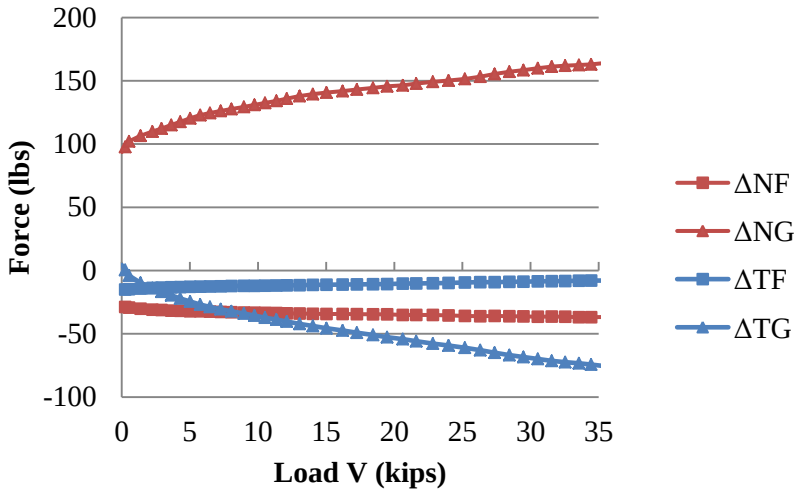

Figure 5.14 Change of the Normal and Tangential Force Under 2 kips Lateral and Various Vertical Wheel Loads

To capture the change of the normal and tangential components of the clamping force under wheel load, the same strain gauge pattern was used as shown in **Figure 5.10** to record the clip deformation. To deal with large amount of data, it is impossible to use the numerical program described above to calculate the increment of clamping force. However, as one vertical displacement measurement (from potentiometer) was recorded from gauge side rail base, the increment of clamping force can be obtained by combing the clip deformation and the clip tip deflection. Because in May 2013 TTCI testing only the vertical rail base measurement at gauge side of the rail was measured, the following discussion will be focused on the gauge side clip behavior.

The change of normal and tangential forces can be calculated using the equations below:

$$\Delta N = D_G \cdot (1250lbs / 0.289in)$$

$$\Delta T = \left(\frac{-e_t + e_b}{2} - \frac{\Delta N d(t/2)\cos\varphi}{EI}\right) \cdot \frac{EI}{d(t/2)\sin\varphi}$$

Where,

ΔN is the change of normal force N

ΔT is the change of tangential force T

e_t and e_b are the strains measured from strain gauges

φ is the angle shown in Figure 1.2

d is the distance shown in Figure 1.2

E is the elastic modulus for steel used for the clips

A is the area of the cross-section of each toe

I is the moment of inertia of the cross-section of each toe

t is the thickness of the clip

D_G is the vertical rail base deflection

The assumptions used for calculation are listed below:

1) The normal component of clamping force (N_F and N_G) can be expressed by $\Delta N=kD_G$ (in linear range), where k is the clip opening stiffness, which can be obtained from the manufacturer manual and FEM analysis, or from simple component testing. For Amsted RPS UAB 2000 clips, k is designed to be 8650 lbf/in, and the initial clamping force (normal component) is 2500 lbf.

2) Displacement vertically to the clip toe can be expressed by the vertical deflection D_F and D_G relative to the crosstie measured at the tip of the rail base. As the inclination of rail base is 14.2°, cos(14.2°)=0.97~1, it is reasonable to use the vertical displacement relative to tie to the displacement vertical to top surface of rail base or the clip toe.

3) When the tangential component of the clamping force is greater than the maximum static friction force, which means the friction cannot hold the clip toe from sliding, there is a relative movement between the clip toe and the rail along the rail base. The vertical component of the sliding relative to the crosstie is assumed to be negligible compared to the vertical deflection at the rail base.

4) The rail base remained straight, which has been examined in the laboratory experimentation. The curvature at rail base was negligible.

Under vertical wheel load, the normal component of clamping force is anticipated to decrease; while under lateral load, the gauge side clamping force will cause yielding. As shown in **Figure 3.64**, instrumented clips were installed at both field and gauge side of the rail at location E, S, U and W. Under current analysis methodology, only the change of clamping force at gauge side can be determined. The Track Loading Vehicle (TLV) was used at TTC to apply the vertical and lateral wheel load.

When only vertical wheel load was applied by the TLV, the rail pad was compressed evenly if the vertical load was applied right above the center of rail seat. The variation of the change of normal and tangential forces was found to be very small, and it is sufficient to use the average value showing the trend. The increment of normal and tangential components of clamping under 0-40 kip vertical wheel load at RTT is shown in **Figure 5.15**, when the TLV static wheel load was applied directly above each rail seat.

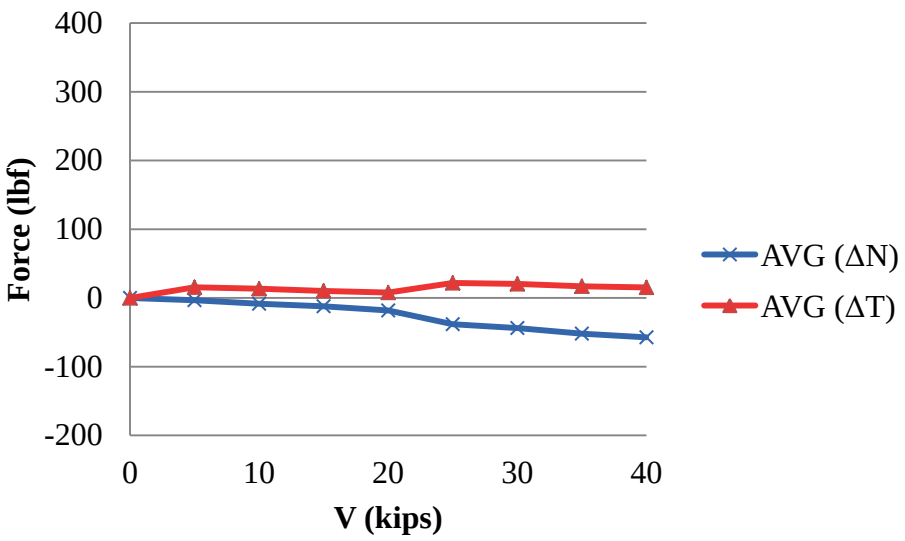

Figure 5.15 Change in Normal and Tangential Force under Various Vertical Wheel Loads

The compression of the rail pad is equivalent to the action of spring relief to the clips. From **Figure 5.15**, it can be seen that the normal component of clamping force decreased slightly, which agrees with this spring relief action. Under a 40 kips vertical wheel load, the average change in the normal component of clamping force was -57 lbf which was -2.3% of initial normal force. And the change of tangential force was only 15 lbf. This observation revealed a fact that there was almost no lateral translation of rail base under pure vertical wheel load.

Because the normal force always decreased and the tangential force almost remained constant under a vertical force, referred to the trend found in **Figure 5.7**, the maximum strain at clips would decrease. In other words, only vertical wheel load was not harmful to the clips.

When the vertical wheel load applied by the TLV reached 40 kip at both sides of rail (at RTT), this vertical force was held while applying a lateral force to both rails pointing to field

side. **Figure 5.16** shows the average increments in normal and tangential force due to this lateral wheel load.

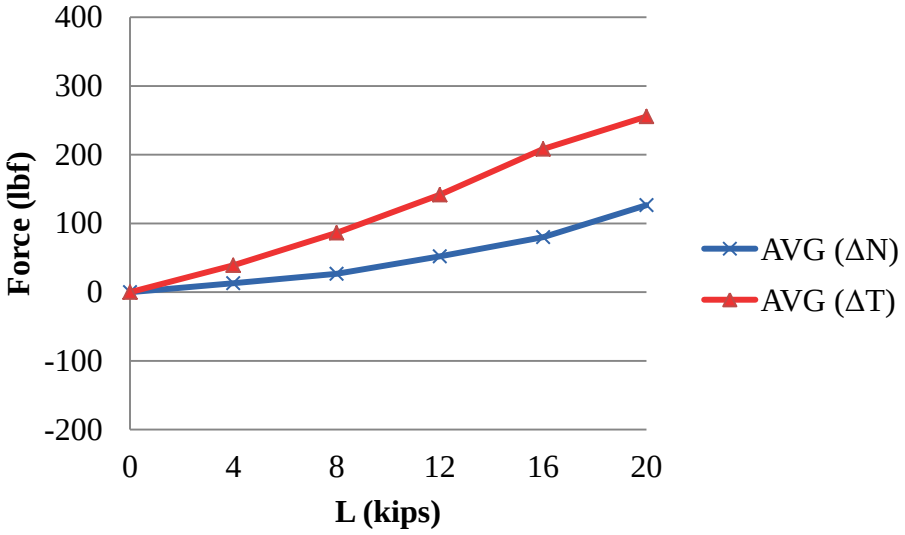

Figure 5.16 Change in Normal and Tangential Force under 40 kip Vertical and Various Lateral Wheel Loads

Due to the rail rotation coming consequently with the lateral wheel load application, the gauge side clips were lifted upwards, and the normal component of clamping force increased as shown in **Figure 5.16**. Gauge side clip at rail seat E experienced the greatest lifting, which led to an average increase of normal force of 127 lbf, which was 5.1% of the initial normal force. From rail displacement measurements, the rail base was found translating towards the field side under a lateral wheel load. Due to this rail movement, the recorded change in tangential force was as large as 256 lbf on average under a 20 kip lateral force. The tangential force recorded from the four instrumented clips agreed very well with each other, varying in a narrow range from 230 lbf to 270 lbf.

Referred to **Figure 5.7**, increase in normal and tangential forces will raise up the maximum strain (both in tensile and compressive). From the calculation, if assuming 2500 lbf normal force and zero lateral force were applied to each clip initially, after 40 kip vertical and 20 kip lateral wheel loads being applied, the normal and tangential forces came up to 2578 lbf and 219 lbf for the gauge side clip at E, 2537 lbf and 129 lbf for S, 2534 lbf and 192 lbf for U, 2630 lbf and 199 lbf for W. The extreme tensile and compressive strain under the final clamping forces were calculated as +/-8200 ms, +/-8000 ms, +/-8100 ms and +/-8400 ms, which were 3.1%, 1.0%, 1.8% and 5.6% higher than the yielding strain.

Because actuators were used to apply the same loadings to both rails at HTL, the static testing on the HTL should be considered as duplicated tests. From the analysis of the results, similar conclusions were found.

As, for the distribution of the change of clamping force, it is hypothesized that the change of clamping forces at rail seats adjacent to the rail seat being loaded is 50% of that at the loaded rail seat. The distribution of the change of clamping force is discussed in this section for when the wheel load was applied over a specific rail seat. Referring to the field instrumentation map shown in **Figure 3.64**, the TLV applied static loading (both in vertical and lateral directions) over crosstie BQ, CS, EU, GW and crib FV and DT. When 40 kip vertical wheel load was applied over the center crosstie EU (at RTT), the distribution of the change of normal and tangential force are shown in **Figure 5.17**.

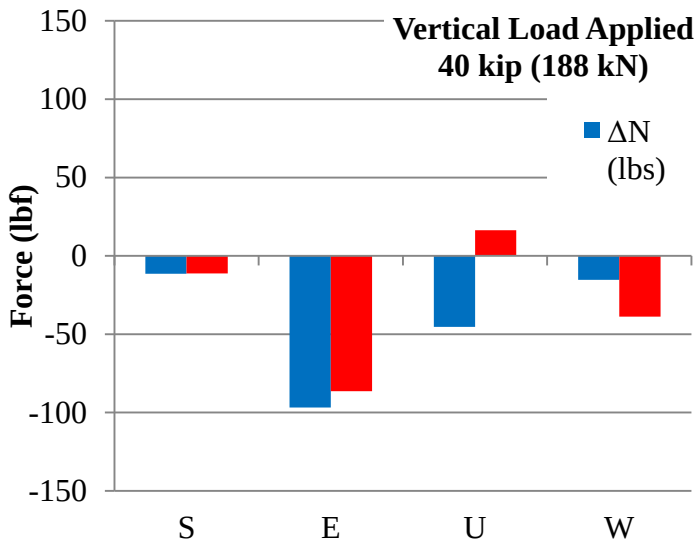

Figure 5.17 40 kip Vertical Load Applied by TLV at Crosstie EU

In general, maximum change of the normal force took place at the loading rail seat. The adjacent gauge side clips recorded less than 50% of the change of normal force. Due to crosstie skewing and uneven support conditions as well as wheel loading eccentricity, the distribution of the change in tangential force didn't follow this trend quite well. The gauge side clip located at the center rail seat U reported a positive value for the change of tangential force, while negative values were read from all the other three clips.

When a 40 kip vertical and a 20 kip lateral wheel load were applied at the rail head above the same crosstie, the distribution of the increment of clamping force is shown in **Figure 5.18**.

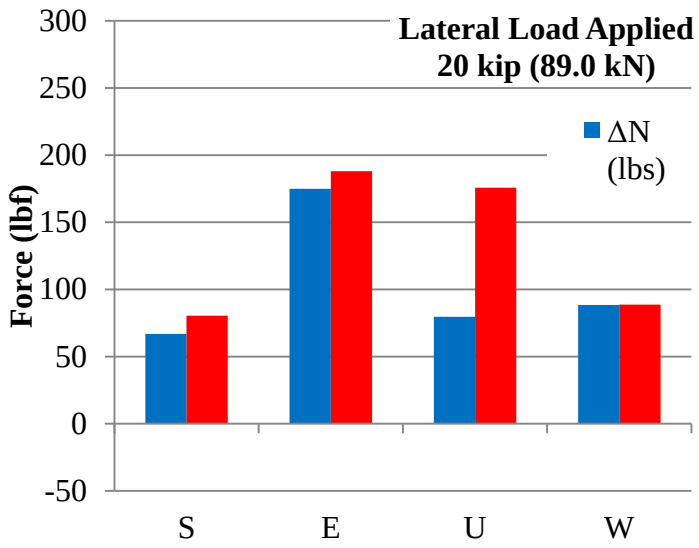

Figure 5.18 20 kip Lateral Load Applied by TLV at Crosstie EU

As seen in **Figure 5.18** above, the increments of normal and tangential forces were 175 lbf and 188 lbf for the gauge side clip E, 80 lbf and 176 lbf for clip U, which were both directly beneath the loading. For the clips at adjacent crossties, about 50% of increment in normal and tangential forces was recorded.

Again, the experimental inspection from HTL brought a similar result, about 50% of both normal and tangential components of clamping forces were recorded from the clips on the crossties adjacent to the loading.

5.3 Change of Clamping Force under Dynamic Wheel Load

5.3.1 Under Constant Speed Wheel Load

It is hypothesized that clamping force may increase past the yielding limit under applied static loads. In this section, the change in clamping force under constant speed wheel loads was examined. Because the constant wheel loads were applied by the TLV moving at a specific

speed, the clips were anticipated to behave similarly as to under the static loads. From the static analysis, the change of clamping force was found to be highly dependent on the lateral wheel load. In the following discussion, the vertical wheel load was held constant at 40 kip as various lateral loads were applied. The speed of the TLV was always set to be 15 mph. Again, as the TLV provided the same loading for both rails, the clip behavior at the high rail and the low rail should not be different. Only the data recorded from RTT is shown.

Figure 5.19 shows the increment of normal and tangential components of the clamping force.

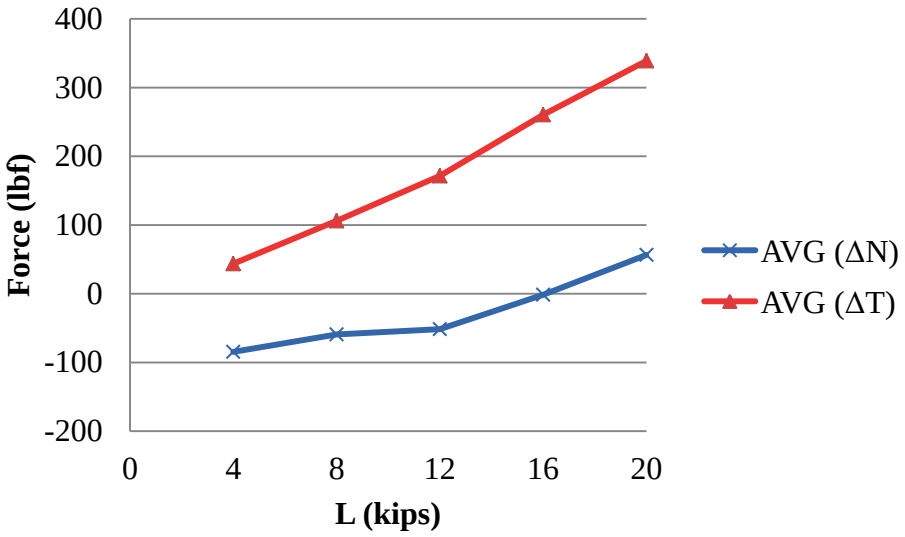

Figure 5.19 Change in Normal and Tangential Force at Gauge Side Clips under 40 kip Vertical Load and Various Lateral Loads (TLV speed = 15 mph)

A greater variation was found in both the normal force and the tangential force. A similar trend was found, and the magnitude of the change of normal force decreased from 127 lbf to 57 lbf under 20 kips lateral force; while the tangential force increased from 256 lbf to 339 lbf.

5.3.2 Comparison Between Passenger and Freight Consist

Before the comparison between the change of clamping forces under passenger and freight, the following hypotheses were made: (i) heavier axle loads from the freight consist will cause greater clamping forces than from the passenger consist; (ii) clamping forces change proportionally to car weight (axle load) (i.e. if one car weighs four times more than another car, the change of clamping forces under this car will also be four times greater); and (iii) peak (extreme) loads are the result of impact loads caused by flaws at the wheel-rail interface.

For the testing conducted at RTT, the passenger consist was made up of one locomotive, which weighed 260 kips, and nine passenger cars, which weighed 87 kips each. Tests for the passenger consist were run at 2 mph, 15 mph, 30 mph, 60 mph, 80 mph, 90 mph and 105 mph. The freight consist was made up of one locomotive which weighed 260 kip and ten freight cars of three different weights: 260 kip, 286 kip and 315 kip. Tests for the freight consist were run at 2 mph, 15 mph, 30 mph, 45 mph, 60 mph and 70 mph. The gauge side clip at the center rail seat in the testing section (rail seat U) will be focused on in the following discussion.

As lateral wheel load highly affected the rail rotation or the raise up of the rail base at gauge side, it might also control the change of clamping force. **Figure 5.20** and **Figure 5.21** show the correlation between the change of normal and tangential component of clamping force with the lateral wheel load. Generally, the tangential force was found to be more correlated with the lateral wheel load than the vertical wheel load. When the lateral wheel load went up, the change of tangential force increased. Here, it should be noticed that the lateral wheel load was measured at the center of each crib, and it might be different with the actual lateral load applied directly above clips. This can be the main source of the variation shown in **Figure 5.20** and **Figure 5.21**.

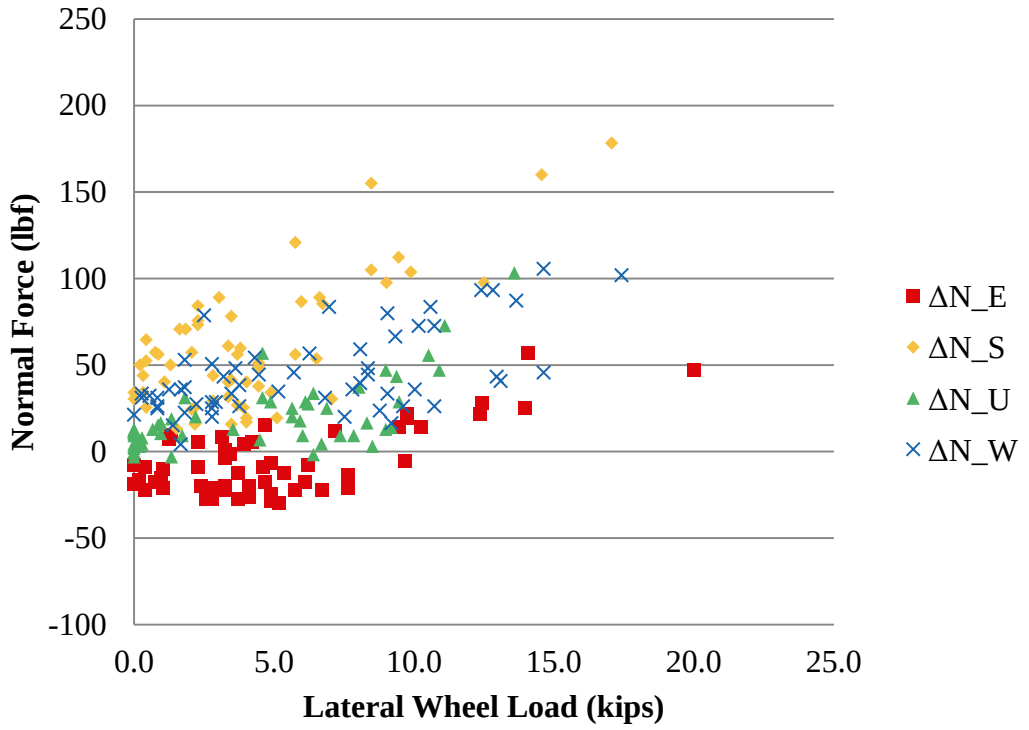

Figure 5.20 Change of Normal Force of Gauge Side Clips under 45 mph (HTL)

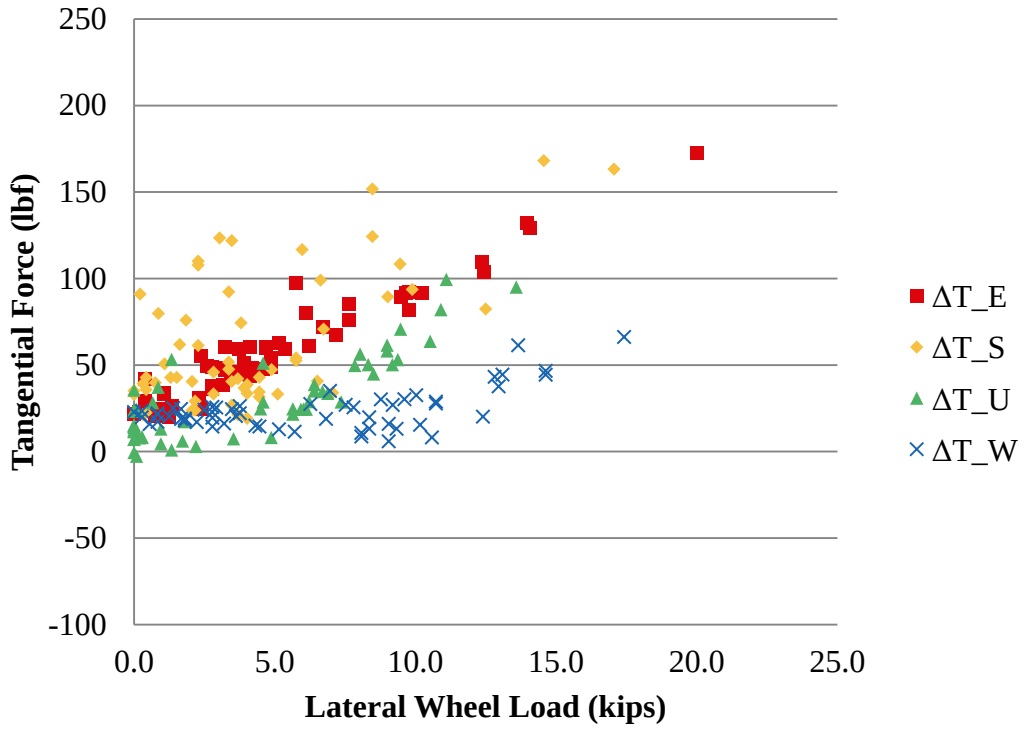

Figure 5.21 Change of Tangential Force of Gauge Side Clips under 45 mph (HTL)

Figure 5.22 and Figure **5.23** show the change of normal and tangential components of the clamping force with respect to the train speed and car weight for the passenger consist. **Figure 5.24** and **Figure 5.25** show the change of normal and tangential components of the clamping force measured from this clip with respect to the train speed and car weight for the freight consist.

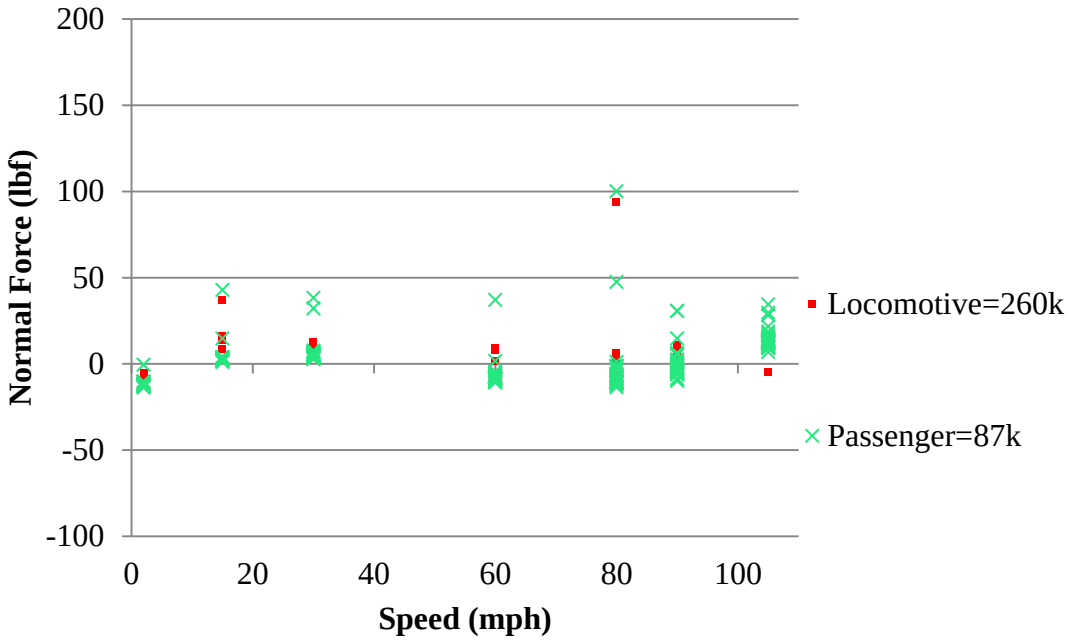

Figure 5.22 Change of Normal Force of Gauge Side Clip at Rail Seat U (RTT)

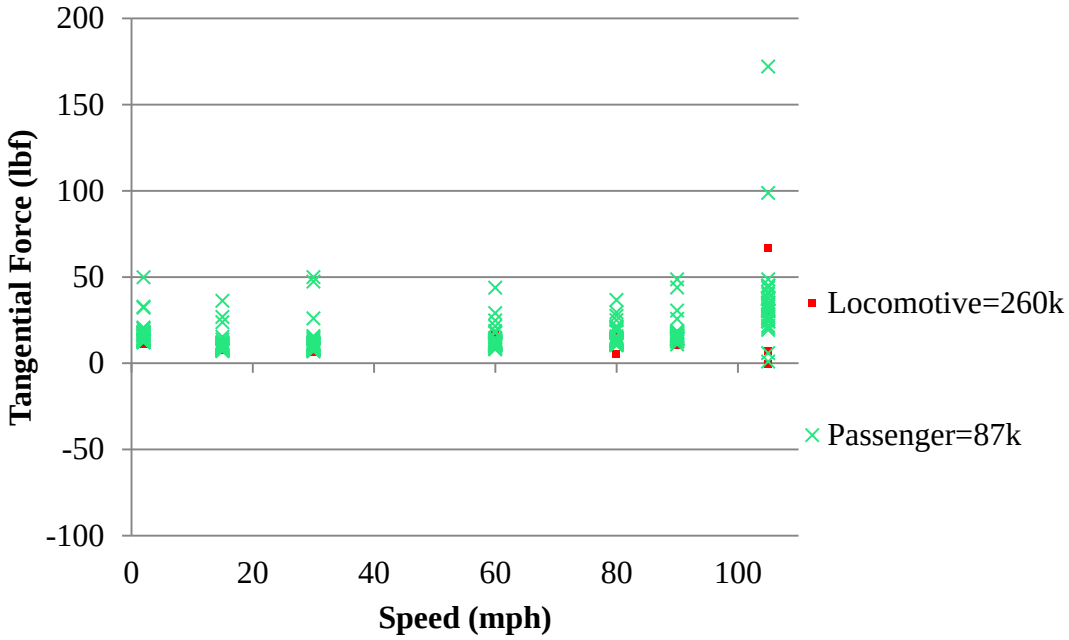

Figure 5.23 Change of Tangential Force of Gauge Side Clip at Rail Seat U (RTT)

From **Figure 5.22** and **Figure 5.23**, it can be seen that the maximum change of both normal and tangential forces was below 200 lbf. The effect of train speed was not significant to the magnitude of the change of forces. Additionally, although the locomotive weighed twice as much as the passenger car, the change of clamping forces recorded under the locomotive was not twice that of the passenger cars. When the train speed exceeded 80 mph, the change of clamping force (both normal and tangential components) might be even higher under lightweight passenger cars. With the train speed of 105 mph, the change of tangential force under the 87 kip passenger car was as high as 175 lbf. This could be because higher speeds may cause larger impact loads, which was confirmed from sections of the analysis of vertical wheel load and rail seat load. By comparing with the change of the normal and tangential forces measured from the other instrumented clips, similar conclusions were made.

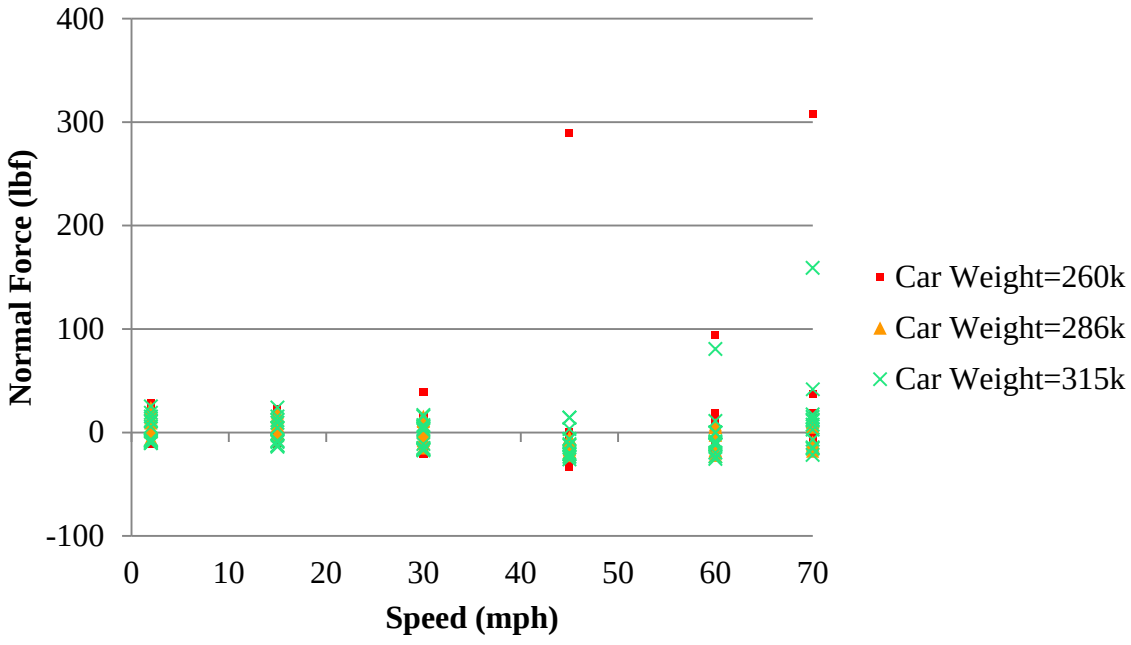

Figure 5.24 Change of Normal Force of Gauge Side Clip at Rail Seat U (RTT)

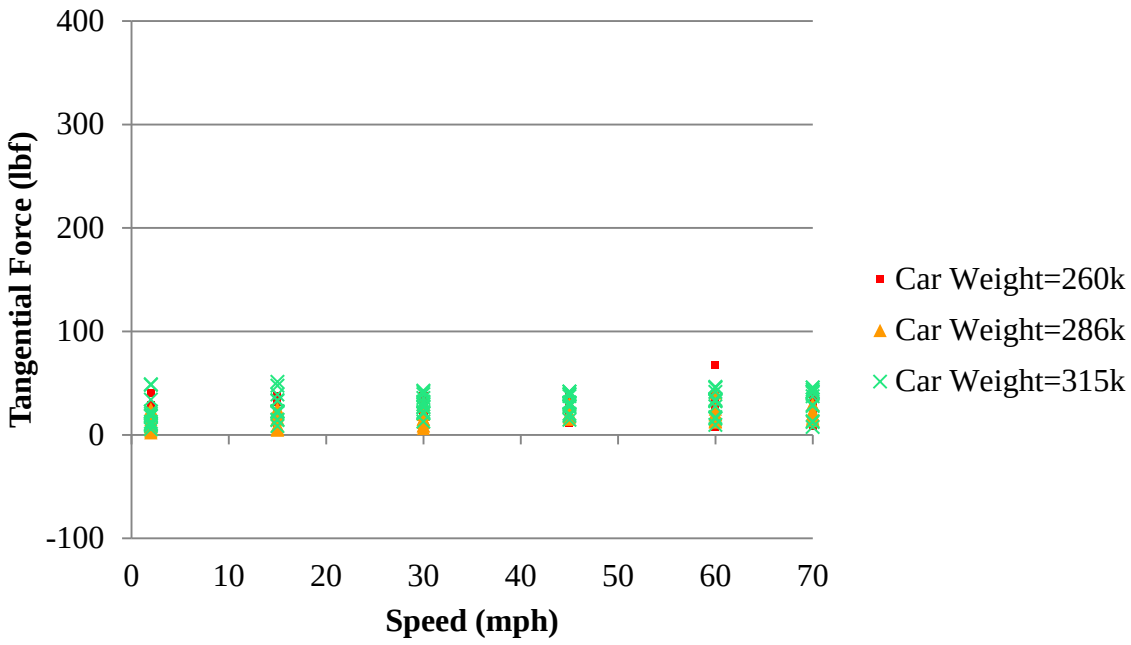

Figure 5.25 Change of Tangential Force of Gauge Side Clip at Rail Seat U (RTT)

From **Figure 5.24** and **Figure 5.25**, even though the change of normal and tangential force was mostly below 100 lbf, the extreme value for the change of the normal force was 310 lbf, which was from the 260 kip car running with a speed of 70 mph. Because a wheel with a flat spot was set on that 260 kip car, the big change in the normal force can be attributed to an impact load caused by the flat wheel. The change of the tangential force remained below 100 lbf, even under the flat wheel running with a high speed. Similarly as the finding from the passenger series, the effect of train speed was not significant to the magnitude or the variation in the change of clamping forces. By comparing with the change of the normal and tangential forces measured from clips E, S and W, similar conclusions were made.

The maximum change of normal forces was found to be 142 lbf, which was much lower than the 310 lbf at RTT. The reason for this is likely the impact load caused by the flat wheel on the 260 kip freight car was more significant at the higher speed. At HTL, the maximum testing

speed was only 40 mph. The magnitude of the change in normal or tangential force was found to be higher than RTT, however that should be explained by the variability of each single crosstie and clip. Until more instrumented clips were tested from both the low rail and high rail, any conclusion drawn from the comparison between the clips at these two rails should be considered immature.

5.4 Evaluation of Current Clip Design

Based upon the analysis made above, the maximum strain of a clip is approaching 90% of the yielding point of steel right after installation. Due to the increase of clamping force caused by the applied wheel load, it is highly possible that the maximum strain attains the plastic zone. Therefore, it can be concluded as the safety margin set in the clip design is not enough. One possible solution is to close up the gap between the two toes in the current design, but that requires a higher material consumption.

6. Evaluation of the Structural Behavior of Concrete Crosstie

To investigate the load path in the concrete, embedment strain gauges were installed in the concrete forms before the sleepers were cast, and surface strain gauges were installed after casting. Through the analysis of these measurements, the load path can be determined.

High strength concrete is used to manufacture the concrete crossties. The concrete properties including its strength and Young's modulus were given by the crosstie manufacturer. The average strength and Young's modulus obtained from the compressive cylinder test are shown in **Table 6.1**.

Table 6.1 Concrete properties

	$f'_c(psi)$	$E_c(psi)$
1 days	--	3.68×10^6
7 days	--	4.00×10^6
28 days	11,730	4.26×10^6

As the laboratory and field experiments were performed one year after the concrete was cast, the 1 year concrete strength and Young's modulus was also tested. A core drill was used to remove cylinder samples from the concrete crossties. Six concrete core cylinders with a diameter of 3 inches and height of 3 inches were tested, the average concrete strength obtained from the compressive test were converted to ACI standardized uniaxial strength. The concrete strength at 1 year was found to be 11,000 psi which is slightly lower than its 28 days strength; this is attributed to the small sample size. The Young's modulus was found to be 4.5×10^6 psi which is slightly greater than its 28 days modulus. The tensile strength (cracking stress) of concrete was not measured directly but can be obtained using the equation below:

$$f'_t = 7.5\sqrt{f'_c} = 7.5\sqrt{11,000} = 787\,psi$$

The material properties obtained from compressive core test were used in the following analysis.

6.1 Distribution of Crosstie Bending Moment Measured from Laboratory and Field Experiments

The instrumented concrete crosstie was tested using the Static Tie Tester (STT). First, the bending behavior of a concrete crosstie was evaluated through the center-positive bending test (**Figure 3.42**). The testing specimen was not loaded to the point of flexural tension cracking, but the bending strains acquired from the crosstie surface strain gauges were used to compare with the analytical calculated values.

The maximum vertical load used in this experiment was calculated to make sure the crosstie would not crack when the loading was applied (**Figure 3.43**). The cracking moments at the rail seats and center were calculated using the Euler-Bernoulli beam theory. The concrete tensile strength was obtained in Section 3.6.2, and the crosstie dimensions and the locations of the prestressed wires were provided by the manufacturer (CXT). The calculated cracking moments at rail seats and the crosstie center are shown in **Table 6.2**. The positive cracking moment was 196.8 kips-in at the crosstie center, and the critical loading was calculated as 13.1 kips. In the center-positive bending test, the maximum vertical load was limited to 10 kips, and no cracking was found.

Figure 6.1 Vertical Rail Seat Loading Applied by STT

As shown in **Figure 3.42**, six strain gauges were installed on one side of the crosstie. The pair of strains recorded from the crosstie center was used to calculate the Young's modulus of concrete. Theoretically, the lateral strain immediately above the support should be zero, and the strain was indeed very small (<10 ms). This test specimen and the recorded strains were used in the subsequent laboratory tests with the Full Scale Track Loading System (TLS) and the field tests.

Table 6.2 Concrete Crosstie Cracking Moments (Values in kips-in)

Moment	Rail seat	Crosstie center
Positive	405.6	196.8
Negative	219.6	256.8

When 10 kips of vertical load was applied, the top strain (S_{L4}) was -82 ms in compression and the bottom strain (S_{L3}) was 43 ms in tension. The load versus strain relationship was relatively linear throughout the loading process, and the strain went back to zero when the load

was removed. Using the Euler-Bernoulli beam theory, the centroid axis was found to be 3.8 inches below the top surface or 3.7 inches above the bottom surface of the crosstie. This experimental result agreed with the location of the actual centroid axis of the transformed cross-section. Young's modulus of the concrete was calculated as 4,525 ksi, which was close to the modulus we obtained in Section 3.6.2 with an error of 0.6%.

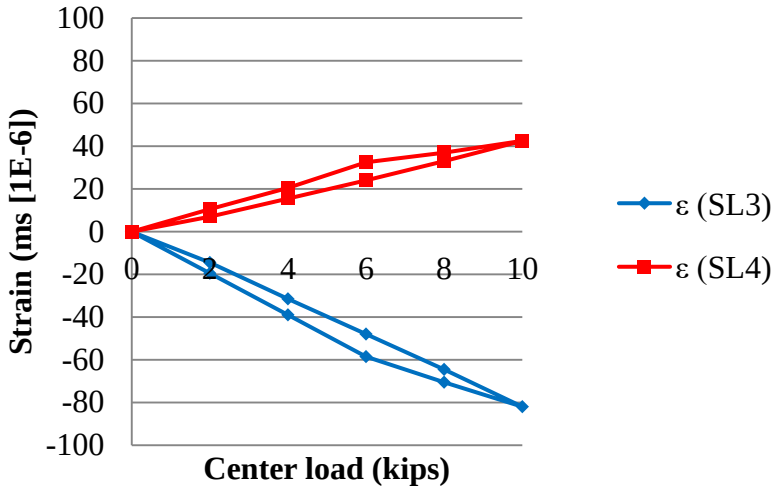

Figure 6.2 Crosstie Strain Recorded from Center-Positive Bending Test

In the field investigation, external strain gauges were used to determine the bending moment at the integral sections of the concrete crossties. As what was described in the section 3.8.4, six strain gauges were installed on each crosstie (CS, EU and GW in the field instrumentation map) to make three measurements which including the moments at both rail seats and the moment at the crosstie center. Due to the limitation of the maximum number of the channels that were available, only the strain gauges on crosstie CS and EU were connected to NI DAQ. The locations for the surface strain gauges are shown in **Figure 6.3**

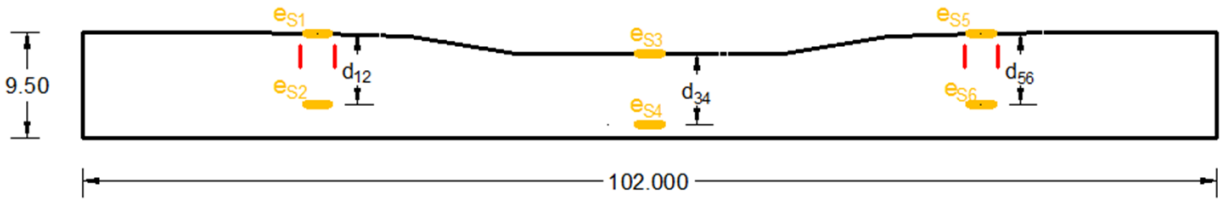

Figure 6.3 Locations of Concrete Surface Strain Gauges

The following equations are used to calculate the bending moments:

$$M(railseat1) = (e_{S2} - e_{S1})E_c I_{12} / d$$
$$M(center) = (e_{S4} - e_{S3})E_c I_{34} / d$$
$$M(railseat2) = (e_{S6} - e_{S5})E_c I_{56} / d$$

Where,

e_{S1}-e_{S6} are the strains recorded from concrete surface strain gauges as noted in **Figure 6.3**

E_c is the elastic modulus of concrete material

I_{12}-I_{56} are the moment of inertia of the concrete cross section at the location of each strain gauges pair

d is the vertical distance between the two strain gauges in each pair

The current design criterion mandates that cracking should not occur under the design wheel load. To determine if this criterion is satisfied, the measured bending moments are compared with the cracking moments found for a specific crosstie using linear elastic analysis. These cracking moments are the same as calculated before and listed in **Table 6.1**.

The distribution of the bending moments along a crosstie can be determined from the three moment measurements measured by the embedment strain gauges. Using these measured moments, the support conditions underneath the crosstie can be back-calculated. The support

conditions found from the testing are used to compare with the “newly tamped track” defined in AREMA recommendations, where the ballast reaction occurs beneath the rail seats with little to no reaction at the tie center.

Referring to AREMA, under dynamic interaction of wheel and rail, an amplification factor can be used to calculate the crosstie bending moment. Currently, AREMA calls for a 200% increase (or a factor of 3). This amplification factor can be found from field testing by dividing the dynamic load recorded in the field by the static wheel load (from the known car weight).

It is expected that under a given support condition that the bending moment will increase with increasing vertical wheel load. Additionally, it is hypothesized that the bending moments measured in field testing at the TTC will not exceed the cracking moment of the crosstie. As stated in the field experimentation plan, the TLV was used to apply the static wheel load which including the vertical and lateral forces being loaded separately. For both of the 2012 and 2013 testing, data was collected from these embedment strain gauges. For both of the tangent track (RTT) and curved track (HTL), static wheel loading was applied over each instrumented rail seat and the crib between the rail seats. In 2012 testing, the data was re-zeroed to 5 kips. Thus, all the rail seat loadings recorded in 2012 started to increase beginning at 5 kips vertical wheel load.

In the following analysis, the wheel-rail contact point was assumed to occur directly over the center line of a rail seat. And thus, the wheel load is modelled as a point load occurring at the center of the rail base. Rail cant is also neglected in this analysis. **Figure 6.4** and **Figure 6.5** show the bending moments measured from crossties CS and EU under 0-40 kips vertical wheel load, when the TLV static wheel load was applied directly above each crosstie.

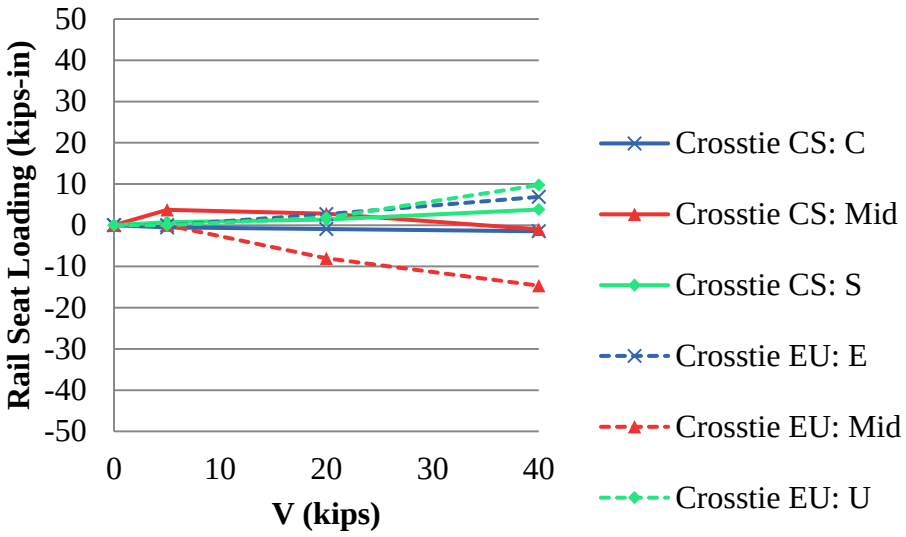

Figure 6.4 Crosstie Bending Moments Under Various Vertical Wheel Loads (RTT, 2012)

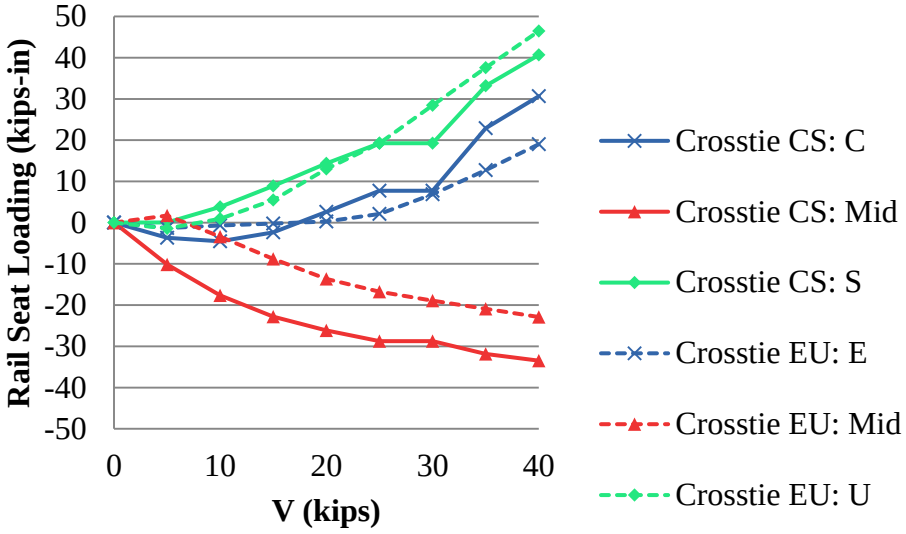

Figure 6.5 Crosstie Bending Moments Under Various Vertical Wheel Loads (RTT, 2013)

The bending moments recorded from 2012 testing were always positive and were no higher than 10 kips-in at rail seats. At the crosstie center, the bending moments were always negative and no greater than 15 kips-in. In 2013 testing, the bending moments recorded from crossties showed a similar trend, but the magnitude for both positive and negative bending

moments were higher. The positive bending moments at rail seat could be as high as 47 kips-in, and the negative moments at crosstie center could be -33 kips-in in maximum both under a 40 kips wheel load. In both tests, if the wheel load was higher, higher bending moments were read from crossties. The bending moments recorded were positive at the rail seats and negative at the crosstie center. Generally, the bending moments measured were much lower than the crosstie cracking moment shown in **Table 6.1**. This shows that under these support and loading conditions there is no expectation of cracking in the crosstie.

One interesting point shown in **Figure 6.5** was that the bending moments at rail seat U didn't start to increase until the vertical wheel loads reached 10 kips; and for rail seat E, the bending moment didn't increase until the wheel load was as great as 20 kips. For rail seat C, the bending moments even dropped below zero (i.e. negative moments) at first, then turned back to increase at about 10 kips vertical load. This suggests that there was some separation between the bottom of the tie and the ballast and a pre-load was required to engage the ballast and cause tie bending. This is commonly called "hanging tie".

A bending moment diagram for a crosstie can be drawn by connecting the bending moments measured with the strain gauges placed at rail seat and crosstie center. This bending moment diagram can then be used to estimate the support conditions. Crosstie EU from 2013 testing is taken as an example to illustrate the methodology of the support condition analysis. As shown in **Figure 6.6 (a)**, 40 kips vertical wheel loads were applied to both rails directly above the rail seat E and U. The three measurements of bending moment were marked in **Figure 6.6 (b)** and were connected with straight lines to express the distribution of bending moment along the crosstie.

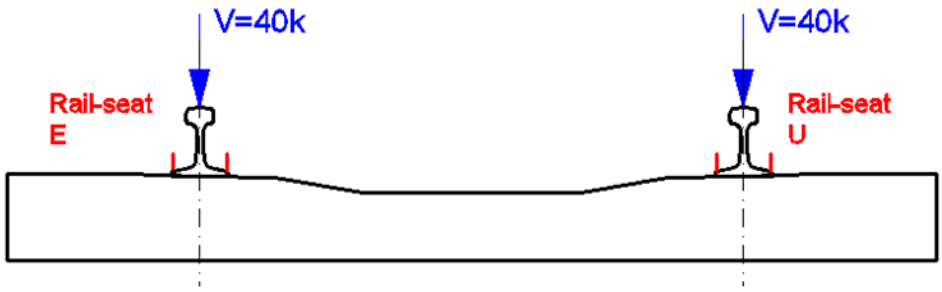

a)

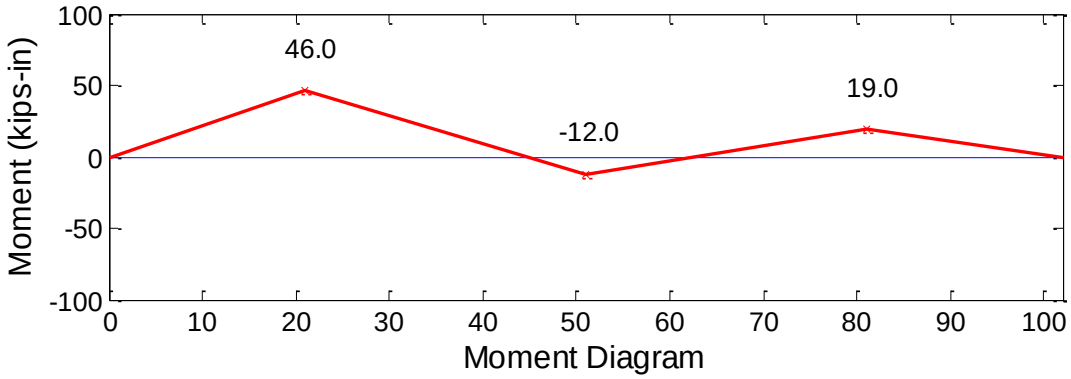

b)

Figure 6.6 a) 40 kips Vertical Wheel Loads Applied to Both Rails b) the Distribution of Bending Moment Along the Crosstie

The rail seat reaction forces measured from the embedded strain gauges were found as 28.5 kips at rail seat E and 13.5 kips at rail seat U. A numerical program was developed with Matlab to determine the support conditions based on the bending moment values and the applied loads. The measured rail seat loads and the calculated support conditions are shown in **Figure 6.7 (a)**. The distribution of bending moment along the crosstie under this loading and support conditions is calculated and shown in **Figure 3.5 (b)**. The calculated bending moments (**Figure 6.7 (b)**) under the assumed support conditions matched the bending moment measurements

(**Figure 3.4 (a)**) quite well, except for at the center of the crosstie. Because the magnitude of the bending moment was small (1 kip rail seat reaction force can result in as much as 15 kips-in bending moments at the crosstie center, depending on the support width), this error is within the tolerance. These assumed support conditions suggest that that neither the ends nor the center region of the crosstie were in contact with the ballast. This observation partially conflicts with the "newly tamped track" assumption made in AREMA, in which both ends of the crosstie are supported.

In laboratory tests conducted at the TLS, two more locations between each rail seat and the center of a crosstie were examined. With the help of more measurements, a more detailed supported condition could be found through the same computer program; and the simulated moment diagram under this boundary condition shows a better fit (**Figure 6.8**)

Ultimately, the measured bending moments fell far below the theoretical cracking moments listed in **Table 3.1**. This suggests that there is no cracking occurring under the given loading and support conditions.

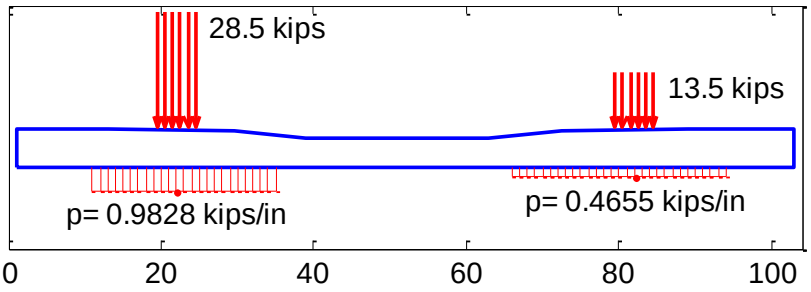

a

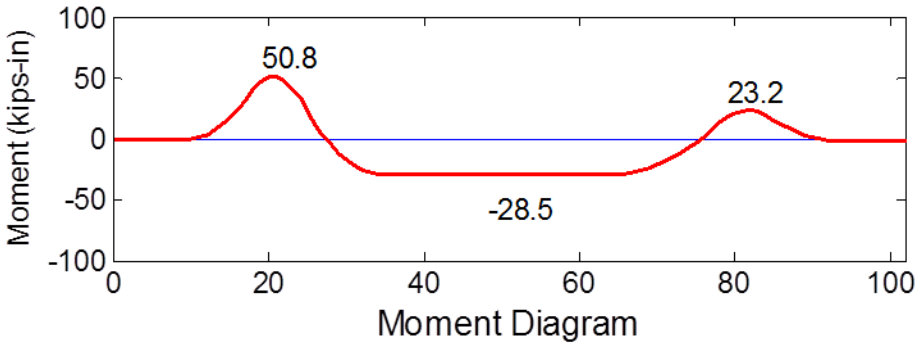

b

Figure 6.7 a) The Loading and Support Conditions for the Crosstie (Rail Seat Loading from Measurements, Support Conditions from Calculation; b) the Distribution of Bending Moment Along the Crosstie from Calculation

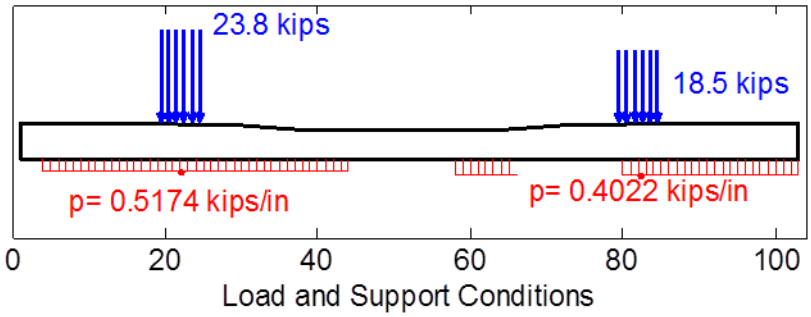

a

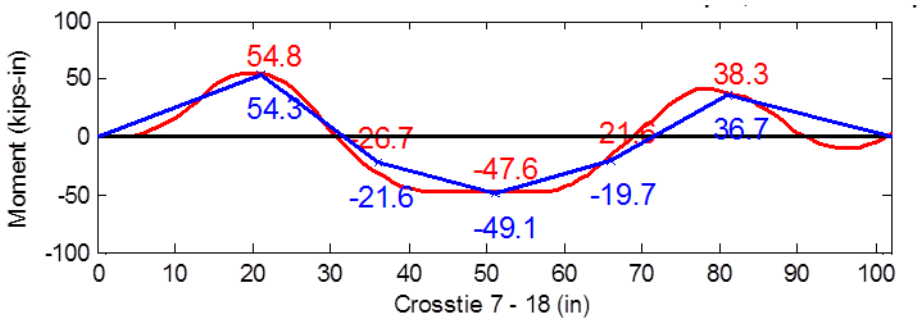

b

Figure 6.8 a) The Loading and Support Conditions for the Crosstie (Rail Seat Loading from Measurements, Support Conditions from Calculation; b) Measured (Blue) and Simulated (Red) Moment Diagram

It was hypothesized that the application of lateral load would not affect the magnitude of the rail seat moment by more than 5%, but would cause a significant (>20%) increase in the magnitude of center moment. In the field testing, the same lateral loads were applied by the TLV to both rails simultaneously, which differed from the lateral loading caused by train runs. Theoretically, the increment of the crosstie bending moment at rail seat is equivalent to the lateral force going into each rail seat (including the friction force below the rail base and the

lateral force going through the shoulder face) multiplied by the vertical distance between the wheel-rail contact point and the rail seat. The effect of the lateral wheel load (RTT) is shown in **Figure 6.9** and **Figure 6.10**. The 40 kips vertical wheel load was maintained, and a lateral wheel load was applied monotonically up to 20 kips.

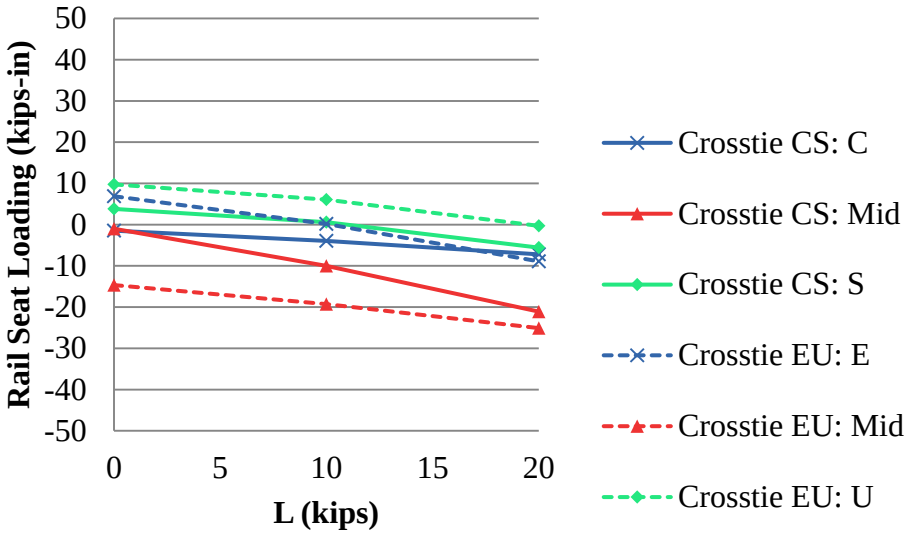

Figure 6.9 Crosstie Bending Moments Under Various Vertical Wheel Loads (RTT, 2012)

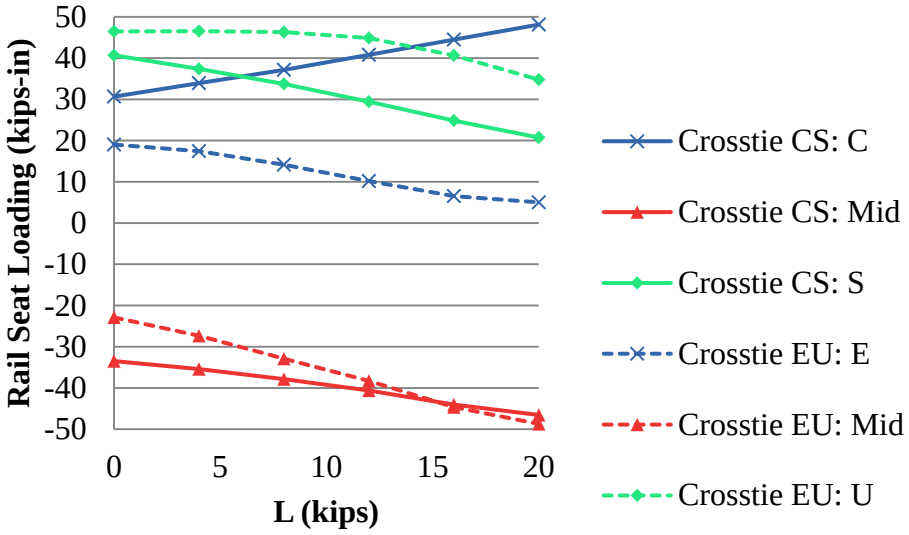

Figure 6.10 Crosstie Bending Moments Under Various Vertical Wheel Loads (RTT, 2013)

Figure 6.9 and **Figure 6.10** show that the application of lateral forces would lead to a change in the magnitude of the rail seat bending moments by more than 5%. This rejects the initial hypothesis. Interestingly, there was a trend of reduction in rail seat bending moment. An exception was the bending moment recorded from rail seat C in 2013 testing, where the value went up with an increasing lateral force. This could be explained by the change of support condition due to the rotational deformation of the crosstie under a lateral force. Similar results were found during testing on the HTL. In summary, applying a lateral load causes a significant (>5%) decrease in magnitude of rail seat bending moment. Additionally, **Figure 6.9** and **Figure 6.10** show that the application of lateral forces would lead to an increase in magnitude of center bending moment by more than 20%. This supports the hypothesis and suggests that lateral load has a significant impact on the bending moment at the crosstie center. At the same time, it should be noticed, the lateral load in this field testing was applied by lateral actuator to both rails at the same time with same magnitude, which conflicts with sources of lateral load under dynamic train passage. The dynamic train passage testing data suggests that the lateral load going through one rail was due to the flange contact and frictions; and the lateral load going through the other rail was only due to frictions. Therefore, the lateral force applied to both rails is assumed to have the same direction with different magnitude.

To fully under the load path going through the concrete crossties as well as the support conditions, it is worth well to examine the crosstie global displacements. With the TLS in laboratory tests, under vertical loading, vertical and lateral crosstie global displacements were measured from the end of each crosstie (**Figure 6.11** and **Figure 6.12**). The deflections (both in vertical and lateral directions) measured from crosstie 6-17 and 8-19 were found higher than the others, although very little rail seat reaction force was recorded. This observation implied that

the rail seat load doesn't necessarily correlate with crosstie global vertical displacement. The large deflections were resulted by the poor support conditions below these two rail seats. When a 40 kip vertical wheel load was applied, the vertical crosstie displacement varied between 0.030 inch (crosstie 4-15) and 0.134 inch (crosstie 8-19). The crosstie lateral displacements were oriented toward the field side, and ranged from 0.008 inch (crosstie 4-15) to 0.057 inch (crosstie 8-19).

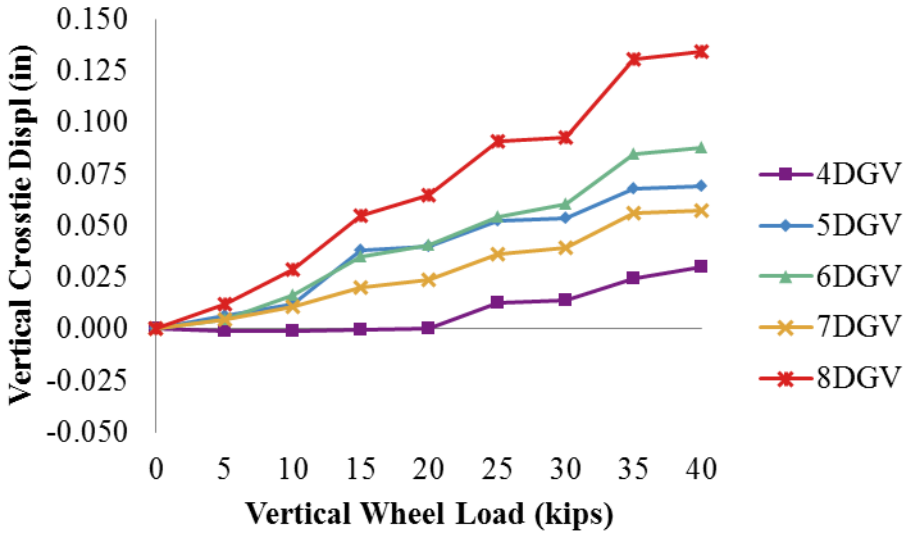

Figure 6.11 Crosstie Vertical Deflection Under Vertical Wheel Loads Applied Directly Over Each Crosstie

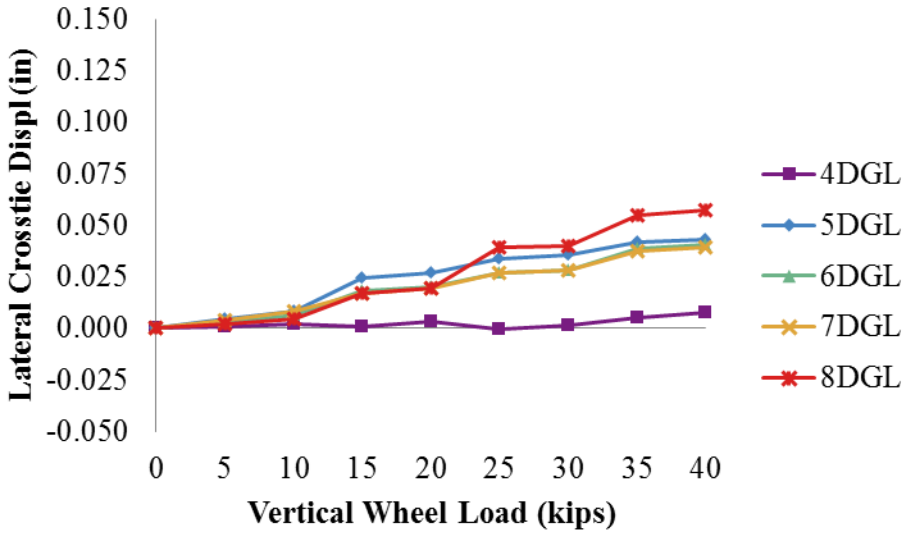

Figure 6.12 Crosstie Lateral Deflection Under Vertical Wheel Loads Applied Directly Over Each Crosstie

In the field testing, under dynamic wheel loading, it was hypothesized that the average of crosstie bending moments would be about the same as under static loading. Also, the dynamic wheel loading would cause large variation in crosstie bending moments. In addition, it was hypothesized that dynamic amplification factor in bending moments is directly proportional to the train speed. The passenger train series consisted by one locomotive which weighted 260 kips and nine passenger cars which weighted 87 kips. Different speeds of train were tested which including 2 mph, 15 mph, 30 mph, 60 mph, 80 mph, 90 mph and 105 mph. When each train wheel was rolling above the instrumented crossties CS, EU and GW, the bending strains were recorded by concrete surface strain gauges. Crosstie bending moments were calculated from these external strains. The calculated bending moments with respect to the train speed and car weight are shown in **Figure 6.13** and **Figure 6.14** from 2013 testing.

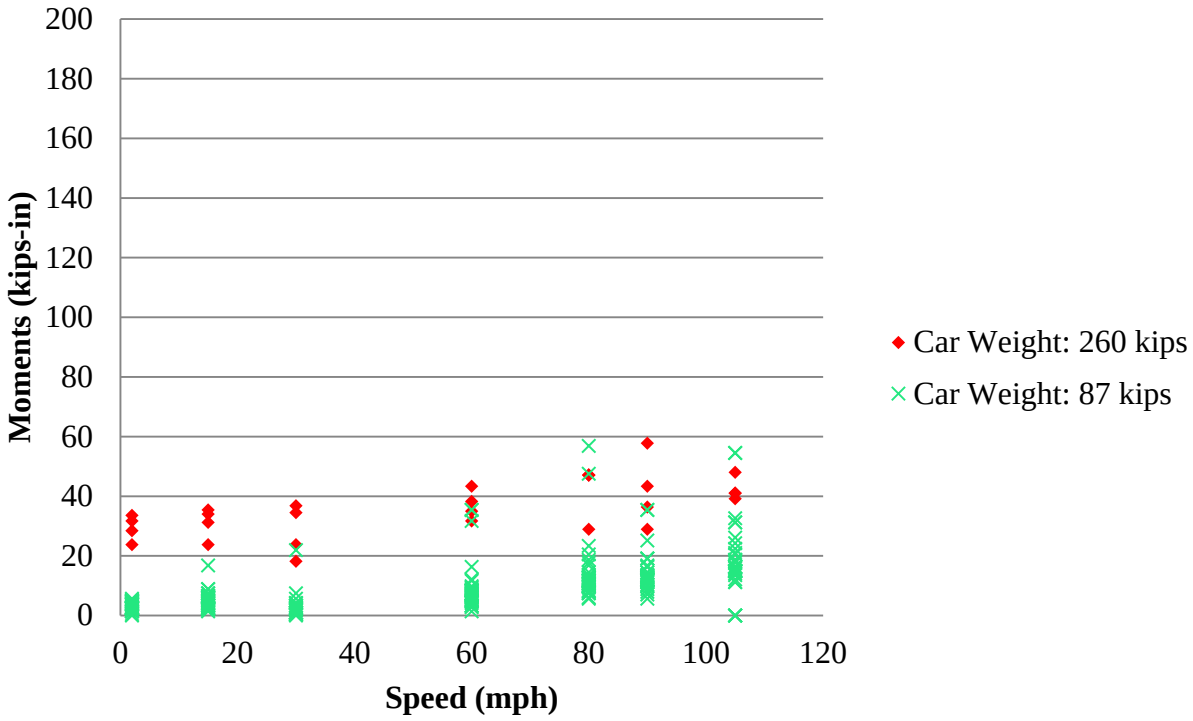

Car Weight	Speed	2 mph	15 mph	30 mph	45 mph	60 mph	70 mph
260	Max	34	35	37	58	43	47
	Mean	29	31	28	42	37	43
	Min	24	24	18	29	32	29
286	Max	6	17	22	35	35	57
	Mean	3	5	1	14	9	14
	Min	-1	1	-5	6	1	6

Figure 6.13 Bending Moments Recorded from Rail Seat S Corresponding to the Car Weight and Train Speed (RTT, 2013)

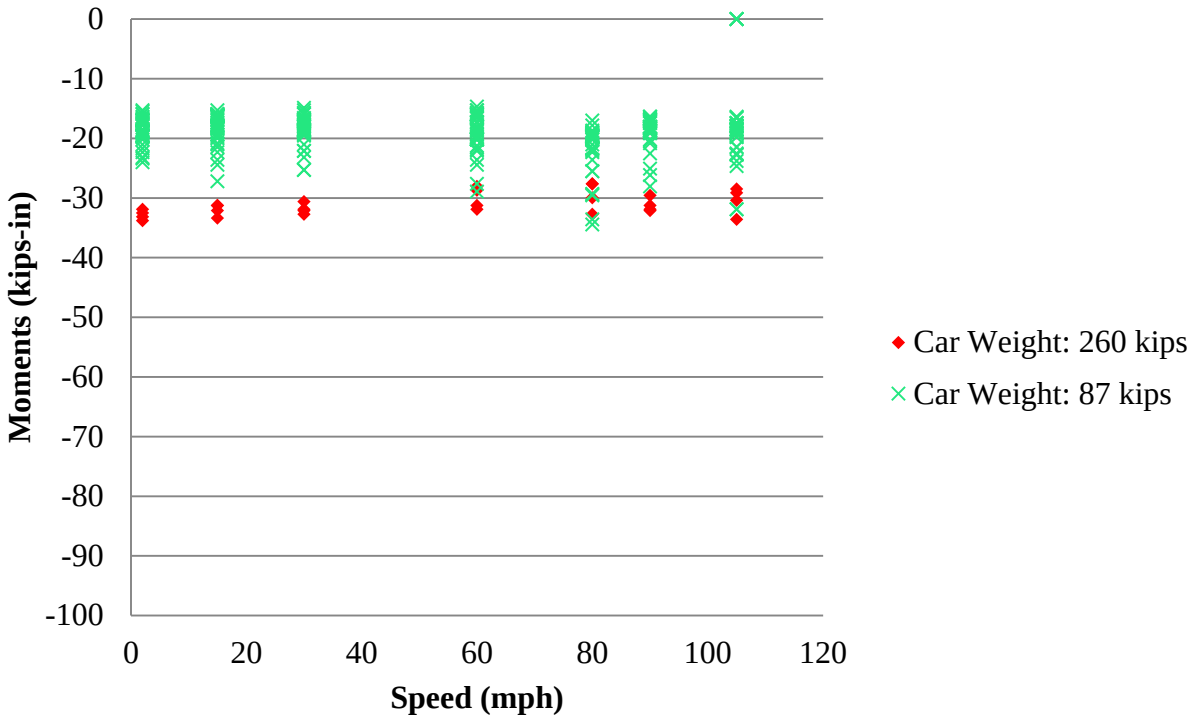

Car Weight	Speed	2 mph	15 mph	30 mph	45 mph	60 mph	70 mph
260	Max	-32	-31	-31	-30	-28	-30
	Mean	-33	-32	-32	-31	-30	-32
	Min	-34	-33	-33	-34	-32	-33
286	Max	-15	-15	-15	-16	-15	-17
	Mean	-19	-18	-19	-19	-19	-22
	Min	-24	-27	-25	-28	-29	-34

Figure 6.14 Bending Moments Recorded from the Center of Crosstie CS Corresponding to the Car Weight and Train Speed (RTT, 2013)

Both the locomotive (260 kips) and passenger cars (87 kips) had four axles, and the average static wheel load can be roughly calculated as the car weight divided by eight (the number of wheels per car). Thus, the static wheel load for the locomotive and passenger car were approximately 32.5 kips and 10.9 kips, respectively. Referring to the static bending moment measurements shown in **Figure 6.5**, these wheel loads should correspond to bending

moments at 28 kips-in and 5 kips-in, respectively for rail seat S. Applying these same principles to the center bending moment of crosstie CS, the static estimates are -30 kips-in for the locomotive and -19 kips-in for the passenger car. In **Figure 6.13** and **Figure 6.14**, it can be seen that the measured bending moments are close to these values, regardless of the train speed. It is important to note that the variation was found to be greater at higher train speeds. For example, the bending moment recorded at rail seat S in **Figure 6.13** for a train speed of 105 mph varied from 1 to 51 kip-in, whereas at 2 mph it only varied from 1 to 8 kip-in.

The freight train series consisted of one locomotive (with six axles) with weight of 390 kips and ten freight cars (with four axles) with weights of 260, 286, and 315 kips. The train speed ranged from 2 to 70 mph. The bending moments with respect to train speed and car weight are shown in **Figure 6.15** and **Figure 6.16** from the 2013 testing.

The freight train passes resulted in behavior similar to the passenger train. Generally, the magnitude of the crosstie bending moment was not greatly affected by the train speed, but train speed did increase the variance of bending moments recorded. A good example of this increased variation can be found at rail seat S with train speed of 45 mph. Due to the dynamic interaction, the bending moment under a 260 kip weight freight was recorded as high as 164 kips-in, which is almost 5 times higher than the static moment. This abnormally high bending moment was due to a 3 in^2 flat spot located on the fourth wheel of a 260 kips weight car. This provides an example for the extreme amplification of bending moments due to severe impact loads.

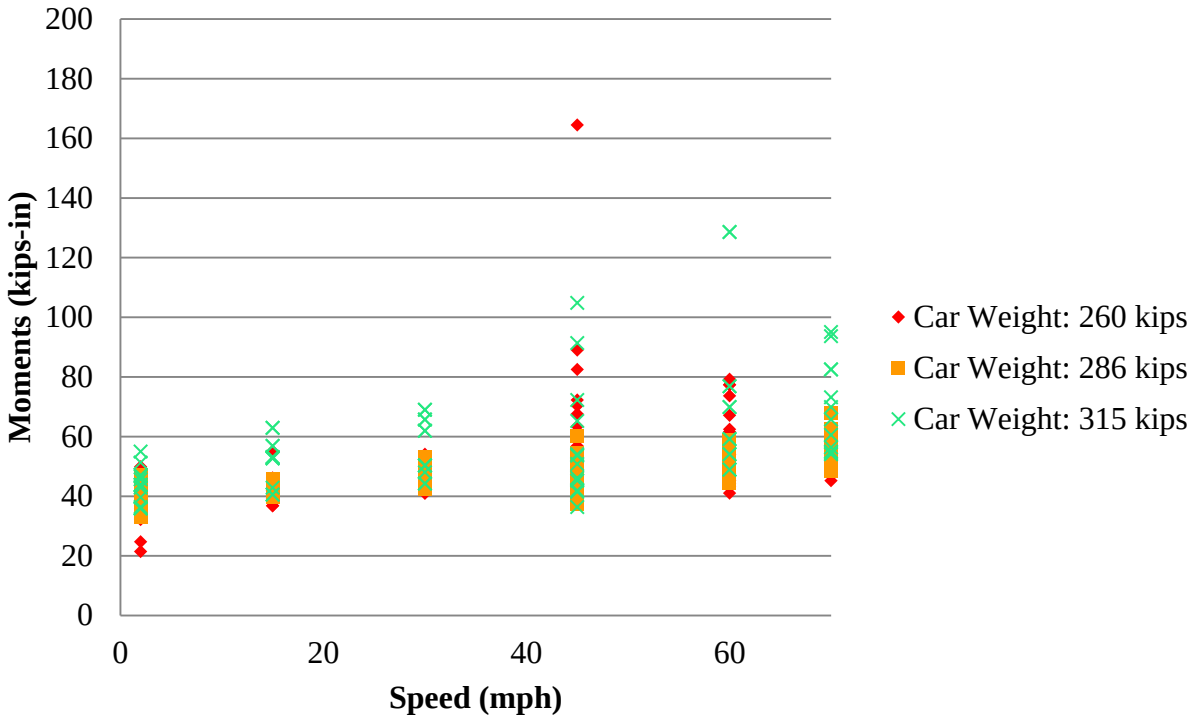

Car Weight	Speed	2 mph	15 mph	30 mph	45 mph	60 mph	70 mph
260	Max	50	55	61	164	77	89
	Mean	37	43	49	56	54	64
	Min	21	37	41	40	44	51
286	Max	47	46	53	60	59	68
	Mean	41	43	49	48	53	57
	Min	33	40	42	37	44	48
315	Max	55	63	69	105	129	95
	Mean	44	52	57	59	73	70
	Min	36	41	44	36	49	54

Figure 6.15 Bending Moments Recorded from Rail Seat S Corresponding to the Car Weight and Train Speed (RTT, 2013)

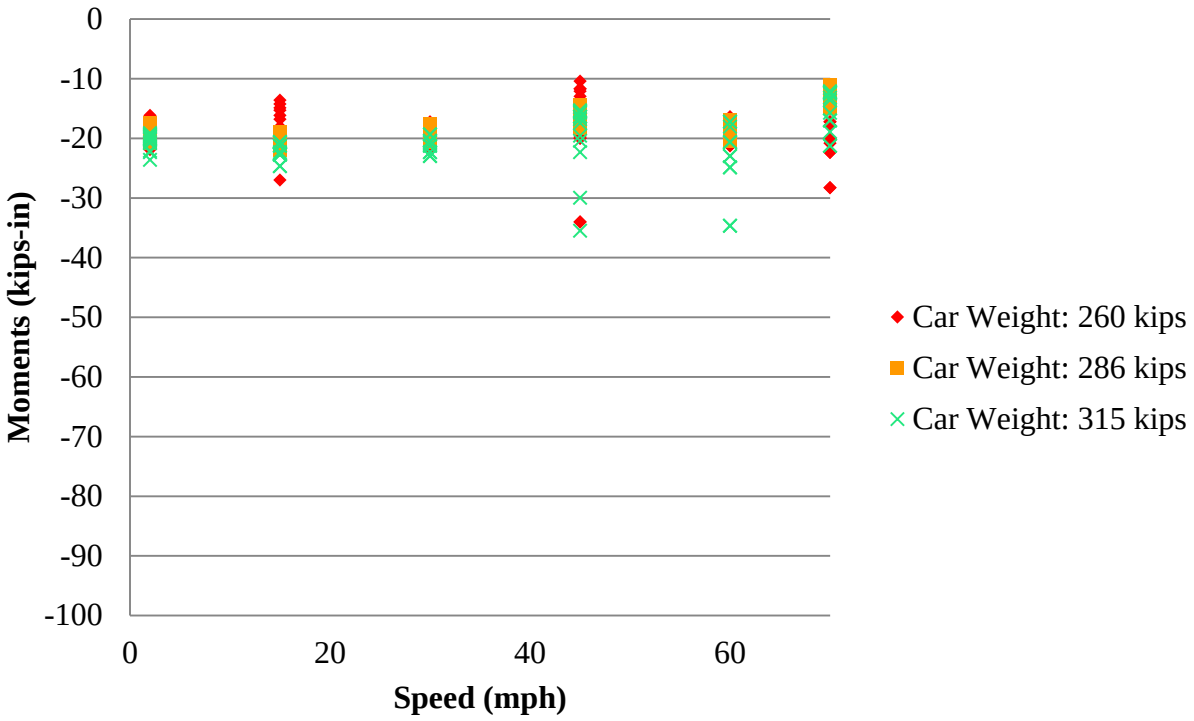

Car Weight	Speed	2 mph	15 mph	30 mph	45 mph	60 mph	70 mph
260	Max	-16	-17	-16	-14	-17	-10
	Mean	-19	-20	-20	-19	-22	-14
	Min	-22	-22	-22	-54	-34	-20
286	Max	-17	-19	-18	-14	-17	-11
	Mean	-19	-21	-19	-16	-19	-13
	Min	-21	-22	-21	-18	-20	-15
315	Max	-19	-21	-19	-15	-17	-12
	Mean	-21	-22	-21	-20	-23	-16
	Min	-24	-25	-23	-36	-35	-21

Figure 6.16 Bending Moments Recorded from the Center of Crosstie CS Corresponding to the Car Weight and Train Speed (RTT, 2013)

6.2 Improving the Current Design Recommendations

Because the current design practice recommended by AREMA doesn't follow the rule of mechanistic design quite well, it is necessary to revise the calculation methodology used in crosstie design.

Based on the bending and compressive behavior of the concrete crossties, as well as the load path going through concrete crosstie were investigated in both laboratory and field environment, the following conclusions have been made:

1. Elastic beam theory can be applied for crosstie bending analysis as long as there is no crack generated which is less likely to happen for a newly temped track under static loading.
2. The crosstie support conditions were able to be found using the measured rail seat loads and the distribution of crosstie bending moments.
3. Lateral wheel loads applied by TLV would bring a more than 5% change in crosstie bending moments, however, this loading condition is different from the train passage.
4. Gap might be existing between the bottom surface of concrete crosstie and ballast, which will lead to a decrease in rail seat loading and crosstie bending moments.
5. Under dynamic cyclical wheel loading, hysteresis loops were observed from the recorded vertical and lateral crosstie global deflections, which represent the energy dissipation.
6. The correlation between the crosstie bending moments and train speeds was not significant, but high values may be found due to impact loads.

In this study, only three to five adjacent concrete crossties were instrumented with surface and embedment strain gauges. Two newly temped field conditions were examined. To

fairly evaluate the behavior of concrete crosstie corresponding to various loading and support conditions, more field tests need to be conducted. The future in-depth laboratory and field experimentation will consider the limitation of the current test set-up, and better address the load path going through concrete crossties.

7. Evaluation of the Track Dynamic Behavior Under Impact Loading

Rail wheel flat spots are a primary cause of dynamic impact loads imparted to the railway track infrastructure. The formation of a wheel flat is generally attributed to the braking of a train. Braking slows the rotation of wheels and can cause the wheels to slide along the rails so that the train is decelerated by the friction between the wheels and rails. However, the sliding can wear off a portion of the wheel treads and result in a flat spot (Dukkipati and Dong 1999). The size and shape of wheel flats, as well as wheel load and train speed, are the factors that affect the impact load; and certain combinations of these factors can result in huge impact loads that may cause serious damage to track structures (Bian et al 2013). In addition, as the magnitude of impact loads can be much higher than the cyclic loads from the passage of wheels, and the track components are prone to accelerated degradation under the effects of impact loads.

The determination of impact factor is typically highly simplified in practice. The American Railway Engineering and Maintenance-of-Way Association (AREMA) assumes an impact factor of 2.0 for the flexural design of concrete crossties. However, data acquired by wheel impact load detectors (WILD) on Amtrak at Edgewood, Maryland and elsewhere on freight railroads indicated that impact factors could easily exceed the 2.0 design value (Van Dyk et al 2014). There were also instances of loads exceeding the 2.0 design value observed from passenger car wheels. These data suggest that the design impact factor be revisited to accommodate for wheel loads that exceed the current value of 2.0.

In this study, impact load and the induced track behaviour was examined through the field experiments. The field results were used to calibrate the finite-element models prepared by a group from UIUC led by Dr Bassem Andrawes. The results of analysis from the modelling were prepared by Zhe Chen (Chen et al 2014) and Zijian Zhang (Zhang et al 2016). In the field, a

wheel with a flat spot on its tread was placed on the third axle of the 9th car of the freight consist. The diameter of the flat spot was measured as approximately 2 inches (**Figure 7.1**). Static and dynamic finite-element models including the wheel with a flat spot, rail and fastening system, concrete crossties and foundations was built with Abaqus.

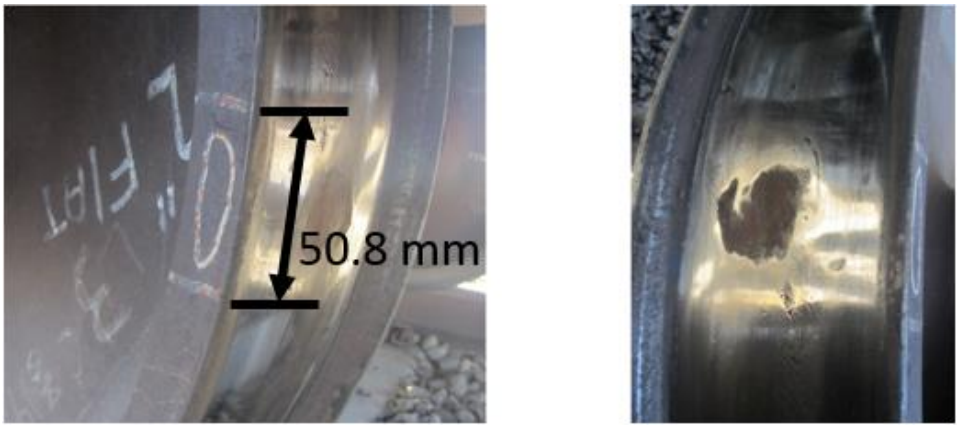

Figure 7.1 Flat Spot on the Wheel

7.1 Finite Element Model Overview

In order to gain insight into the effects of impact loads caused by wheel flats on railway tracks, a FE model was developed using commercial software Abaqus. The finite-element model simulated the rolling of two railcar wheels of an axle, one of which was with a flat spot, on a finite length of a railway track. **Figure 7.2** shows the wheels and the cross-section of the track system in the model.

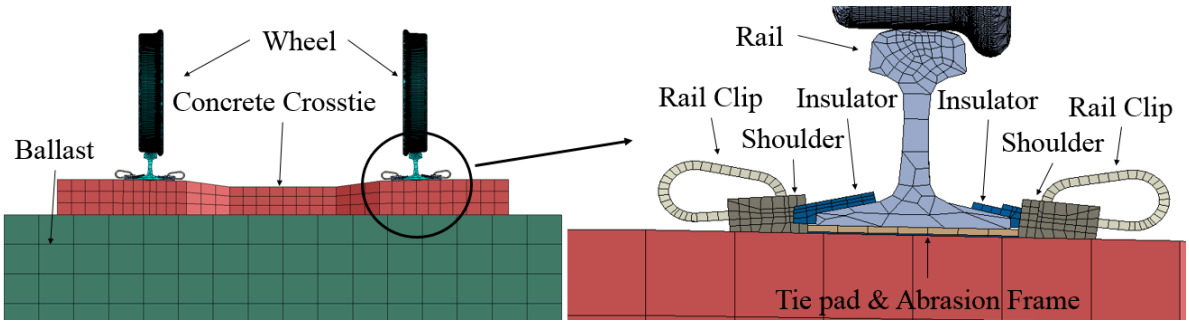

Figure 7.2 Schematic View of the FE Model (Prepared by Zijian Zhang)

The finite-element model included a tangent track with two railcar wheels, that is, one wheel on each rail. Field experimental results indicated that vertical loadings from the adjacent axles had almost no effect on the track segment under the influence of the flat wheel. In addition, it is assumed the distribution of rail seat pressure for concrete crosstie track extended less than 6 ft to both sides of wheel load application, which was less than the axle spacing of the passenger coach in the field conditions. Therefore, incorporating one railcar wheel on each rail was deemed a reasonable assumption. In the modelled track system, 136 RE rails, Safelok I fastening systems and concrete crossties were used. As illustrated in **Figure 7.2**, the Safelok I fastening system included a rail clip, shoulder, rail pad assembly (i.e. rail pad and abrasion frame), and insulator. The wheel was modelled as a narrow flange railcar wheel with 1:40 tapered wheel tread, and the geometries of the wheel web was simplified from curved to flat surfaces. In addition, a rectangular area of flat surface, as shown in **Figure 7.3**, was created on the tread of one wheel to simulate a wheel flat. The size of the wheel flat, measured tangentially along the wheel perimeter, was specified to 2 inches to meet the dimensions of the flat spot in field testing. The geometry of track, wheel, and flat spot are consistent with the measurements from field experimentation for model validation.

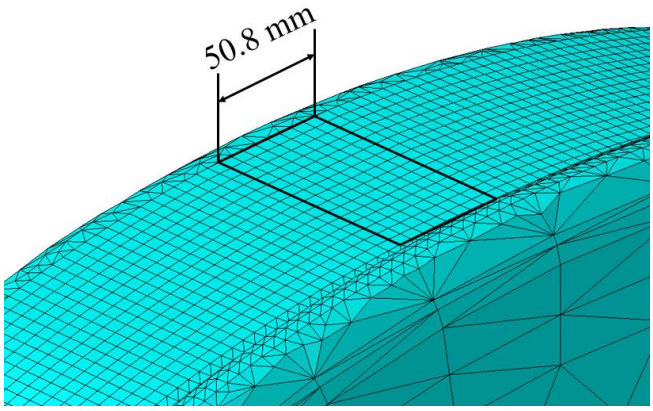

Figure 7.3 Flat Spot on the Wheel Tread (Prepared by Zijian Zhang)

The modelled track system, as shown in **Figure 7.4**, consisted of 19 sets of crossties and fastening systems with uniform crosstie spacing. The end segments of the track were provided so that, as the impact hit the center of the track, the ends of the rails were not affected by the rail flexural bending under wheel load. The ends of the end segments had free boundaries and the two end segments served as boundary conditions to the center segment.

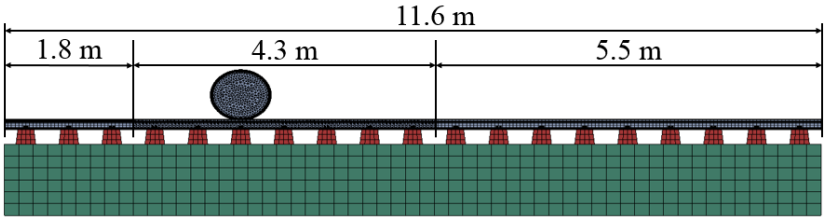

Figure 7.4 FE Model Track Overview (Longitudinal View) (Prepared by Zijian Zhang)

All track components were modelled using four-node tetrahedron and eight-node hexahedron 3D deformable solids except for the prestressing strands which were modelled using two-node linear beam elements in the crossties. Because the element size at the contact interface between the wheel and rail is expected to have a significant effect on the accuracy of the output vertical contact force between the two contact bodies during dynamic simulation, refined elements were used on the railhead for the middle rail segment. Elements were used for mesh

transition from the refined contact interface to the rest of the rail (**Figure 7.5**). Similarly, refined elements were implemented on the perimeter of the wheel tread with a transition to coarser elements towards the centre of the wheel.

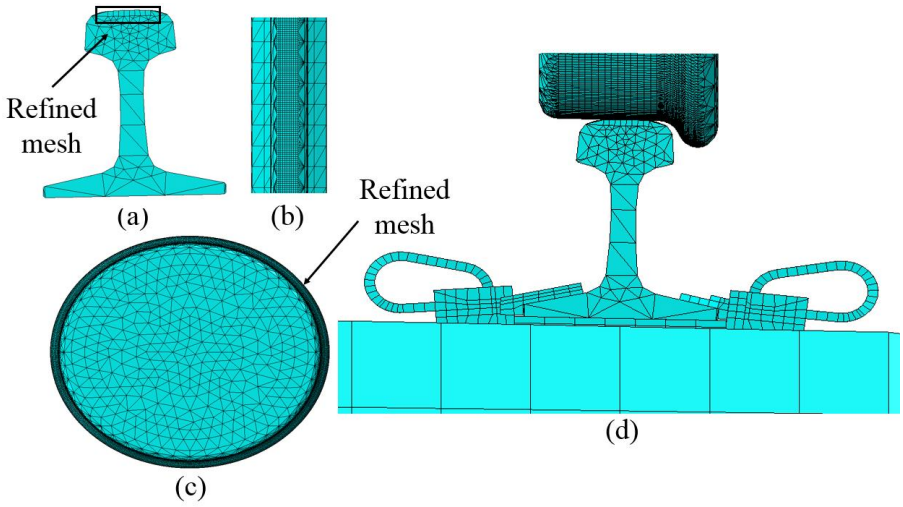

Figure 7.5 (a) Cross-section View of the Centre Rail; (b) Top view of the Centre Rail; (c) Wheel in Figure 7.1; (d) Wheel-rail Contact Interface (Prepared by Zijian Zhang)

Contact interactions between track components were formulated using surface-to-surface contact discretization, and a master and a slave surface were defined for each contact pair. This contact formulation method prevents large and undetected penetrations of nodes on master surface into slave surface, providing more accurate stress and strain results compared to other methods. The basic Coulomb friction model with the penalty friction formulation was used to simulate the frictional force response at the contact interface. The maximum allowable frictional stress is related to contact pressure by coefficient of friction (COF) between contacting bodies. The COFs of the contact pairs in the model were based on the laboratory tests in Chapter 3.

No axle was applied in the FE model to connect the two wheels; instead, a reference node was created at the centroid of the wheel to simulate an axle, and the "rigid body" constraint was

used to bind the translational and rotational degrees of freedom of all nodes on the wheel with that of the reference node. In other words, the rotation and translation of the reference node were transmitted to the wheel.

The finite-element analysis consisted of two phases. The first phase was the static loading phase that served to stabilize the track system in a static sense before a dynamic simulation. The static analysis phase included prestressing concrete crossties with strands, clamping clips onto the rail, applying gravity loads to the system, and applying the wheel load. Following the manufacturer's specification, the tensile capacity of all the prestressing strands was 8.75 kips/strand. A prestressing force of 7 kips was applied to each of the 20 strands embedded in each concrete crosstie, which was 80% of the tensile strength of a strand. When the prestressing force was released, the deformation of strands would engage concrete with compressive force. In the model, the assembly of clips was initiated in the same step. Pressures were first applied to lift up the toes of clips over the insulators. With the pressures applied, clip toes deflected towards the rail and the clip inserts were socketed into the grooves on the shoulders. As the tips of clips were directly placed over insulators, lifting pressure was decreased and the clips, then, clamped onto the insulators. The following step was to apply gravity loads to the superstructure components of the track system to simulate the resistance to upward deflection resulted from the vertical wheel load. In addition, the wheel load was applied to the reference point of the wheel. **Figure 7.6** illustrates the loading and boundary conditions in each step.

The following phase was the dynamic simulation as shown in **Figure 7.6**, Steps 7 – 9. Abaqus provides two types of integration schemes for dynamic simulation: explicit and implicit time integration schemes. An explicit dynamic analysis is computationally efficient for

analysing large models with relatively short dynamic response times and for analysing events or processes that are extremely discontinuous. It takes small time increments and is typically chosen for transient time dynamic analysis. In contrast, an implicit dynamic analysis usually gives acceptable and/or more stable solutions with time increments typically larger than explicit schemes by one to two orders of magnitude. As the total dynamic step running time was expected to be relatively long, explicit schemes are less computationally efficient. Therefore, implicit schemes were selected for the dynamic simulation. The increment time around time of impact was refined such that the transient effects could be simulated accurately. In the three dynamic analysis steps, a rotational speed and a translational speed were both applied to the reference nodes at the centre of the wheels. The total dynamic simulation time was deemed sufficient as the wheel-rail interaction force could reach dynamical equilibrium prior to impact and the wheel could keep rolling some distance after the impact.

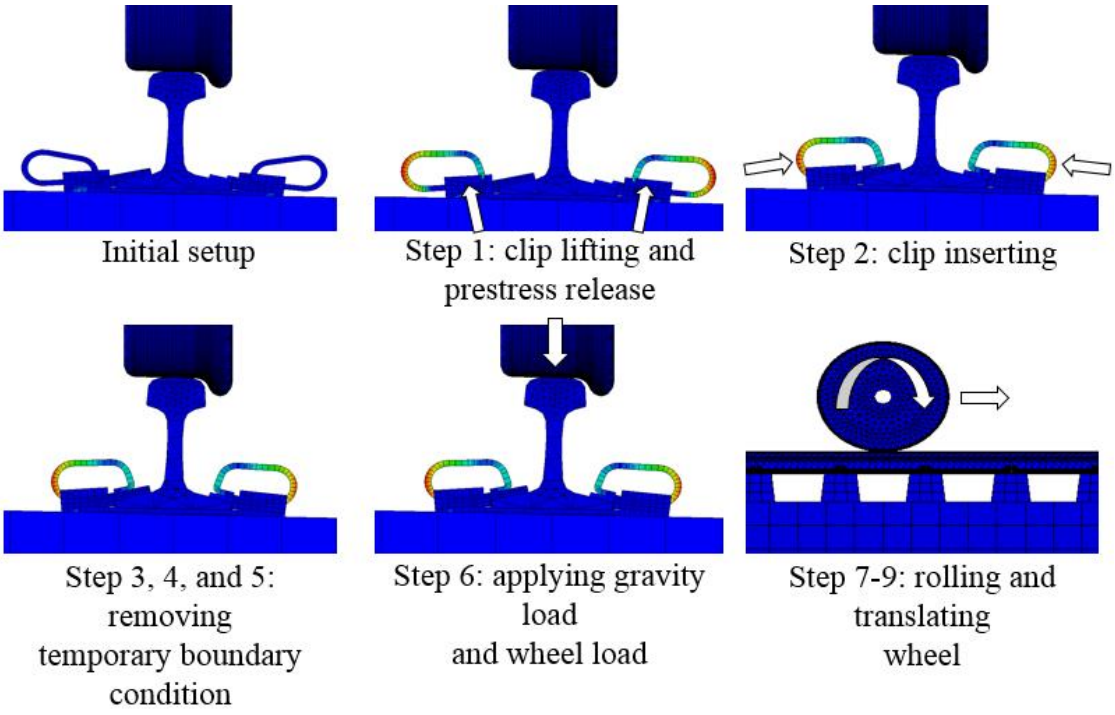

Figure 7.6 Sequence of Application of Loadings and Boundary Conditions in the FE Model (Prepared by Zhe Chen and Moochul Shin)

7.2 Finite Element Model Validation Using Field Data

To calibrate the finite element model built with Abaqus, field data was used. The instrumentation map can be found in **Figure 3.64**. The finite-element model was first validated with the absence of an impact load; two recorded time histories were compared with the output history from the model: vertical strains in the rail web and vertical internal strains of the concrete crosstie read from embedment strain gauges.

The validation based on the vertical strains in the rail web ensured that the vertical reaction forces transmitted from the wheel to the rail was physically making sense. **Figure 7.7** presents the comparisons between the field and numerical results. A section of signal containing eight peaks is shown, in which the first two peaks are caused by the last two axles of a car, the

middle four peaks are due to all the four axles of the car following, and the last two peaks are from the first two axles of the third car. Due to the rail roughness and other geometry imperfections, slight fluctuation was observed in the field data. Because of the limitation of the length of the track in the finite element model, short during of signal was recorded. To make an appropriate comparison, the peak of finite element output is aligned to the first peak of the field data. Comparing the output from the finite element model with the field data, the shapes of the two curves exhibited good agreement. Both curves show that the vertical strain in the rail web decreases first and reaches a minimum value (maximum compression), then starts to increase after the wheel passage. The finite-element model gave a maximum compressive strain value of 150 micro strain which was 4.7% higher than the 143 micro strain measured in the field. All though the upper half of the signal from the finite element result looks like narrower than that from the field test, it could be explained by the fact that only one axle was modelled in the finite element analysis, which neglected the affect from the adjacent axles. Therefore, a good agreement between field and numerical results for vertical strain in rail web was achieved.

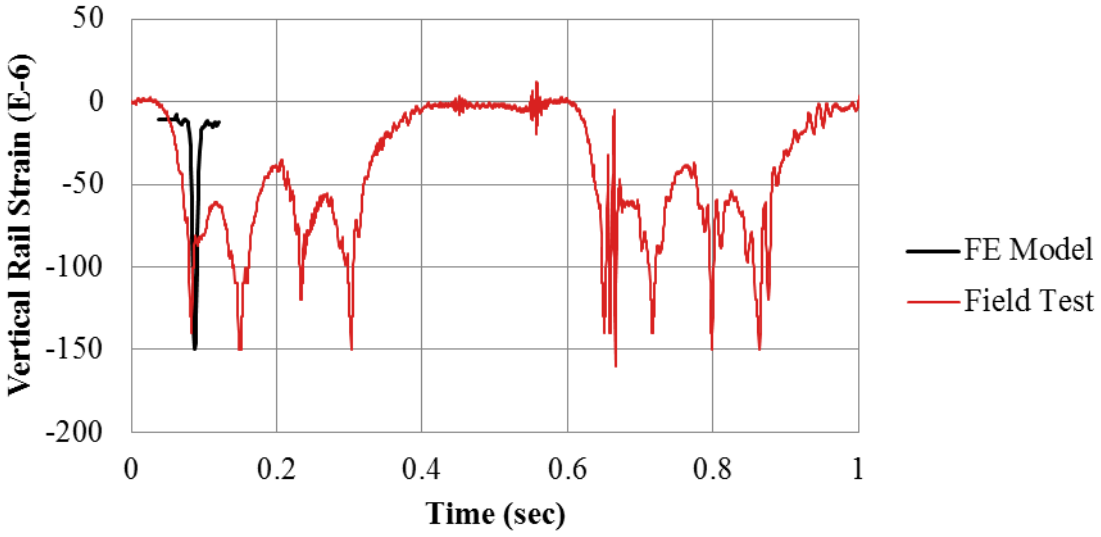

Figure 7.7 Vertical Strain in Rail Web with no Impact Load

In addition to the vertical strain in the rail web, longitudinal strain measured 2 inches below the surface of the concrete crosstie at the rail seat was also calibrated against field data. **Figure 7.8** illustrates the comparisons between the field results and the numerical solutions. Similar as **Figure 7.7**, the finite element signal was aligned to the first peak of the field data. Despite the fluctuations in the field data caused by imperfect field conditions, the curves exhibited similar trend. A maximum compressive strain was observed during the passage of a wheel, indicating the measurement area was subjected to compression. The maximum compressive strain value measured from the field was 84 micro strain and was 5.2% higher than the numerical solution, hence good agreement was shown.

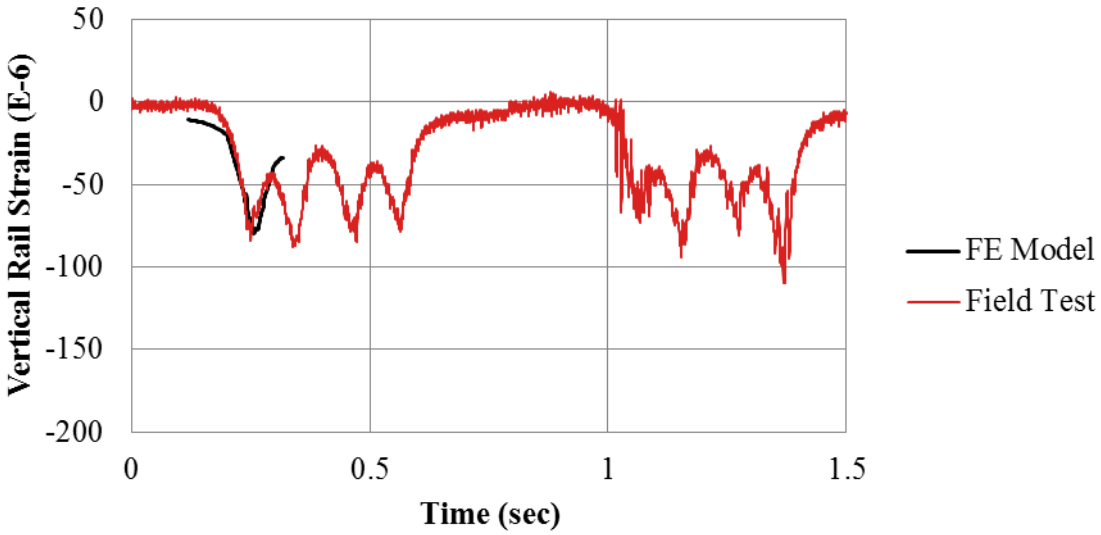

Figure 7.8 Embedment Strain in Concrete Crosstie with no Impact Load

The next step is to validate the finite-element model using the history with impact loading. **Figure 7.9** presents the time history of the four axles of the 9th car rolling over the instrumented track section. It should be noted that the calibration of the bridges were conducted under various static loads applied immediately above the centre of two Chevron patterns. Therefore, the history of the measured vertical wheel loads is only valid at the centre point of

each peak. In **Figure 7.9**, the measured dynamic vertical loads due to the second, third and fourth wheel are all about 150 kN. Due to the existence of the flat spot located at the first wheel, the first peak in **Figure 7.9** splits up into two much narrower peaks, which exceed the magnitude of the other readings by a factor of two. The separated peaks could be explained by the vibrations of rail and wheel aroused by the large impact load caused by the flat pattern.

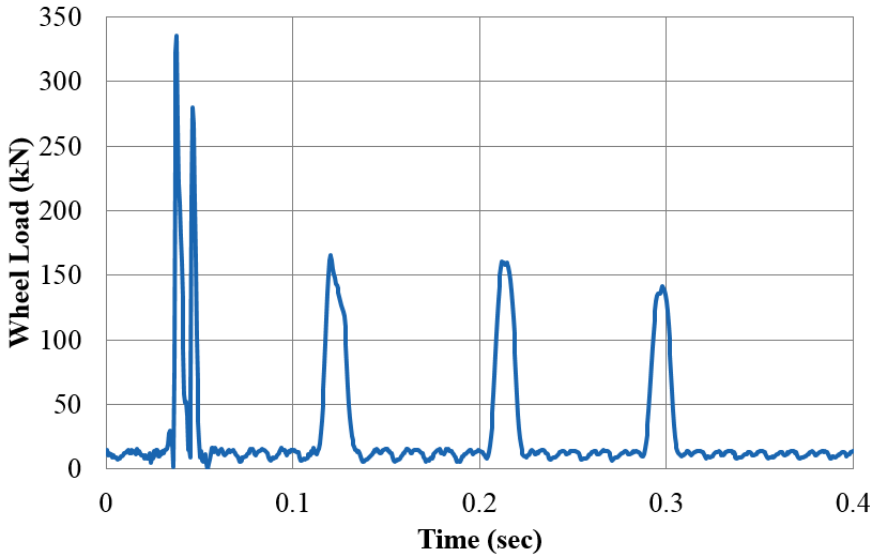

Figure 7.9 Time History of the Vertical Loading Output from a Strain Gauge Bridge

As a comparison, in the finite-element model, three cases of impact loading caused by the flat spot were examined: the flat spot hitting directly above the centre line of a rail seat, 6 inches before approaching the rail seat, and immediately above the centre line of a crib. The monitored wheel load history for the three cases is shown in **Figure 7.10**. Because **Figure 7.10** presents the actual wheel-rail contact force output from the model directly, it shouldn't be used to compare with the shape as shown in **Figure 7.9**. From the wheel load history, it could be found, regardless of the flat spot hitting location, the shape of the impact load is very similar. The magnitude of the impact load recorded from the model is approximately 330 kN (74 kips), which is about 1% lower than the peak of the impact load measured from the field. In addition, split

peaks were also observed in the numerical results, which confirmed the vibration of the rail and wheel as a result of the impact.

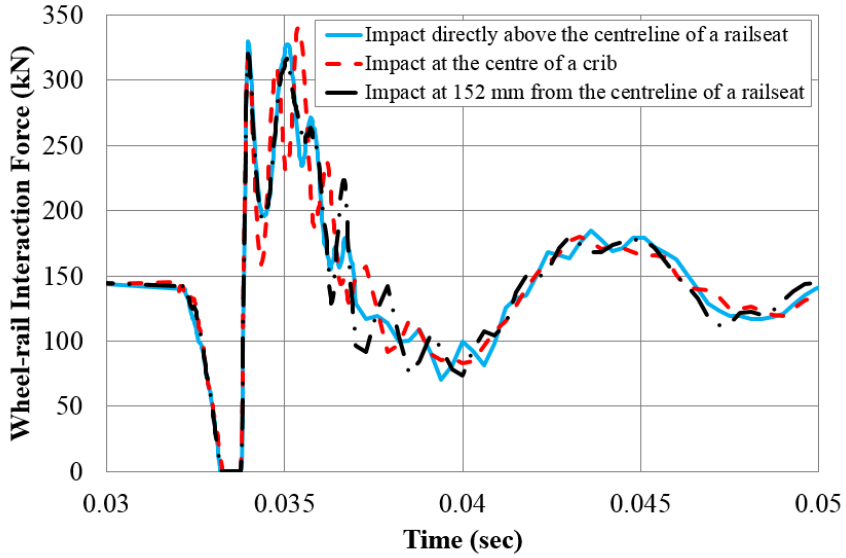

Figure 7.10 Wheel Load History Output from FE Model (Prepared by Zijian Zhang)

In all three cases, the interaction force exhibited an abrupt decrease to zero prior to the occurrence of wheel impact, which indicated a loss of contact between the wheel and the rail. As illustrated in **Figure 7.11**, this observation can be attributed to the sudden change of contact from the intact wheel tread to a flat spot, which causes the wheel to lose contact with the rail for a transient time. In addition, the impact loadings were superimposed by multiple peak loads which were caused by different mechanisms. The first peak load was a result of the colliding of wheel and rail as shown in **Figure 7.11**, hence referred to as the direct impact load. The peak loads that followed were from the vibrations of the track system under the influence of wheel impact, and thus were the vibration-induced impact loads.

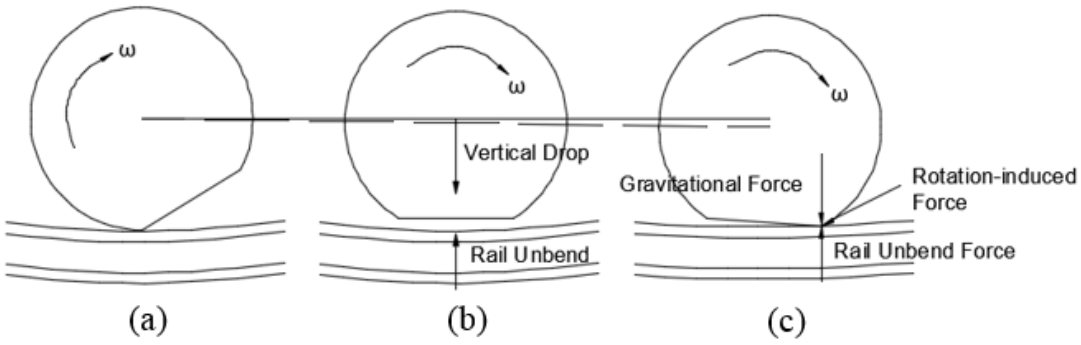

Figure 7.11 Changes of Wheel-rail Contact with a Flat Wheel (Bian et al 2013)

As shown in **Figure 7.10**, the magnitudes of impact loading were similar and not significantly affected by the location of impact. When the impact occurred directly above the centreline of the rail seat, the impact loading was 330 kN (74 kips), which slightly increased to 340 kN (76 kips) when the location of impact was above the centreline of the crib. In addition, an impact loading of 321 kN (72 kips) was observed as impact location was moved 6 inches away from the rail seat. However, a considerable difference was observed for the patterns of wheel-rail interaction force. In the case where the impact occurred at the centre of a crib, the fluctuations of loading history were found to be stronger, indicating a larger extent of vibrations in the track system. In addition, the maximum impact load was the vibration-induced load as opposed to the other two cases in which the direct impact load was larger. It indicates that loads caused by the vibrations of the track system have a potential to surpass the loads produced by the impact of the wheel on the rail, and therefore, both the direct impact load and vibration-induced impact load need to be attenuated in order to mitigate the damage from impact loadings.

Vertical rail strains were also used to validate the FE model. In the same manner used for wheel load validation, the flat spot hit the rail at three locations in the FE model. **Figure 7.12** - **Figure 7.13** present the comparison of the field and numerical results under these three loading conditions. The section of signal caused by the flat wheel from seven different runs in the field

testing was selected to compare with the finite element output. It has been validated that the maximum vertical rail strain due to round wheel is about 150 micro strain in compression (**Figure 7.7**). When the flat wheel hit immediately above the centreline of rail seat (**Figure 7.13**), due to the superposition of regular wheel load and impact, the magnitude of strain was raised up to about 170 micro strain in compression. This was demonstrated by both FE and field testing results. Similar to the wheel load, split peaks were found, followed by smaller fluctuations. When the flat spot hit 6 inches ahead of the rail seat (**Figure 7.13**), the magnitude of the first peak was decreased, followed with a high peak with a magnitude of about 160 micro strain in compression. The reduction in strain following the first peak could be explained by the short duration of disengagement of wheel and rail when the flat spot rolled directly above the rail, which has weakened the effect of wheel load. The second peak was due to the re-engagement of the wheel and rail which could be seen as the source of the impact. When the flat spot hit the centre of the crib beyond the location of strain measurement (**Figure 7.14**), a secondary peak was recorded next to the main peak due to the round wheel. Because the impact occurred 6 inches away from the strain measurement, its influence was not as strong as the first and second cases. The maximum strain due to the impact corresponding to the third case was found to be 75 micro strain in compression.

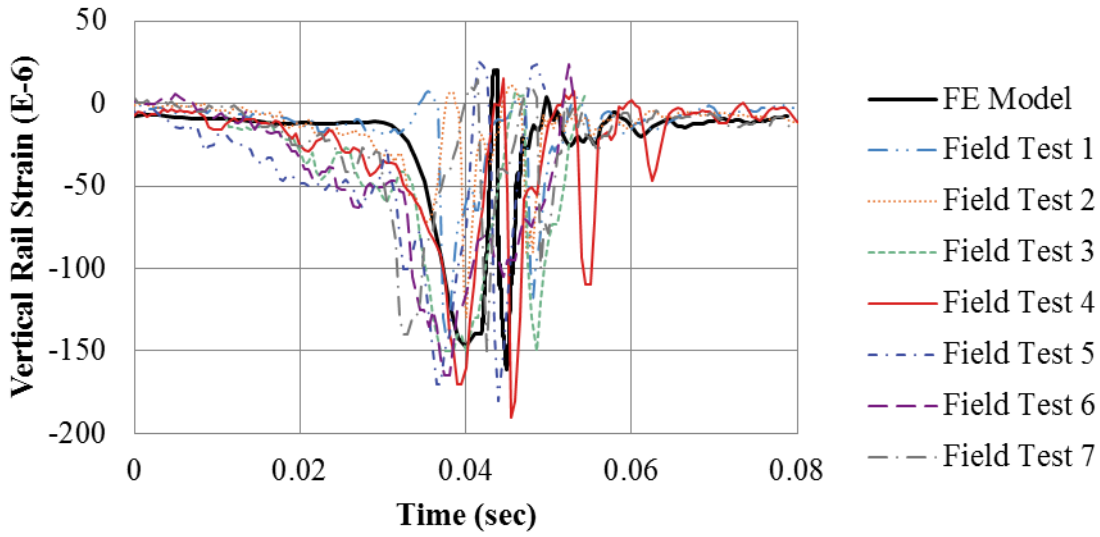

Figure 7.12 Vertical Rail Strain due to Flat Spot Hit Directly Above the Centreline of Rail Seat

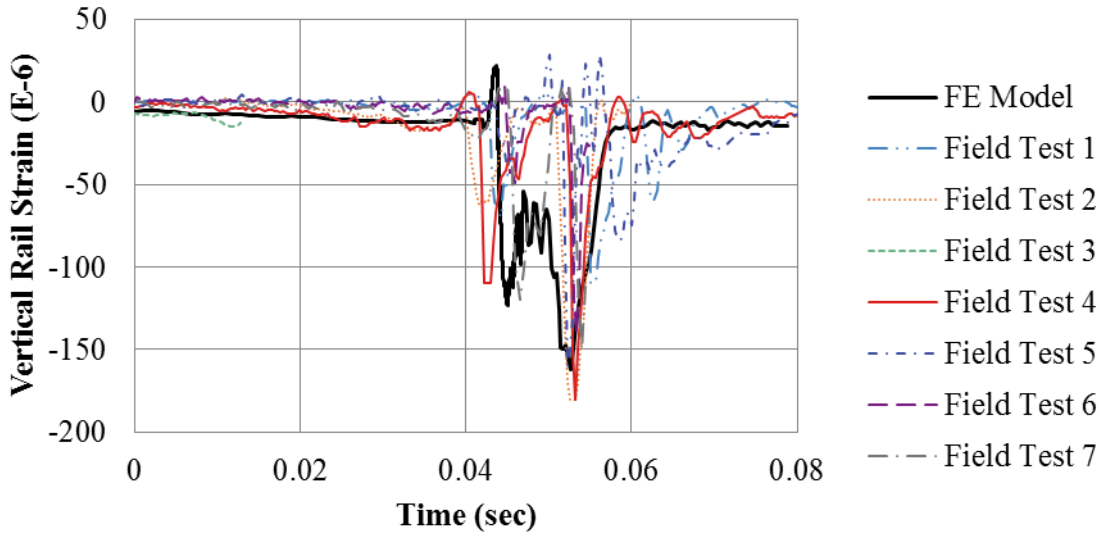

Figure 7.13 Vertical Rail Strain due to Flat Spot Hit 152 mm Ahead of the Centreline of Rail Seat

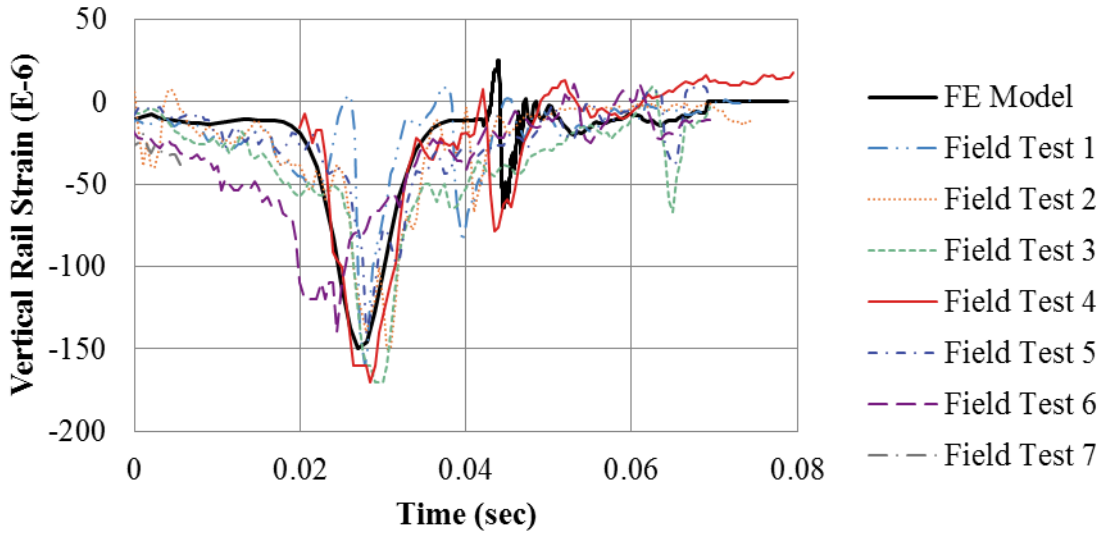

Figure 7.14 Vertical Rail Strain due to Flat Spot Hit Directly Above the Centreline of Rail Crib

7.3 Parametric Study

Upon the validation of the FE model, a series of parametric studies was conducted. Parameters used in the parametric studies were the stiffness of rail pad and the train speed.

7.3.1 Rail Pad Stiffness

According to Harper (1996) and Hepburn (1982), the stiffness of rail pad ranges from 128 MN/m to 1,282 MN/m. Three additional cases including 128 MN/m, 337 MN/m, and 481 MN/m were simulated to compare with the previous case in which a stiffness of 240 MN/m was used as per the manufacturer. The time history of the wheel-rail interaction force corresponding to each case is shown in **Figure 7.15**.

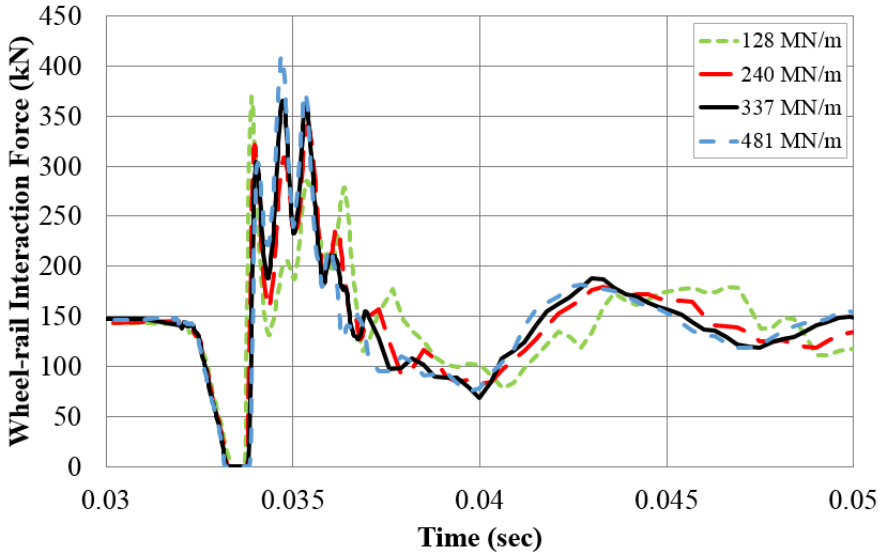

Figure 7.15 Time Histories of Wheel-rail Interaction Force with Rail Pads of Four Different Stiffness (Prepared by Zijian Zhang)

It can be realized that softer rail pads were able to attenuate vibration-induced peak loads yet failed to reduce the direct impact load. Compared to stiff pads, soft pads allowed for larger vertical rail deflection, causing the rail to bend more. As the flat spot passed over the rail, the loss of contact between the rail and wheel gained the rail an upward action (**Figure 7.11** b). The larger rail deflection allowed by soft rail pads would result in a higher rail unbend acceleration. Therefore, a higher force could be incurred when the wheel and rail collided (**Figure 7.11** c). In contrast to the increase in the direct impact load, vibration-induced peak loads were reduced as softer rail pads attenuated the vibrational interactions between the rail and concrete crosstie. When the stiffness was increased to 481 MN/m, an exact opposite behaviour of impact loads to the case with softer pads was observed. Stiffer rail pads were able to attenuate the direct impact load; however, the vibration-induced peak loads increased significantly.

In order to quantify the effect of rail pad stiffness on the impact factor, that is, the ratio between the maximum impact load and nominal wheel load, their relationship is illustrated in **Figure 7.16**. Rail pads with a stiffness of 240 MN/m provided best impact attenuation with an

impact factor of 2.35. Even though softer pads reduced vibration-induced peak loads, the impact factor was increased to 2.56. Stiffer rail pads further increased the value to 2.53 and 2.84.

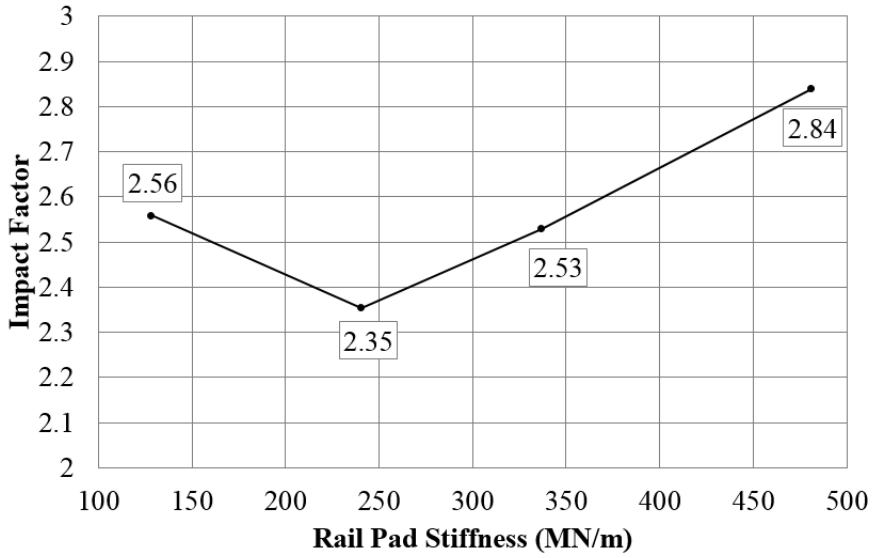

Figure 7.16 Effect of Rail Pad Stiffness on Impact Attenuation (Prepared by Zijian Zhang)

According to Dean et al. (1983) who did a single tie impact test which utilized a drop hammer to produce impact loading, softer pads led to significant reductions in impact factor. Dukkipati and Dong (1999) reached the same conclusion using finite-element analysis and the stiffness values used in their study were 200 MN/m and 850 MN/m. Their observations agree with the right (ascending) branch of the curve in **Figure 7.16**. With the results gained from this study, it was made aware that the selection of rail pad with small stiffness should be made with extra caution.

7.3.2 Speed

In addition to the rail pad stiffness, the speed of a train can also have an effect on impact factor. To compare with the previous case in which the wheel had a speed of 72 kph, three higher speeds of 144 kph, 193 kph, and 362 kph were simulated. As presented in **Figure 7.17**, impact factor kept increasing with increasing train speed. As illustrated in **Figure 7.11** c, the wheel-rail

impact was essentially the collision between the edge of wheel flat and rail. In other words, the impact force was resulted from both rotation-induced force and rail unbend force. A higher train speed directly increased the force induced by wheel rotation, and thus, led to higher impact load at the time of wheel-rail impact.

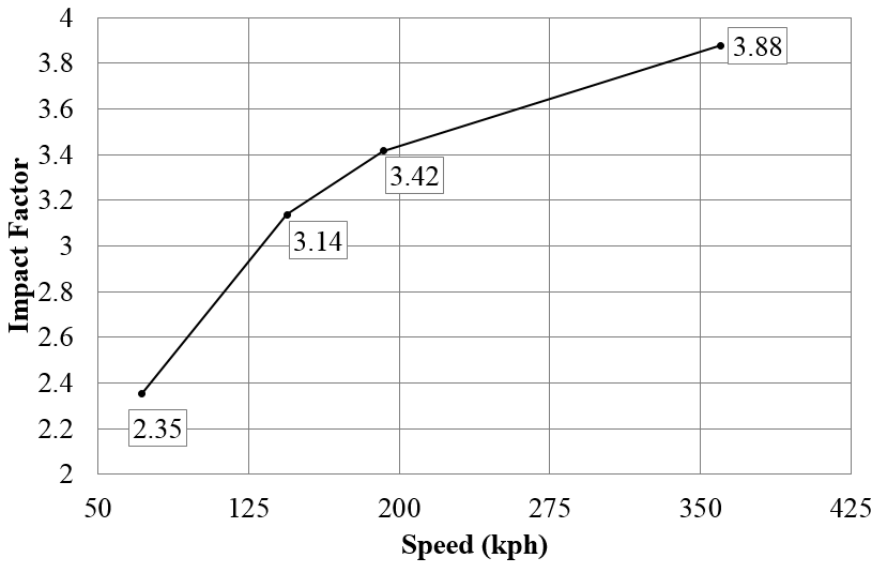

Figure 7.17 Effect of Speed on Impact Factor (Prepared by Zijian Zhang)

In addition, vibration-induced impact loads diminished at high train speeds. **Figure 7.18** presented the time history of wheel-rail interaction force when the speed of train was 193 kph. The profile of vibration-induced impact load was not as conspicuous as at a lower speed (**Figure 7.15**). Its magnitude was only 240 kN and was 29% lower than when the speed was 72 kph. The loss of wheel-rail contact prior to impact was much shorter at high speeds, which averted most of the unbend action of the rail (**Figure 7.11**). Consequently, the vibration of the track was alleviated, hence fiddling loads from track vibration.

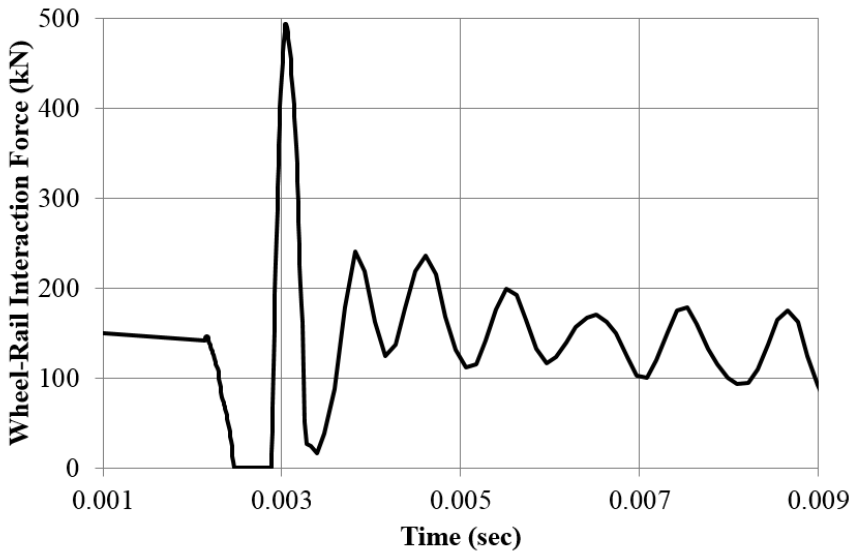

Figure 7.18 Time History of Wheel-rail Interaction Force at 193 kph Train Speed (Prepared by Zijian Zhang)

7.4 Conclusions

The results indicated rail pad with an intermediate stiffness, 240 MN/m in this case, performed best in attenuating impact load. Rail pad with a lower stiffness, 128 MN/m, led to an 8.9% increase in the impact factor. An increase of 7.7% in impact factor was also observed for rail pad with a higher stiffness of 337 MN/m. To investigate the relationship between train speed and impact factor, four different speeds, ranging from 72 kph to 362 kph, were simulated in the finite-element model. It was realized that the increase in impact factor was more significant at lower speeds as opposed to higher speeds. Increasing train speed by twice, from 72 kph to 144 kph, the impact factor was increased by 34%. In comparison, a mere 13% increase was resulted as the train speed was raised by 88%, from 193 kph to 362 kph.

Some additional conclusions can be made based on the results from the analysis:

- Impact loading consists of two mechanisms, direct wheel impact and vibration-induced impact;

- The location of wheel impact has an effect on the behaviour of impact loading, that is, more vibrations are caused in the track system when impact hits the centreline of a crib and thus more severe vibration-induced impact loads, however, this effect is found to be insignificant;
- Direct impact load increases with decreasing rail pad stiffness while vibration-induced impact load increases as rail pad becomes stiffer and an optimized rail pad stiffness exists to reach the highest attenuation of impact loads;
- Impact load increases with increasing train speed.
- Vibration-induced impact load diminishes as train speed increases.

8. Conclusions

This on-going research contributes to exploring the nature of load transfer from vehicle-rail interaction through the concrete crosstie and fastening system to ballast. The wheel load demand was measured from the field testing; a simplified load profile was applied in the laboratory testing. All the reaction forces including rail seat load, clip load, lateral force transferred through shoulder and rail base frictions were measured with various methods in both laboratory and field. The displacement and deformation (strain) of each component in the system including, rail, clips, insulator and concrete crosstie were also measured. The statistical results were examined. And the following conclusions can be drawn from the laboratory and field experimentation as well as analytical analysis.

8.1 Vertical Load Path

- 45-60% of vertical wheel load was resisted by each rail seat, when the rail seat was "well" supported; however, if the support was very poor (gap between concrete crosstie and ballast), the rail seat load directly under the wheel set could be very low (close to zero).
- With newly tamped track, the static applied load had a distributed response over about 3 to 5 crossties.
- Lateral wheel load didn't affect much to the vertical load path (in other words, the vertical rail seat reaction force was not significantly affected by the lateral wheel load).
- In general, dynamic wheel loads were not significantly higher than static wheel loads.
- When the train speed was low, vertical rail seat reaction force increased linearly corresponding to the growth of vertical wheel load; when the train speed was high, large variation may happen.

- The gap between concrete crosstie and ballast needed to be closed up first, then the vertical rail seat load started to grow.
- On a curved track, a greater portion of vertical loading was supported by the high rail with a higher speed.
- Concrete crosstie global vertical deflection started to grow linearly corresponding to the vertical wheel load when the gap between concrete and ballast was fully closed up.

8.2 Lateral Load Path

- 2.1 On average, lateral loading demands were measured 3 to 6 times as high on curved track than on tangent track.
- Lateral loads appeared to be primarily distributed among three to five crossties under static wheel loads.

8.3 Clip Behavior

- Tangential component of clamping force would significantly affect the maximum strain of a clip.
- Change of normal and tangential component of clamping force under dynamic wheel load was below 250 lbf, and wasn't significantly affected by the speed.

8.4 Concrete Crosstie Behavior

- Crosstie bending moment measured below rail seats was far below cracking limit.
- A small region of concrete (short width) below rail seats with low measured bending moment contacted ballast under static wheel load.

8.5 Dynamic Interaction Under Impact Loading

- Impact loading consists of two mechanisms, direct wheel impact and vibration-induced impact.
- The location of wheel impact has an effect on the behavior of impact loading.
- Direct impact load increases with lower rail pad stiffness while vibration-induced impact load increases with higher rail pad stiffness.
- Impact load increases with increasingly train speed.
- Vibration-induced impact load diminishes as train speed increases.

Reference

Agarwal, M.M. (1974). *Indian Railway Track*. Manglik Prakashan, Saharanpur

Andersson, E., Berg, M., Stichel, S. (2013). *Rail Vehicle Dynamics*. Railway Group, KTH, Stockholm, Sweden

AREMA (2012). *Manual for Railway Engineering, Chapter 30: Ties*. 2014

Bian, J., Gu, Y., & Murray, M. (2013). Numerical Study of Impact Forces on Railway Sleepers under Wheel Flat. *Advances in Structural Engineering*, 127-134.

Birmann, F., et al. (1966). Serial measurements on rails to determine wheel lateral forces. *Railway Technical Review*, pp. 155-164

Chen, Z., Shin, M., Wei, S., Andrawes, B., and Kuchma, D.A. (2014). "Finite element modeling and validation of fastening systems and concrete sleepers in North America", Journal of Rail and Rapid Transit, 2014, Vol. 228(6) 590-602

Clarke, C.W. (1957). Track loading fundamentals. *The Railway Gazette*, Part 1, 45-48, Part 2, 103-107, Part 3, 157-163, Part 4, 220-221, Part 5, 274-278, Part 6, 335-336, Part 7, 479-481

Dahlberg, T., Lundqvist A. (2005). Load impact off railway track due to unsupported sleepers. Institution of Mechanical Engineers, Part F: *Journal of Rail and Rapid Transit*, 2005, 219:67-77

Dean, F., Harrison, H., Prause, R. H., & Tuten, J. M. (1983). *Investigation of the Effects of Tie Pad Stiffness on the Impact Loading of Concrete Ties in the Northeast Corridor*. Washington, D.C.: Federal Railroad Administration, Office of Research and Development.

Doyle, N.F. (1980). *Railway Track Design: A Review of Current Practice*. BHP Melbourne Research Laboratories, Bereau of Transport Economics

Dukkipati, R., & Dong, R. (1999). Impact Loads due to Wheel Flats and Shells. *Vehicle System Dynamics*, 1-22.

Eisenmann, J. (1972). Germane gain a better understanding of track structure. *Railway Gazette International*, Vol 128, No. 8/305

EN 13230 (2009). *Railway Application, Track, Concrete Sleepers and Bearers, Parts 1 & 2*. European Committee for Standardization. 2009

Fröhling, R.D. (1998). Low frequency dynamic vehicle/track interaction: modelling and simulation. *Vehicle System Dynamics*, 01/1998, 29:30-46

Grasse, J.S, Wei, S., Edwards, J.R., Kuchma, D.A., and Lange, D.A. (2014). "Field study of load path in concrete crosstie and fastening system", Electronic Journal of Structural Engineering, Volume 14, 29-38, 2014

Greve, M.J., Dersch, M.S., Edwards, J.R., Barkan, C.P.L., Thompson, H., Sussmann T.R.Jr., and McHenry., M.T. (2015). Examination of the effect of concrete crosstie rail seat deterioration on rail seat load distribution. Transportation Research Record: Journal of the Transportation Research Board. 2476: 1-7.

Harper, C. (1996). *Handbook of plastics, elastomers, and composites (3rd ed.).* New York: McGraw-Hill.

Hay, W.W. (1982). *Railroad Engineering Chapter 23: Concrete and Other Artificial Ties*. Edition 2nd International Heavy Haul Association (IHHA) (2001). Guidelines to Best Practices for Heavy Haul Railway Operations, Wheel and Rail Interface Issues, D. & F. Scott Publishing, Inc. North Richland Hills, Texas, 2001

Hepburn, C. (1982). *Polyurethane elastomers.* London: Applied Science.

International Heavy Haul Association (IHHA) (2009). Guidelines to Best Practices for Heavy Haul Railway Operations, Infrastructure Construction and Maintenance Issues, D. & F. Scott Publishing, Inc. North Richland Hills, Texas, 2009

Kash, D. (1983). *Rail Systems Using Concrete Crossties*. Lone Star Industries, Inc.

Kerokoski, O., Nurmikolu A., Rantala, T. (2012). Loading tests of concrete monoblock railway sleepers. *Nordic Concrete Research*, Vol 45, 1-13, June 2012

Koffman, J.L. (1972). Locomotive Axleloads. Rail Engineering International, Vol 2, 414-415

Lombard, P.C. (1974). Track structure: a relationship between structure parameters. *Traffic Loading and Maintenance*. Draft of master thesis, University of Pretoria, South Africa

Mendis, P., (2003). Design of high-strength concrete members, state-of-the-art. *Structural Engineering and Materials*, 5(1), 1-15

NGI 2005. Sustained performance of railway tracks. Norwegian Geotechnical Institute (NGI)

Olson, E., Johnsson, S. (1960). Lateral forces between wheels and rails, ASME Paper No. 60-RR-6

ORE (1965). *Stresses in Rails, Question D 17, Stresses in the Rails, the Ballast and the Formation Resulting from Traffic Loads*. Report D71/RPI/E, Utrecht

Prause, R.H., Meacham, H.C. (1974). *Assessment of Design Tools and Criteria for Urban Rail Track Structures, Vol.1, At-Grade-Tie-Ballast Track*. Battelle Columbus Laboratories, UMTA Report No. UMTA-MA-06-0025-74-4, National Technical Information Service, US Dept. of Commerce, Springfield, VA

Remennikov, A.M., Kaewunruen, S. (2007). Investigation of free vibrations of voided concrete sleepers in railway track system. Institution of Mechanical Engineers, Part F: Journal of Rail and Rapid Transit, 2007, 221: 495-507

RT&S (2008). M/W budgets to climb in 2008. Railway Track & Structures, New York, NY, Simmons-Boardman Publishing Company, 104(1): 18-25, January, 2008

Schramm, G. (1961). *Permanent Way Technique and Permanent Way Economy*. Otto Elsner Verlagsgesellschaft Darmstadt

Taherinezhad, J., Sofi, M., Mendis, P.A., Ngo, T. A review of behavior of prestressed concrete sleepers. *Electronic Journal of Structural Engineering*, 13(1) 2013

Thun, H., Utsi, S., Elfgren, L. (2008). Loading carrying capacity of cracked concrete railway sleepers. *Structural Concrete*, Volume 9, Issue 3, 01 September 2008, pages 153 –161

UIC (2004). *UIC 713-2004: Design of Monoblock Concrete Sleepers*. International Union of Railways (UIC)

Van Dyk, B.J., Dersch, M.S., Edwards, J.R. (2012). International concrete crosstie and fastening system survey – final results. Submitted for US DOT and FRA

Van Dyk, B.J., Dersch, M.S., Edwards, J.R., Ruppert, C.J., Barkan, C.P.L. (2014). Evaluation of dynamic and impact wheel load factors and their application for design. Transportation Research Board 93rd Annual Meeting

Wei, S., Kuchma, D.A., Edwards, J.R., Dersch, M.S., and Kernes, R.G. (2014). "Gauging of concrete crossties to investigate load path in laboratory and field testing", Joint Rail Conference, April 2-4, 2014, CO, USA

Williams, B.A., Edwards J.R., Kernes, R.G. and Barkan, C.P.L. (2014). Analysis of the Lateral Load Path in Concrete Crosstie Fastening Systems. In: Proceedings of the 2014 Joint Rail Conference, Colorado Springs, USA, April 2014.

Yu, H., Jeong D. (2010). Finite element modeling of railroad concrete crossties – a preliminary study. ICRE2010 – International Conference on Railway Engineering, Beijing, China, 2010

Yu, H., Jeong, D., Choros, J., Sussmann, T. (2011). Finite element modeling of prestressed concrete crosstie with ballast and subgrade support. ASME 2011 International Design

Engineering Technical Conference & Computers and Information in Engineering Conference, Washington, DC, USA, 2011

Zarembski, A.M. (1993) Concrete vs. wood ties: making the economic choice. Conference on Maintaining Railway Track: Determining Cost and Allocating Resources, Arlington, VA

Zeman, J.C., Edwards, J.R., Barkan, C.P.L., Lange, D.A. (2009). Failure mode and effect analysis of concrete ties in north America. International Heavy Haul Association Conference, Shanghai, China

Zhang, Z., Wei, S., Andrawes, B., Kuchma, D.A., and Edwards, J.R. (2016). "Numerical and experimental study on dynamic behavior of concrete sleeper track caused by wheel flat", International Journal of Rail Transportation, Vol 4, Issue 1, 2016